ABSTRACT

Title of dissertation: TRANSPORT IN RAYLEIGH-STABLE EXPERIMENTAL TAYLOR-COUETTE FLOW AND GRANULAR ELECTRIFICATION IN A SHAKING EXPERIMENT

Freja Nordsiek, Doctor of Philosophy, 2015

Dissertation directed by: Professor Daniel P. Lathrop
Department of Physics

This dissertation consists of two projects: Rayleigh-stable Taylor-Couette flow and granular electrification.

Taylor-Couette flow is the fluid flow in the gap between two cylinders rotating at different rates. Azimuthal velocity profiles, dye visualization, and inner cylinder torques were measured on two geometrically similar Taylor-Couettes with axial boundaries attached to the outer cylinder, the Maryland and Twente T3C experiments. This was done in the Rayleigh stable regime, where the specific angular momentum increases radially, which is relevant to astrophysical and geophysical flows and in particular, stellar and planetary accretion disks. The flow substantially deviates from laminar Taylor-Couette flow beginning at moderate Reynolds number. Angular momentum is primarily transported to the axial boundaries instead of the outer cylinder due to Ekman pumping when the inner cylinder is rotating faster than the outer cylinder. A phase diagram was constructed from the transitions identified

from torque measurements taken over four decades of the Reynolds number. Flow angular velocities larger and smaller than both cylinders were found. Together, these results indicate that experimental Taylor-Couette with axial boundaries attached to the outer cylinder is an imperfect model for accretion disk flows.

Thunderstorms, thunder-snow, volcanic ash clouds, and dust storms all display lightning, which results from electrification of droplets and particles in the atmosphere. While lightning is fairly well understood (plasma discharge), the mechanisms that result in million-volt differences across the storm are not. A novel granular electrification experiment was upgraded and used to study some of these mechanisms in the lab. The relative importance of collective interactions between particles versus particle properties (material, size, etc.) on collisional electrification was investigated. While particle properties have an order of magnitude effect on the strength of macroscopic electrification, all particle types electrified with dynamics that suggest a major role for collective interactions in electrification. Moreover, mixing two types of particles together does not lead to increased electrification except for specific combinations of particles which clump, which further points towards the importance of collective phenomena. These results help us better understand the mechanisms of electrification and lightning generation in certain atmospheric systems.

TRANSPORT IN RAYLEIGH-STABLE EXPERIMENTAL TAYLOR-COUETTE FLOW AND GRANULAR ELECTRIFICATION IN A SHAKING EXPERIMENT

by

Freja Nordsiek

Dissertation submitted to the Faculty of the Graduate School of the
University of Maryland, College Park in partial fulfillment
of the requirements for the degree of
Doctor of Philosophy
2015

Advisory Committee:
Professor Daniel P. Lathrop, Chair/Advisor
Professor Derek C. Richardson, Dean's Representative
Professor Adil B. Hassam
Professor Wolfgang Losert
Professor Rajarshi Roy

Preface

This thesis is on two different projects in non-linear dynamics.

The first part, which is Chapters 1–6, is on Taylor-Couette flow. Taylor-Couette flow is in the subject of fluid dynamics.

The second part, which is Chapters 7–11, is on granular electrification. Granular electrification is in the subject of granular media & flows.

The chapters titles for each part are prefixed with TC and GE to denote that they are for Taylor-Couette flow and Granular Electrification respectively.

Acknowledgments

The work on the three experiments presented in this thesis would not have been possible without the guidance, expertise, and work from our technicians Don Martin, Nolan Ballew, Gert-Wim Bruggert, Martin Bos, and Bas Benschop. Similarly, this research would not have been possible without the help of Nancy Boone, Dorothea Brosius, Edward Condon, Roxanne Defendini, Leslie Delabar, Margaret Hess, Jane Hessing, Mohini Kaul, Joanita Leferink, Linda Ohara, and Kathryn Tracy in the IREAP and Department of Physics of UMD and the Physics of Fluids Group at the University of Twente staffs. In addition, the Maryland Taylor-Couette experiment as well as the laboratory it is housed in would be in serious trouble if it wasn't for the staff in Operations & Maintenance who have kept the AC's drain from clogging and flooding the lab as well as coming in to unclog it when it first started to periodically clog and leak water, including once at 3 AM in the morning.

Special thanks goes to my Ph.D advisor Daniel P. Lathrop. It has been a good 5 years and his advice was particularly crucial in the early days of both projects as well as learning to become a better scientific writer and "bricolage cowboy", as some have put it.

I also want to thank my undergraduate advisor Raymond A. Shaw. He has continued to be a strong mentor since I left his group, and we have had many useful scientific discussions on the projects in this thesis.

The granular electrification project owes considerably to the past work on the project, including construction of much of the current apparatus, by and discus-

sions with Paul Lathrop, Zack Lasner, Julia Salevan (Salevan 2012), Tyler Holland-Ashford, Eric Speiglan, and Allison Bradford.

I would like to thank the many members, past and present, of my research group (the Nonlinear Dynamics Laboratory) at University of Maryland for all their help, discussions, advice, editing of manuscripts, editing of this thesis, etc. such as Matthew Adams, Robby Blum, Barbara Brawn-Cinani, Tyler Holland-Ashford, Onur Kara, Zack Lasner, Daniel. P. Lathrop, Don Martin, Peter Megson, David P. Meichle, Matthew S. Paoletti, Julia Salevan, Daniel Serrano, Sonali Shukla, Eric Speiglan, Doug Stone, Santiago Triana, and Daniel S. Zimmerman.

I want to thank my collaborators Sander G. Huisman, Detlef Lohse, Chao Sun, and Roeland C.A. van der Veen at the University of Twente. In addition to taking data and writing a paper together, we had many useful discussions and I learned a lot from them. Moreover, they along with the Joanita Leferink, Gert-Wim Bruggert, Martin Bos, and Bas Benschop made the collaboration possible, useful, and enjoyable.

This work would not have been possible without the helpful discussions and advice from Marc Avila, Bruno Eckhardt, Eric M. Edlund, Dennis P.M. van Gils, Hantao Ji, Siegfried Grossmann, Aaron Hagerstrom, Matthew Harrington, Christine M. Hartzell, Rodolfo Ostilla-Mónico, Seth J. Putterman, Derek Richardson, and Devaraj van der Meer. I also thank Scott R. Waitukaitis for the suggestion to use 69%:31% ZrO_2:SiO_2 particles in the granular electrification experiment.

Several researchers have given me access to their data, some of which was used directly in this thesis, but all of which was indispensable. I want to thank Marc

Avila (Avila 2012), Hantao Ji (Kageyama et al. 2004; Schartman et al. 2012; Edlund and Ji 2014), Eric M. Edlund (Edlund and Ji 2014), Ethan Schartman (Schartman et al. 2012), Bruno Eckhardt (Brauckmann and Eckhardt 2013), Matthew S. Paoletti (Paoletti and Lathrop 2011), Julia Salevan (Salevan 2012), and Allison Bradford for the use of their data.

I thank John H. Abrahams III at the Center for Nanophysics and Advanced Materials at the University of Maryland College Park for the microscopy characterizing the powders. In addition, I thank John W. Merck, Jr. and Mike Lyvers for permission to use their images of lightning.

This research was partially funded by the National Science Foundation of the USA (Grant No. NSF-DMR 0906109) and the Julian Schwinger Foundation.

Table of Contents

List of Tables

List of Figures

List of Abbreviations and Symbols

The description begins with "TC" or "GE" to indicate that it is was used in the Taylor-Couette and granular electrification parts of the thesis respectively. Some symbols are used in both parts, either with the same meaning or different meanings. In the latter case, both meanings are given.

α	TC local powerlaw scaling exponent (Equation 5.2)
β	TC coefficient of the local powerlaw (Equation 5.2)
δ	TC separation between parallel plates (Figure 1.2)
η	TC radius ratio (Equation 1.19)
λ	GE dimensionless particle slab thickness (Equation 8.2)
ν	TC fluid kinematic viscosity
μ	TC ratio of outer to inner rotation rates (Equation 1.29)
ϕ	GE phase in oscillation cycle
ρ	density
$\hat{\rho}$	TC dimensionless density
σ	TC geometric Prandtl number (Equation 1.26)
τ	TC azimuthal shear stress
ω	TC fluid angular velocity
ω_s	TC super-rotation angular velocity
$\widetilde{\omega}$	TC normalized fluid angular velocity (Equation 1.32)
$\widetilde{\omega}_{\text{lam}}$	TC normalized laminar fluid angular velocity (Equation 1.35)
Γ	TC aspect ratio (Equation 1.20)
Ω	TC angular velocity
$\vec{\mathbf{\Omega}}$	TC angular velocity vector
$\hat{\mathbf{\Omega}}$	TC angular velocity unit vector
Ω_i	TC inner cylinder angular frequency of rotation
Ω_o	TC outer cylinder angular frequency of rotation
a	TC negative ratio of outer to inner rotation rates (Equation 1.30) GE acceleration amplitude of the cell
b	TC fitting constant
c	TC fitting constant
d	TC gap width GE particle diameter (or effective particle diameter for powders)
$\vec{\mathbf{f}}$	TC body force per unit mass
$\hat{\mathbf{f}}$	TC dimensionless body force per unit mass
g	GE acceleration due to gravity on Earth's surface
h	GE particle slab thickness (Equation 8.1)

ℓ	TC specific axial angular momentum
p	TC pressure
$\hat{p}$	TC dimensionless pressure
p_0	TC zeroth order term of polynomial fits
p_1	TC first order term of polynomial fits
p_2	TC second order term of polynomial fits
q	TC parameter to quantify global rotation (Equation 1.23)
r	TC cylindrical radial coordinate
$\widetilde{r}$	TC normalized radial coordinate (Equation 1.31)
$\vec{\mathbf{r}}$	TC position vector
$\hat{\mathbf{r}}$	TC dimensionless position vector
r_c	TC transition radius (Equation 3.5)
$\widetilde{r}_c$	TC normalized transition radius (Equation 3.6)
r_i	TC inner cylinder radius
r_o	TC outer cylinder radius
r_{inj}	TC radial position of the injector
$\widetilde{r}_{\text{inj}}$	TC normalized radial position of the injector
t	time
$\hat{t}$	TC dimensionless time
u_θ	TC azimuthal velocity
$u_{\theta,\text{lam}}$	TC laminar azimuthal velocity (Equation 1.34)
u^*	TC friction velocity
x_i	TC the ith component of the position vector
$\hat{x}_i$	TC the ith component of the dimensionless position vector
y_0	TC thickness of the viscous sublayer
y_0^+	dimentionless thickness of the viscous sublayer
z	TC axial height from the bottom axial boundary
z_c	GE vertical position of the inside surface of the cell's bottom plate
z_p	GE vertical position of the kinematic model particle (Section 8.3.2)
A	TC plate area.
D	GE cell diameter
F	TC force (Figure 1.2)
G	TC dimensionless torque (Equation 1.33)
G_{lam}	TC dimensionless laminar torque (Equation 1.37)
$G_{+\infty}$	TC dimensionless torque for pure inner rotation
H	GE cell height
K	GE polarity kernel (Equation 10.2)
L	TC height of the cylinders GE stroke length

$\mathcal{L}$	TC length scale
L_e	TC height of the top and bottom sections of the inner cylinder
L_{mid}	TC height of the inner cylinder middle section
N_p	GE number of particles
N_{against}	TC number videos where fluid rotates against the inner cylinder
N_{both}	TC number videos where fluid rotates both directions
N_{with}	TC number videos where fluid rotates with the inner cylinder
$N_{b\to t}$	GE number of phase bins for model particle from bottom to top plate
$N_{t\to b}$	GE number of phase bins for model particle from top to bottom plate
Nu_ω	TC "Nusselt number"
P	GE polarity value (Equation 10.1)
$\hat{P}$	TC dimensionless reduced pressure
$\mathcal{R}$	TC density scale
$\hat{R}$	TC dimensionless distance in a plane orthogonal to the axis of rotation
R_Ω	TC rotation parameter (Equation 1.27)
Re	TC Reynolds number
Re_i	TC inner cylinder Reynolds number (Equation 1.21)
Re_o	TC outer cylinder Reynolds number (Equation 1.21)
Re_S	TC shear Reynolds number (Equation 1.22)
Re_{mid}	TC Reynolds number about mid-gap (Equation 1.24)
Ro	TC Rossby number (Equation 1.28)
T	$\begin{cases}\text{TC torque}\\ \text{GE shaker oscillation period}\end{cases}$
T_k	TC temperature
T_{lam}	TC laminar torque (Equation 1.36)
T_{offset}	TC torque offset
T_ν	TC torque just from shear stress (Equation 3.7)
$T_{\nu,\text{flat}}$	TC quasi-Keplerian torque lower bound (Equation 3.8)
$T_{+\infty}$	TC torque for pure inner rotation
Ta	TC Taylor number (Equation 1.25)
U	TC fluid velocity
$\vec{\mathbf{U}}$	TC fluid velocity vector
$\vec{\mathbf{U}}'$	TC fluid velocity vector in the rotating frame
$\hat{\mathbf{U}}$	TC dimensionless fluid velocity vector in the rotating frame
$\mathcal{U}$	TC fluid velocity scale
W	TC degree that the fluid rotates with the inner cylinder (Equation 4.1)

DAQ	Data Acquisition System
DNS	Direct Numerical Simulation
DRUM	Digital Repo. at the Univ. of Maryland (`http://drum.lib.umd.edu`)

GE	Granular Electrification
IREAP	Institute for Research in Electronics and Applied Physics
LDA	Laser Doppler Anenometry (also called LDV)
LDV	Laser Doppler Velocimetry (also called LDA)
MRI	Magneto-Rotational Instability
PIV	Particle Image Velocimetry
PS	polystyrene
PTFE	polytetrafluoroethylene
QK	quasi-Keplerian
RMS	Root Mean Squared
SR	sub-rotating
STD	Standard Deviation
TC	Taylor-Couette (also called Couette-Taylor)
T^3C	Twente Turbulent Taylor-Couette
UDV	Ultrasound Doppler Velocimetry
UN	Rayleigh-unstable
ZrO	69%:31% ZrO_2:SiO_2

Chapter 1: TC: Introduction

Partially adapted from and expanded upon the arXiv version of

F. Nordsiek, S. G. Huisman, R. C. A. van der Veen, C. Sun, D. Lohse, and D. P. Lathrop. Azimuthal velocity profiles in Rayleigh-stable Taylor-Couette flow and implied axial angular momentum transport. *Journal of Fluid Mechanics*, 774:342–362, July 2015.

DOI: 10.1017/jfm.2015.275

ADS: 2015JFM...774..342N

arXiv: 1408.1059 [physics.flu-dyn]

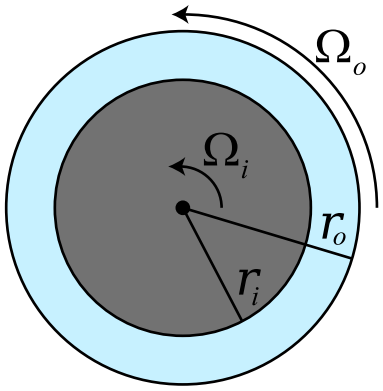

Figure 1.1: Taylor-Couette flow from above. The inner cylinder, shaded dark grey, has radius r_i and rotates at an angular velocity Ω_i. The outer cylinder, outer black circle, has radius r_o and rotates at an angular velocity Ω_o. A fluid, shaded light blue, fills the gap between the two cylinders.

1.1 Overview

Rotating shear flows are common in nature. Geophysical and astrophysical examples include the interiors of planets and stars, planetary atmospheres, and stellar and planetary accretion disks. Since direct observations and measurements are hard to perform for many of these flows, laboratory models that incorporate the essential features of these flows can be useful.

A common simple rotating shear flow that can be implemented in the laboratory is Taylor-Couette (TC) flow, which is the flow in the fluid-filled gap between two coaxial rotating cylinders. A downward view from above the cylinders is shown in Figure 1.1. Note that it is sometimes known as Couette-Taylor flow. Taylor-Couette flow has found particular applicability as a model for astrophysical accretion disks in determining their stability properties and the outward angular momentum flux which is necessary in order for material to be transported inward onto the central body (Zeldovich 1981; Richard and Zahn 1999; Richard 2001; Dubrulle et al. 2005a;

Ji and Balbus 2013). Taylor-Couette experiments have produced contradictory answers to questions regarding stability and the rate of angular momentum transport, causing great debate centered on the effects of the no-slip axial boundaries found in Taylor-Couette experiments which do not match the open stratified boundaries of accretion disks (Balbus 2011; Avila 2012; Schartman et al. 2012; Ji and Balbus 2013; Edlund and Ji 2014).

1.2 Fluid Mechanics

Fluids are materials that continuously strain under the influence of any stress applied to them, no matter how small. A simplest example is the case of a fluid contained between two parallel plates when a tangential force is applied to one plate, which is shown in Figure 1.2. No matter how small the applied force is, the plate will move and the fluid will move in the direction of the moving plate.

A Newtonian fluid is defined as a fluid for which the fluid flows horizontally at a velocity $U(z)$ that is linear in the coordinate across the gap z and proportional to the applied force F for small enough F. The force is then $F/A = \nu\rho U\left(\delta\right)/\delta$ where A is the area of the plate, δ is the plate separation, ρ is the fluid density, and ν is a proportionality constant and has units of $length^2/time$. This proportionality constant is called the kinematic viscosity. Physically, it is the diffusivity of momentum. For a Newtonian fluid, it is not a function of the stress or strain (movement of the plate in this example). Most gases and liquids without suspended particles are Newtonian fluids. Examples include water and air. For the Taylor-Couette part of

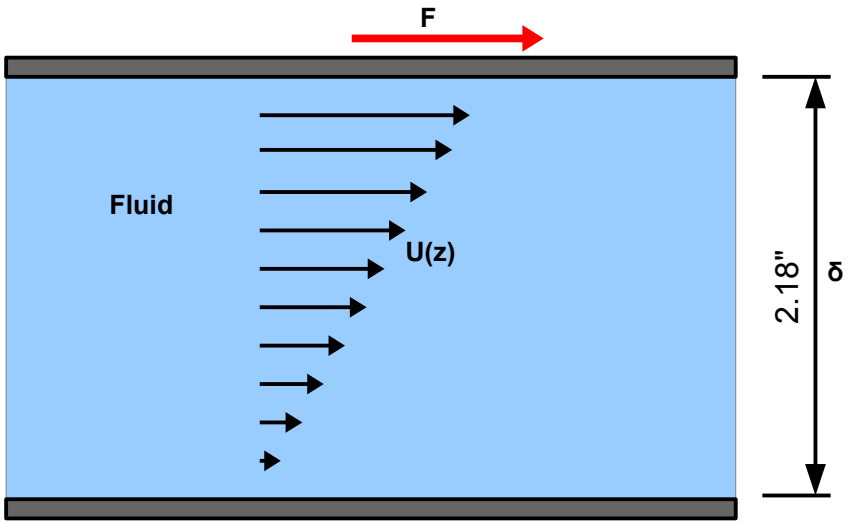

Figure 1.2: Fluid (light blue) being sheared between two parallel plates (dark grey) separated by a distance δ. A horizontal force F is applied to the top plate. The fluid between the plates is moving in the direction of the force with velocity $U(z)$ where z is the vertical coordinate between the plates.

this thesis, only Newtonian fluids are considered.

The motion of Newtonian fluids can be described by continuum equations that are partial differential equations. We consider the case of an incompressible fluid. For fluid velocities much less than a the speed of sound in the fluid, as we consider exclusively in this thesis, this is a good approximation (Holton 2004). For an incompressible Newtonian fluid, the equations of motion are

$$\frac{\mathrm{D}\vec{\mathbf{U}}}{\mathrm{D}t} = -\frac{1}{\rho}\nabla p + \nu\nabla^2\vec{\mathbf{U}} + \vec{\mathbf{f}} \tag{1.1}$$

$$\nabla \bullet \vec{\mathbf{U}} = 0 \tag{1.2}$$

where $\vec{\mathbf{U}}$ is the fluid velocity vector, p is the pressure, $\vec{\mathbf{f}}$ is the external force on the fluid per unit mass, and $\frac{\mathrm{D}}{\mathrm{D}t}$ is the material derivative (Holton 2004). The first

equation (Equation 1.1) is Newton's 2nd Law for a Newtonian fluid, which is known as the Navier-Stokes Equations. The left side is equivalent to the acceleration. The terms on the right hand side are the pressure gradient force, diffusion of momentum, and external body forces per unit mass.

The second equation (Equation 1.2) is conservation of mass for an incompressible fluid, which is known as the Continuity Equation. The material derivative is the operator that takes the time derivative while following the fluid itself, which takes into account advection of the fluid. Newton's 2nd Law is applied to objects. Since the fluid parcel that one is applying Newton's 2nd Law to is moving (advecting), our time derivative has to follow the fluid as it flows. The material derivative is defined as

$$\frac{\mathrm{D}}{\mathrm{D}t} \equiv \frac{\partial}{\partial t} + \left(\vec{\mathbf{U}} \bullet \nabla\right) = \frac{\partial}{\partial t} + \sum_i U_i \frac{\partial}{\partial x_i} \tag{1.3}$$

where x_i are the ith spatial coordinate and U_i is the ith component of $\vec{\mathbf{U}}$. Since $\mathrm{D}\vec{\mathbf{U}}/\mathrm{D}t$ has products of the components of $\vec{\mathbf{U}}$ with their spatial derivatives, the Navier-Stokes Equations are non-linear. Despite concerted effort for over 150 years, general solutions to Equations 1.1 and 1.2 have not yet been found in two or three dimensions due to this non-linearity. In fact, this problem is even one of the Millennium Problems (`http://www.claymath.org/millennium-problems`).

It is desirable to look at the Navier-Stokes Equations (Equation 1.1) in a rotating frame since Taylor-Couette, as well as many astrophysical and geophysical flows, rotate. In a reference frame rotating at a constant angular velocity $\vec{\mathbf{\Omega}}$ about

an axis going through the origin, they are

$$\frac{\partial \vec{\mathbf{U}}'}{\partial t} + \left(\vec{\mathbf{U}}' \bullet \nabla\right) \vec{\mathbf{U}}' = -\frac{1}{\rho}\nabla p + \nu \nabla^2 \vec{\mathbf{U}}' - \vec{\mathbf{\Omega}} \times \left(\vec{\mathbf{\Omega}} \times \vec{\mathbf{r}}\right) - 2\left(\vec{\mathbf{\Omega}} \times \vec{\mathbf{U}}'\right) + \vec{\mathbf{f}} \quad (1.4)$$

where $\vec{\mathbf{U}}' = \vec{\mathbf{U}} - \vec{\mathbf{\Omega}} \times \vec{\mathbf{r}}$ is the fluid velocity in the rotating frame and $\vec{\mathbf{r}}$ is the vector position (Holton 2004). The terms on the right-hand side involving rotation are the "centrifugal force" and "Coriolis force" terms (they are fictitious forces that appear in rotating reference frames). By adopting a characteristic length scale $\mathcal{L}$, fluid velocity scale $\mathcal{U}$, density scale $\mathcal{R}$, time scale $\frac{\mathcal{L}}{\mathcal{U}}$, and pressure scale $\mathcal{R}\mathcal{U}^2$; we can make Equation 1.4 dimensionless by the transformations

$$x_i \Rightarrow \mathcal{L}\,\hat{x}_i \tag{1.5}$$

$$\vec{\mathbf{U}}' \Rightarrow \mathcal{U}\,\hat{\mathbf{U}} \tag{1.6}$$

$$t \Rightarrow \left(\frac{\mathcal{L}}{\mathcal{U}}\right)\hat{t} \tag{1.7}$$

$$\rho \Rightarrow \mathcal{R}\,\hat{\rho} \tag{1.8}$$

$$p \Rightarrow \mathcal{R}\mathcal{U}^2\,\hat{p} \tag{1.9}$$

$$\frac{\partial}{\partial x_i} \Rightarrow \left(\frac{1}{\mathcal{L}}\right)\frac{\partial}{\partial \hat{x}_i} \tag{1.10}$$

$$\frac{\partial}{\partial t} \Rightarrow \left(\frac{\mathcal{U}}{\mathcal{L}}\right)\frac{\partial}{\partial \hat{t}} \tag{1.11}$$

$$\nabla \Rightarrow \left(\frac{1}{\mathcal{L}}\right)\hat{\nabla} \tag{1.12}$$

$$\frac{\mathrm{D}}{\mathrm{D}t} \Rightarrow \left(\frac{\mathcal{U}}{\mathcal{L}}\right)\frac{\hat{\mathrm{D}}}{\hat{\mathrm{D}}\hat{t}} \tag{1.13}$$

$$\vec{\mathbf{r}} \Rightarrow \mathcal{L}\,\hat{\mathbf{r}} \tag{1.14}$$

$$\vec{\mathbf{f}} \Rightarrow \left(\frac{\mathcal{U}^2}{\mathcal{L}}\right)\hat{\mathbf{f}} \tag{1.15}$$

where the ith component of $\hat{\nabla}$ is $\frac{\partial}{\partial \hat{x}_i}$. This results in the following dimensionless Navier-Stokes Equations in a rotating frame

$$\frac{\hat{\mathrm{D}}\hat{\mathbf{U}}}{\hat{\mathrm{D}}\hat{t}} = -\frac{1}{\hat{\rho}}\hat{\nabla}\hat{P} + \frac{1}{Re}\hat{\nabla}^2\hat{\mathbf{U}} - \frac{2}{Ro}\left(\hat{\mathbf{\Omega}} \times \hat{\mathbf{U}}\right) + \hat{\mathbf{f}} \tag{1.16}$$

where $\hat{P} = \hat{p} - \left(\frac{\mathcal{R}}{2Ro^2}\right)\hat{R}^2 = \hat{p} - \left(\frac{\mathcal{R}}{2Ro^2}\right)\hat{\mathbf{\Omega}} \times \left(\hat{\mathbf{\Omega}} \times \hat{\mathbf{r}}\right)$ is the dimensionless reduced pressure, $\hat{R}$ is the dimensionless distance in a plane orthogonal to the axis of rotation, $\vec{\mathbf{\Omega}} = \Omega\hat{\mathbf{\Omega}}$, Re is the Reynolds number, and Ro is the Rossby number. The Reynolds

and Rossby numbers are defined as

$$Re = \frac{\mathcal{U}\mathcal{L}}{\nu} \tag{1.17}$$

$$Ro = \frac{\mathcal{U}}{\mathcal{L}\Omega}\,. \tag{1.18}$$

Physically, the Reynolds number is the ratio of inertia to viscous dampening; and the Rossby number is the ratio of inertia to the "Coriolis force".

When $\nu = 0$, Equation 1.16 reduces to the Euler Equation. When ν and $\frac{\hat{\mathrm{D}}\hat{\mathbf{U}}}{\hat{\mathrm{D}}\hat{t}}$ are negligible, we get geostrophic flow (Holton 2004). When $Re \to \infty$ and advection is negligible (only the time derivative term in $\frac{\hat{\mathrm{D}}\hat{\mathbf{U}}}{\hat{\mathrm{D}}\hat{t}}$ is significant), we get a Poincaré Equation which then allows for inertial waves (Zhang et al. 2001; Liao and Zhang 2009; Zimmerman 2010; Triana 2011).

1.3 Parameterization

1.3.1 Parameter Space

In addition to the specification of the axial boundaries, Taylor-Couette flow requires a total of four dimensionless parameters to specify its parameter space. Two are needed for the geometry to specify the cylinder radii and the gap height, and two are needed to specify the rotation rates of the cylinders. The two parameters that are the most popular to specify the geometry are the radius ratio, η, and the aspect ratio, Γ, given by

$$\eta = r_i/r_o \tag{1.19}$$

$$\Gamma = L/\left(r_o - r_i\right) \ . \tag{1.20}$$

where r_i is the outer radius of the inner cylinder, r_o is the inner radius of the outer cylinder, and L is the height of the cylinders. Physically, Γ is the ratio of the height of the cylinders L to the gap width $d = r_o - r_i$.

Two dimensionless parameters specifying the rotation rates of the cylinders can be obtained by defining a Reynolds number for each cylinder using the gap-width d as the length scale $\mathcal{L}$, $r_i\Omega_i$ and $r_o\Omega_o$ as the velocity scales $\mathcal{U}$ where the inner (outer) cylinder angular velocities are Ω_i (Ω_o), and the fluid's kinematic viscosity ν. They are

$$Re_i = \frac{\Omega_i\, r_i\, (r_o - r_i)}{\nu}, \quad Re_o = \frac{\Omega_o\, r_o\, (r_o - r_i)}{\nu} \ . \tag{1.21}$$

Rather than using Re_i and Re_o, we use a single parameter to quantify the shear (difference in cylinder rotation rates) and another to quantify the global rotation (relates to the ratio of rotation rates). We will primarily use the shear Reynolds number Re_S and the so-called q parameter, detailed below, to compare different parts of the parameter space. The shear Reynolds number $Re_S \propto |\Omega_i - \Omega_o|$, which

quantifies shear (Dubrulle et al. 2005a), is defined as

$$Re_S = \frac{2}{1+\eta} \left| Re_i - \eta Re_o \right| \ . \tag{1.22}$$

The q parameter (Ji et al. 2006; Schartman et al. 2012) is defined as

$$\eta^{-q} = \frac{\Omega_i}{\Omega_o} = \frac{Re_i}{\eta Re_o} \tag{1.23}$$

The q parameter is real for co-rotating cylinders, the case exclusively dealt with in this paper. Hence, we will define both Ω_i and Ω_o to be both positive throughout this paper. Note that $\eta < 1$. Solid-body rotation $\Omega_i = \Omega_o$ corresponds to $q = 0$, $\Omega_i > \Omega_o$ gives $q > 0$, $\Omega_i < \Omega_o$ gives $q < 0$, and pure inner and pure outer rotation correspond to $q = +\infty$ and $q = -\infty$ respectively.

Different dimensionless parameters other than Re_S and q have been used in the literature, which we present here for comparison. Other ways to quantify the shear include a Reynolds number $Re_{\rm mid}$ using mid-gap as the distance to calculate angular velocities (Schartman et al. 2009, 2012; Paoletti et al. 2012) and a Taylor number Ta that is approximately Re_S^2 (Eckhardt et al. 2007; van Gils et al. 2011b, 2012), which are defined as

$$Re_{\rm mid} = \frac{(r_o - r_i)(r_i + r_o)(\Omega_i - \Omega_o)}{2\nu} = \sqrt{\sigma} Re_S \tag{1.24}$$

$$Ta = \sigma \left[\frac{(r_o - r_i)(r_i + r_o)(\Omega_i - \Omega_o)}{2\nu} \right]^2 = (\sigma\, Re_S)^2 \tag{1.25}$$

where σ is the geometric Prandtl number (Eckhardt, Grossmann, and Lohse 2007), which is defined as

$$\sigma = \left(\frac{1+\eta}{2\sqrt{\eta}} \right)^4 . \tag{1.26}$$

For the Taylor-Couette experiments in this thesis have$\eta \approx 0.72$, and therefore $\sigma \approx 1$.

Alternative parameters quantifying global rotation are the rotation parameter R_Ω (Dubrulle et al. 2005a), a Rossby number Ro (Paoletti and Lathrop 2011), and the ratio of the cylinder rotation rates Ω_o/Ω_i and its negative. They are defined as

$$R_\Omega = \frac{(1-\eta)(Re_i + Re_o)}{\eta Re_o - Re_i} = \frac{(1-\eta)(\eta^{q-1}+1)}{\eta^q - 1} \tag{1.27}$$

$$Ro = \frac{\Omega_i - \Omega_o}{\Omega_o} = \eta^{-q} - 1 \tag{1.28}$$

$$\mu = \frac{\Omega_o}{\Omega_i} = \eta^q \tag{1.29}$$

$$a = -\left(\frac{\Omega_o}{\Omega_i} \right) = -\eta^q . \tag{1.30}$$

This definition of the Rossby number is in the frame of the outer cylinder (Ω_o is the rotation rate), uses r_i as the length scale $\mathcal{L}$, and uses the tangential velocity inner cylinder in the frame of the outer cylinder $r_i(\Omega_i - \Omega_o)$ as the velocity scale $\mathcal{U}$.

We will be specifying the parameter space primarily in terms of (q, Re_S, η, Γ), but occasionally in terms of (Ro, Re_S, η, Γ) and (Re_i, Re_o, η, Γ). Note that the cylinder rotation rates can be quantified uniquely up to absolute sign (relative sign is specified) by choosing any any pair of parameters from different sets of the

following four sets: $\{Re_i\}$, $\{Re_o\}$, $\{Re_S, Re_{\text{mid}}, Ta\}$, and $\{q, R_\Omega, Ro, \mu, a\}$.

1.3.2 Velocities and Torque

We define u_θ as the fluid azimuthal velocity. Then the fluid azimuthal angular velocity is $\omega = u_\theta / r$. It is convenient to look at the azimuthal velocities in terms of the normalized radial position and the normalized angular velocity given by

$$\widetilde{r} = \frac{r - r_i}{d}\,, \tag{1.31}$$

$$\widetilde{\omega} = \frac{\omega - \Omega_o}{\Omega_i - \Omega_o}\,, \tag{1.32}$$

where $d = r_o - r_i$ is the width of the gap. The expression for $\widetilde{r}$ gives $\widetilde{r} = 0$ at the inner cylinder and $\widetilde{r} = 1$ at the outer cylinder. Regardless of which cylinder has the larger angular velocity, the expression for $\widetilde{\omega}$ gives $\widetilde{\omega} = 0$ whenever $\omega = \Omega_o$ and $\widetilde{\omega} = 1$ whenever $\omega = \Omega_i$. Note the sign change in the denominator when $\Omega_i < \Omega_o$ ($q < 0$).

The angular velocity is bounded by that of the cylinders ($\omega \in [\min(\Omega_i, \Omega_o), \max(\Omega_i, \Omega_o)]$) if and only if $\widetilde{\omega} \in [0, 1]$. Otherwise, we have one of the two following situations:

super-rotating flow

The fluid is rotating faster than both cylinders ($\omega > \Omega_i, \Omega_o$). For $q > 0$, this corresponds to $\widetilde{\omega} > 1$, which is $\omega > \Omega_i > \Omega_o > 0$. For $q < 0$, this corresponds to $\widetilde{\omega} < 0$, which is $\omega > \Omega_o > \Omega_i > 0$.

sub-rotating flow

The fluid is rotating slower than both cylinders ($\omega < \Omega_i, \Omega_o$). For $q > 0$, this corresponds to $\widetilde{\omega} < 0$, which is $\Omega_i > \Omega_o > \omega$. For $q < 0$, this corresponds to $\widetilde{\omega} > 1$, which is $\Omega_o > \Omega_i > \omega$.

Let T be the torque required to rotate the inner cylinder at a constant Ω_i (torque applied to the fluid by the inner cylinder). We can construct a dimensionless torque G defined as

$$G = \frac{T}{\rho\nu^2 L_{\text{mid}}} \tag{1.33}$$

constructed from the torques T measured over the middle section of the inner cylinder of length L_{mid}, which will be discussed further in Chapter 2. Note that some definitions of G have a factor of 2π in the denominator. This difference is rarely relevant since the torque is almost always normalized by the dimensionless torque at the same Re_S either for pure inner rotation $G_{+\infty}$ ($q = +\infty$) or for laminar Taylor-Couette flow (Equation 1.37) that will be discussed in the next Section.

1.4 Laminar Taylor-Couette Flow

At low Re_S, before the formation of Taylor-vortices, and in the absence of Ekman pumping from axial boundaries (e.g. periodic or free-slip axial boundary conditions); the flow is purely azimuthal and is a function only of the cylindrical

radial coordinate r. The azimuthal velocity profile is

$$u_{\theta,\mathrm{lam}}(r) = Ar + \frac{B}{r}, \quad A = \frac{\Omega_o - \eta^2\Omega_i}{1-\eta^2}, \quad B = \frac{r_i^2\left(\Omega_i - \Omega_o\right)}{1-\eta^2} \ . \tag{1.34}$$

We will refer to this as laminar Taylor-Couette flow.

The laminar Taylor-Couette azimuthal velocity profile, which in the normalized variables is independent of Ω_i and Ω_o, is

$$\widetilde{\omega}_{\mathrm{lam}} = \frac{\eta^2\left(1-\widetilde{r}\right)\left(\widetilde{r}\left(1-\eta\right)+1+\eta\right)}{\left(1+\eta\right)\left(\widetilde{r}\left(1-\eta\right)+\eta\right)^2} \ . \tag{1.35}$$

As laminar Taylor-Couette flow has no Reynolds stresses and ω is uniform over a cylinder of radius r (Equation 1.34), the total laminar Taylor-Couette torque is

$$T_{\mathrm{lam}} = \frac{2\pi\rho\nu^2 L_{\mathrm{mid}}\eta}{\left(1-\eta\right)^2} Re_S \ \mathrm{sign}\left(Re_i - \eta Re_o\right) \ . \tag{1.36}$$

Then the dimensionless laminar Taylor-Couette torque G_{lam}, obtained from Equation 1.33, is

$$G_{\mathrm{lam}} = \frac{2\pi\eta}{\left(1-\eta\right)^2} Re_S \ . \tag{1.37}$$

In most cases in this thesis, torques are going to be normalized by the laminar Taylor-Couette torque for the same Re_S, which will be labeled as G/G_{lam}. Note that in the literature, this quantity is often described as a "Nusselt number" and given the symbol Nu_ω, making an analogy to Rayleigh-Bénard convection (Eckhardt et al. 2007; van Gils et al. 2011b; Ostilla-Mónico et al. 2014c; Sun and Zhou 2014).

1.5 Rayleigh Stability And Accretion Disks

1.5.1 Rayleigh Stability Criterion

Some rotating flows have radially increasing specific angular momentum. Such flows, as long as they are purely hydrodynamic, barotropic, and stably stratified as we consider here, are stable to infinitesimal perturbations (i.e. linearly stable) according to the Rayleigh criterion (Rayleigh 1917). The Rayleigh criterion is

$$\text{sign}\left(\frac{\partial \ell}{\partial r}\right) = \text{sign}\left(\ell\right) \tag{1.38}$$

where $\ell = r^2\omega$ is the specific angular momentum.

For Taylor-Couette flow, this corresponds to $q < 2$. Hence $q = 2$ is referred to as the Rayleigh line.

Flows for which $q > 2$ are linearly unstable (unstable to an infinitesimal perturbation) at sufficiently high Reynolds numbers (Taylor 1923), which is often called the centrifugal instability. The Rayleigh-stable region includes sub-rotation ($\Omega_i < \Omega_o$), solid-body rotation ($\Omega_i = \Omega_o$), and super-rotation ($\Omega_i > \Omega_o$). The flow in the super-rotating region is often referred to as quasi-Keplerian, since it includes cylinder rotation rates ($q = 3/2$) obeying Kepler's 3rd law relating orbital radius and period. These different regions are shown in the Taylor-Couette rotation parameter space in Figure 1.3.

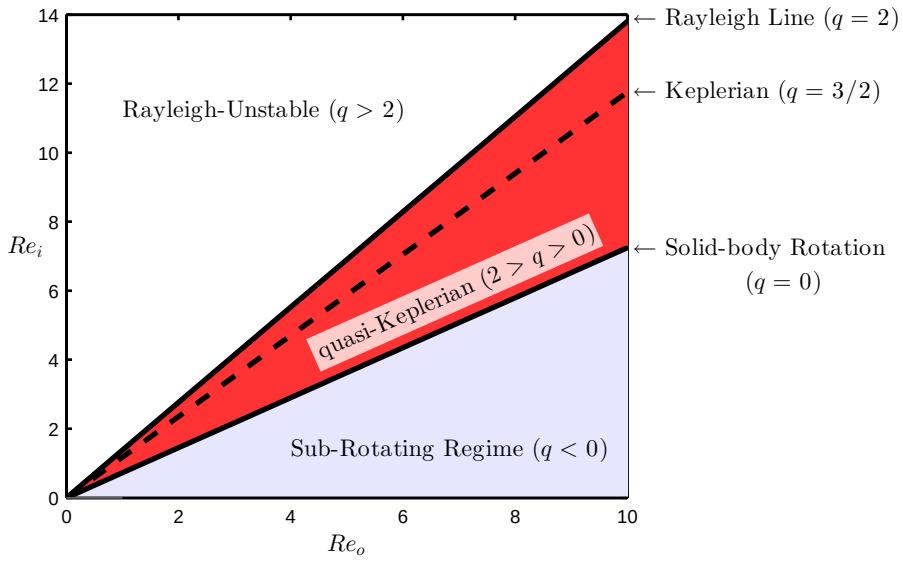

Figure 1.3: Taylor-Couette parameter space. The different regions are shown as well as three important lines of constant q: the Rayleigh line ($q = 2$), the Keplerian line ($q = 3/2$), and solid-body rotation ($q = 0$). The whole Rayleigh-stable region ($q < 2$) is shaded with different colors for the quasi-Keplerian regime (red) and the sub-rotating regime (grey).

1.5.2 Astrophysical Accretion Disks

This regime is of particular relevance to astrophysical systems such as accretion disks since they are Rayleigh-stable with azimuthal flow profiles in the plane of the disk that are expected to not deviate significantly from Kepler's 3rd law when the disk's self-gravitation and relativistic effects are negligible (Richard and Zahn 1999; Richard 2001; Dubrulle et al. 2005a; Ji and Balbus 2013).

Accretion disks are Rayleigh-stable but are known to have accretion rates requiring radial fluxes of angular momentum far greater than the flux provided by viscous diffusion in laminar Taylor-Couette-like disks, indicating that they are in fact unstable (Richard and Zahn 1999; Richard 2001; Dubrulle et al. 2005a; Ji and

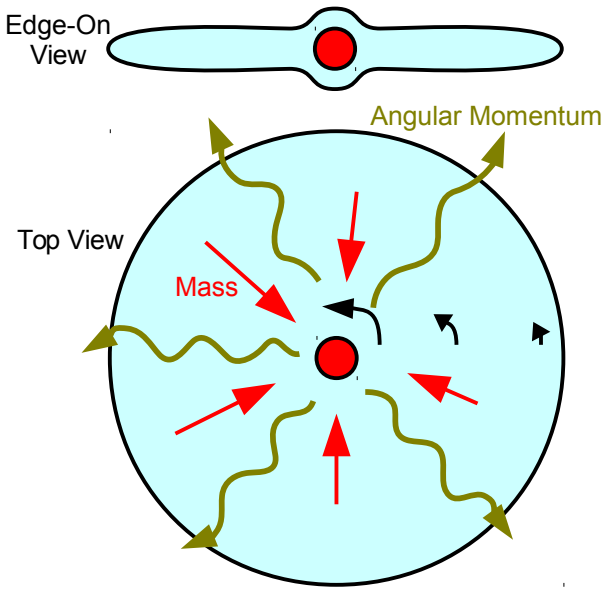

Figure 1.4: Diagram of an astrophysical accretion disk. The top part is an edge-on view and the bottom part is a view from the top. The central body of mass is shown as a red circle in the middle and the dust making up the disk is shaded blue. Red arrows show the direction of mass flux while dark yellow squiggly arrows show the direction of angular momentum transport. The black arrows (partial arcs around the central body) show the rotation of the disk.

Balbus 2013). Otherwise, it would be impossible to form stars and planets on the observed time scales (Richard 2001; Dubrulle et al. 2005a; Paoletti et al. 2012). A diagram is shown in Figure 1.4.

There has been a search for the instabilities at play in these flows. Disks sufficiently ionized to be electrically conductive are known to be linearly unstable via the Magneto-Rotational Instability (MRI) (Ji and Balbus 2013, and description therein). For weakly ionized disks or parts of disks, investigation has focused on stability in the presence of stratification (Dubrulle et al. 2005b; Le Bars and Le Gal 2007; Le Dizès and Riedinger 2010; Marcus et al. 2015) and stability to finite amplitude perturbations (non-linear stability) which has been the subject of several Taylor-Couette experiments including those in this thesis (Richard 2001; Ji et al.

2006; Paoletti and Lathrop 2011; Paoletti et al. 2012; Schartman et al. 2012; Edlund and Ji 2014; Nordsiek et al. 2015).

1.5.3 Stability in Taylor-Couette Flow And Ekman Pumping

For an incompressible fluid in the Rayleigh-stable region of Taylor-Couette flow and compressible accretion disk flow, the possibility of a non-linear instability has not yet been ruled out for all Re_S. Plane Couette flow and pipe flow are both examples of linearly stable flows that have non-linear instabilities at sufficient Re (Grossmann 2000; Avila et al. 2011; Shi et al. 2013, and references therein). In Rayleigh-stable Taylor-Couette flow, Maretzke et al. (2014) found transient growth, a necessary prerequisite for a non-linear instability. Accretion disks have very high Reynolds numbers with Re_S possibly as high as 10^{14} (Paoletti et al. 2012; Ji and Balbus 2013). Therefore, it is reasonable to ask whether Rayleigh-stable Taylor-Couette flow is non-linearly stable or unstable.

In prior experimental work, visualization via Kalliroscope particles, angular momentum transport measurements, and velocimetry measurements were done, yielding contradictory results on the presence of a non-linear instability, especially for quasi-Keplerian flow (Wendt 1933; Taylor 1936a,b; Coles 1965; Richard 2001; Ji et al. 2006; Borrero-Echeverry et al. 2010; Paoletti and Lathrop 2011; Burin and Czarnocki 2012; Schartman et al. 2012; Paoletti et al. 2012; Edlund and Ji 2014). These experiments have, to varying degree, Ekman pumping driven by the no-slip boundary conditions on the axial boundaries.

Ekman pumping occurs whenever fluid is rotated about an axis but does not match the rotation (or lack of rotation) of no-slip boundary axially above or below it. In order for the fluid to be rotating about the axis of rotation, there has to be a centripetal force, which in most cases comes from a pressure gradient pointing towards the axis of rotation. If the fluid is approximately hydrostatic, as is considered in this thesis, the pressure gradient is transmitted axially to the boundary. In the limit of contact with the boundary, the fluid has to rotate the same way as the boundary due to the no-slip boundary condition. Since the fluid away from the boundary is rotating differently than the boundary, the fluid near the boundary is not getting the pressure gradient it needs to rotate with the boundary. This excess pressure gradient then drives horizontal fluid flow towards or away from the axis of rotation above the boundary. This secondary flow is known as Ekman pumping or Ekman circulation. The case of Ekman pumping driven by the inner cylinder driving azimuthal flow rotating faster than the bottom axial boundary is shown in Figure 1.5.

The Ekman pumping could destabilize the flow depending on the axial end configuration in a way that would not be found in astrophysical accretion disks (Balbus 2011; Avila 2012; Schartman et al. 2012; Ji and Balbus 2013; Edlund and Ji 2014), which have open stratified axial boundaries. Axial boundaries that rotate with the outer cylinder, such as those on the apparatus presented in this thesis, were found to have Ekman pumping effects that spanned the whole flow volume (Avila 2012; Schartman et al. 2012; Edlund and Ji 2014), which might explain the large, and likely turbulent, angular momentum transport found by the Maryland

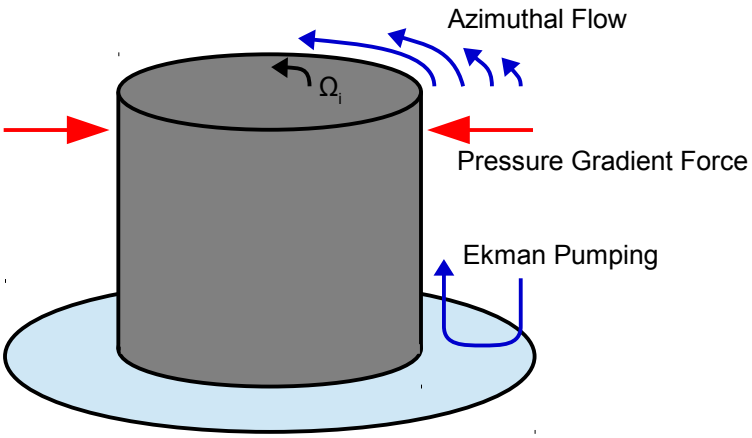

Figure 1.5: Diagram of Ekman pumping in Taylor-Couette flow with the axial boundaries attached to the outer cylinder. The bottom section of the inner cylinder is shown in dark grey while the outer cylinder is not shown for clarity. The azimuthal fluid flow (blue arrows in the top-right) due to the inner cylinder's rotation relative to the outer cylinder creates an inward pressure gradient (red arrows) needed for the centripetal acceleration of the azimuthal flow. This induces a flow, Ekman pumping, at the bottom axial boundary (blue arrow in the bottom-right).

experiment (Paoletti and Lathrop 2011) in contrast to the low angular momentum transport steady laminar flow found in the Princeton MRI and HTX experiments which reduced the Ekman pumping by splitting the axial boundaries into rings rotated at speeds between that of the two cylinders (Ji et al. 2006; Schartman et al. 2012; Edlund and Ji 2014).

The effect of the Ekman pumping on the flow state and angular momentum transport in wide-gap ($\eta < 0.34$) low aspect-ratio ($\Gamma < 3$) Rayleigh-stable experiments, such as the Princeton MRI and HTX experiments, has been the subject of several investigations. When the axial boundaries are attached to the outer cylinder as opposed to rotating at intermediate speeds, there are large fluctuations and mixing near the inner cylinder (Dunst 1972; Edlund and Ji 2014) and quiescent flow rotating close to Ω_o near the outer cylinder (Dunst 1972; Kageyama et al. 2004;

Schartman et al. 2012; Edlund and Ji 2014). Speeding up the part of the axial boundaries near the inner cylinder causes the fluctuations near the inner cylinder to decrease and the azimuthal velocities to more closely match laminar Taylor-Couette flow (Edlund and Ji 2014). In the reduced Ekman pumping configuration, perturbations by jets from the inner cylinder were found to decay up to the maximum $Re_S \approx 10^6$ that could be obtained (Edlund and Ji 2014).

The effect of the Ekman pumping in medium-gap ($\eta \approx 0.7$) larger aspect-ratio ($\Gamma \sim 10$) experiments, such as the Maryland and Twente T^3C experiments presented in this thesis, has not received as much attention, though it has been strongly expected to be similar, which would resolve the contradictory results. In Direct Numerical Simulations (DNS) for low Reynolds number, $Re_S < 10^4$, axial boundaries attached to the outer cylinder were found to destabilize the flow (Avila 2012). However, Avila (2012) also found that the axial boundaries in the Princeton MRI experiment's geometry with the axial rings rotated optimally destabilized the flow. Yet, the flow has low velocity fluctuations and angular momentum transport consistent with laminar Taylor-Couette flow at much higher $Re_S \sim 10^6$ experimentally on the Princeton MRI experiment and their similar HTX experiment (Ji et al. 2006; Schartman et al. 2012; Edlund and Ji 2014). This suggests that there might be increased stabilization at higher Re_S or that the deviations from laminar Taylor-Couette flow are small and increase the angular momentum transport negligibly, which may or may not also happen in medium-gap larger aspect-ratio Taylor-Couette experiments. For $Re_S \leq 10^5$ Direct Numerical Simulations (DNS) with periodic axial boundaries and $\eta = 0.714$ in the quasi-Keplerian regime, Ostilla-

Mónico et al. (2014c) found that initial turbulent states always decay to laminar Taylor-Couette flow.

1.6 Phase Space Explored And Past Results

Due to the greater mechanical simplicity of having only one cylinder rotate, pure inner-rotation ($q = +\infty$) and pure outer-rotation ($q = -\infty$) have been the most explored. This next most popular regimes to investigate have been the Rayleigh unstable regime for both co-rotation (q is real and $q > 2$) and counter-rotation (q is complex). Compared to other regions in the parameter space of Taylor-Couette flow, there has been relatively little work for $q < 2$ except for $q = -\infty$. Most of the work in the Rayleigh-stable regime has been recent and has been related to the question of whether the flow is stable to finite perturbations (nonlinearly stable) discussed earlier (Richard 2001; Dubrulle et al. 2005a; Ji et al. 2006; Paoletti and Lathrop 2011; Balbus 2011; Schartman et al. 2012; Paoletti et al. 2012; Avila 2012; Ji and Balbus 2013; Maretzke et al. 2014; Edlund and Ji 2014; Nordsiek et al. 2015).

Little is known about the Rayleigh-stable regime, specifically, as a whole with any sort of axial boundaries. Only one of its boundaries, pure outer-rotation ($q = -\infty$), has had major exploration. In addition to being sparsely sampled, most investigation has focused on three small regions within it. One is the low $Re_S < 6000$ part of the quasi-Keplerian regime (Kageyama et al. 2004; Avila 2012). Another is the high $Re_S \geq 10^5$ part of the quasi-Keplerian regime (Kageyama et al. 2004; Ji et al. 2006; Paoletti and Lathrop 2011; Schartman et al. 2012; Edlund and Ji 2014;

Nordsiek et al. 2015; Edlund and Ji 2014). Another region is defined by a limited range of q to either being near the Rayleigh line ($2 > q > 1.9$) or at $q = 3/2$ (Richard 2001; Kageyama et al. 2004; Ji et al. 2006; Schartman et al. 2012; Edlund and Ji 2014; Edlund and Ji 2014).

At the present time, the community does not have Re_S scalings of the angular momentum transport, velocity profiles, etc. in the Rayleigh-unstable regime except for $Re_S < 6000$ at $q = 1.909$ (Avila 2012), unlike in the Rayleigh-unstable regime (Wendt 1933; Taylor 1936a; Lathrop et al. 1992a; Lewis and Swinney 1999; Racina and Kind 2006; Ravelet et al. 2010; van Gils et al. 2011b, 2012; Huisman et al. 2012a; Merbold et al. 2013). Essentially, there is no equivalent to Figure 1.6, which shows the Re_S scaling of the torque for pure inner-rotation ($q = +\infty$) for four experiments across nearly a century of research. Having these scalings is important not only for understanding the flow's transport and statistical properties, but also because flow state transitions can be found like the transition that occurs at an $Re_S > 10^4$ for $q = +\infty$ (Lathrop et al. 1992a; van Gils et al. 2012; Ostilla-Mónico et al. 2014a,b), to the so called "ultimate regime" where the boundary layers become fully turbulent (van Gils et al. 2012; Ostilla-Mónico et al. 2014a,b), which was first found in the torque scalings.

The q (or equivalently Ro) scaling of the torque in our geometries for $Re_S > 3.5 \times 10^5$ has been found (Paoletti and Lathrop 2011; Paoletti et al. 2012), which is shown in Figure 1.7. Paoletti et al. (2012) found that when the torques are normalized by that for pure inner-rotation $G_{+\infty}$ at the same Reynolds number, the torques collapse together to a single curve for both Taylor-Couette experiments

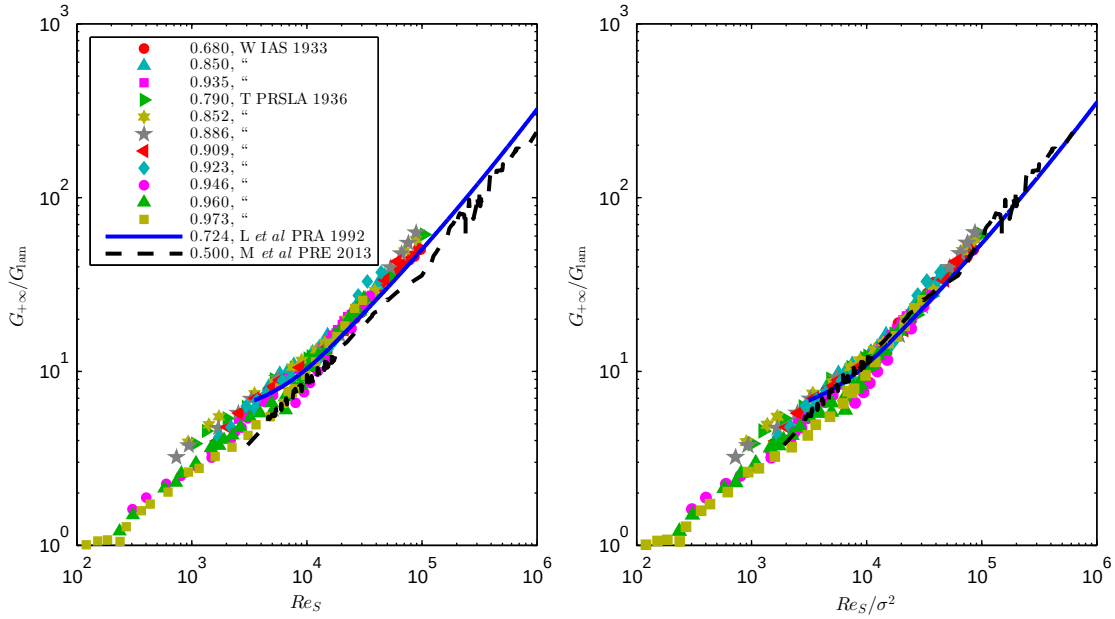

Figure 1.6: The pure inner-rotation ($q = +\infty$) torque $G_{+\infty}$ normalized by the laminar Taylor-Couette torque G_{lam} as it varies by Re_S from four different experiments. The legend in (a), which applies to both plots, gives the η followed by the paper the torque measurements come from. The symbols are the individual torque measurements of Wendt (1933) and Taylor (1936a) at different η, which are abbreviated as W IAS 1933 and L PRSLA 1936 in the legend respectively. The blue solid line gives the scaling that Lathrop et al. (1992a), abbreviated as L *et al* PRA 1992 in the legend, fitted to their torque measurements of the 8-vortex state. The black dashed line connects the torque measurements of Merbold et al. (2013), abbreviated as M *et al* PRE 2013 in the legend. (a) the torque scalings with respect to the shear Reynolds number Re_S. (b) the torque scalings with respect to Re_S/σ^2, which collapses in the "ultimate regime" for $Re_S/\sigma^2 \geq 2 \times 10^4$, where σ is the Taylor-Couette geometric Prandtl number (Equation 1.26).

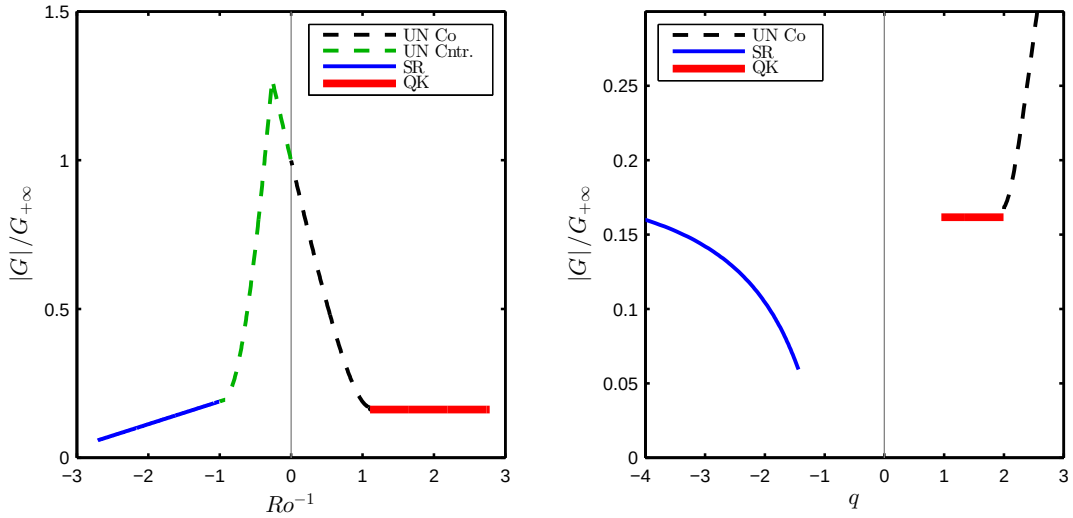

Figure 1.7: The Ro^{-1}, q scaling of $|G|/G_{+\infty}$ found by Paoletti et al. (2012). UN Co is the co-rotating Rayleigh-unstable regime, UN Cntr. is the counter-rotating Rayleigh-unstable regime, SR is the sub-rotating regime ($q < 0$), and QK is the quasi-Keplerian regime ($2 > q > 0$). (a) scaling in terms of the inverse of the Rossby number Ro^{-1}. (b) scaling in terms of q.

presented in this thesis. The scaling extends into the Rayleigh-stable regime.

Phase diagrams of the flow states have been constructed for the Rayleigh-unstable regime (Andereck et al. 1986; Ostilla-Mónico et al. 2014a). To the best of our knowledge, a similar phase diagram for the Rayleigh-stable regime of Taylor-Couette flow with axial boundaries has not yet been constructed.

1.7 Outline

The two Taylor-Couette experiments used in this thesis, the Maryland experiment and the Twente T^{3}C, are presented in Chapter 2. Azimuthal velocimetry profiles in the Rayleigh-stable regime (both $2 > q > 0$ and $q < 0$) on the Twente T^{3}C and the implied transport directions of angular momentum are presented in

Chapter 3. Dye injection measurements and the direction of the flow relative to the outer cylinder (rotating in its frame) are presented in Chapter 4. Re_S scalings of the torque for four quasi-Keplerian q measured on the Maryland experiment and the resulting quasi-Keplerian phase diagram are presented in Chapter 5. Conclusions, open questions, and areas for further investigation are detailed in Chapter 6.

Chapter 2: TC: Experiment

Partially adapted from and expanded upon the arXiv version of

F. Nordsiek, S. G. Huisman, R. C. A. van der Veen, C. Sun, D. Lohse, and D. P. Lathrop. Azimuthal velocity profiles in Rayleigh-stable Taylor-Couette flow and implied axial angular momentum transport. *Journal of Fluid Mechanics*, 774:342–362, July 2015.

DOI: 10.1017/jfm.2015.275

ADS: 2015JFM...774..342N

arXiv: 1408.1059 [physics.flu-dyn]

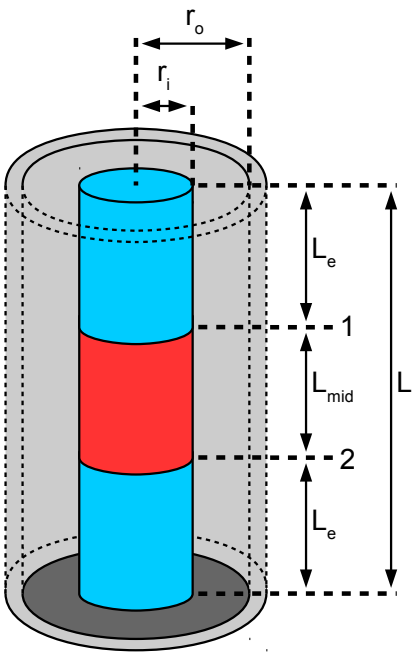

Figure 2.1: Sketch of the Maryland and Twente T^{3}C experiments used for the measurements presented in this thesis. The inner cylinder is split into three sections with lengths, from top to bottom, of L_e, L_{mid}, and L_e. There is a small gap of size L_g between each section marked as positions 1 and 2. Note that the relative scales have been modified for clarity.

2.1 General

The measurements presented in this thesis were conducted on two different Taylor-Couette experiments with a similar geometry and complementary instrumentation. The two experiments are

Maryland

Sometimes known as the Maryland-Texas experiment. The experiment was originally constructed and operated at the University of Texas at Austin (USA) before moving to the University of Maryland at College Park (USA) where the measurements in this thesis were performed. The

experiment is described in detail by Lathrop et al. (1992b), Lathrop et al. (1992a), Lathrop (1992), and Paoletti and Lathrop (2011).

T3C

Twente Turbulent Taylor-Couette (T^3C). The experiment was constructed and then continuously operated at the University of Twente (the Netherlands) by the Physics of Fluids Group. The experiment is described in detail by van Gils et al. (2011a), Huisman et al. (2012b), and van Gils et al. (2012).

The two experiments, in addition to having a similar geometry, share many design features. The basic design is shown schematically in figure 2.1. Images of the two experiments are shown in Figure 2.2. The experimental geometry, dimensionless parameters, operating limits, working fluids, and the measurement systems that were available and/or used are listed in Table 2.1.

Both experiments have similar $\eta \approx 0.72$ and $\Gamma \approx 11.6$. **The axial boundaries are attached to the outer cylinder.** The inner cylinder, constructed of stainless steel in both experiments, is divided axially into three sections as shown in Figure 2.1. The length of the middle section is L_{mid}. Both end sections have equal length L_e. There is a small gap of size L_g between each section, labeled 1 and 2 in figure 2.1. Both experiments used water as working fluids (though at different temperatures, T_k). The Maryland experiment also used air and solutions of water and glycerol ($C_3H_8O_3$, also known as glycerin, glycerine, and propane-1,2,3-triol). Both experiments can measure the torque to rotate the inner cylinder, but the Maryland

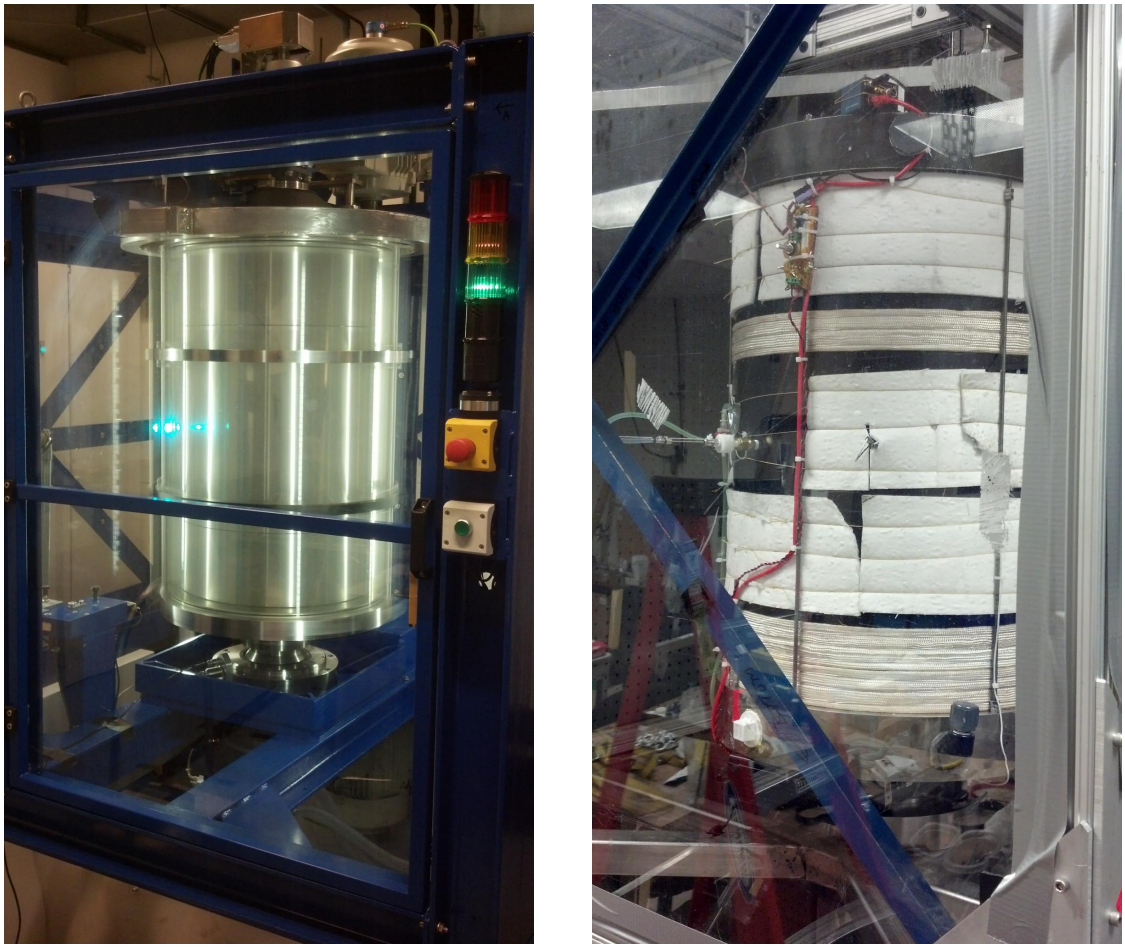

(a) (b)

Figure 2.2: Images of the two Taylor-Couette experiments. (a) the Twente T^3C experiment. The stainless steel inner cylinder, transparent outer cylinder, experiment's frame, and the split laser beams from the LDA are all visible. (b) the Maryland experiment. The anodized aluminum outer cylinder (black), heaters (light tan), insulation (white), experiment's frame, and the dye injection and visualization system (injector on the side of outer cylinder and the camera on top of the axial boundary) are shown.

Table 2.1: The parameters and measurement systems available for the Maryland and T^{3}C experiments. The rows are broken up into four groups. In order, they are experimental geometry, experimental working fluids and temperatures used for this thesis and operating limitations, dimensionless parameters, and measurement systems available and/or used. For the measurement systems part, a checkmark means the measurement system was available and used for the results presented in this thesis, "not used" means it was available but not used, and blank means it wasn't available.

	Maryland	T^{3}C
r_i (cm)	16.000	20.00
r_o (cm)	22.085	27.94
d (cm)	6.085	7.94
L (cm)	69.5	93.2
L_{mid} (cm)	40.64	53.6
L_e (cm)	15.69	19.35
L_g (mm)	0.5	2.5
axial boundaries	attached to outer cylinder	attached to outer cylinder
working fluids	water, water-glycerol, air	water
operating T_k (C)	19-50	21—22
max $\lvert\Omega_i/2\pi\rvert$ (Hz)	20	20
max $\lvert\Omega_o/2\pi\rvert$ (Hz)	10	10
η	0.7245	0.716
Γ	11.47	11.74
σ	1.053	1.057
max $\lvert Re_i\rvert$	2.2×10^6 *	2.1×10^6 †
max $\lvert Re_o\rvert$	1.5×10^6 *	1.5×10^6 †
measure torque	✓	not used
wall shear stress	not used	not used
LDA/LDV		✓
PIV		not used
UDV	not used	
dye injection	✓	

* Calculated for 50 C water.
† Calculated for 22 C water.

experiment can only measure it for the middle section while the T^{3}C can measure it for all three sections. Dye injection measurements were performed on the Maryland experiment to get azimuthal flow directions relative to the outer cylinder. Laser Doppler Anenometry (LDA), which is also known as Laser Doppler Velocimetry (LDV), was performed on the T^{3}C experiment to obtain azimuthal velocity profiles. The Particle Image Velocimetry (PIV) and Ultrasound Doppler Velocimetry (UDV) systems were not used.

The inner cylinder was divided into three sections originally on the Maryland experiment to exclude everything within $2.58\,(r_o - r_i)$ of the axial boundaries from the torque measurement (Lathrop et al. 1992a). This excludes the torque from the regions where the secondary circulation set up by finite boundaries (Ekman pumping) is strongest. However, the secondary flow from the Ekman pumping destabilizes the flow and changes it along the whole axial length compared to the case of free-slip or open axial boundaries (Avila 2012; Schartman et al. 2012; Edlund and Ji 2014; Edlund and Ji 2014), which will be further shown in Chapter 3. The T^{3}C experiment's inner cylinder was designed similarly except that it can also measure the torques on both of the end sections (van Gils et al. 2011a).

2.2 Twente: Azimuthal Velocimetry

The system was filled with water and operated at room temperature with cooling applied at the axial boundaries. The azimuthal velocity profiles were obtained using Laser Doppler Anemometry (LDA). A schematic of the LDA system and how

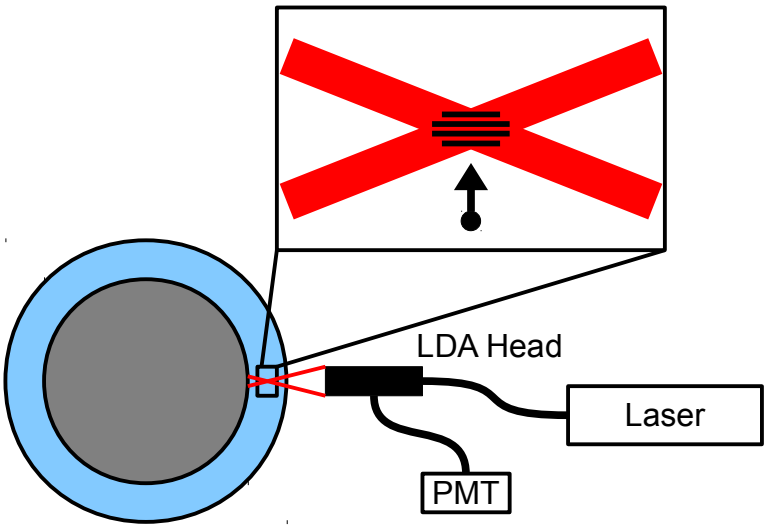

Figure 2.3: Schematic of the Laser Doppler Anemometry (LDA) system for the T^3C experiment. A laser beam is split into two parts (splitter not shown) that then go into the LDA head where they are sent into the experiment such that they cross in the Taylor-Couette's gap. An inset expands the region where the split laser beams cross, also showing the interference pattern setup, and a particle moving towards the view volume (where the beams cross). Note, the laser is drawn red for clarity as opposed to matching the laser we used.

LDA works is shown in Figure 2.3.

LDA works by taking a laser beam, splitting it in two with a beam splitter, and then crossing the split beams at the location that fluid velocities are desired. The crossed beams form an interference pattern. Whenever a small particle crosses the pattern, it scatters light with an intensity that oscillates at a frequency determined by the laser frequency, the index of refraction of the fluid where the split beams cross, the crossing angle of the two split beams, and the particle speed along an axis orthogonal to the direction that the split beams are coming from and in the plane of the split laser beams. This scattered light is then collected and measured, which in our experiment was done by a lens and a Photo Multiplier Tube (PMT). Since this mode of operation can only give the particle's speed along one axis and has problems

measuring small speeds, our LDA system shifts the frequency of one of the split laser beams so that the interference pattern is sweeping the view volume faster than any particle can move through it. This allows both the sign and the magnitude of the component of the particle's velocity along the axis to be measured, even when that component is near zero.

The outer cylinder is made of transparent acrylic, allowing for easy use of optical methods to obtain fluid velocities. Our LDA configuration used backscatter from seed particles in a measurement volume of approximately 0.07 mm $\times$ 0.07 mm $\times$ 0.3 mm. Dantec PSP-5 particles with a 5 μm diameter and 1.03 g/cm^3 density were used. The optical effect of the outer cylinder curvature on the LDA measurements was corrected by using the calculations of Huisman et al. (2012b). The velocimetry was calibrated using radial and axial profiles of solid-body rotation at different rotation rates. The error in the mean velocity profiles from the calibration, which was the dominant source in the mean profiles, was smaller than 0.1%. For all LDA measurements a statistical convergence of 1% was achieved, which translates to between 1% and 6% of $|\Omega_i - \Omega_o|$, which prevents investigation into fluctuations and deviations from axisymmetry. When measuring close to the inner cylinder, reflections from the metal inner cylinder were found to be problematic. Hence, the radial profiles presented in this paper were done at the axial height of the 2.5 mm gap between the bottom and middle inner cylinder sections, which corresponds to an axial height $z/L = 0.209$ off the bottom, so that the LDA laser would be absorbed in the gap on a black o-ring as opposed to being reflected off the cylinder surface.

2.3 Maryland: Torque And Dye Injection

The Maryland experiment originally had a transparent acrylic outer cylinder that could not rotate (Lathrop et al. 1992b,a; Lathrop 1992; Lewis and Swinney 1999). The outer cylinder was replaced by an anodized aluminum cylinder with the same inner radius $r_o = 22.085$ cm and length $L = 69.50$ cm, and the system modified to allow the outer cylinder to rotate independently (Paoletti and Lathrop 2011). Both angular velocities are measured precisely by magnetic shaft encoders and controlled to within 0.2% of the set value.

The temperature, for which we use the symbol T_k throughout this thesis, was measured by a platinum RTD probe embedded into the outer cylinder close to the working fluid at midheight. The probe and its measurement circuit were calibrated against a thermocouple.

The torque to rotate the inner cylinder is measured by a load cell (Omega LCEC-50) at the end of a strain arm connecting the middle section of the inner cylinder to the shaft (section would freely rotate on its low friction bearings otherwise). A diagram and an image of the torque system are shown in Figure 2.4. The sensor is read using an amplifier circuit inside the inner cylinder and a lock-in amplifier (Stanford Research Systems SR830) in the lab frame connected to it through a slip ring.

The torque had to be finely calibrated, especially at torques below ~ 0.300 Nm, in order to measure the small Rayleigh-stable torques accurately. The torque setup was calibrated by erecting the assembled middle section of the inner cylinder and

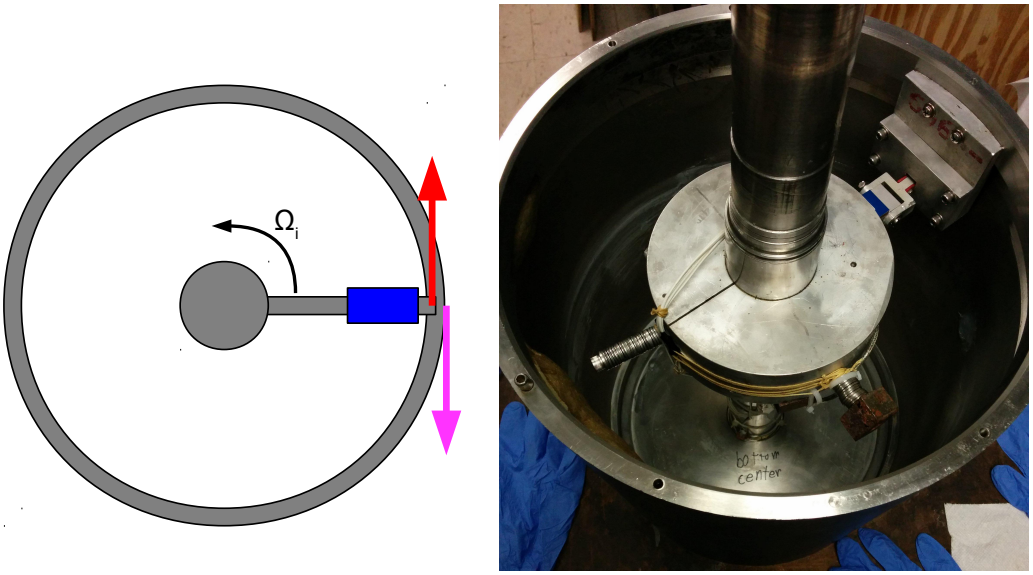

(a) (b)

Figure 2.4: Torque measurement system on the Maryland experiment inside the middle section of the inner cylinder. (a) diagram from above the measurement system. The inner shaft (central grey circle) rotating at Ω_i connects to the inner cylinder (grey circular shell) through an arm with a load cell at the end (blue rectangle). Due to the torque from the fluid, the cylinder exerts a force (magenta arrow) on the load cell. In order to keep the cylinder rotating at Ω_i, the arm and load cell exert an equal and opposite force on the cylinder (red arrow). (b) image of the inside of the inner cylinder. The shaft (middle), load cell (blue object to the upper-right of the shaft), mountings, and balancing weights are shown.

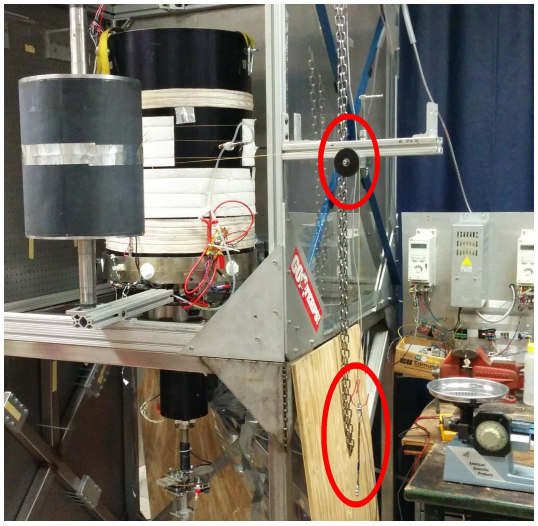

Figure 2.5: Image of the torque calibration. The middle section of the inner cylinder (painted black in this image) and the shaft are aligned vertically while a string is connected to the cylinder (yellow with foil duct tape attaching it to the cylinder), run over a pulley (circled in red), and weights suspended (see the wrench circled in red).

inner shaft vertically, connecting a thin light strap around the cylinder and running it over a low friction pulley, and placing weights on the other end of the strap and measuring the torque signal (see Figure 2.5). The suspended weight was finely stepped, especially at the low end to characterize the torque sensor for low torques and find any non-linearities (it turned out to be piecewise linear). This has given an improved torque measurement uncertainty of 0.005 Nm. A major source of uncertainty is in finding the zero of the torque sensor. The output of the torque system was always measured before a sequence of runs while the experiment was at rest to get the approximate location of the zero. Additional adjustments are discussed in Chapter 5.

Any slight angular misalignment of the load cell would lead to a component of the centripetal force needed to rotate the end of the load cell being read as

a torque (an apparent "centrifugal torque"). This was calibrated by rotating the inner cylinder at many equal rotation rates in both directions with the outer cylinder stationary while the gap was filled with air to minimizes the actual fluid torque. The fluid torque from the air when rotating at $+\Omega_i$ changes sign but should have approximately the same magnitude when rotating at $-\Omega_i$. There would be a small difference if say the 8-vortex state was entered in one direction but the 10-vortex state was entered in the other (Lathrop et al. 1992a; Lathrop 1992). The apparent "centrifugal torque" should have the form $b\,\Omega_i^2$ for some constant b, meaning that it should be the same independent of the sign of Ω_i. Then the average of the two torques gives the apparent "centrifugal torque" at $+\Omega_i$ and $-\Omega_i$ while the difference is twice the magnitude of the fluid torque. The apparent "centrifugal torque" was fitted to a quadratic $b\,\Omega_i^2 + c$ where c is the zero offset.

We constructed a dye injection and visualization system for the experiment, which is shown in Figure 2.6. We used fluorescein dye for our visualization since it is a strong fluorescent dye even in low concentrations, and its absorption and emission frequencies are in the visible. The dye is injected into the gap at midheight on the outer cylinder through a stainless steel tube with an outer diameter of 1.58 mm (1/16 inches) and an inner diameter of 0.46 mm (0.022 inches). The dye is pumped by a syringe pump articulated by a stepper motor (Figure 2.6c) mounted to the bottom axial boundary on the axis of rotation so that it would neither break nor jam (a major problem in early videos) under rotation.

The dye in the fluid is both illuminated and viewed through a window in the top axial boundary, directly above the injector. An inline illumination system

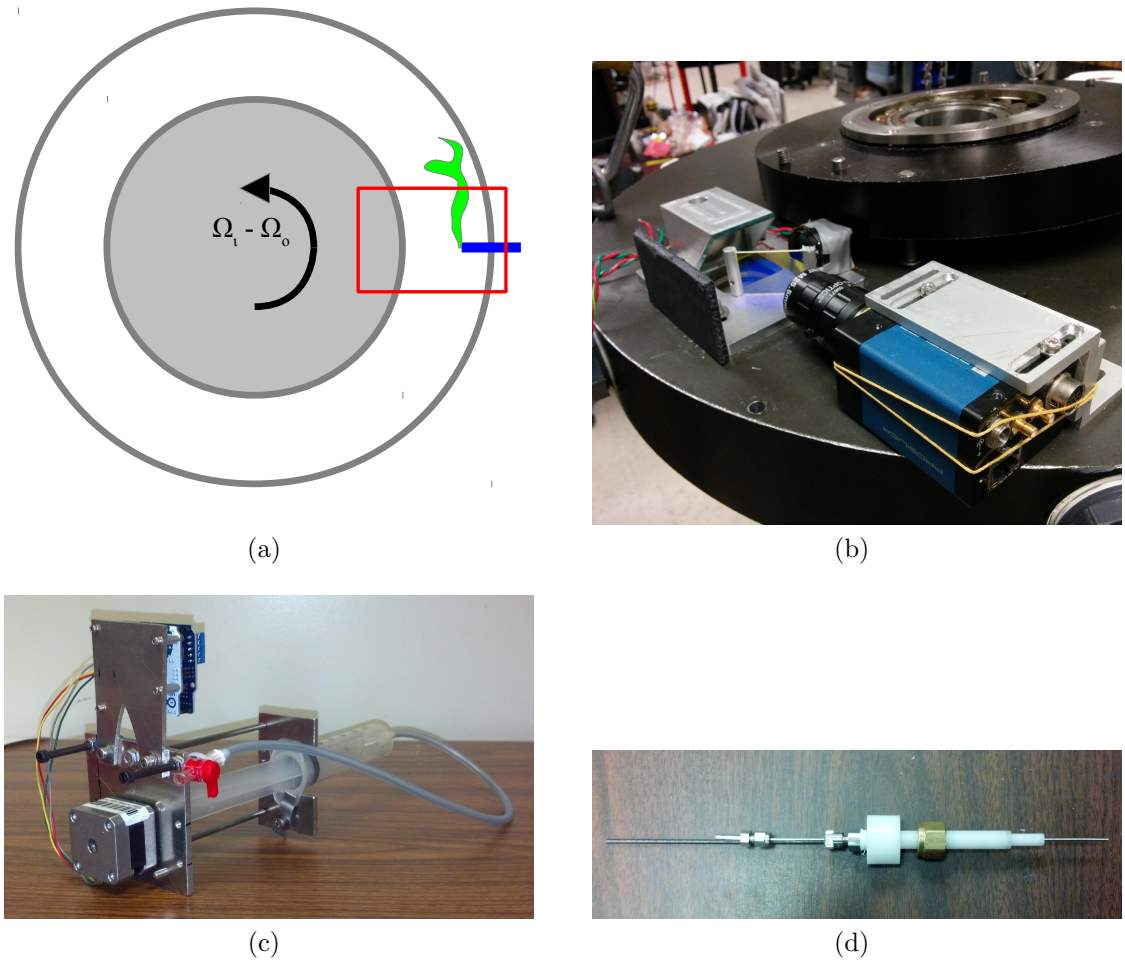

(a) (b)

(c) (d)

Figure 2.6: Dye injection and visualization system. (a) an above view of the Taylor-Couette (cylinders are the grey circles). The injector (blue) is injecting dye (green) into the gap. The camera's field of view is shown as the red rectangle around the injector. (b) image of the camera and optics mounted to the top axial boundary. The camera with lens and bandpass filter, illumination blue LED with bandpass filter, dichoric beam splitting filter, black cardboard keeping external light from the dichoric filter, and the mirror above the viewing window are all shown. (c) syringe pump for the dye. (d) the injector with the tip protruding (right side).

is used with the aid of a dichoric filter (Edmund Optics 495 nm Dichoric Filter 25.2×35.6 mm #67-079). This takes advantage of the illumination and emitted wavelengths being different. The dichoric filter is aligned at 45° to reflect blue light from an LED (blue Cree XRE) into the window via a mirror. The emitted light traveling back through the window and the mirror then passes through the dichoric filter to reach the camera (AVT Prosillica GE 680C). To reduce contaminating light, a piece of black cardboard was use to keep outside light from hitting the dichoric filter and into the camera, a bandpass filter put on the LED (Edmund Optics 448 nm Bandpass Filter, 20 nm bandpass, OD6 Blocking, 25 mm Dia #86-983), and a bandpass filter put on the camera (Edmund Optics 525 nm Bandpass Filter, 45 nm bandpass, OD6 Blocking, 25 mm Dia #86-984). In addition, the inner cylinder and the part of the bottom axial boundary in the field of view were painted barbecue black to reduce reflected light (the outer cylinder didn't need to be painted since it was black due to its anodization). A 25 mm compact fixed focal length lens (Edmund Optics #59-871) was used. The optics and camera were firmly mounted to the top axial boundary so that they could withstand rotation up to $|\Omega_o/2\pi| = 5$ Hz.

The camera was operated in 8-bit greyscale mode and focused on midgap. Video was acquired via Gigabit ethernet using a miniature computer attached to the bottom axial boundary rotating with the outer cylinder.

The system was calibrated by taking videos of dye injections when the cylinders had been at rest for a long time. The stream of the dye hits the outer cylinder giving the location of the injector and the location of the inner cylinder directly across from it. The location of the outer cylinder where the injector emerges was found with

the help of fluorescent spheres (Cospheric UVBGPMS 250-300 μm) attached to the injector flush against the outer cylinder with adhesive. Then the inner cylinder was rotated slowly at 0.1 Hz and a video taken while dye was injected to identify which direction in the images is counter-clockwise.

Chapter 3: TC: Azimuthal Velocities

Partially adapted from the arXiv version of

F. Nordsiek, S. G. Huisman, R. C. A. van der Veen, C. Sun, D. Lohse, and D. P. Lathrop. Azimuthal velocity profiles in Rayleigh-stable Taylor-Couette flow and implied axial angular momentum transport. *Journal of Fluid Mechanics*, 774:342–362, July 2015.

DOI: 10.1017/jfm.2015.275

ADS: 2015JFM...774..342N

arXiv: 1408.1059 [physics.flu-dyn]

3.1 Introduction

In order to investigate the differences in the flow between the Maryland and Twente experiments with the Princeton MRI and HTX experiments (Ji et al. 2006; Schartman et al. 2012; Edlund and Ji 2014), radial profiles across the gap of the azimuthal velocity in the Maryland and Twente geometry are needed. We measured these profiles using an LDA on the Twente experiment (Section 2.2) in collaboration with the Physics of Fluids group at the University of Twente, the Netherlands.

3.2 Measurements Performed

An introduction to the Twente experiment and our azimuthal velocity measurements is provided in Section 2.2. Due to the problematic reflections from the metal inner cylinder when close to the inner cylinder, we present full-gap radial profiles only at the axial height of the 2.5 mm gap between the bottom and middle inner cylinder sections, which corresponds to an axial height $z/L = 0.209$ off the bottom, so that the LDA laser would be absorbed in the gap on a black o-ring as opposed to being reflected off the cylinder surface. The axial dependence of the angular velocity was found to be less than 2% of $|\Omega_i - \Omega_o|$ from axial profiles at midgap from midheight to 1.5 cm off the bottom, and between radial profiles over the outer half of the gap at five heights $z = \{0.195, 0.223, 0.414, 0.464, 0.927\}$ m off the bottom, which are at $z/L = \{0.209, 0.238, 0.444, 0.497, 0.995\}$. The last one, $z/L = 0.995$ is 5 mm from the top axial boundary. Thus, a radial profile at

Table 3.1: The q values for which velocity profiles were measured and their corresponding rotation rate ratios (Ω_i/Ω_o), rotation parameter R_Ω, and Rossby number Ro. We also give the region of the Taylor-Couette parameter space the measurement is in, and for what Re_S measurements were taken. The regions are abbreviated as UN (Rayleigh-unstable), QK (quasi-Keplerian), and SR (sub-rotating).

					Re_S		
q	Ω_i/Ω_o	R_Ω	Ro	Region	2.07×10^4	1.04×10^5	7.81×10^5
2.100	2.018	−0.9533	1.018	UN		✓	✓
1.909	1.893	−1.047	0.893	QK		✓	✓
1.500	1.651	−1.333	0.651	QK	✓	✓	✓
1.258	1.523	−1.587	0.523	QK		✓	
0.692	1.260	−2.900	0.260	QK		✓	
0.333	1.118	−6.062	0.118	QK		✓	
−0.500	0.8461	4.141	−0.1539	SR		✓	
−1.000	0.7158	2.113	−0.2842	SR		✓	
−2.000	0.5124	1.113	−0.4876	SR		✓	

$z/L = 0.209$ is representative, other than possibly for radial positions closer than 2.5 mm to the inner cylinder. The boundary layers on the axial boundaries are confined to within 5 mm of the boundaries.

Velocimetry was performed for five quasi-Keplerian q values including Keplerian ($q = 1.500$), three sub-rotating values of q, and one unstable but very close to the Rayleigh line q value ($q = 2.100$); which are all listed in Table 3.1. The value $q = 1.909$ was chosen to match the simulations of Avila (2012) on a nearly identical geometry and the Princeton experimental work at $q = 1.9$ (Ji et al. 2006; Schartman et al. 2012). Also, $q = \{1.909, 1.500, 1.258, 0.692\}$ were chosen to match the torque measurements on the Maryland experiment presented in Chapter 5. Measurements for all values of q were taken at $Re_S = 1.04 \times 10^5$, the three values of $q \geq 1.500$ at $Re_S = 7.81 \times 10^5$, and $q = 1.500$ at $Re_S = 2.07 \times 10^4$. All of the azimuthal velocity profiles, radial profiles at all 5 heights and the axial profile at midgap, are available in the supplementary material of the paper this chapter is adapted from

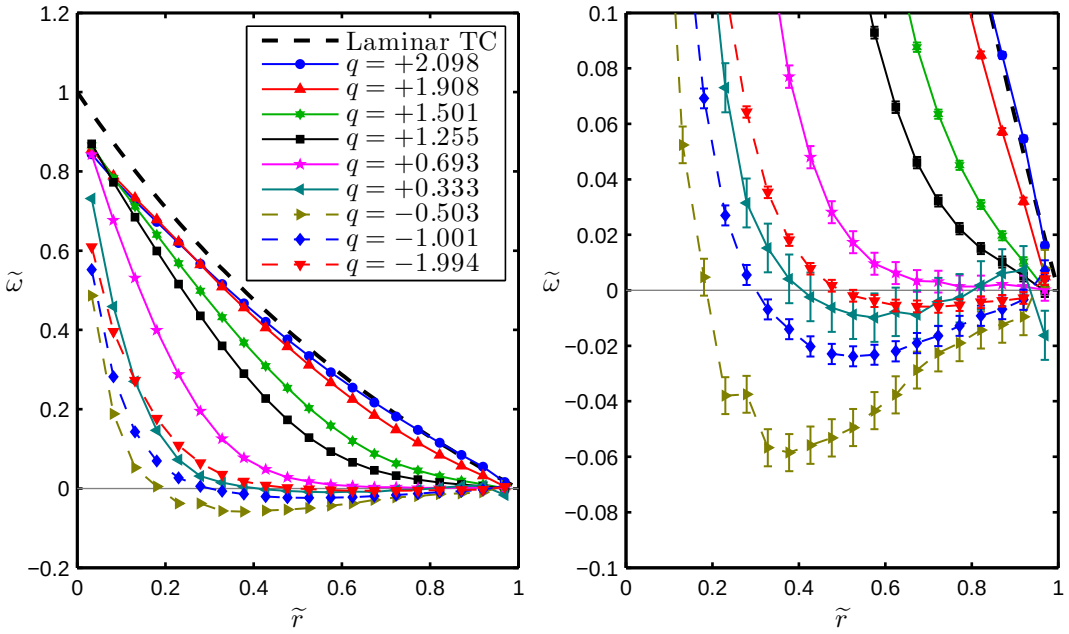

Figure 3.1: Comparison of the normalized angular velocity $\widetilde{\omega} = (\omega - \Omega_o) / (\Omega_i - \Omega_o)$ profiles across the gap for different values of the q parameter at $Re_S = 1.04 \times 10^5$. (a) shows the full scale of $\widetilde{\omega}$ (error bars are smaller than the symbols) and (b) shows an expansion around $\widetilde{\omega} = 0$, using the same symbols to emphasize the parts of the profiles close to rotation at Ω_o. Connecting lines are drawn to guide the eye. The profile for laminar Taylor-Couette flow is drawn for comparison.

(Nordsiek et al. 2015). Each pair of q and Re_S was reached by starting with both cylinders at rest, linearly increasing Ω_i and Ω_o to their final values over 120 s while maintaining constant q, and then waiting at least 600 s for transients to decay before doing measurements.

3.3 Results on The Azimuthal Profiles

The $\widetilde{\omega}$ profiles for all values of q at $Re_S = 1.04 \times 10^5$ are compared to each other and to the laminar Taylor-Couette profile in Figure 3.1. None of the profiles matched the laminar Taylor-Couette profile. Approaching solid-body rotation ($q \rightarrow$

0) at fixed Re_S in both regimes, deviation from the laminar Taylor-Couette profile increased and the part of the profile near the inner cylinder steepened. For the quasi-Keplerian regime, as we approach solid-body rotation, the rest of the profile flattens towards $\widetilde{\omega} = 0$. For the sub-rotating regime, $\widetilde{\omega} < 0$ away from the inner cylinder. This indicates that the fluid is *super-rotating* in terms of angular velocity compared to both cylinders ($\omega > \Omega_o > \Omega_i > 0$) with the degree of super-rotation, as a fraction of $|\Omega_i - \Omega_o|$, increasing as we approach solid-body rotation. This flow super-rotation will be further discussed in Section 3.4.1.

The resulting profiles of the specific angular momentum $\ell = r^2\omega$ at $Re_S = 1.04 \times 10^5$ are shown in Figure 3.2. For the quasi-Keplerian regime, the specific angular momentum profiles all follow the same pattern of having an inner flat region connected to an outer region rotating at Ω_o, which will be discussed further in Section 3.4.2. The flat region in ℓ indicates that the flow was well mixed in that region.

Keplerian ($q = +1.500$) profiles for three different Re_S are compared in Figure 3.3. They all have a similar shape; but as Re_S is increased, $\widetilde{\omega}$ decreases towards solid-body rotation at Ω_o, especially in the outer parts of the gap. In terms of the specific angular momentum, increasing Re_S leads to a sharper transition between the flat region and the rotation at Ω_o region.

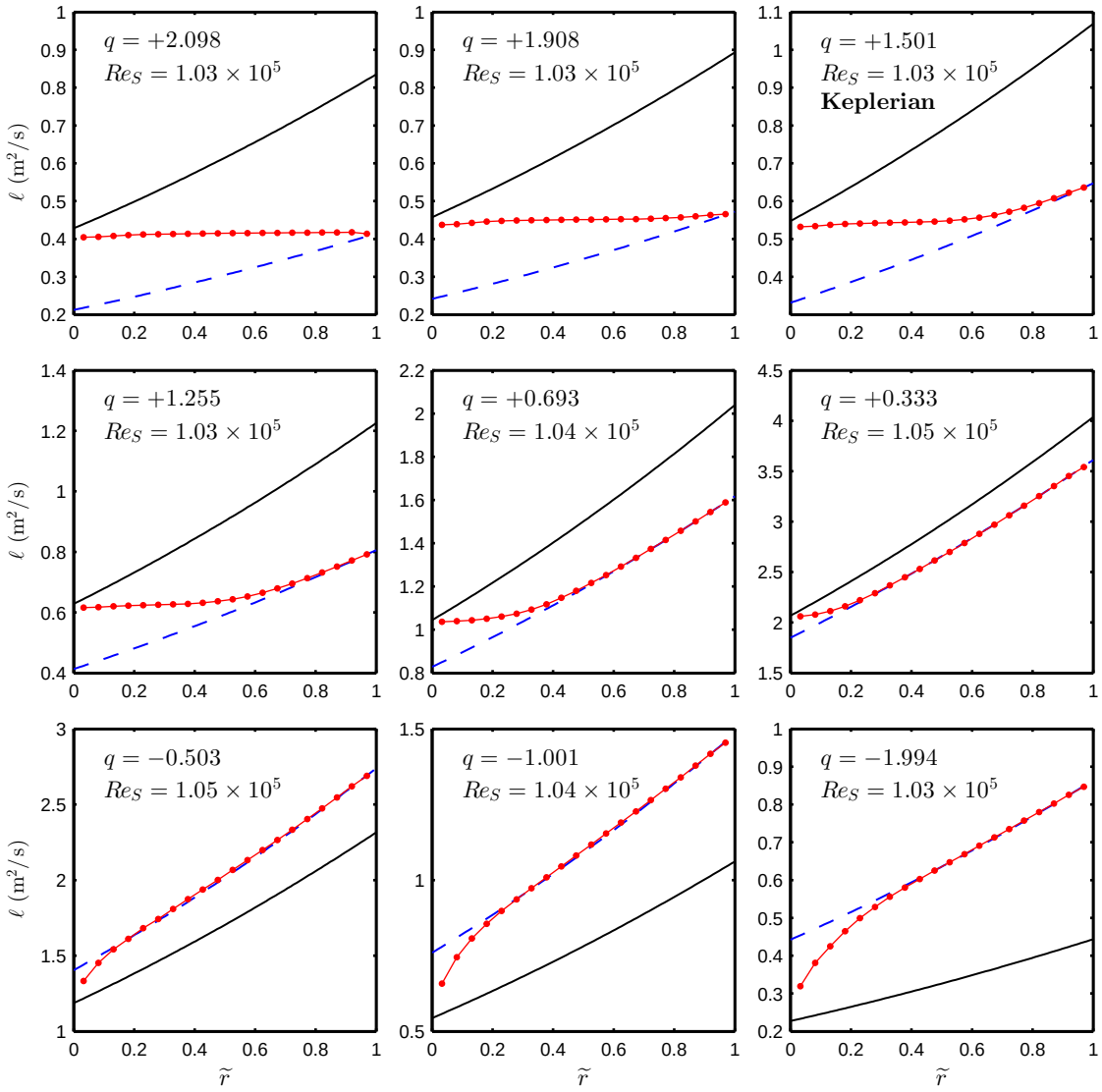

Figure 3.2: The specific angular momentum ($\ell = r^2\omega$) profiles across the gap for the different q values at $Re_S \approx 1.04 \times 10^5$. The red circles (●) are the specific angular momentum profiles of the flow, with connecting lines to guide the eye. Error bars are smaller than the symbols. The solid black line (—) and dashed blue line (– –) are the specific angular momentum profiles for $\omega(\widetilde{r}) = \Omega_i$ and $\omega(\widetilde{r}) = \Omega_o$, respectively. The vertical axes have the same units and the horizontal axes are the same for all plots. The Keplerian configuration is shown at the top-right.

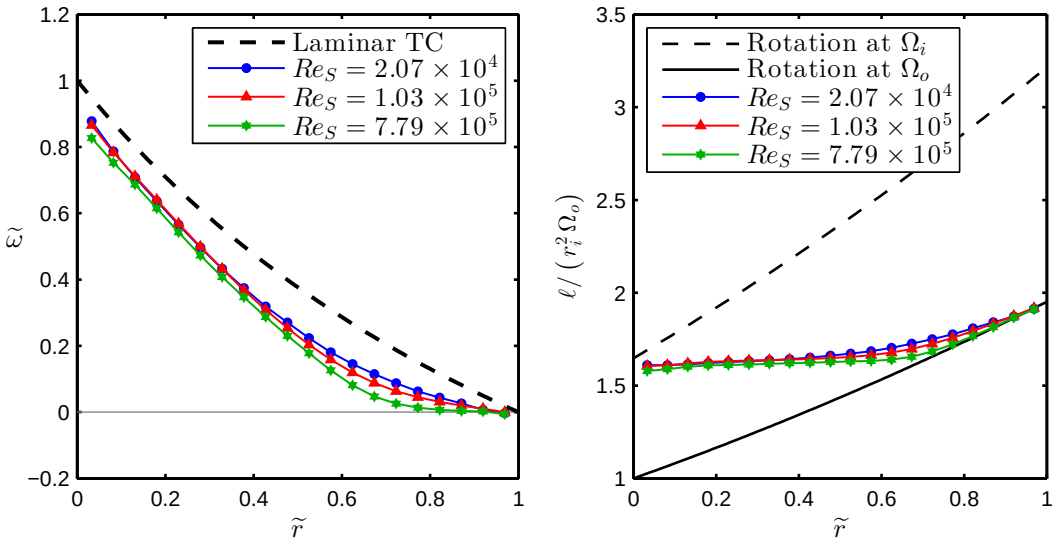

Figure 3.3: Comparison of the normalized angular velocity and specific angular momentum profiles across the gap for the Keplerian cylinder rotation ratio ($q = +1.500$) at three different Re_S. (a) the normalized angular velocity $\widetilde{\omega}$ with the laminar Taylor-Couette profile drawn for comparison and (b) the specific angular momentum ℓ normalized by $r_i^2\,\Omega_o$ with lines for solid-body rotation at the inner and outer cylinder rotation rates ($r^2\Omega_i$ and $r^2\Omega_o$, respectively). The error bars are smaller than the symbol heights.

3.4 Further Analysis And Discussion

3.4.1 Super-rotating Flow for The Sub-rotating Regime

As seen in Figure 3.1 for all three sub-rotating profiles, $\widetilde{\omega} < 0$ except near the inner cylinder indicating flow super-rotation (Figure 3.1b). The flow super-rotation can be quantified by taking the minimum $\widetilde{\omega}$ in the profile to be the strength of the super-rotation, and finding its radial position along with where the linear interpolation of where the profile crosses $\omega = \Omega_o$ ($\widetilde{\omega} = 0$) to super-rotation. The strength of the super-rotation is shown in Figure 3.4a, and the radial locations of

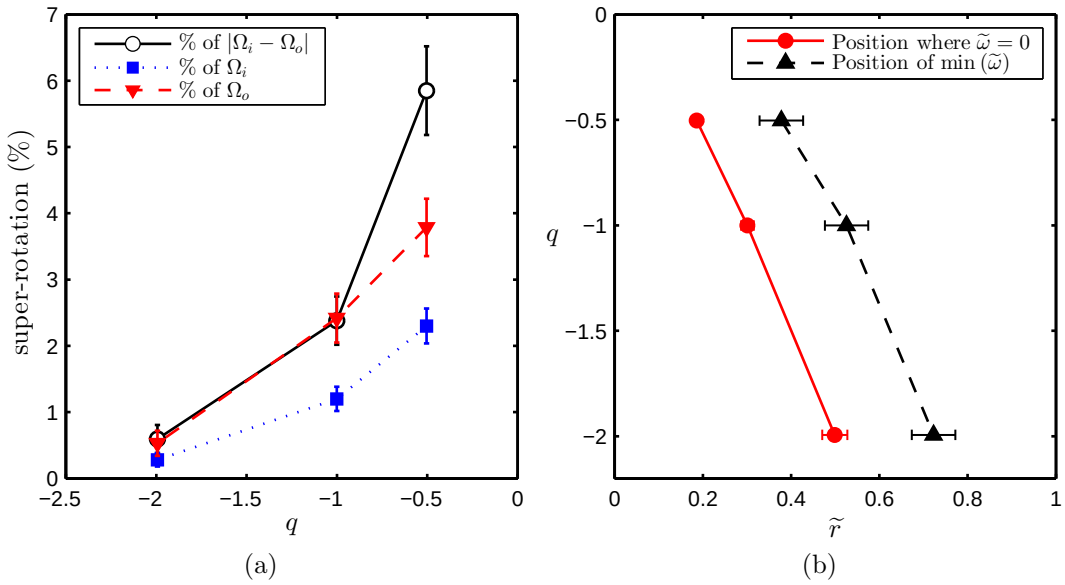

Figure 3.4: Super-rotating flow strength and locations in the sub-rotating regime at $Re_S = 1.04 \times 10^5$. (a) Flow super-rotation ($\omega > \Omega_o > \Omega_i > 0$) strength $\omega - \Omega_o$ at each q as a percentage of $|\Omega_i - \Omega_o|$, Ω_i, and Ω_o. (b) The radial positions where the profile crosses $\widetilde{\omega} = 0$ ($\omega = \Omega_o$) to be super-rotating, and the radial position where the super-rotation is at its maximum (minimum $\widetilde{\omega}$). Connecting lines are drawn to guide the eye in both plots.

the maximum super-rotation and of $\widetilde{\omega} = 0$ are shown in Figure 3.4b. Approaching solid-body rotation ($q \to 0$) at fixed non-zero Re_S, the strength of super-rotation increases, and the radial positions of the super-rotation maximum and of $\widetilde{\omega} = 0$ both move towards the inner cylinder. This is a singular limit, which is very different from the limit $q \to 0$ in which case one would get $\omega(r) = \Omega_i = \Omega_o$. The distance between these radial positions was approximately the same for all three q, namely a value of 0.2 gap-widths. The flow super-rotation was seen at all five heights for which radial profiles of the velocity were taken. They vary from each other by $\Delta\widetilde{\omega} < 0.01$ axially over the outer half of the gap. The 0.2 gap-width separation was seen at the other heights for $q = -0.503$, but could not be resolved for $q = \{-1.001, -1.994\}$ since

the point where $\widetilde{\omega} = 0$ lies in the inner half of the gap.

The specific angular momentum profiles in Figure 3.2 were slightly greater than for solid-body rotation with the outer cylinder, except close to the inner cylinder, which is another way of saying there is flow super-rotation. The Navier-Stokes equation does not constrain angular velocities to be bound by Ω_i and Ω_o due to its non-linear term, unlike the temperature field in Rayleigh-Bénard flow, which is contrained between the two plate temperatures as the temperature advection equation is linear. Even with the super-rotation, we still have $\partial\ell/\partial r > 0$ over the parts of the gap that are resolved; and ℓ is bound between the specific angular momenta of the outer cylinder and the axial boundaries at $\widetilde{r} = 0$, which are the locations of the largest and smallest ℓ on the axial boundaries, respectively. Angular momentum is transported to the inner cylinder in this regime since the torque on the inner cylinder is negative (Paoletti and Lathrop 2011). With inward advection of angular momentum across the gap (there is also the possibility of axial transport), the outer cylinder and axial boundaries must be the source of angular momentum to sustain the flow super-rotation against spin down to $\omega = \Omega_o$. This also allows one to estimate the maximum flow super-rotation that could be seen. If fluid from the outer cylinder having specific angular momentum $\ell = r_o^2\Omega_o$ is transported to the inner cylinder while conserving ℓ, it will have an angular velocity $\omega_s = \Omega_o/\eta^2$. Normalizing the flow super-rotation $\omega_s - \Omega_o$ respectively by $|\Omega_i - \Omega_o|$, Ω_i, and Ω_o, we get

$$\frac{\omega_s - \Omega_o}{|\Omega_i - \Omega_o|} \leq \left(\frac{1-\eta^2}{\eta^2}\right)\left|\frac{1}{\eta^{-q}-1}\right| , \tag{3.1}$$

$$\frac{\omega_s - \Omega_o}{\Omega_i} \leq \left(\frac{1-\eta^2}{\eta^2}\right)\eta^q , \tag{3.2}$$

$$\frac{\omega_s - \Omega_o}{\Omega_o} \leq \frac{1-\eta^2}{\eta^2} \tag{3.3}$$

as estimates of the super-rotation upper bound. For our $\eta = 0.716$, $(1-\eta^2)/\eta^2 = 0.95$. The flow super-rotations we see in Figure 3.4a are one to two orders of magnitude smaller than the estimated bounds. As Equation 3.1 diverges as $q \to 0$, an open question is whether the magnitude of the flow super-rotation normalized by $|\Omega_i - \Omega_o|$ diverges as $q \to 0$ at fixed non-zero Re_S.

3.4.2 Quasi-Keplerian Angular Momentum Profile And Transport

For all the quasi-Keplerian profiles in Figure 3.2, there is a pattern in the profiles. Namely, they are split into three regions: an inner region whose angular momentum profile is nearly flat with a slight positive slope, an outer region where the flow is nearly in solid-body rotation at Ω_o, and a middle transition region in which the angular momentum profile curves upward from being flat to solid-body rotation at Ω_o. At $q = 1.908$, the inner region extends over nearly the whole gap. As q decreases for fixed Re_S, the inner region shrinks until for $q = 0.333$ it is nearly absent, with the outer region having grown to be almost the whole gap.

As seen in Figure 3.3b, as Re_S is increased, the inner and outer regions appear to grow while the middle region shrinks. The same pattern is seen going from

$Re_S = 1.03 \times 10^5$ to $Re_S = 7.82 \times 10^5$ for $q = 1.909$, which is not shown here but can be seen in the data in the supplementary material of the paper this chapter is adapted from (Nordsiek et al. 2015). The pattern suggests that in the limit $Re_S \to \infty$, the middle region might disappear entirely. If we approximate the inner region as a completely flat angular momentum profile, approximate the outer region as rotating at exactly Ω_o, ignore any boundary layer on the inner cylinder, and assume that the pattern holds for the rest of the quasi-Keplerian regime and that no flow state transitions at higher Re_S break it; then the angular velocity profile for the quasi-Keplerian in the asymptotic limit $Re_S \to \infty$ regime in our geometry would be

$$\omega(r) = \begin{cases} (r_i/r)^2 \, \Omega_i & \text{for } r < r_c \\ \\ \Omega_o & \text{for } r \geq r_c \end{cases} \tag{3.4}$$

with

$$r_c = r_i \sqrt{\frac{\Omega_i}{\Omega_o}} = r_i \, \eta^{-q/2} \, , \tag{3.5}$$

$$\widetilde{r}_c = \frac{\eta}{1-\eta} \left(\eta^{-q/2} - 1 \right) \, , \tag{3.6}$$

where r_c is the transition radius between the flat angular momentum profile and solid-body rotation at Ω_o. For large but finite Re_S, Equation 3.4 can serve as an

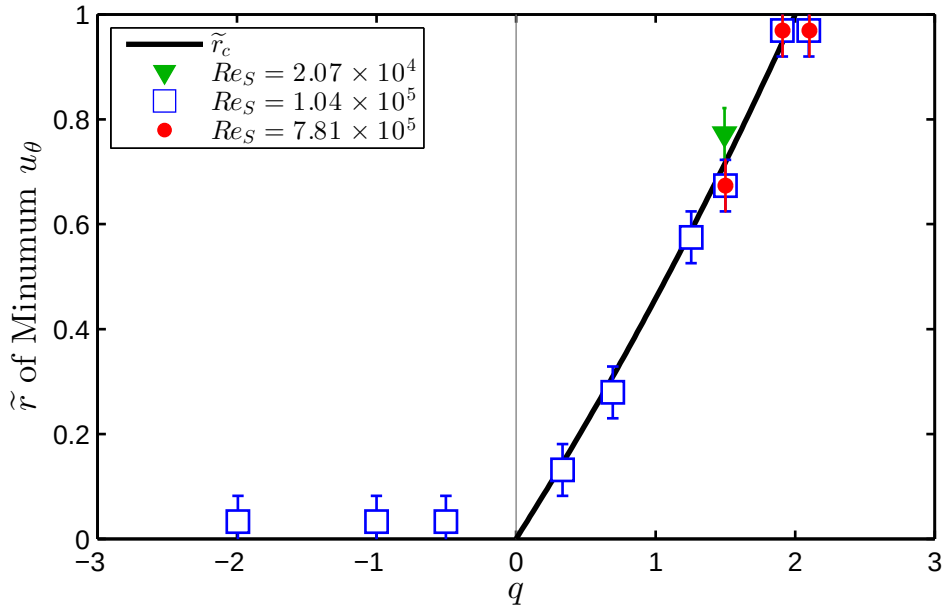

Figure 3.5: Radial positions of the minimum in the azimuthal velocity u_θ as a function of q (x-axis) and Re_S (different symbols). In the quasi-Keplerian regime, $\widetilde{r}_c$ from Equation 3.6 is shown for comparison (solid line).

approximate profile. This approximate profile was derived independently by Dunst (1972) by assuming that the inner region had a flat angular momentum profile, based on his observation of a well-mixed inner region in his Taylor-Couette experiment.

For the approximately constant specific angular momentum $\ell = r^2\omega = ru_\theta$ inner region, $\partial u_\theta/\partial r < 0$. Then for the outer regions rotating at approximately Ω_i, $\partial u_\theta/\partial r > 0$. Hence, we can quantify the radial position of the transition region by finding the radial positions for which the azimuthal velocity profiles $u_\theta(r)$ are at their minimum. They are shown in Figure 3.5. In the quasi-Keplerian regime, we find that the position of the minimum velocity corresponds very well with $\widetilde{r}_c$ in Equation 3.6, giving merit to the approximate profiles of Equation 3.4. Outside of the quasi-Keplerian regime, the position of the minimum is located at the inner cylinder for $q < 0$, and at the outer cylinder for $q > 2$.

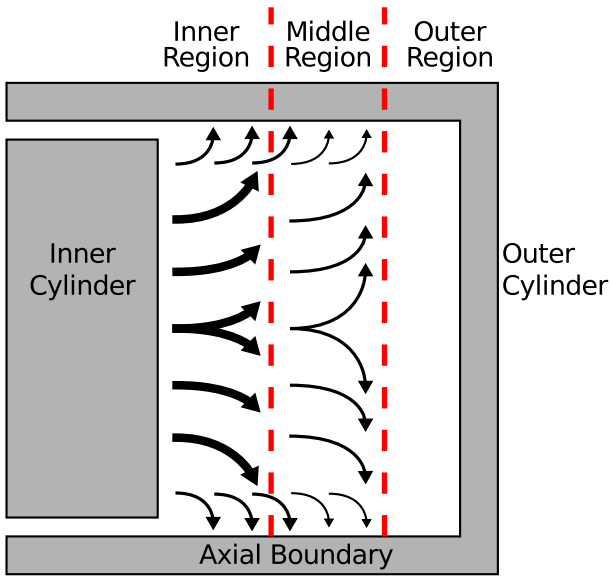

Figure 3.6: Schematic drawing of the angular momentum transport in the quasi-Keplerian regime when the axial boundaries are attached to the outer cylinder. Red dashed lines denote the boundaries between the inner, middle, and outer flow regions. Black arrows denote the transport of angular momentum. The radius and aspect-ratios (η and Γ) have been changed for visual clarity. Angular momentum is transported radially off the inner cylinder and then transported axially to the axial boundaries in the inner and middle regions.

The approximately flat angular momentum profile in the inner region, when away from the Rayleigh line where the laminar Taylor-Couette profile is flat, indicates that the angular momentum is well mixed with advection-dominated transport in the radial direction. In contrast, there is likely little radial angular momentum transport by advection or diffusion in the outer region as the profile is close to solid-body at Ω_o. A large amount of angular momentum is transported radially from the inner cylinder based on the torque measurements with the similar Maryland experiment (Paoletti and Lathrop 2011) and on the upcoming analysis of Section 3.4.3. The large amount of angular momentum transported off the inner cylinder and mixed in the inner region has to go somewhere, but the outer region, if present, is

likely not transporting much angular momentum. Then, when an outer region is present such as when $q < 2$ far from the Rayleigh line, most of the angular momentum must be transported axially to the axial boundaries in the inner and possibly middle regions, as shown schematically in Figure 3.6. As q increases at fixed Re_S towards the Rayleigh line, the outer region disappears and an increasing fraction of the angular momentum can be transported to the outer cylinder through the middle region instead of being transported to the axial boundaries. For $q \geq 2$, there is no middle region and a boundary layer forms close to the outer cylinder that steepens with increasing q (van Gils et al. 2012), indicating that an increasing fraction of the angular momentum is transported to the outer cylinder instead of to the axial boundaries. Finally, nearly all of the angular momentum is transported to the outer cylinder.

These features are also seen in wide-gap low aspect-ratio experiments. Using dye injection from the inner cylinder, Dunst (1972) found a well mixed inner region and a quiescent outer region with poor mixing. In Figure 3.7, the angular velocity and the specific angular momentum profiles for $q \approx 1.9$ from Schartman et al. (2012), Edlund and Ji (2014), and Kageyama et al. (2004) are compared to each other and to the results from our apparatus. The profiles for Schartman et al. (2012) and Edlund and Ji (2014) were constructed by extracting velocities from their figures (6 and 2, respectively). Kageyama et al. (2004) did velocimetry at five different axial heights. Profiles for Kageyama et al. (2004) were constructed by splitting the range $\widetilde{r} \in [0, 1]$ into bins of width 0.02 and averaging the ω within each bin.

They all deviate from the laminar Taylor-Couette profile and show the same

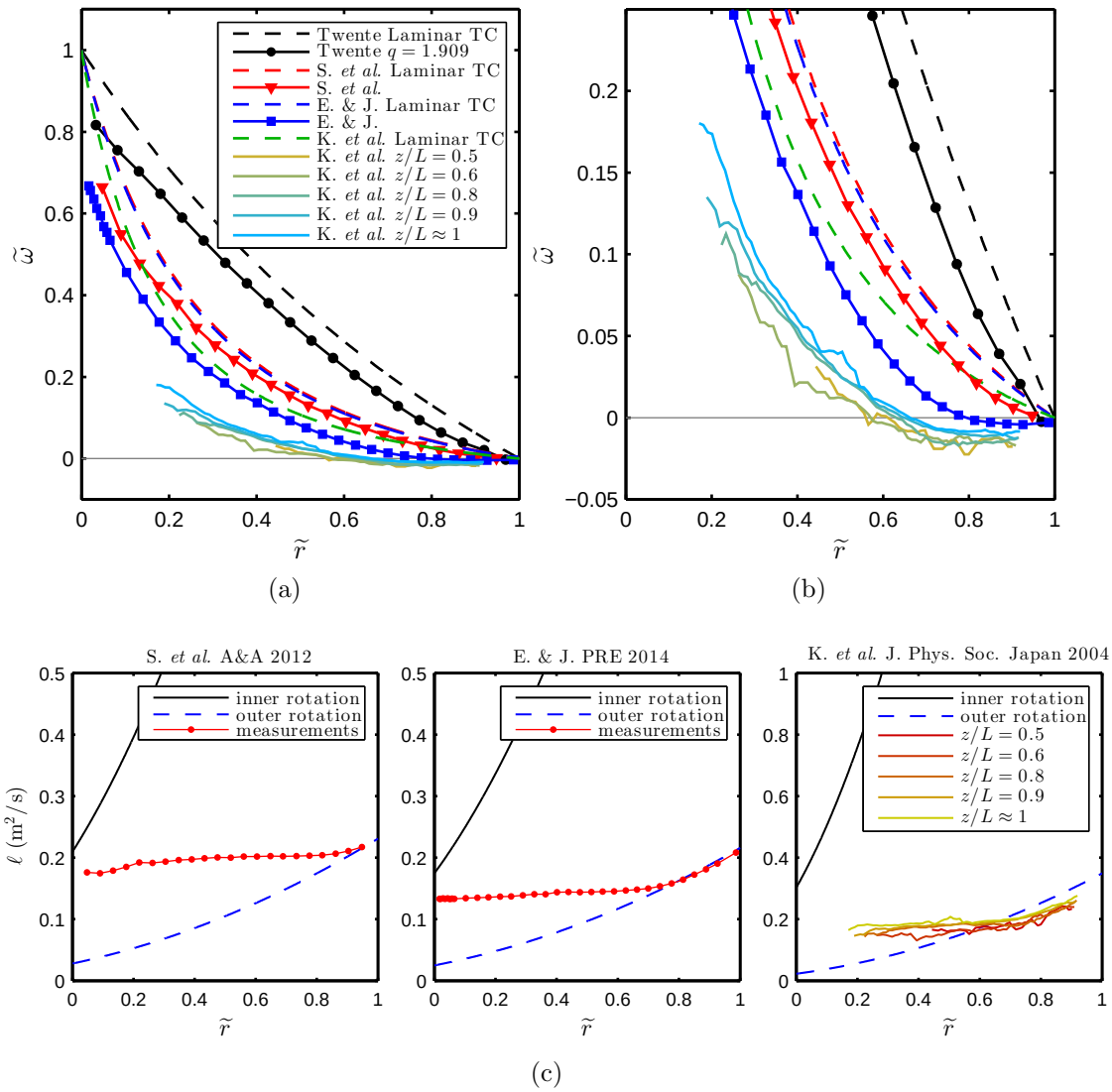

Figure 3.7: Comparison of the azimuthal velocimetry for $q \approx 1.9$ between different experiments. This includes our experiment (Twente) with $\eta = 0.716$ at $q = 1.909$ and $Re_S = 7.82 \times 10^5$, Schartman et al. (2012) with $\eta = 0.348$ at $q = 1.908$ and $Re_S = 5.05 \times 10^5$, Edlund and Ji (2014) with $\eta = 0.340$ at $q = 1.803$ and $Re_S = 4.34 \times 10^5$, and Kageyama et al. (2004) with $\eta = 0.255$ at $q = 1.896$ and $Re_S = 1.30 \times 10^6$. Normalized angular velocities $\widetilde{\omega}$ profiles are compared (a) at full scale and (b) expanded around $\widetilde{\omega} = 0$ using the same symbols to emphasize the parts of the profiles close to rotation at Ω_o. Dashed lines are the laminar Taylor-Couette profiles for each experiment. (c) The specific angular momentum ($\ell = r^2\omega$) profiles for each experiment side by side with the same horizontal axes and with vertical axes in the same units. The solid black line (—) and dashed blue line (– –) are the specific angular momentum profiles for $\omega(\widetilde{r}) = \Omega_i$ and $\omega(\widetilde{r}) = \Omega_o$, respectively.

three regions with a relatively flat ℓ close to the inner cylinder and rotate close to Ω_o close to the outer cylinder. However, the relatively flat ℓ inner region is offset downward from the specific angular momentum on the inner cylinder, indicating the presence of a boundary layer on the inner cylinder more significant than in our experiment. The experiments of Kageyama et al. (2004) and possibly Edlund and Ji (2014) also exhibit flow sub-rotation ($\omega < \Omega_o < \Omega_i$) in the middle and outer regions. The axial transport of angular momentum and the presence of three regions in the quasi-Keplerian azimuthal velocity profiles appear to be more general than just occuring in our specific apparatus with its geometry and ranges of Re_S and q, although the strength of the boundary layer on the inner cylinder appears to depend on η and/or Γ.

3.4.3 Torque on The Inner Cylinder

The velocity gradients near the inner cylinder were larger than in laminar Taylor-Couette as the $\widetilde{\omega}$ values at the point closest to the inner cylinder in Figures 3.1 and 3.3a are below that of the laminar Taylor-Couette profile. This steepness means that the torque on the inner cylinder must be larger than in laminar Taylor-Couette flow. If boundary layers were present, the profiles would be even steeper at the inner cylinder, and thus the torques even larger.

Assuming a turbulent boundary layer, the thickness y_0 of the viscous sublayer on the inner cylinder is $y_0 = (\nu/u^*)\, y_0^+$ where $u^* = \sqrt{|\tau|/\rho}$ is the friction velocity, ρ is the fluid density, and y_0^+ is the sublayer thickness in dimensionless units (Schlichting

1979). From measurements in our apparatus for pure inner cylinder rotation at comparable Re_S, y_0^+ is in the range of 5–10 (Huisman et al. 2013). Then for $Re_S = 10^5$, we get $y_0 \leq 2$ mm since $T \geq T_{\text{lam}}$ and $y_0^+ \leq 10$. Since $r - r_i = 2.6$ mm was the point closest to the inner cylinder where the flow velocity was resolved, our azimuthal velocimetry did not extend into the viscous sublayer. Due to not resolving the viscous sublayer, the torque in our apparatus cannot be obtained from the velocity profiles; meaning direct comparisons cannot be done to the torque measurements of Paoletti and Lathrop (2011) on the Maryland experiment with near identical geometry. However, lower bounds on the torque can be obtained because the azimuthal profiles can give the shear stress, instead of both the shear and Reynolds stresses.

The azimuthal shear stress, when averaged azimuthally, is $\tau = -\rho\nu r\,(\partial\omega/\partial r)$ where ρ is the fluid density (see page 48, Landau and Lifshitz 1987). The torque on a cylinder of radius r from just the shear stress is $T_\nu = 2\pi r^2 L\tau$, which in terms of the angular velocity is

$$T_\nu = -2\pi\rho\nu L r^3 \frac{\partial\omega}{\partial r}\,. \tag{3.7}$$

To get the lower bound for the torque on the inner cylinder, $\partial\omega/\partial r$ was obtained from the difference between ω at the point closest to the inner cylinder ($r - r_i = 2.6$ mm which is $\widetilde{r} = 0.033$) and Ω_i at the inner cylinder. It must be noted that the velocity profile was taken at the axial height of one of the small separations in the inner cylinder, which is 2.5 mm thick, and therefore the gradients in ω we

Table 3.2: The ratios of the lower bounds of the torque on the inner cylinder T_ν to the laminar Taylor-Couette torque T_{lam} for each set of measurements, ordered by Re_S and then by q.

q	Re_S	T_ν/T_{lam}
1.493	2.07×10^4	2.32 ± 0.05
2.098	1.03×10^5	2.99 ± 0.04
1.908	1.03×10^5	2.75 ± 0.04
1.501	1.03×10^5	2.56 ± 0.05
1.255	1.03×10^5	2.49 ± 0.06
0.693	1.04×10^5	3.02 ± 0.09
0.333	1.05×10^5	5.12 ± 0.18
−0.503	1.05×10^5	9.79 ± 0.12
−1.001	1.04×10^5	8.55 ± 0.06
−1.994	1.03×10^5	7.45 ± 0.04
2.102	7.83×10^5	3.66 ± 0.04
1.909	7.82×10^5	3.50 ± 0.04
1.500	7.79×10^5	3.31 ± 0.05

calculate might be perturbed compared to other axial heights due to the vicinity to the separation.

The torque lower bounds are listed in Table 3.2. The lower bounds were all larger than the laminar Taylor-Couette torque (Equation 1.36), which supports the $|T/T_{\text{lam}}| \gg 1$ result of Paoletti and Lathrop (2011) on the similar Maryland experiment in both regimes for $Re_S > 3.5 \times 10^5$. The measurements in this paper extend this result of Paoletti and Lathrop (2011) towards solid-body rotation in both regimes.

For the quasi-Keplerian regime, we can use the approximate flatness of the specific angular momentum profile in the inner region to make an analytical approximate torque lower bound. Treating the inner region as having a flat specific angular momentum profile from the inner cylinder with no boundary layer as in Equation 3.4 and applying Equation 3.7, the ratio of the torque lower bound $T_{\nu,\text{flat}}$

to the laminar Taylor-Couette torque (Equation 1.36) is

$$\frac{T_{\nu,\text{flat}}}{T_{\text{lam}}} = \frac{1-\eta^2}{1-\eta^q} \quad \text{for } 0 < q \leq 2 \, . \tag{3.8}$$

The ratio is always larger than one, approaching one at $q = 2$. It diverges as $q \to 0$, which is due to the width of the inner region shrinking towards zero since $r_c \to r_i$ in Equation 3.5. The decrease in r_c means that ω changes from Ω_i to Ω_o over an ever smaller radial distance, giving a sharper gradient of ω in the inner region, which becomes infinite as $q \to 0$. However, if the inner region of a flat angular momentum profile disappears entirely as $q \to 0$ at a given Re_S, then this lower bound may no longer hold. For $Re_S = 1.04 \times 10^5$, the inner region might be close to disappearing by $q = 0.333$ based on the angular momentum profiles in Figure 3.2. As the middle region shrinks with increasing Re_S (Figure 3.3b), the q at which the inner region might disappear decreases with increasing Re_S.

The torque lower bounds can be compared to the torque scaling that Paoletti et al. (2012) fit to the Maryland torque measurements in the Rayleigh-stable and unstable regimes (Paoletti and Lathrop 2011) and the torque measurements on the apparatus presented in this paper in the unstable regime (van Gils et al. 2011b). The scaling was for the ratio of the torque on the inner cylinder to the torque $T_{+\infty}$ for pure inner rotation ($q = +\infty$) at the same Re_S, which in this paper was obtained from torque measurements in the very similar Maryland experiment (equation (9) in Lathrop et al. 1992a). The lower bounds are compared to the torque scaling $Re_S > 3.5 \times 10^5$ (equation (12) in Paoletti et al. 2012) in Figure 3.8.

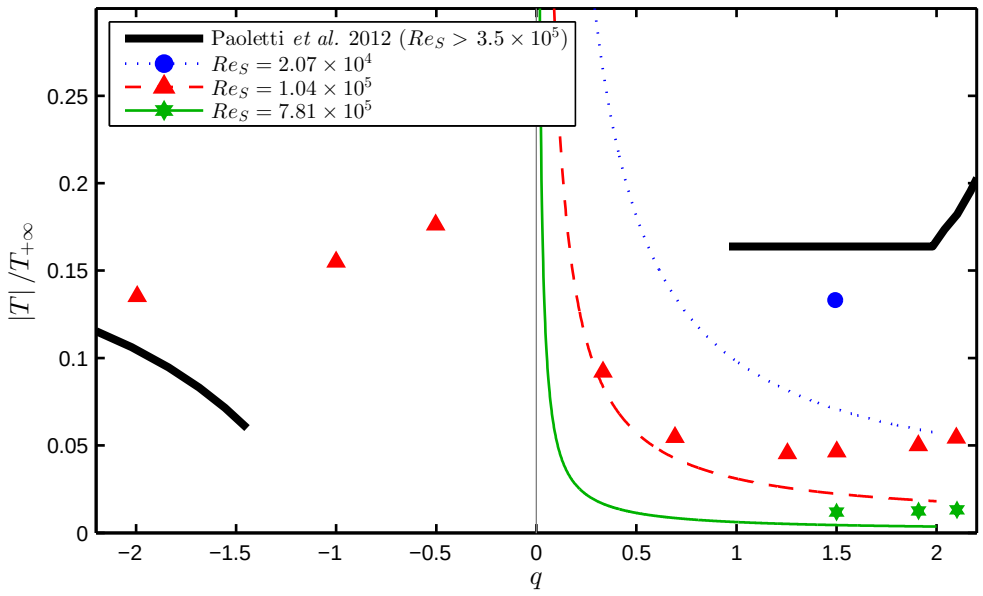

Figure 3.8: Comparison of inner cylinder torque lower bounds calculated at $z/L = 0.209$ to the torques measured by Paoletti et al. (2012). Torques are normalized by the torque for pure inner rotation at the same Re_S. The scaling of Paoletti et al. (2012) for $Re_S > 3.5 \times 10^5$ is the thick black solid line. The torque ratio lower bounds obtained from the velocity profiles are the symbols, coded by Re_S. The lower bound torques from the quasi-Keplerian flat inner angular momentum profile approximation in Equation 3.8 for each Re_S are the thin lines with the same colors as the symbols, which increase with decreasing Re_S. Error bars are smaller than the symbols.

As the torque ratios must be positive, the torque scaling must start curving upwards on the sub-rotating regime side when approaching solid-body rotation at some $q > -1.5$ to avoid crossing zero. The three sub-rotating regime torque lower bounds for $Re_S = 1.04 \times 10^5$ give $|T|/T_{+\infty}$ values that are larger than those for $Re_S > 3.5 \times 10^5$ (Paoletti et al. 2012). Thus, the $|T|/T_{+\infty}$ scaling of Paoletti et al. (2012) must increase if extended to $Re_S = 1.04 \times 10^5$.

On the quasi-Keplerian side, comparisons can be made between our measurements at $Re_S = 7.81 \times 10^5$ to those of Paoletti et al. (2012) for $Re_S > 3.5 \times 10^5$. Our $|T|/T_{+\infty}$ lower bounds from both the measured velocity profiles and the flat in-

ner region approximation from Equation 3.8, are considerably smaller than those of Paoletti et al. (2012). As our lower bounds only considered shear stress (diffusion), the difference in torques on the inner cylinder must be due to Reynolds stresses (advection) in the region of $\widetilde{r} \leq 0.033$. The divergence of the torque lower bound for the flat inner region angular momentum approximation as $q \to 0$ suggests that the flat quasi-Keplerian $|T|/T_{+\infty}$ scaling of Paoletti et al. (2012) will deviate from being flat if extended to $q < 1$, unless the inner region disappears or is distorted close to solid-body rotation.

Chapter 4: TC: Dye Injection

4.1 Measurements

To verify the super-rotating flow found in the azimuthal velocimetry on the T^{3}C experiment (Section 3.4.1), dye injection visualization was performed on the Maryland experiment. In addition, we want to see if the quasi-Keplerian regime in our geometry has sub-rotating flow, as was seen by Kageyama et al. (2004) and possibly Edlund and Ji (2014). The measurements were performed at the same $Re_S = 1.04 \times 10^5$ as in Chapter 3 and half that value, $Re_S = 5.2 \times 10^4$. This was done at the same nine q (Table 3.1). In addition, the dye injection was performed at higher q, going into the unstable region all the way to pure inner rotation (2.500, 3.000, and $+\infty$), and lower q, going all the way to pure outer rotation (-4.00 and $-\infty$) for both Re_S. For $Re_S = 5.2 \times 10^4$, the experiment could get closer to solid-body rotation ($q = 0$) so three additional values were done (0.333, 0.250, and -0.250). The q are all shown in Table 4.1.

Three different injector depths, r_{inj}, were used. Measured from the inner cylinder towards the outer cylinder, they were midgap, $\frac{3}{4}$ gap, and flush with the outer cylinder. Normalizing the radial position of the injector (Equation 1.31), the injector positions were $\widetilde{r}_{\text{inj}} = \{0.50, 0.75, 1.0\}$.

Table 4.1: The q values for which dye injection measurements were measured and their corresponding rotation rate ratios (Ω_i/Ω_o), rotation parameter R_Ω, and Rossby number Ro.

q	Ω_i/Ω_o	R_Ω	Ro
$+\infty$	$+\infty$	-0.275	$+\infty$
3.000	2.630	-0.678	1.630
2.500	2.238	-0.805	1.238
2.100	1.968	-0.953	0.968
1.909	1.850	-1.047	0.850
1.500	1.622	-1.330	0.622
1.258	1.500	-1.587	0.500
0.692	1.250	-2.900	0.250
0.333	1.113	-6.058	0.113
0.250	1.084	-8.091	0.084
-0.250	0.923	8.196	-0.077
-0.500	0.851	4.131	-0.149
-1.000	0.725	2.105	-0.275
-2.000	0.525	1.105	-0.475
-4.000	0.276	0.630	-0.724
$-\infty$	0	0.380	-1.000

Table 4.2: The length of time the dye was pumped, the camera frame rate, and the duration that videos were taken at for each Re_S.

Re_S	injection time (s)	frame rate (fps)	video duration (s)
$Re_S = 5.2\times10^4$	50	10	60 or 120
$Re_S = 1.04\times10^5$	25	20	30 or 60

At least two videos of dye injection were taken for each injector depth for each (q, Re_S). The dye was pumped for an extended duration while video was taken. In later runs, the videos were run for twice as long to capture the dye rotating back around into view, or doing so more times. The dye pumping and video parameters are in Table 4.2.

A total of 262 videos were taken. The number of videos taken was large since many videos had problems such as too much dye in the water saturating the camera, the left half of the videos becoming corrupted, or the dye failing to pump (syringe pump jammed).

4.2 Flow Direction

Single frames from the videos for six different Rayleigh-stable q are shown in Figure 4.1 with a mask showing the locations of the cylinder and which direction the inner cylinder is rotating in the rotating frame. Note, both cylinders are rotating counter-clockwise in the stationary lab frame.

Perhaps the simplest aspect of the videos to discern is which direction the flow is moving at the dept of the dye injector in the rotating frame of the outer cylinder. The dye will either go upward or downwards or both in each video, which is visually discernible. This has the advantage of being straightforward to determine even for the videos with problems.

We went through each of the videos one by one and determined the direction of the flow by eye at the radial position of the injector as one of the following three

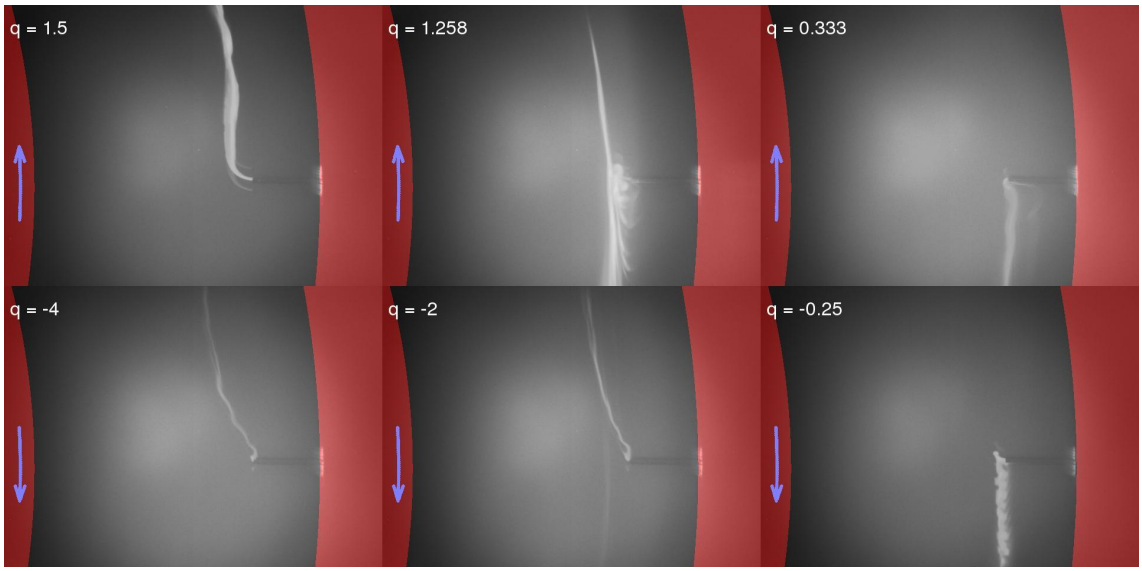

Figure 4.1: Video stills of dye being injected from the injector at $\widetilde{r}_{\text{inj}} = 0.75$ for $Re_S = 5.2 \times 10^4$. Videos for six different q are shown (they are labeled in the top-left corners). The top row of videos are quasi-Keplerian ($2 > q > 0$) and the bottom row are in the sub-rotating regime ($q < 0$). The images have a red mask to show where the two cylinders are. In addition, there is a blue arrow on the inner cylinder indicating which direction it is rotating in the rotating frame of the video.

Table 4.3: For $Re_S = 5.2 \times 10^4$, the number of videos that showed each of the three cases of flow (with, against, and both) for each q at all three injector positions $\widetilde{r}_{\text{inj}}$.

	$\widetilde{r}_{\text{inj}} = 0.50$			$\widetilde{r}_{\text{inj}} = 0.75$			$\widetilde{r}_{\text{inj}} = 1$		
q	with	both	against	with	both	against	with	both	against
$+\infty$	2	0	0	4	0	0	2	0	0
3.000	2	0	0	4	0	0	2	0	0
2.500	2	0	0	4	0	0	2	0	0
2.100	2	0	0	4	0	0	2	0	0
1.909	3	0	0	4	0	0	2	0	0
1.500	3	0	0	4	0	0	0	2	0
1.258	3	0	0	0	4	0	0	2	0
0.692	0	2	1	0	0	4	0	2	1
0.333	0	0	4	0	0	4	0	2	0
0.250	0	0	4	0	0	5	0	2	1
-0.250	0	0	4	0	0	4	0	2	0
-0.500	4	0	0	4	0	0	2	0	1
-1.000	3	0	0	4	0	0	3	0	0
-2.000	2	0	1	4	0	0	2	0	0
-4.000	0	3	0	4	0	0	1	1	0
$-\infty$	0	0	2	0	0	4	0	2	0

Table 4.4: For $Re_S = 1.04 \times 10^5$, the number of videos that showed each of the three cases of flow (with, against, and both) for each q at all three injector positions $\widetilde{r}_{\text{inj}}$.

	$\widetilde{r}_{\text{inj}} = 0.50$			$\widetilde{r}_{\text{inj}} = 0.75$			$\widetilde{r}_{\text{inj}} = 1$		
q	with	both	against	with	both	against	with	both	against
$+\infty$	2	0	0	4	0	0	2	0	0
3.000	2	0	0	4	0	0	2	0	0
2.500	2	0	0	5	0	0	2	0	0
2.100	2	0	0	5	0	0	2	0	0
1.909	3	0	0	6	0	0	2	0	0
1.500	3	0	0	4	0	0	0	3	0
1.258	4	0	0	0	3	0	0	2	0
0.692	0	4	0	0	0	2	0	2	0
-0.500	0	0	4	0	0	2	0	2	0
-1.000	3	0	0	2	0	0	2	0	0
-2.000	2	0	0	1	0	1	2	0	0
-4.000	0	0	3	0	2	0	0	2	0
$-\infty$	0	0	3	0	0	2	0	1	1

cases:

with

The fluid is rotating in the same direction as the inner cylinder in the rotating frame of the camera.

against

The fluid is rotating in the opposite direction as the inner cylinder in the rotating frame of the camera.

both

The fluid is rotating in both directions in the rotating frame of the camera. This includes both oscillating flow and two close radial layers flowing in opposite directions. Videos exhibiting each one and both were found.

Figure 4.1 shows all three cases.

For each combination of $(q, Re_S, \widetilde{r}_{\text{inj}})$, the total number of videos exhibiting

each case were counted. Let their counts be N_{with}, N_{against}, and N_{both}. The counts are given in Table 4.3 for $Re_S = 5.2 \times 10^4$ and Table 4.4 for $Re_S = 1.04 \times 10^5$.

To better elucidate whether the flow is in the same direction as the inner cylinder in the rotating frame of the outer cylinder, the opposite direction, or both; we define the quantity

$$W = \frac{N_{\text{with}} - N_{\text{against}}}{N_{\text{with}} + N_{\text{both}} + N_{\text{against}}} \ . \tag{4.1}$$

For flow that is purely in the same direction as the inner cylinder in the rotating frame, $W = 1$. For flow that is purely in the opposite direction, $W = -1$. Intermediate values mean that the flow goes in each directions at least some of the time, though it is not a good measure of how much time is spent going in each direction. Figure 4.2 shows W as a function of q at all three injector positions together.

For Rayleigh-unstable flow ($q > 2$), the flow is always in the direction of the inner cylinder's rotation. In the quasi-Keplerian regime as $q \to 0$, an increasing radial fraction of the outer part of the gap near the outer cylinder starts to get negative values of W, which indicates the presence of sub-rotating flow ($\Omega_i > \Omega_o > \omega$) at least some of the time. The change in direction occurs closer to the outer cylinder for larger q. This is the outer-region described in Section 3.4.2 where the flow rotates closer to Ω_o as q decreases. Sub-rotating flow was not definitively seen in the azimuthal velocity profiles in Figure 3.1, though for the two smallest q values (0.693 and 0.333), sub-rotating flow was within the statistical margin of error. At the outer cylinder, the flow was oscillating between both directions in the videos

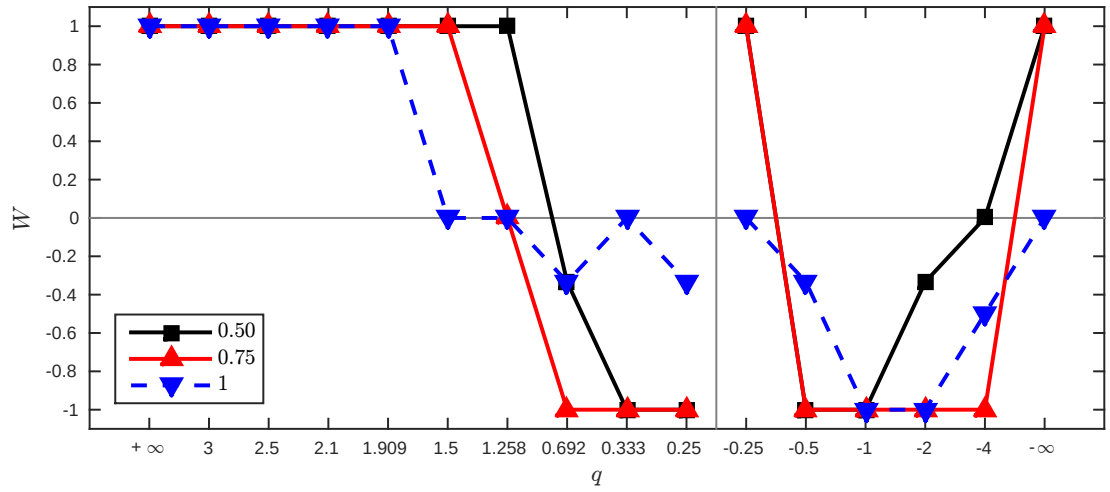

(a)

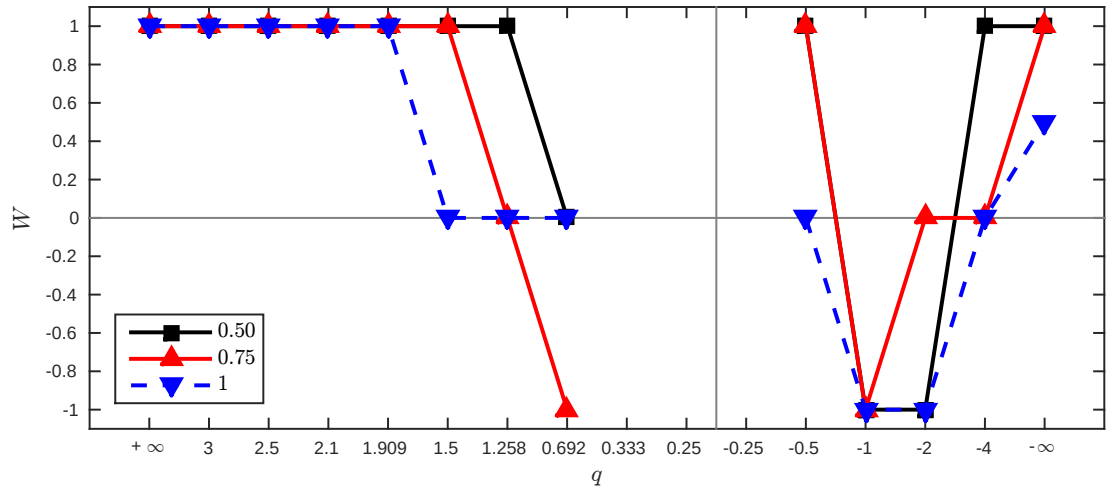

(b)

Figure 4.2: The degree W (Equation 4.1) to which the flow at the injector is in the same direction of the inner cylinder's rotation in the rotating frame of the outer cylinder (and camera) as a function of q for each injector position (their $\widetilde{r}_{\text{inj}}$ are shown in the legend). (a) $Re_S = 5.2 \times 10^4$. (b) $Re_S = 1.04 \times 10^5$.

(this is why $W \approx 0$). This may be the source of the peaks in the spectrograms of the wallshear stress on the outer cylinder at midheight in the quasi-Keplerian regime measured on the Maryland experiment by Paoletti and Lathrop (Fig. 3, 2011).

For the sub-rotating regime ($q < 0$), we see super-rotating flow ($W < 0$) for $q = \{-2, -1, -0.5\}$ confirming what was seen in the velocimetry in Section 3.4.1. Interestingly, as q is further increased towards solid-body rotation ($q \to 0$), the super-rotation begins to disappear with more and more of the flow being in the direction of the inner cylinder in the rotating frame. Additionally, both flow directions are found at the outer cylinder for pure outer rotation ($q = -\infty$).

Chapter 5: TC: Torque Scaling And Phase Diagram

5.1 Measurements Performed

Measurements of the torque required to rotate the middle section of the inner cylinder on the Maryland experiment over almost four decades of Re_S ($190 < Re_S < 1.0 \times 10^6$) were taken for four quasi-Keplerian q (not all q had the same range), which are shown in Table 5.1. For our geometry, these measurements connect the low Re_S simulations by Avila (2012) to the high Re_S torque measurements by Paoletti and Lathrop (2011) and velocimetry measurements in Chapter 3. We used the exact q that Avila (2012) simulated for the same geometry as our experiment ($q = 1.909$), which is also close to the q values done by Kageyama et al. (2004), Ji et al. (2006), Schartman et al. (2012), and Edlund and Ji (2014). We also included Keplerian flow ($q = 3/2$) and two others closer to solid-body rotation ($q = 1.258, 0.692$). The azimuthal velocimetry at $Re_S \sim 10^5$ for all four of these q was presented in Chapter 3.

Sequences of runs at the same q but increasing Re_S were done together. For each sequence, the acceleration rates for the motors driving each cylinder were set in the motor drives such that the spin-up of the cylinders stayed approximately on the same q. The acceleration rate was set so that the outer cylinder would take

Table 5.1: The four q that were investigated expressed in terms of the ratio of cylinder rotation rates as well as the rotation parameter R_Ω (Equation 1.27) and the Rossby number Ro (Equation 1.28). The minimum allowed torque for each q, the range of Re_S sampled, and the number of torque measurements for that q are also listed.

q	Ω_i/Ω_o	R_Ω	Ro	min Re_S	max Re_S	min. allow T (Nm)	# torques
1.909	1.850	-1.047	0.850	269.9	1.04×10^6	0.05	501
1.500	1.620	-1.333	0.620	185.3	3.22×10^5	0.05	439
1.258	1.500	-1.587	0.500	271.9	3.92×10^5	0.05	341
0.692	1.250	-2.899	0.250	273.1	1.25×10^5	0.02	410

180 s to reach $|\Omega_i/2\pi| = 10$ Hz.

Torques smaller than the minimum amounts for each q listed in Table 5.1 were not used. The minimum is smaller for the smallest $q = 0.692$ since it has much smaller dimensional torques and thus a smaller minimum was needed to keep a sufficient number of measurements to minimize gaps in the Re_S scaling.

Due to limits in the sensitivity of the torque sensor, the full range of Re_S cannot be obtained with a single fluid. Instead, we used water and several water-glycerol solutions as the working fluids to have a wide range of ν, and thus Re_S, available.

For water, the density, ρ, and ν were obtained from tables. The viscosity of water-glycerol solutions is a strong function of the glycerol mass fraction and the temperature, while ρ is a weaker function of them. With each water-glycerol solution, the ρ of a small sample was found to within 0.005 g/cm^3 by measuring its volume and mass at room temperature. Using the measured ρ, the mass fraction was estimated and then the ρ at other temperatures was calculated (Tables 7–2 and 7–10, Miner and Dalton 1953). The uncertainty in the measured density dominates the uncertainty in the density calculated at other temperatures since the

Table 5.2: Each working fluid, its glycerol mass fraction, base operating temperature, and torque offset. The density, kinematic viscosity, and thermal coefficient of its kinematic viscosity are given at its base operating temperature.

fluid #	glyc. m. frac. (%)	base T_k (C)	ρ (g/cm^3)	ν (cSt)	$d\nu/dT_k$ (cSt/K)	T_{offset} (Nm)
1	84.2	22	1.018	110.	-8.2	0
2	77.6	22	1.016	45.2	-2.9	0
3	70.4	22	1.014	24.9	-1.4	0
4	64.9	22	1.013	15.5	-0.80	0
5	57.3	22	1.011	10.0	-0.47	0
6	55.1	22	1.011	8.15	-0.37	0
7	51.0	20	1.010	6.99	-0.31	-0.014
8	49.1	21	1.010	5.69	-0.25	-0.012
9	42.2	20	1.008	4.65	-0.19	-0.014
10	36.8	21	1.007	3.29	-0.12	-0.013
11	21.5	21	1.003	2.09	-0.063	-0.015
12	7.9	21	1.000	1.45	-0.040	-0.015
13	0	24	0.997	0.911	-0.022	0
14	0	37	0.993	0.692	-0.013	-0.013
15	0	50	0.988	0.547	-0.0090	-0.015

thermal expansion coefficient of the density isn't sensitive to this imprecise mass fraction. The kinematic viscosity ν was measured using Cannon-Fenske Routine Viscometers immersed in a water bath at three different temperatures (20 C, 23 C, and 26 C) to obtain ν to within 2% and $d\nu/dT_k$ in the temperature range 19-27 C using a quadratic fit. The working fluids and their properties at their base operating temperatures are shown in Table 5.2.

For fluids 14 and 15, the Taylor-Couette was operated above room temperature by heating the aluminum outer cylinder as was done by Paoletti and Lathrop (2011). The heating of the fluid due to the applied shear was insufficient to keep the experiment hot without the aid of the heaters.

For fluids 1—13, the Taylor-Couette was operated near room temperature with no heating of the outer cylinder. There was viscous heating in the working fluid, most likely concentrated near the inner cylinder in the inner-region (Figure 3.6), and cooling to the air of the room on the outer cylinder. The experiment was mixed using slight counter-rotation between each run. This was done to reduce the formation of

thermal gradients that would not be well mixed in Rayleigh-stable Taylor-Couette flow, especially at low Re_S. Thermal gradients could lead to radial stratification and/or thermal convective instabilities. Even the apparently stabilizing thermal stratification of $\partial T_k/\partial r < 0$ might lead to instabilities due to the Ekman pumping from the axial boundaries, or due to the presence of gravity along the axial direction as found in the recent work by Lopez et al. (2013).

There is an additional advantage of using many working fluids with different ν but approximately the same density. At the same (q, Re_S), the dimensionless torque G should be the same for two different ν, but have different dimensional torques T. This allows the torque system's zeros to be refined so that the G from each sequence of runs, which have the same zero, match up between different working fluids at the same q in the range of Re_S that they overlap. Then additive constant torque offsets T_{offset} can be added to the raw torques to compensate. Using the torque data we present in this Chapter (Section 5.2), we found that T_{offset} was approximately constant for each sequence of runs done with the same fluid, so we use a single value for each fluid, which is shown in Table 5.2. T_{offset} was taken to be zero for the most viscous fluid (fluid 1). The values form a bi-modal distribution with some being zero and others being about -0.014 Nm. The difference between the modes is approximately the difference in the torque measurements obtained by rotating the middle section on its bearings to rest on the other side of the arm extending from the load cell.

5.2 Torque

All torque measurements presented here were normalized by the torque of the laminar Taylor-Couette profile G_{lam} (Equation 1.37) at the same Re_S. The Re_S scalings of the normalized torque for all four q are shown in Figure 5.1. The most obvious features are that G/G_{lam} is an increasing function of Re_S for all q, and that they are all greater than unity for $Re_S > 500$. This means that the flow is not simple laminar Taylor-Couette flow for these Re_S, and instead has much larger transport of angular momentum. This result is in agreement with the results of Paoletti and Lathrop (2011) on the same apparatus at $Re_S \sim 10^5$–10^6, and the torque lower bounds on the T^{3}C experiment in Section 3.4.3. It is also in agreement with the results of Schartman et al. (2012) on the Princeton MRI experiment, when the axial rings were rotating at the same rate as the outer cylinder (thus corresponding to the axial boundary conditions of our apparatus) but with very different η and Γ. For $q = 0.692$ for $Re_S > 10^4$, the uncertainties in the torques become much larger, both due to the smaller dimensional torques being measured with the lower ν water-glycerol solutions, and to including runs from smaller differences in the cylinder rotation rates $\Omega_i - \Omega_o$.

Due to the large number data points in (q, Re_S) phase space taken (1691), Figure 5.1 is hard to read. Thus, the measurements for each q were fit to a running local first order polynomial (line) in $(\log_{10} Re_S, \log_{10} G)$ space with a fitting window radius of 0.1 decades. The fits were weighted fits using the uncertainties in the $\log_{10} G$ (error bars in Figure 5.1). The fits correspond to powerlaws in (Re_S, G)

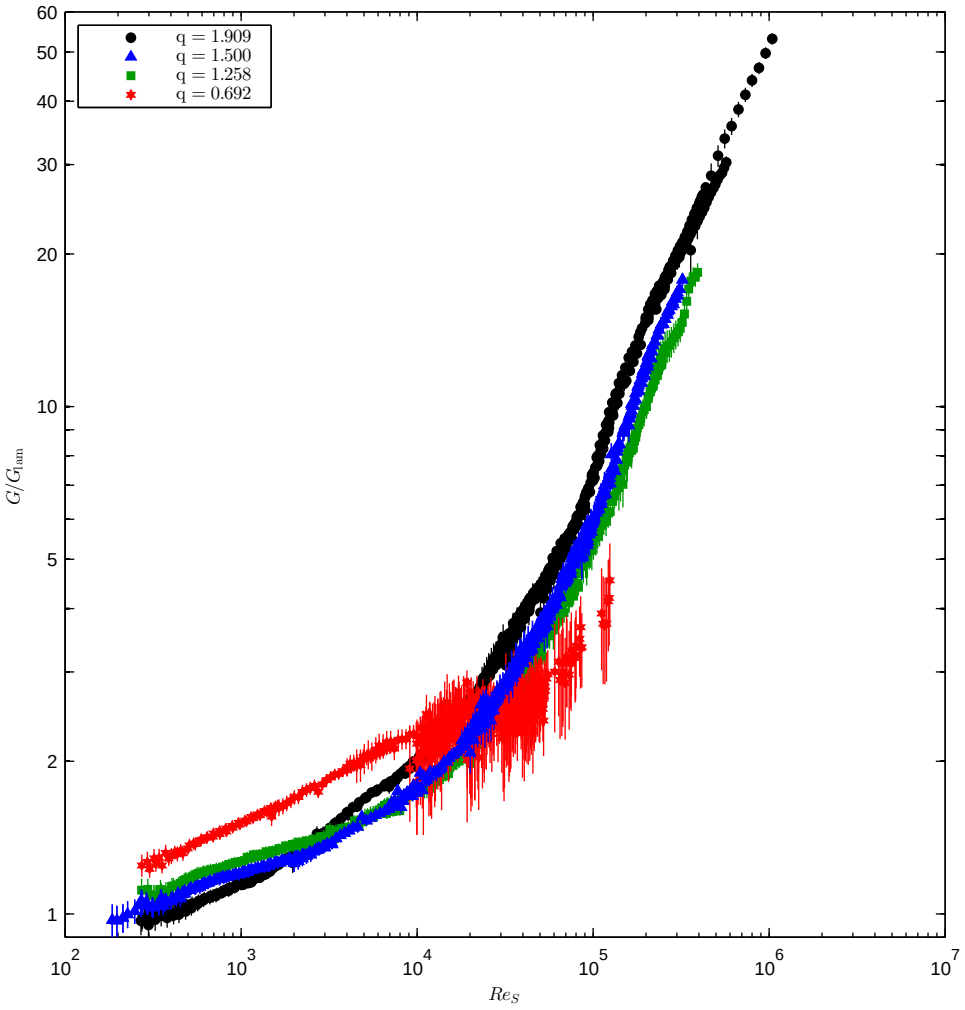

Figure 5.1: The normalized measured torque (G/G_{lam}) for all four q with error bars.

space. Figure 5.2 shows the running local loglog polynomial fit for each q along with a few of the individual torque measurements to show the spread in the torques and their uncertainties.

The q dependence of the torque is non-trivial. For low Re_S, $\frac{\partial G}{\partial q} < 0$ meaning that for fixed Re_S, the torque increases as one goes closer to solid-body rotation ($q \to 0$). Note that this is different than laminar Taylor-Couette flow where G_{lam} (Equation 1.37) is not a function of q at all. Moreover, if we extrapolate the torques to lower Re_S, the torques depart from $G/G_{\text{lam}} = 1$ at lower Re_S for smaller q.

As Re_S increases, the relative ordering of the torques for the different q values reverses so that for the highest Re_S tested, $\frac{\partial G}{\partial q} > 0$ meaning that the torque increases as one approaches the Rayleigh line ($q = 2$). This can be compared to the torque lower bounds from the quasi-Keplerian flat inner angular momentum profile approximation (Equation 3.8) in Section 3.4.3, which the velocimetry matched better as Re_S increased. Its derivative with respect to q is

$$\frac{\partial}{\partial q}\left(\frac{T_{\nu,\text{flat}}}{T_{\text{lam}}}\right) = \frac{\left(1-\eta^2\right)\left(\ln\eta\right)\eta^q}{\left(1-\eta^q\right)^2} < 0\,. \tag{5.1}$$

The derivative is negative because $0 < \eta < 1$ making $\ln\eta < 0$. The lower bound only reflects the shear stress (diffusion of angular momentum), not the Reynolds stresses (advection of angular momentum). Since $\frac{\partial G}{\partial q} > 0$ while the $\frac{\partial}{\partial q}$ of the torque from the shear stress is negative, the fraction of the angular momentum transport (torque) due to Reynolds stresses (advection) increases as q increases towards the Rayleigh line ($q = 2$) for high Re_S.

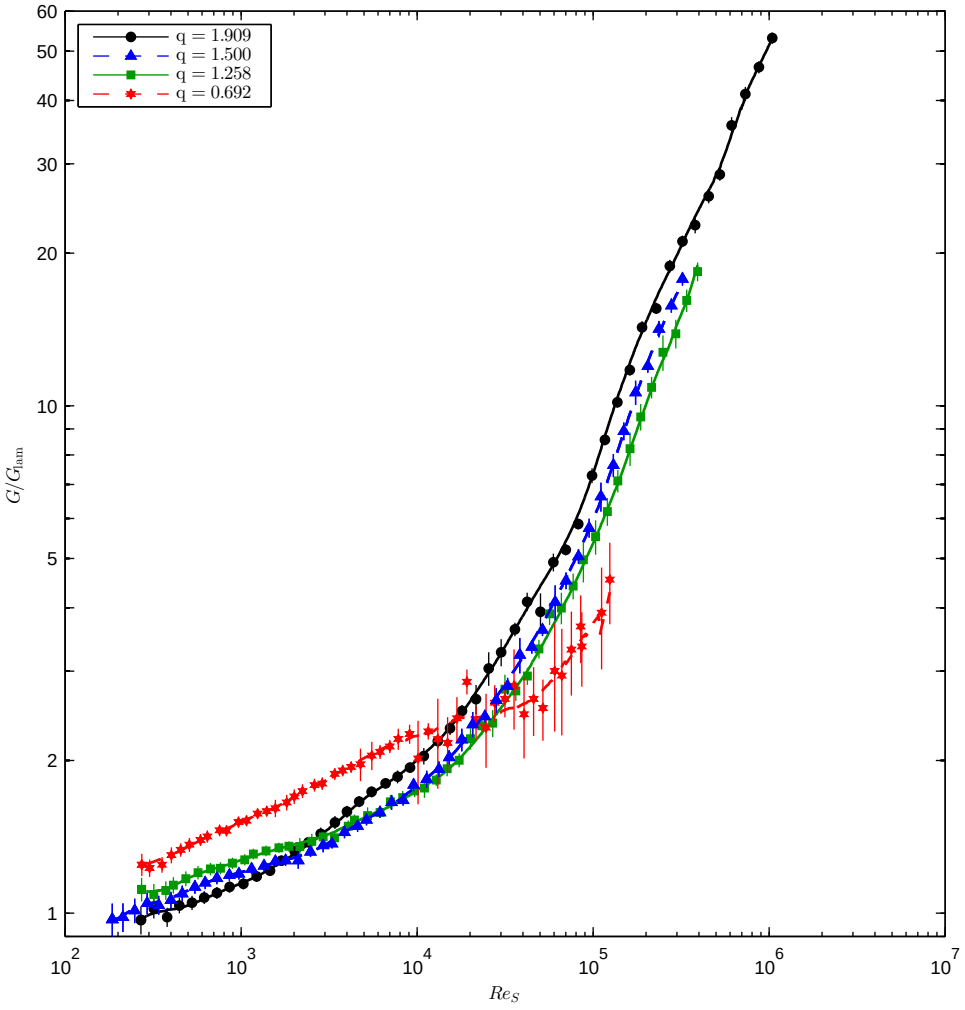

Figure 5.2: The running local polynomial loglog fits (window radius of 0.1 decades) of the normalized measured torque (G/G_{lam}) for all four q (lines) along with subset of 50 individual measurements for each q (symbols with error bars) chosen to be approximately equally spaced.

It was previously found that the dimensionless torque for pure inner rotation, $G_{+\infty}$, on our apparatus does not follow a power law in Re_S, or even a piecewise power law (Lathrop et al. 1992b,a; Lathrop 1992; Lewis and Swinney 1999), which is unlike the laminar Couette profile whose torque scales as $G_{\text{lam}} \propto Re_S$. It is therefore useful to look at G's local power law exponents of Re_S. Let

$$G\left(Re_S\right) = \beta\left(Re_S\right)\ Re_S^{\alpha(Re_S)}\ . \tag{5.2}$$

Right now, this is completely general. Over a small range in Re_S, we can let $\beta\left(Re_S\right)$ and $\alpha\left(Re_S\right)$ be constant in Re_S and find their values α and β respectively. In $(\log_{10} Re_S, \log_{10} G)$ space, this becomes

$$\log_{10} G\left(Re_S\right) = \log_{10}\beta + \alpha \log_{10} Re_S \tag{5.3}$$

which is a line with slope α. The running local loglog polynomial fits are doing exactly this fit. For getting α, we increase the fitting window radius to 0.2 decades to get a smoother result. These local power law exponents α are shown in Figure 5.3 with the α obtained for pure inner rotation on the same apparatus (Lathrop et al. 1992a).

Over the whole range of Re_S measured, $\alpha > 1$ since G/G_{lam} is an increasing function of Re_S ($\alpha = 1$ for laminar Taylor-Couette flow). The quasi-Keplerian q have smaller α than pure inner rotation ($q = +\infty$) for $4 \times 10^3 < Re_S < 7 \times 10^4$ meaning that their torques are growing slower, or in other words, $G/G_{+\infty}$ is decreasing with increasing Re_S. Around $Re_S \approx 10^5$, the quasi-Keplerian torques for the three larger

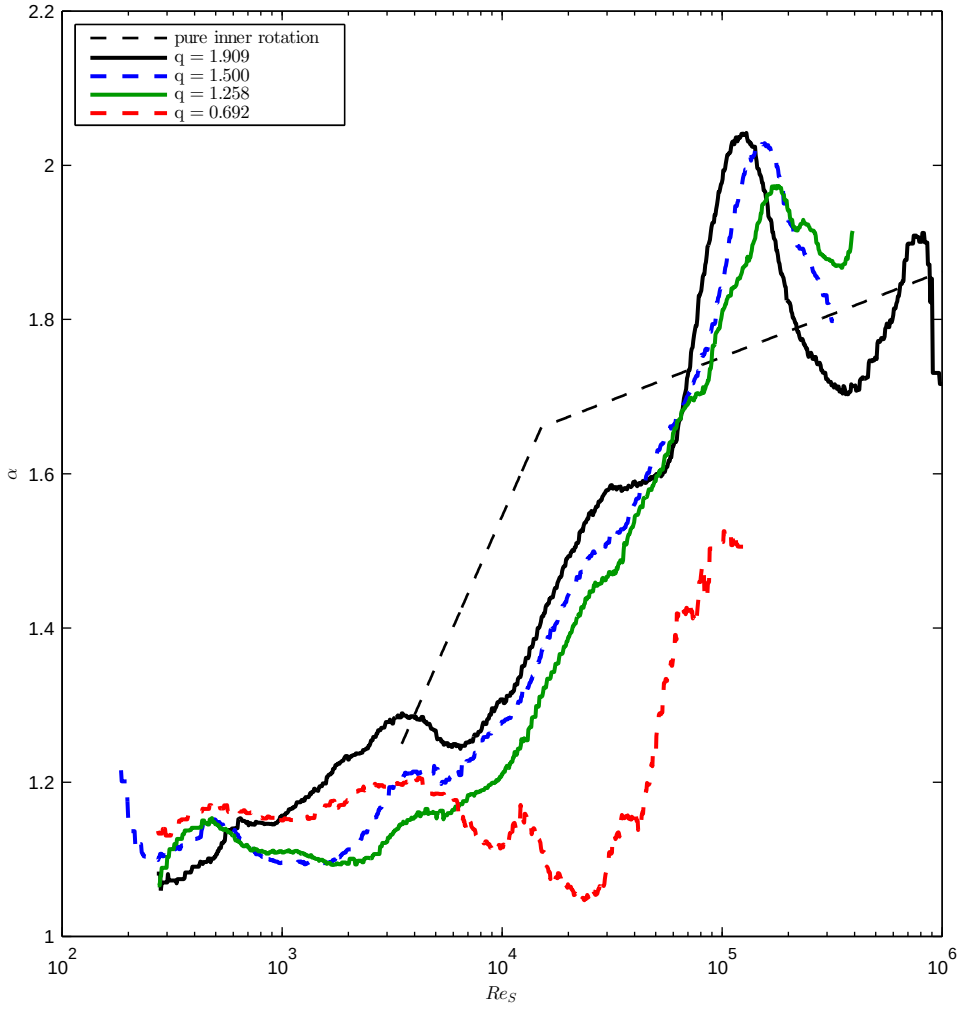

Figure 5.3: The local power law exponents (α) of the measured torques for each q (lines). The fitting window's radius was 0.2 decades. The scaling exponent for pure inner rotation ($q = +\infty$) on the same experiment in the 8-vortex state (Lathrop et al. 1992a) is shown as a thin dashed black line.

q (all except $q = 0.692$) are growing faster than that for pure inner rotation. Then, for higher Re_S, the quasi-Keplerian α's for these same q appear to approximately match α for pure inner rotation, though this is difficult to tell with the limited range of higher Re_S available. Higher Re_S measurements are needed to check this.

5.3 Transitions And Fitting The Torque Scalings

For each quasi-Keplerian q in Figure 5.3, there are ranges of Re_S where $\alpha\left(Re_S\right)$ appears to be constant or a line. This means that α could be constructed reliably from a piecewise polynomial where the highest order in a range of Re_S is one (linear). That fit translates to a piecewise polynomial fit of the measurements in $(\log_{10} Re_S, \log_{10} G)$ space where the order is either one or two (lines and quadratics). In fact, α is just its derivative with respect to $\log_{10} Re_S$.

For pure inner rotation ($q = +\infty$), $\alpha\left(Re_S\right)$ can be fit to two lines (Lathrop et al. 1992a) or two quadratics (Lewis and Swinney 1999). Regardless of which one is chosen, the slope changes abruptly at $Re_S = 1.5 \times 10^4$, which has been identified with the fluid transition to the so called "ultimate regime" where the boundary layers become fully turbulent (van Gils et al. 2012; Ostilla-Mónico et al. 2014a,b). Thus, the boundaries between the pieces of the piece-wise polynomial fits in $(\log_{10} Re_S, \log_{10} G)$ space (or equivalently fits to α) are likely transitions in the fluid flow state. They are discontinuities in α and/or its derivative with respect to $\log_{10} Re_S$.

The locations of these likely transitions and the polynomial orders in each

range of Re_S were identified by eye from $\alpha\,(Re_S)$ in Figure 5.3, with some help from $G/G_{\rm lam}$ in Figures 5.1 and 5.2. In addition, we tried to identify that transitions for which the value of α appeared to be continuous. Note that due to the use of a window to construct the local powerlaw exponents from the torque measurements, the α in Figure 5.3 are smoothed versions of the actual $\alpha\,(Re_S)$ for the system. Due to this, for ranges of Re_S that are small due to transitions being close together or having a lack of range beyond the last transition, the order was treated as zero in α .(constant), which is order one in $(\log_{10} Re_S, \log_{10} G)$ space (line). This was done since a small range can't be used to accurately identify higher order terms.

Starting from the lowest range of Re_S for each q, the torques in $(\log_{10} Re_S, \log_{10} G)$ space were fitted (with weights) to a polynomial of the determined order. If there was a previous range of Re_S fit, the fit was constrained to be continuous in Re_S, and if we determined that α should be continuous, the fit was also constrained so that the first derivative (α) was continuous. This was done for each range in order until the highest range of Re_S was fit. For each piece after the first, the constraints reduced the fit to a single parameter fit. In each piece,

$$\log_{10}(G) = p_0 + p_1\ (\log_{10} Re_S) + p_2\ (\log_{10} Re_S)^2 \tag{5.4}$$

where p_0, p_1, and p_2 are the polynomial coefficients. Since $q = 1.909$ reaches $G/G_{\rm lam} = 1$ at low Re_S, an additional laminar Taylor-Couette torque piece was put on it at the beginning after each piece was fit. The Re_S where the laminar Taylor-Couette piece and the first fitted piece intersect was taken to be the transi-

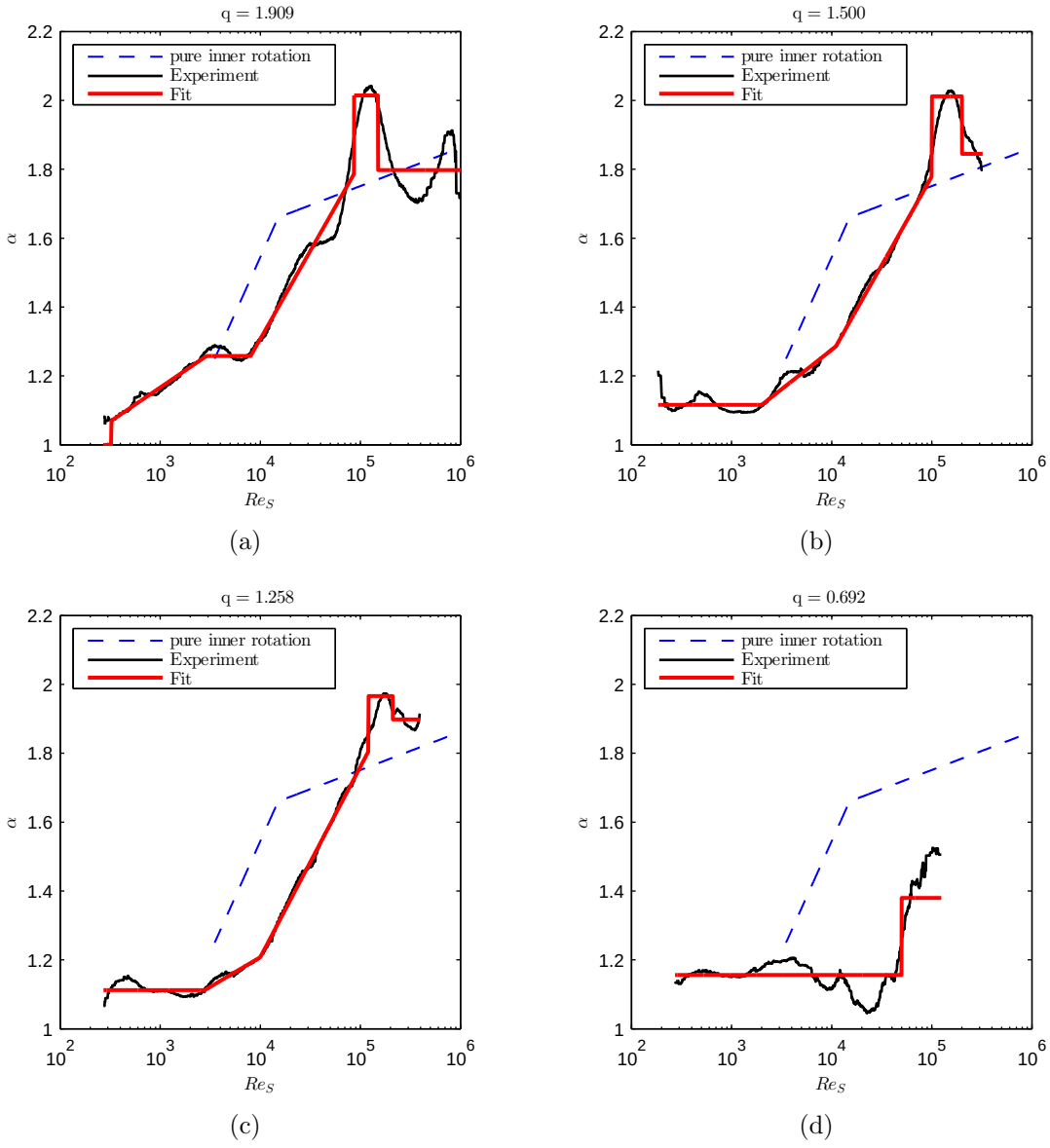

Figure 5.4: The local power law scaling exponent (α) of the torques with one plot for each q. The running local power law fit's scaling exponent (window radius of 0.2 decades) of the measured torque (black line), the scaling exponent of the piecewise polynomial fit (thick red line), and the scaling exponent for pure inner rotation ($q = +\infty$) on the same experiment in the 8-vortex state (Lathrop et al. 1992a) (thin dashed blue line) are shown. (a) $q = 1.909$. (b) $q = 1.500$. (c) $q = 1.258$. (d) $q = 0.692$.

Table 5.3: The Re_S of the transitions for each q in order. The first column is which transition (1st, 2nd, ...) and the other columns are their Re_S for each q.

transition #	$q = 1.909$	$q = 1.500$	$q = 1.258$	$q = 0.692$
1	3.26×10^2	2.00×10^3	2.80×10^3	5.00×10^4
2	2.90×10^3	1.10×10^4	1.00×10^4	
3	8.00×10^3	1.00×10^5	1.20×10^5	
4	8.60×10^4	2.00×10^5	2.10×10^5	
5	1.50×10^5			

tion.

The α of the resulting piecewise polynomial fits are shown with the local powerlaw exponents for each q in Figure 5.4. The Re_S of the transitions are listed in Table 5.3. The number of constraints for each piece and the coefficients of piecewise polynomial fits (p_0, p_1, and p_2) are shown in Table 5.4.

The three largest q have a pair of transitions at $Re_S \approx 10^5$ and $Re_S \approx 2\times10^5$, between which the fitted $\alpha \approx 2$. These two transitions for these three q are likely between the same three flow states (phases). The piecewise polynomial fit α for the two middle q values ($q = 1.500, 1.258$) have the same general shape with the same number of transitions at approximately the same Re_S with each piece having the same order (note that there is less certainty for the two highest Re_S pieces due to their limited fitting ranges); so they likely go through the same flow states. The highest $q = 1.909$ looks similar for $Re_S > 10^4$, but has an additional transition and constant α piece, so another flow state (phase) is accessible close to the Rayleigh line at $q = 1.909$. The lowest $q = 0.692$ has only one discernible transition over its range. The pattern appears to be that smaller q (close to solid-body rotation) have fewer transitions over a given range. However, this apparent pattern could be the result of the maximum Re_S reached for each q being smaller for smaller q (there

Table 5.4: The piecewise polynomial fits for each q. Each row is a piece and the pieces for each q are separated by a blank line. The pieces Re_S range, its polynomial order, and which derivatives are constrained, and the fitted polynomial coefficients (Equation 5.4) are shown. For the constraints, they are the derivatives that must be continuous from the previous piece (0 refers to no derivative taken), or if it is the first piece, then those are the polynomial coefficients that were set from the onset.

q	Re_S range	order	constraints	p_0	p_1	p_2
1.909	1.00 – 325.96	1	0, 1	1.7779	1	
	325.96 – 2.90×10^3	2	0	2.2267	0.57286	0.098893
	2.90×10^3 – 8.00×10^3	1	0, 1	1.0412	1.2577	
	8.00×10^3 – 8.60×10^4	2	0, 1	4.9412	-0.74073	0.256
	8.60×10^4 – 1.50×10^5	1	0	-2.4215	2.0146	
	1.50×10^5 – $+\infty$	1	0	-1.2971	1.7974	
1.500	185.29 – 2.00×10^3	1		1.5099	1.1157	
	2.00×10^3 – 1.10×10^4	2	0, 1	2.7578	0.35965	0.11452
	1.10×10^4 – 1.00×10^5	2	0, 1	5.0917	-0.79531	0.25741
	1.00×10^5 – 2.00×10^5	1	0	-2.5079	2.0117	
	2.00×10^5 – $+\infty$	1	0	-1.6241	1.8449	
1.258	271.86 – 2.80×10^3	1		1.5429	1.1124	
	2.80×10^3 – 1.00×10^4	2	0, 1	2.5669	0.51827	0.086179
	1.00×10^4 – 1.20×10^5	2	0, 1	5.6139	-1.0052	0.27661
	1.20×10^5 – 2.10×10^5	1	0	-2.3426	1.9663	
	2.10×10^5 – $+\infty$	1	0	-1.9787	1.8979	
0.692	273.08 – 5.00×10^4	1		1.4928	1.156	
	5.00×10^4 – $+\infty$	1	0	0.44066	1.3799	

could be additional transitions at higher Re_S). Another pattern is that the Re_S of the first transition between constant α and linear α increases as solid-body rotation is approached ($q \to 0$).

The piecewise polynomial fits are compared to the torques and running local polynomial loglog fits for the full range of Re_S in Figures 5.5, 5.7, 5.9, and 5.11. They are compared for $Re_S < 2 \times 10^4$ in Figures 5.6, 5.8, 5.10, and 5.12. The piecewise polynomial fits match the measurements.

5.4 Phase Diagram

The transitions identified in the torques can be used to construct a phase diagram for our geometry in the quasi-Keplerian regime, much like the phase diagrams of Andereck et al. (1986) and Ostilla-Mónico et al. (2014a) in the Rayleigh-unstable regime. The transitions in Table 5.3 are plotted in phase space in Figure 5.13. In addition, the two transitions for $q = 1.909$ for the same geometry and the first transition, where the flow destabilizes, for the same geometry but for $\Gamma = 10$ (ours is 11.47) for several different q found by Avila (2012) via Direct Numerical Simulation (DNS) are also shown. The first transitions for each q we found in our torque measurements and the second transition for $q = 1.909$ match up well with the transitions found by Avila (2012).

The first transitions for the different q found in our torque measurements and by Avila (2012) are closest to linear in $(q, \log_{10} Re_S)$ space. In addition, the three highest Re_S transitions for the three largest q we measured are close to linear in

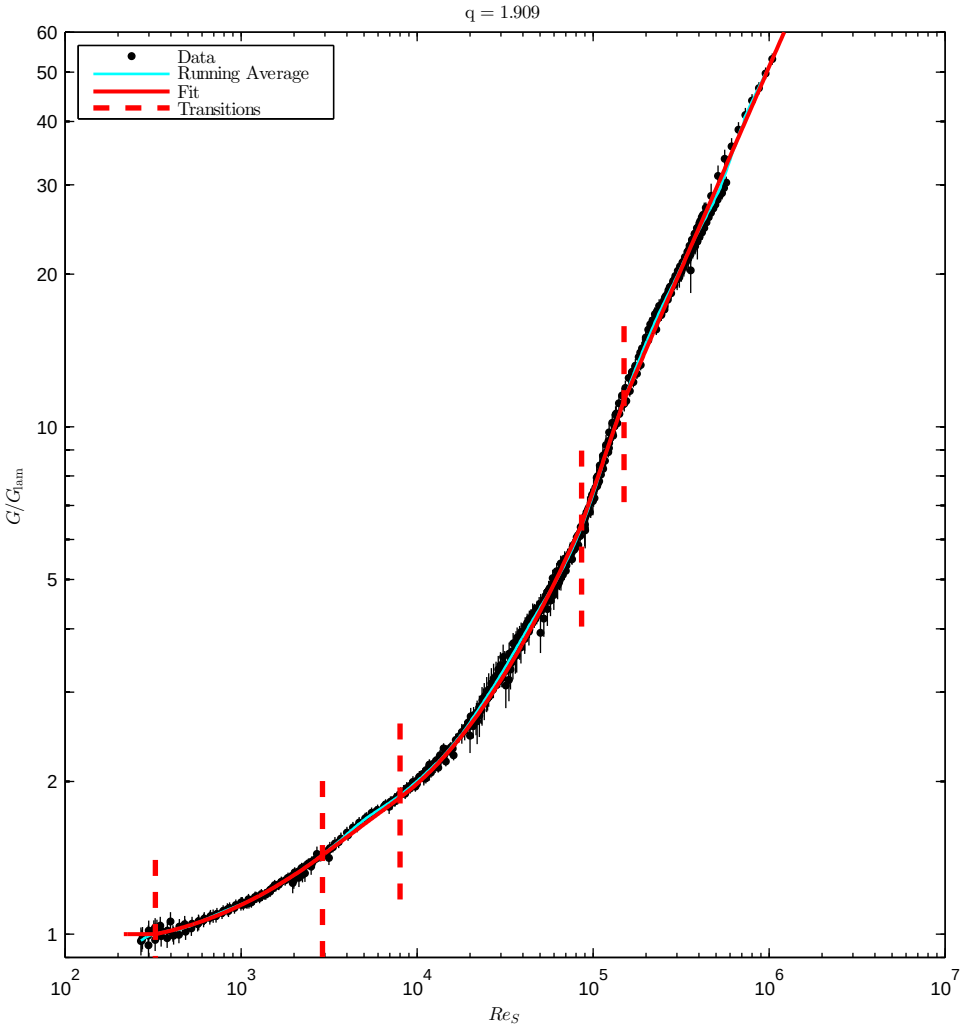

Figure 5.5: The normalized torque (G/G_{lam}) for $q = 1.909$ (black circles with error-bars) along with the running local polynomial fit (cyan line) with a window radius of 0.1 decades, the piecewise polynomial fit (Equation 5.4) to the torque (red line), and the transitions (vertical dashed red lines along the fit where they occur). An expansion for low shear ($Re_S \leq 2 \times 10^4$) is shown in Figure 5.6.

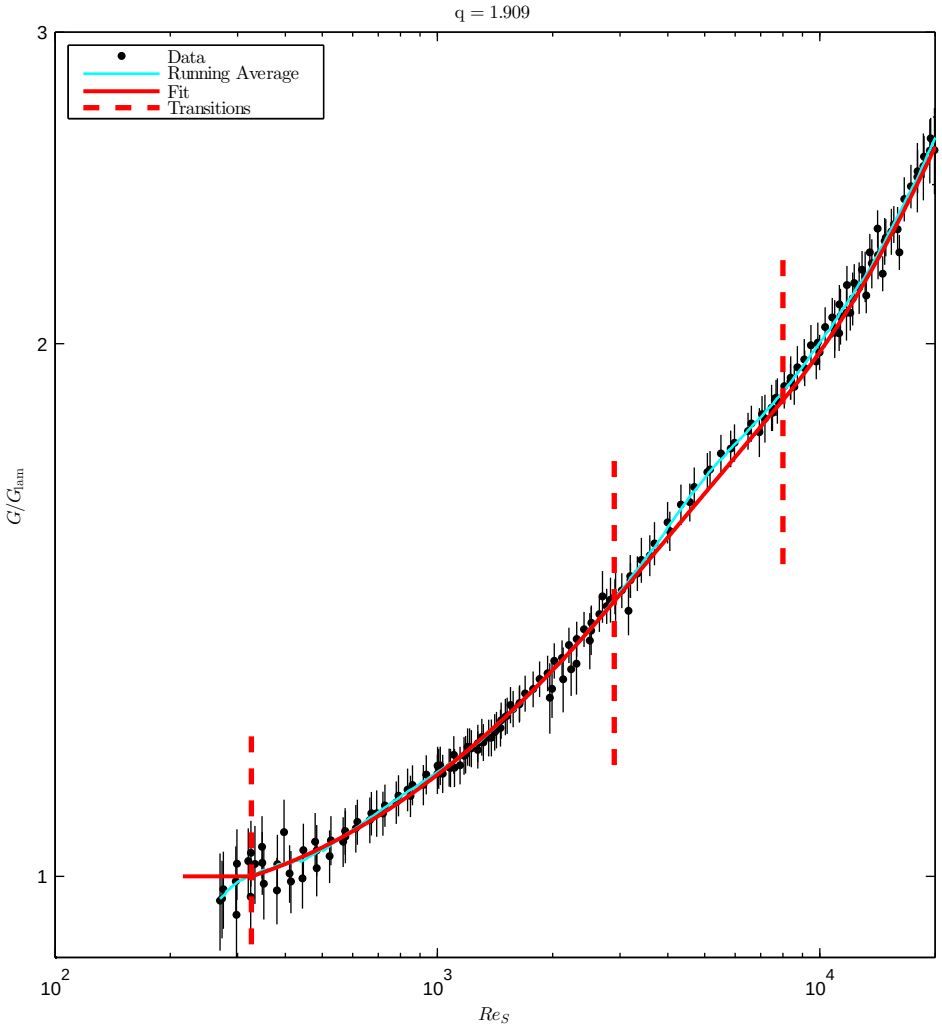

Figure 5.6: For low shear ($Re_S \leq 2 \times 10^4$), the normalized torque (G/G_{lam}) for $q = 1.909$ (black circles with error-bars) along with the running local polynomial fit (cyan line) with a window radius of 0.1 decades, the piecewise polynomial fit (Equation 5.4) to the torque (red line), and the transitions (vertical dashed red lines along the fit where they occur). Figure 5.5 shows the full range of Re_S.

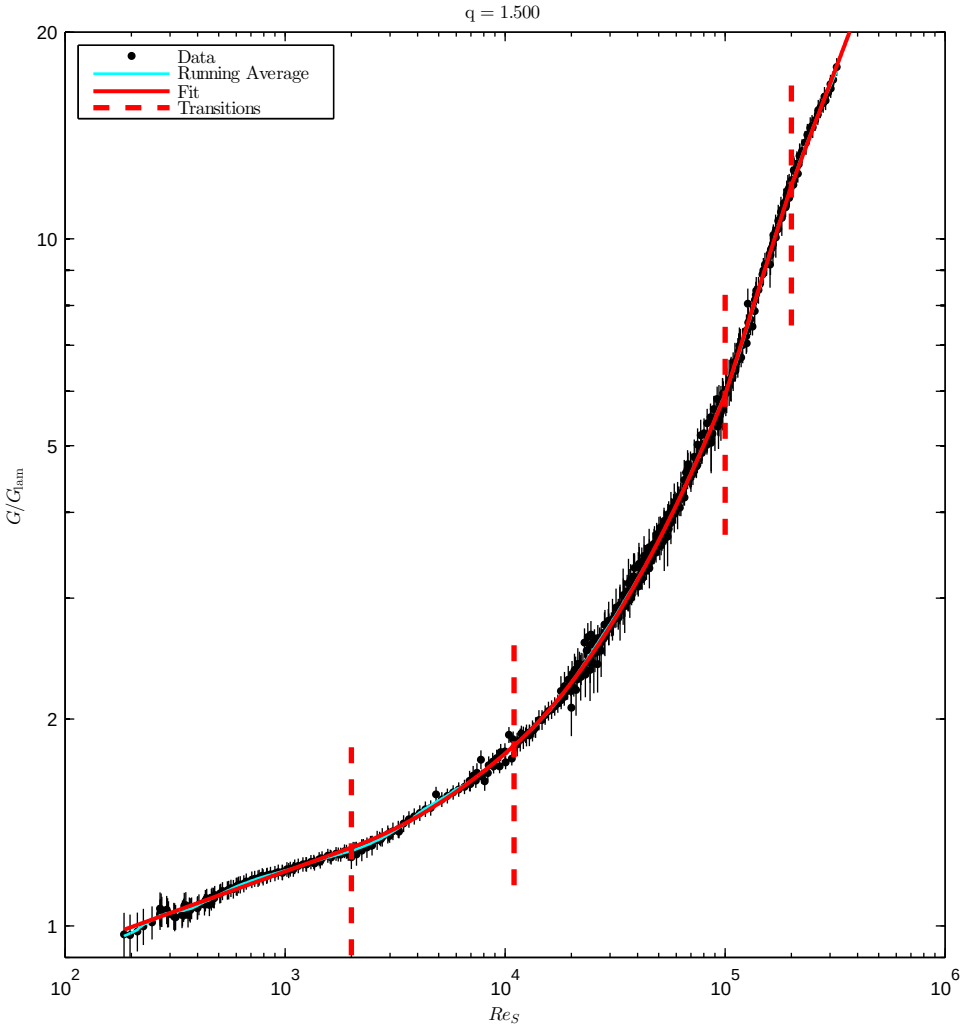

Figure 5.7: The normalized torque (G/G_{lam}) for $q = 1.500$ (black circles with error-bars) along with the running local polynomial fit (cyan line) with a window radius of 0.1 decades, the piecewise polynomial fit (Equation 5.4) to the torque (red line), and the transitions (vertical dashed red lines along the fit where they occur). An expansion for low shear ($Re_S \leq 2 \times 10^4$) is shown in Figure 5.8.

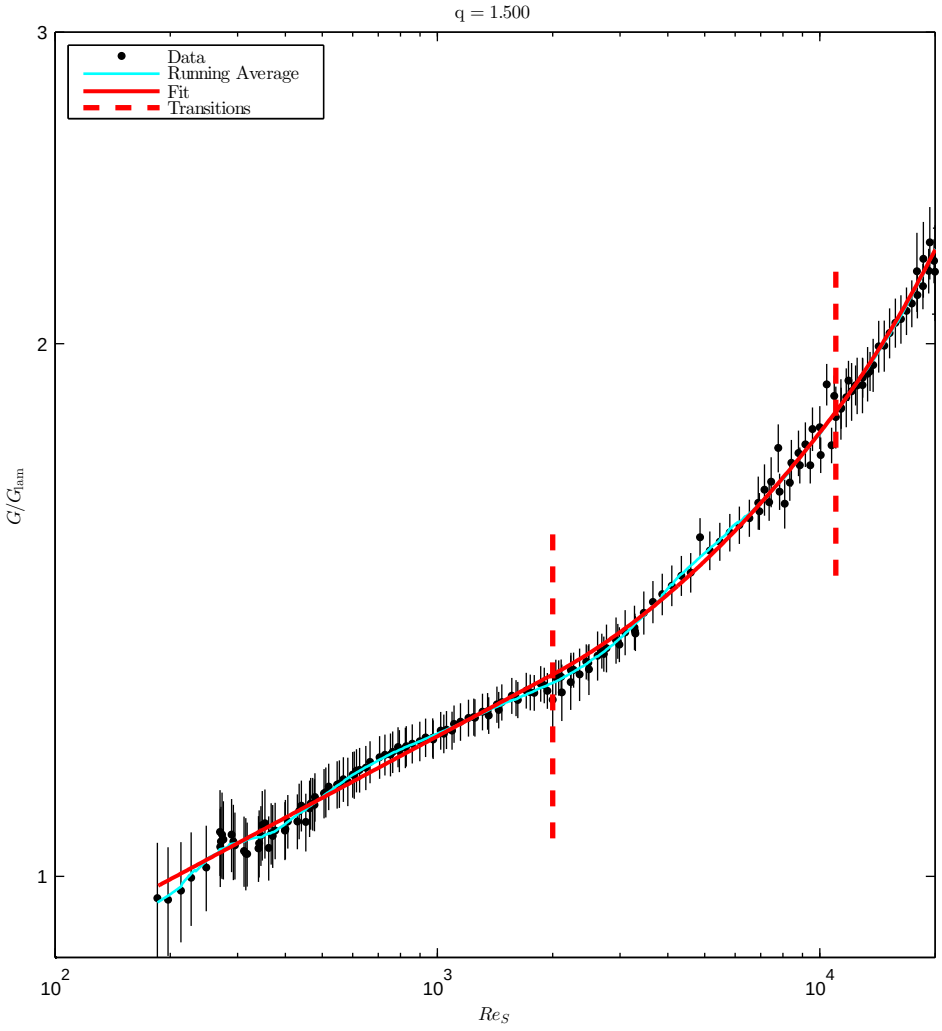

Figure 5.8: For low shear ($Re_S \leq 2 \times 10^4$), the normalized torque (G/G_{lam}) for $q = 1.500$ (black circles with error-bars) along with the running local polynomial fit (cyan line) with a window radius of 0.1 decades, the piecewise polynomial fit (Equation 5.4) to the torque (red line), and the transitions (vertical dashed red lines along the fit where they occur). Figure 5.7 shows the full range of Re_S.

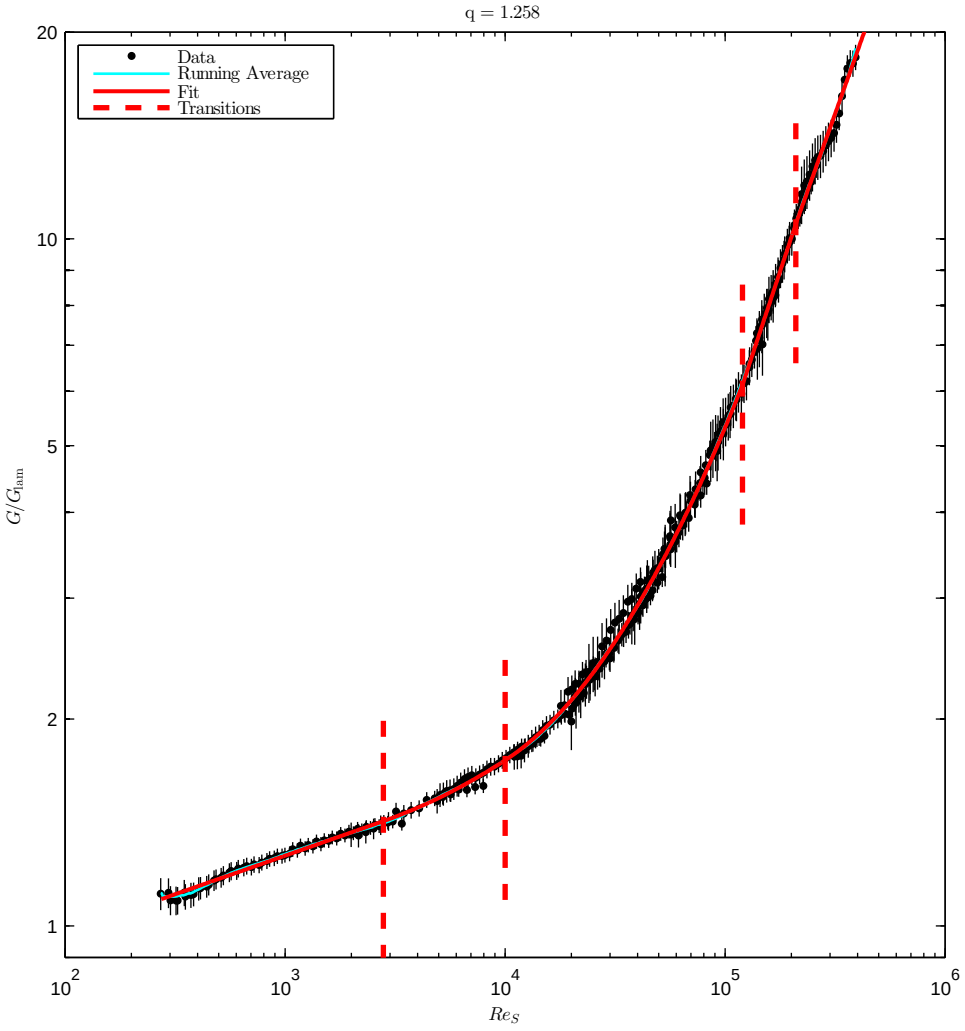

Figure 5.9: The normalized torque (G/G_{lam}) for $q = 1.258$ (black circles with error-bars) along with the running local polynomial fit (cyan line) with a window radius of 0.1 decades, the piecewise polynomial fit (Equation 5.4) to the torque (red line), and the transitions (vertical dashed red lines along the fit where they occur). An expansion for low shear ($Re_S \leq 2 \times 10^4$) is shown in Figure 5.10.

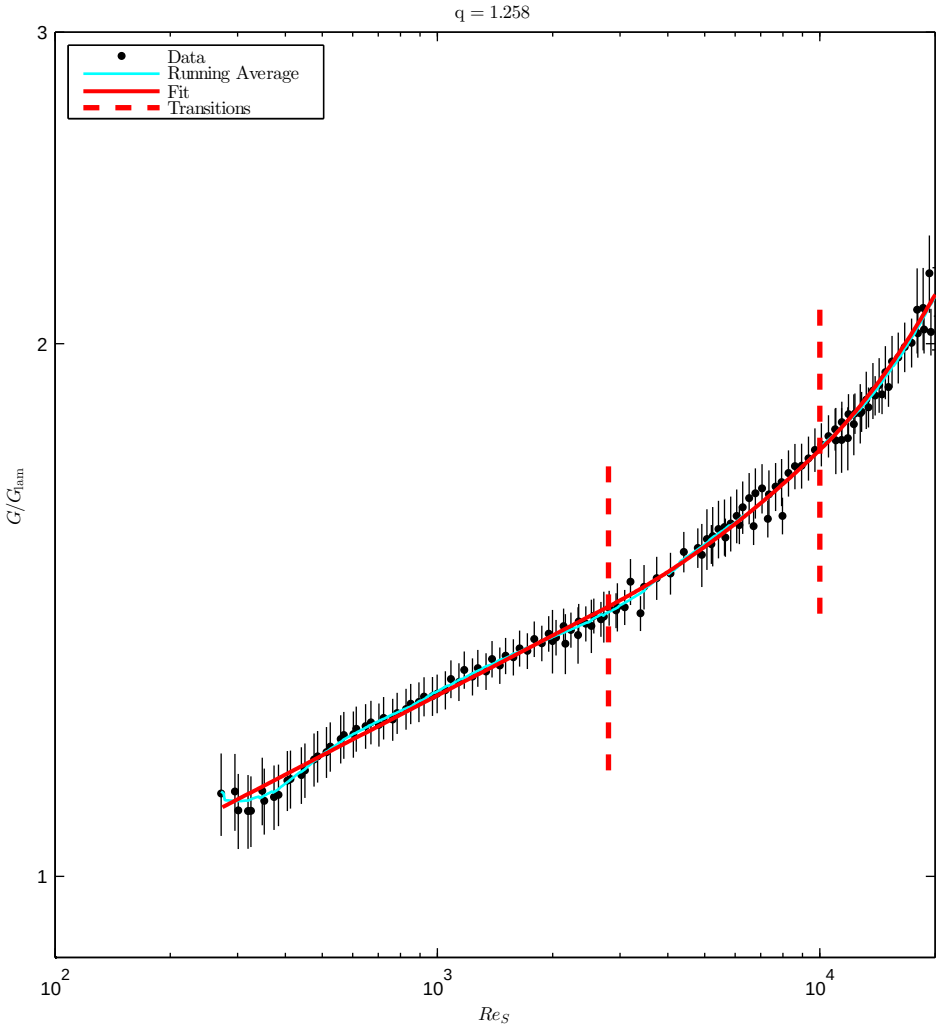

Figure 5.10: For low shear ($Re_S \leq 2 \times 10^4$), the normalized torque (G/G_{lam}) for $q = 1.258$ (black circles with error-bars) along with the running local polynomial fit (cyan line) with a window radius of 0.1 decades, the piecewise polynomial fit (Equation 5.4) to the torque (red line), and the transitions (vertical dashed red lines along the fit where they occur). Figure 5.9 shows the full range of Re_S.

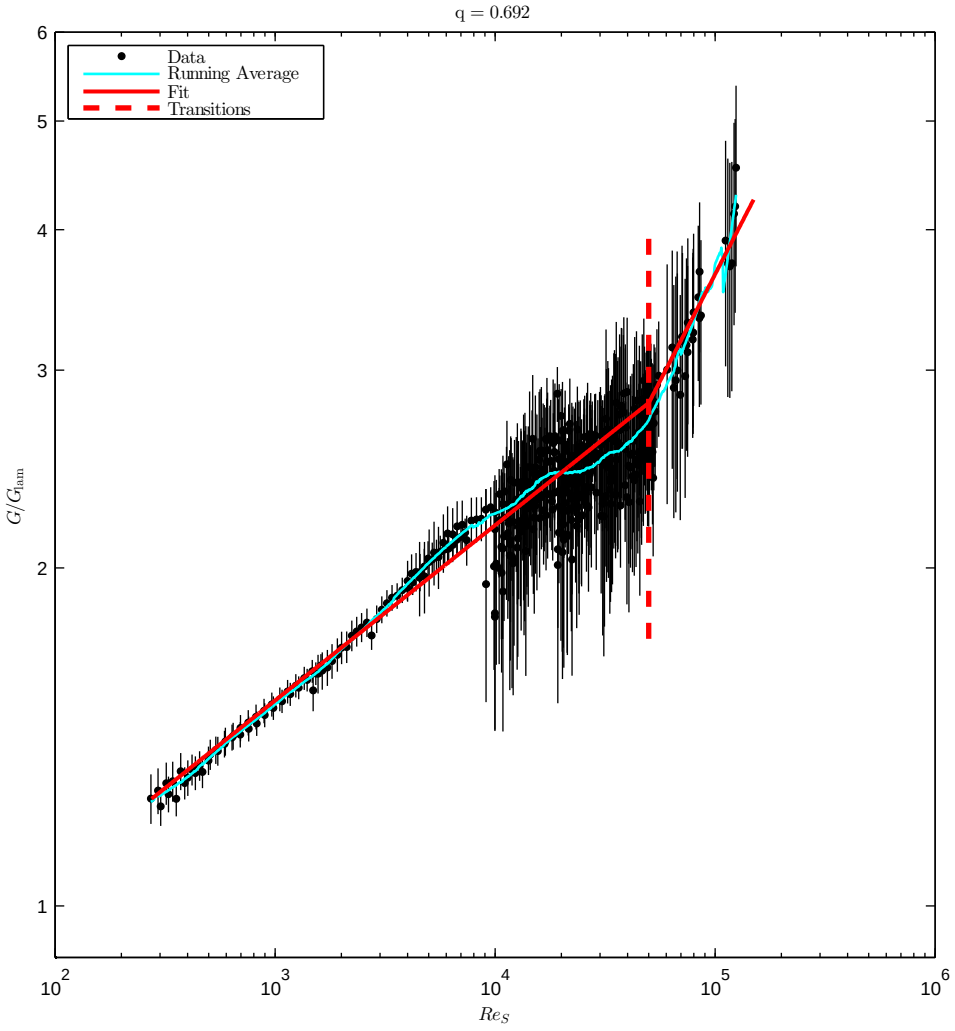

Figure 5.11: The normalized torque (G/G_{lam}) for $q = 0.692$ (black circles with errorbars) along with the running local polynomial fit (cyan line) with a window radius of 0.1 decades, the piecewise polynomial fit (Equation 5.4) to the torque (red line), and the transitions (vertical dashed red lines along the fit where they occur). An expansion for low shear ($Re_S \leq 2 \times 10^4$) is shown in Figure 5.12.

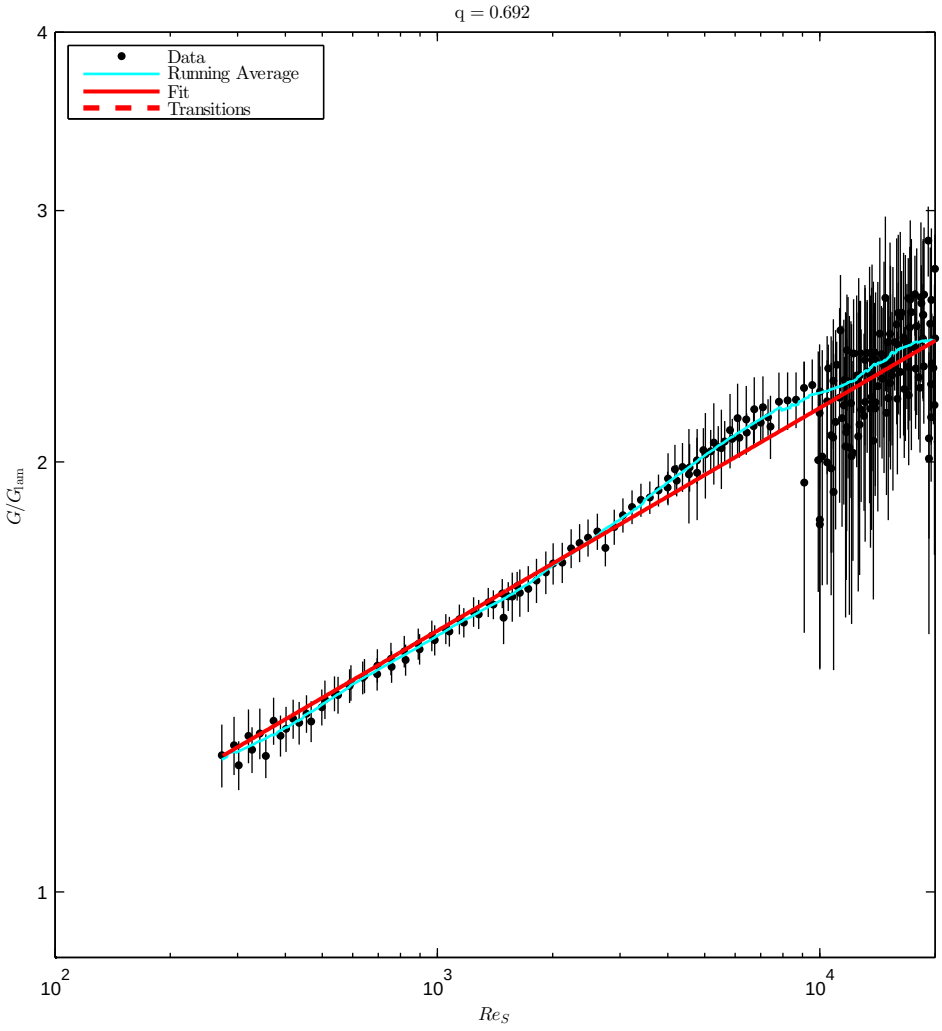

Figure 5.12: For low shear ($Re_S \leq 2 \times 10^4$), the normalized torque (G/G_{lam}) for $q = 0.692$ (black circles with error-bars) along with the running local polynomial fit (cyan line) with a window radius of 0.1 decades, the piecewise polynomial fit (Equation 5.4) to the torque (red line), and the transitions (vertical dashed red lines along the fit where they occur). Figure 5.11 shows the full range of Re_S.

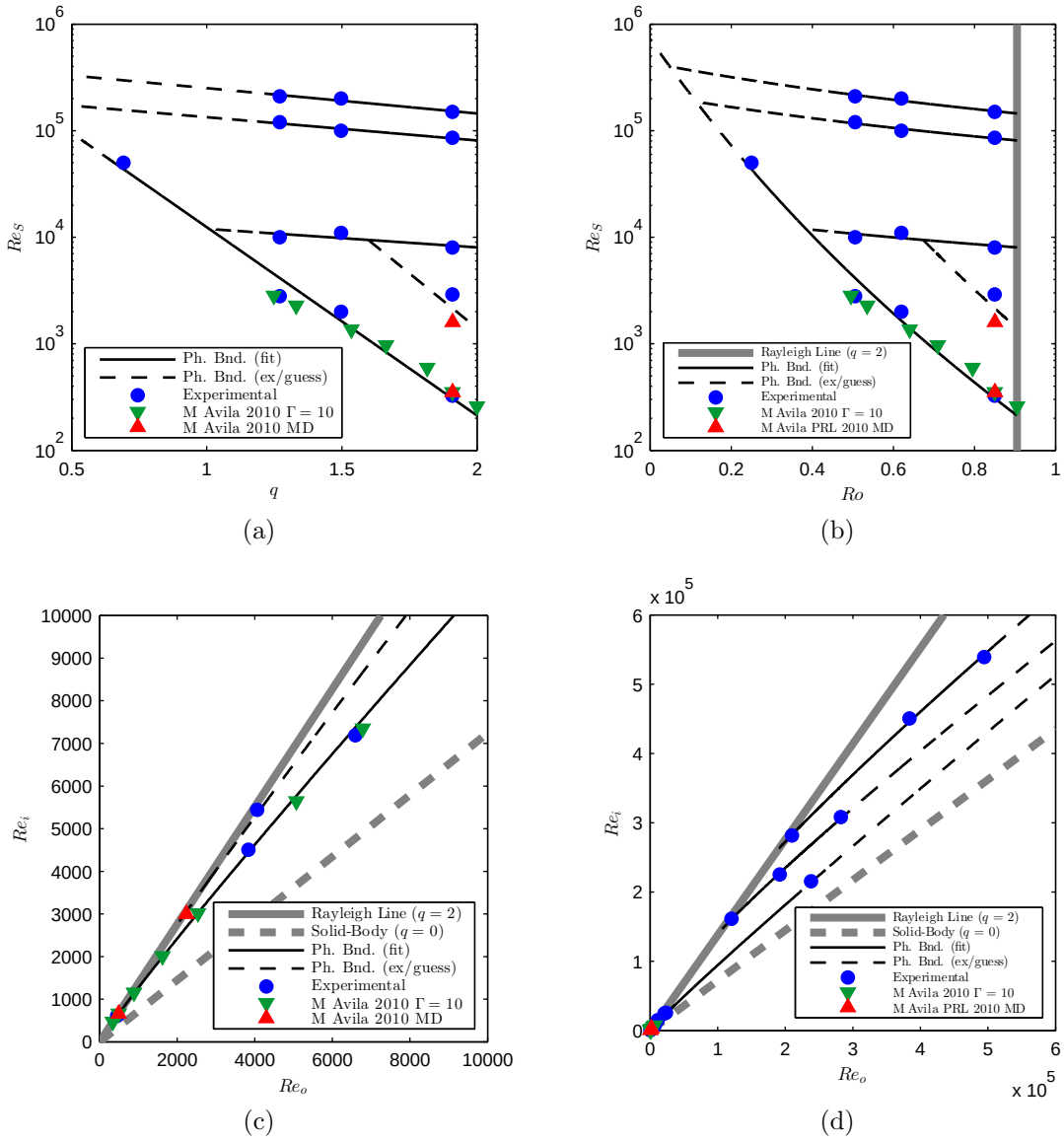

Figure 5.13: Proposed phase diagram in different Taylor-Couette coordinates of the quasi-Keplerian regime ($0 < q < 2$) in $\eta = 0.7245$, $\Gamma = 11.47$ Taylor-Couette with axial boundaries attached to the outer cylinder. Transitions found from looking at the experimentally measured torques are shown as blue circles. Transitions found via DNS (Direct Numerical Simulation) by Avila (2012) for $\Gamma = 10$ and our $\Gamma = 11.47$ (denoted as MD) are shown as green upside down triangles and red triangles respectively. Thick grey lines denote the Rayleigh line ($q = 2$) and solid-body rotation ($q = 0$). Solid black lines are the phase boundaries found by fitting lines in (q, Re_S) space to transitions found in the experiment. Dashed black lines are extrapolations of those same phase boundary lines or are a guessed phase boundary when only one transition is found for the boundary. (a) (q, Re_S) space. (b) (Ro, Re_S) space. (c) (Re_o, Re_i) space for the full range of the Reynolds numbers. (d) (Re_o, Re_i) space for low Reynolds numbers.

Table 5.5: For each phase boundaries, the ranges of q for the phase boundaries, the ranges of q for their extrapolations, and the polynomial coefficients (p_0, p_1) for the phase boundaries in $(q, \log_{10} Re_S)$ space (Equation 5.5).

q range	extrap. q range	p_0	p_1
0.6922 – 2	0 – 0.6922	5.8615	−1.7675
1.27 – 2	1.01 – 1.27	4.2525	−0.17393
1.27 – 2	0.3336 – 1.27	5.3447	−0.2183
1.27 – 2	0.1468 – 1.27	5.6369	−0.23773
	1.598 – 2	7.2651	−2.0595

$(q, \log_{10} Re_S)$ space. Thus, we performed linear fits to the groups of transitions in $(q, \log_{10} Re_S)$ space of the form

$$\log_{10} Re_S = p_0 + p_1 q \tag{5.5}$$

The first transitions from our torque measurements for all four q were fit to lines. The highest Re_S transition for the three largest q were fit with a line. The same was done for the second and third highest Re_S transitions. These lines, from the smallest q used in the fit to the Rayleigh line ($q = 2$), are taken to be phase boundaries. We guess that they continue to be linear for smaller q till they reach $q = 0$ for the first transition or, for the higher transitions, when they intersect with the phase boundary for the first transition. Similarly, we guess that the phase boundary associated with the second transition for $q = 1.909$ is the line running through the mid-point between the transition in our torque and where Avila (2012) found it to be and $Re_S = 1.4 \times 10^3$ on the Rayleigh line ($q = 2$). In Figure 5.13, the phase boundaries are drawn as solid lines and the guessed continuations and one guessed phase boundary are drawn as dashed lines. The phase boundary fits and ranges are listed in Table 5.5.

From this phase diagram, the number of phases available decreases as q decreases since the Re_S of the first transition (where the flow destabilizes) increases. This shows that with increasing importance of the rotation relative to shear ($q, Ro \rightarrow 0$), the flow becomes more stable even in the presence of the axial boundaries attached to the outer cylinder.

We can look where the velocimetry measurements in Chapter 3 and dye injection measurements in Chapter 4 fall in this phase diagram using Table 3.1. Since the highest Re_S transition we found is a bit larger than $Re_S = 10^5$, only the $Re_S = 7.81 \times 10^5$ velocimetry measurements for $q = 1.909, 1.500$ fall in the highest phase. The $Re_S = 1.04 \times 10^5$ measurement for $q = 1.909$ is probably in the second highest Re_S phase we found, while the $q = 1.500$ measurement for the same Re_S might be in that phase or the next lower one. The $q = 1.258, 0.692$ at $Re_S = 1.04 \times 10^5$ measurements are in the next lower phase. Then, the $q = 0.333$ measurement at $Re_S = 1.04 \times 10^5$ appears to not even be at a high enough Re_S to have destabilized (reached its first transition), if the linear extrapolation of the phase boundary is correct. The $q = 1.500$ measurements at $Re_S = 2.07 \times 10^4$ are in third highest phase that we found.

The three velocimetry measurements for $q = 1.500$ were in different phases, which may explain the differences in the azimuthal velocity profiles in Figure 3.3. Despite the quasi-Keplerian velocimetry measurements being taken in four different phases, they still all reasonably match the quasi-Keplerian flat inner angular momentum profile approximation (Equation 3.8). This indicates that the changes to the flow with each transition may result in only small changes in the azimuthally

and temporally averaged azimuthal velocity profiles.

For the dye injection measurements at $Re_S = 5.2 \times 10^4$, $q = \{0.692, 0.333, 0.250\}$ are all at Re_S below the first phase boundary in Figure 5.5. However, the flow exhibits flow super-rotation (Figure 4.2) as well as flow in both directions at the outer-cylinder. This does not match up with the idea of the flow being stable laminar flow. While we wouldn't expect the fluid to match the laminar Taylor-Couette flow velocities in Equation 1.34 due to the axial boundaries, the flow would still be uniform in the azimuthal coordinate and time. This suggests that the flow had destabilized at a smaller Re_S that wasn't noticed in the torque measurements for $q = 0.692$. There are two comparatively similar possibilities. One, there is a linear phase boundary but the stability boundary branches off to smaller q at a triple point. Two, the stability boundary flattens for $q < 1.258$ and the first transition we found in the torques for $q = 0.692$ may be the second or higher transition and is just coincidentally linear with the stability boundary at larger q.

5.5 Comparisons to The Literature

For $q = 1.909$, the measured torques, their piecewise polynomial fits, and α are compared to the torques and α that Avila (2012) obtained via simulation for our geometry and axial boundary conditions in Figure 5.14. While they show a similar trend, our experimental torques are lower than those from the simulations for all Re_S except near $Re_S \approx 2 \times 10^3$. We will now speculate on possible explanations for the discrepancy. One possible explanation is that our experiment has stratification

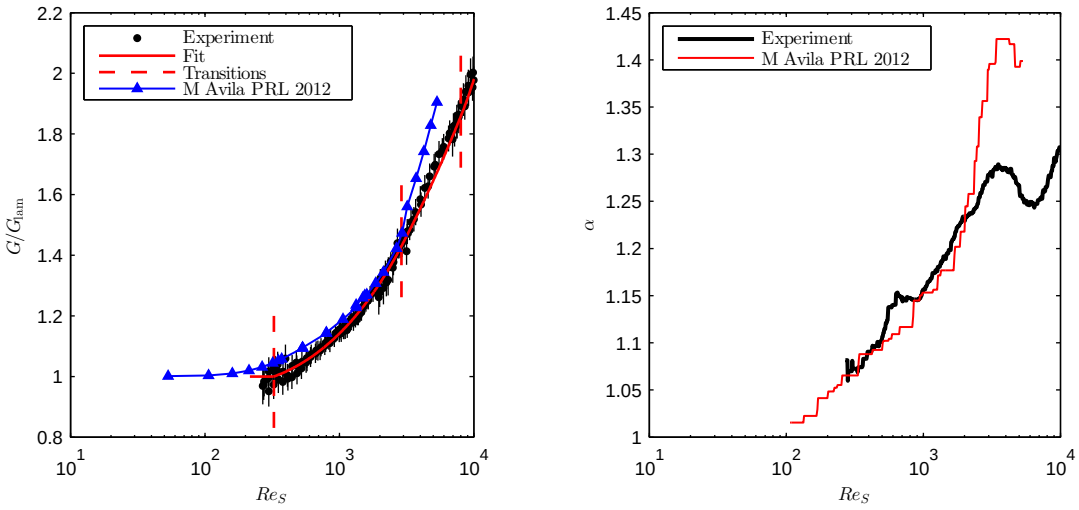

Figure 5.14: Comparison of our normalized torque measurements ($G/G_{\rm lam}$) and scaling exponent, α, to the DNS (Direct Numerical Simulation) results of Avila (2012) for $q = 1.909$. (a) normalized torque ($G/G_{\rm lam}$). Our measured values (black circles with error bars), the global fit to the our torque measurements (red line), the transitions in our torque measurements (vertical dashed red lines along the fit where they occur), and Avila (2012)'s torque results (blue triangles with a connecting line). (b) the scaling exponent (α) for our experiment (black line) and Avila (2012)'s simulations (thin red line). The scaling exponents were found by doing a running local power law fit with a window radius of 0.2 decades.

due to temperature gradients, whereas the simulations were incompressible with a uniform density. The stratification could have slightly reduced the torque compared to what it would be in the absence of stratification, which would indicate stabilizing effects. This assumes that Ekman pumping didn't instead destabilize it, in which case we might expect the opposite – the measured torques being greater than that of the simulation.

While the simulation matched the η, Γ, and axial boundary conditions (axial boundaries rotating with the outer cylinder), there were a few small differences that may be important. In the simulations, L_{mid} was just slightly larger at 60% of the overall height as opposed to 58.5% for the Maryland experiment, but the axial dependence of the torque as seen by Avila (Figure 4(b), 2012) isn't large enough for the observed differences. The simulations used a smoothed boundary condition for the velocity discontinuity where the inner cylinder meets the axial boundaries, which may be quite different to the velocity profile in the gap between the axial boundaries and the inner cylinder in the experiments. In contrast to the simulations, the inner cylinder of our apparatus is physically split into three sections with a gap up to 0.5 mm thick between each section. van Gils et al. (2012) found some subtle but noticeable differences in the azimuthal velocity on both sides of their larger 2.5 mm gaps on the T^3C experiment with nearly identical geometry as can be seen in their Figure 2. While the gaps in our experiment are an order of magnitude smaller, they may have a similar effect and therefore lead to a different flow state than that realized in the simulations.

Our torque measurements are compared to those taken by Paoletti and Lath-

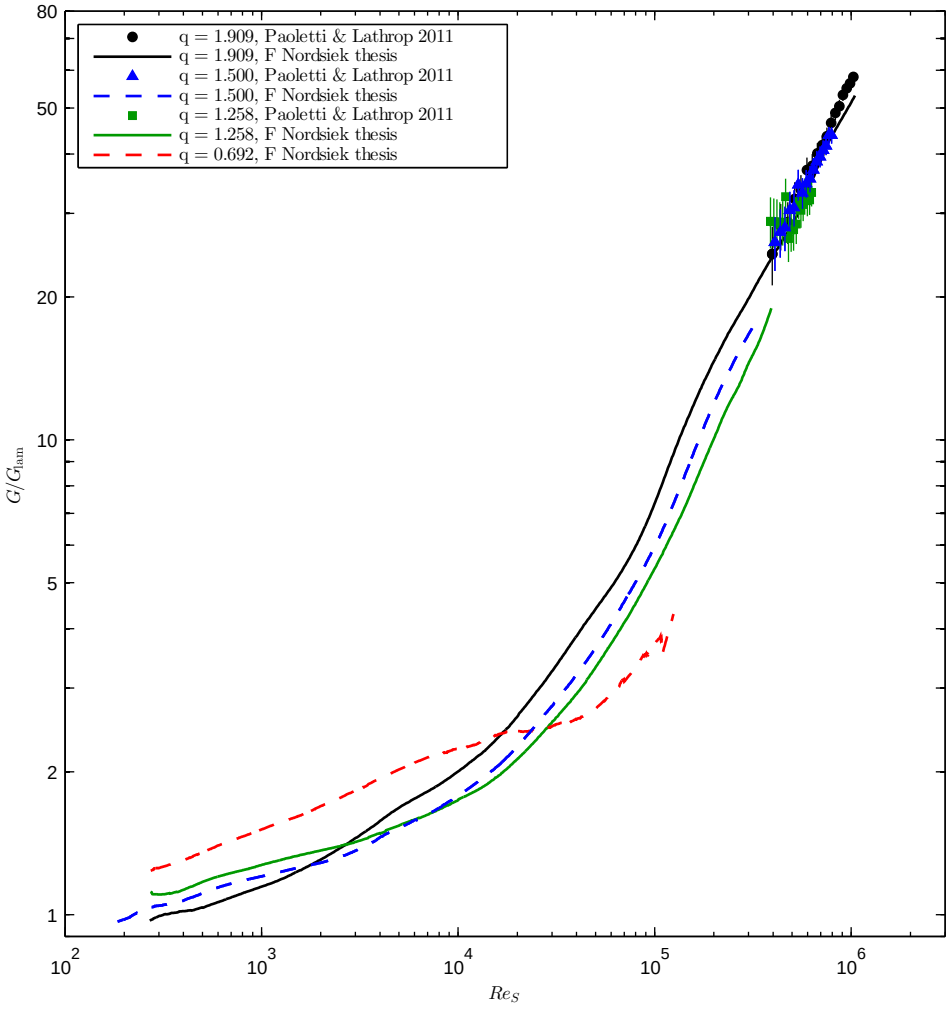

Figure 5.15: Comparison of the running local polynomial fit (window radius of 0.1 decades) of the normalized measured torque (G/G_{lam}) for all four q (lines) to the torque measurements on the same experiment at approximately these same q by Paoletti and Lathrop (2011).

Table 5.6: Windows in q used for grouping the torque measurements of Paoletti and Lathrop (2011) into the q values presented in this thesis (left column).

q	lower q of the window	higher q of the window
1.909	1.892	1.959
1.500	1.439	1.554
1.258	1.195	1.340

rop (2011) on the same experiment in Figure 5.15. The measurements of Paoletti and Lathrop (2011) were not at the same exact q, so windows of finite width in q were used for the comparison. The measurements of Paoletti and Lathrop (2011) don't extend out to $q = 0.692$. The windows are listed in Table 5.6.

The Re_S ranges for $q = 1.909$ overlap. In the overlap, the torque measurements approximately match up. For the other q, our measurements do not extend to Re_S high enough to overlap with the measurements of Paoletti and Lathrop (2011). If $q = 1.500, 1.258$ are going to match up, then G/G_{lam} must increase significantly with Re_S in the gap between the two sets of measurements.

Chapter 6: TC: Conclusions

Partially adapted from the arXiv version of

F. Nordsiek, S. G. Huisman, R. C. A. van der Veen, C. Sun, D. Lohse, and D. P. Lathrop. Azimuthal velocity profiles in Rayleigh-stable Taylor-Couette flow and implied axial angular momentum transport. *Journal of Fluid Mechanics*, 774:342–362, July 2015.

DOI: 10.1017/jfm.2015.275

ADS: 2015JFM...774..342N

arXiv: 1408.1059 [physics.flu-dyn]

6.1 General Results

The azimuthal velocity profiles, transport of dye, and torque required to rotate the inner cylinder were all investigated in Rayleigh-stable ($q < 2$) Taylor-Couette flow on the Maryland and Twente T^{3}C experiments. The two experiments have nearly identical geometries in terms of η and Γ, and both have axial boundaries attached to the outer cylinder. The values of q and Re_S for each measurement technique were chosen to overlap with each other to take advantage of the two experiments being complementary.

All three techniques showed that the flow does not match that of laminar Taylor-Couette (Section 1.4) in the Rayleigh-stable regime. The azimuthal velocity profiles across the gap deviated from the laminar Taylor-Couette profile (Equation 1.35) for both both positive and negative q; and the difference increased as $q \to 0$ and Re_S increased. The deviation consisted of a steepening of the normalized angular velocity $\widetilde{\omega}$ profile close to the inner cylinder for all q, and the flow in the outer parts of the gap approaching solid-body rotation with the outer cylinder and attached axial boundaries for the quasi-Keplerian regime. Videos of the mixing of injected dye showed that the flow is often unsteady with oscillations relative to the outer cylinder, which is in contrast to steady laminar flow. The measured torques were greater than that of laminar Taylor-Couette ($G/G_{\text{lam}} > 1$) for Re_S larger than a few hundred (value depends on q) with G/G_{lam} growing as Re_S increases. The rate with which the torque grew was increasing overall as seen by the increasing local powerlaw exponent α (Figure 5.3). Moreover transitions to higher

flow states were found through the torque measurements via discontinuities in α and $\partial\alpha/\partial \log_{10} Re_S$, which allowed a phase diagram of the quasi-Keplerian regime to be constructed (Figure 8.1).

We found fluid angular velocities not bounded by the angular velocities of the two cylinders ($\omega \notin [\min(\Omega_i, \Omega_o), \max(\Omega_i, \Omega_o)]$) in the outer parts of the gap with both the azimuthal velocity profiles and the dye injection measurements. We found both super-rotating flow in the sub-rotating regime ($\omega > \Omega_o > \Omega_i > 0$) with both measurement systems, and sub-rotating flow in the quasi-Keplerian regime ($\Omega_i > \Omega_i > \omega$) with dye injection. In addition, these flow regions were sometimes oscillatory between being bounded by the angular velocities of the two cylinders and being unbounded. To the best of our knowledge, flow super-rotation for $q < 0$ has not been previously observed in the literature. This includes pure outer-rotation ($q = -\infty$) in our apparatus (van Gils et al. 2011a) and in those of Taylor (1936b), Wendt (1933), and Burin and Czarnocki (2012). But flow sub-rotation in the quasi-Keplerian regime had been found before in the measurements of Kageyama et al. (2004) and possibly Edlund and Ji (2014) in wide-gap low-aspect ratio configurations, though they did not comment on it or investigate it further to the best of our knowledge.

As solid-body rotation is approached at fixed $Re_S = 1.04 \times 10^5$, the strength of the super-rotation increases, reaching 6% of $\Omega_o - \Omega_i$ for $q = -0.503$, and the radial positions of the maximum of super-rotation and where the flow switched from $\Omega_i < \omega < \Omega_o$ to super-rotation moves closer to the inner cylinder. For fixed $Re_S = 5.2 \times 10^4$, an increasingly large radial fraction of the flow near the outer

cylinder can exhibit super-rotation as $q \to 0$, until the trend reverses around $q = -0.5$ and the fraction of the gap showing super-rotation decreases (Figure 4.2). The flow super-rotation must be sustained by inward angular momentum transport from the outer cylinder or axial boundaries.

For the quasi-Keplerian regime, the specific angular momentum profiles show that the flow can be split into three regions across the gap: an inner region where the angular momentum profile is approximately flat, an outer region where the flow is close to solid-body rotation at Ω_o, and a middle transition region between the two. Starting near the Rayleigh line, the middle and outer regions are almost non-existent; and then as solid-body rotation is approached at fixed non-zero Re_S, the inner region shrinks while the outer region grows till the inner region is almost non-existent at $q = 0.333$. As Re_S is increased, the middle region shrinks. Looking at the phase diagram in Figure 8.1, the azimuthal velocity profiles were taken in at least four different flow states, yet they show this same pattern in the azimuthal velocities. We speculate that as $Re_S \to \infty$, the middle region will disappear and the profile will converge towards equation (3.4) (independently derived from dye injection observations by Dunst 1972), though it does not capture the azimuthal variation and time dependence found by our dye injection measurements. This model profile is a good approximation by $Re_S = 7.81 \times 10^5$.

The outer region, when present, likely transports little angular momentum, meaning that almost all of the angular momentum is transported to the axial boundaries as drawn in Figure 3.6. Though it does likely transport some angular momentum since mixing was observed in the outer region in the dye injection

videos.

We found torques much larger than the laminar Taylor-Couette torque just as Paoletti and Lathrop (2011) had found previously on the Maryland experiment for $Re_S > 3.5 \times 10^5$. Due to using fluids with much higher ν at lower Re_S, we connected much larger dimensional torques at low Re_S up to (or almost up to depending on the q) those of Paoletti and Lathrop (2011) at high Re_S. Together with the larger than laminar Taylor-Couette torque lower bounds coming from the azimuthal velocimetry on the T^3C experiment (Section 3.4.3), we rule out the possibility that larger than laminar torques measured by Paoletti and Lathrop (2011) were substantially in error. In the sub-rotating regime, the $|G| / G_{+\infty}$ scaling of Paoletti et al. (2012) needs to be increased if it is extended to $Re_S = 10^5$ or towards solid-body rotation. In the quasi-Keplerian regime, the comparison of the torque lower bounds from the velocimetry, which gives the torque due to shear stress, to the our torque measurements and the torque scaling of Paoletti et al. (2012) show that the bulk of the transport of angular momentum off the inner cylinder is by Reynolds stresses (advection) for $Re_S \sim 10^5$.

From the transitions found in the torque measurements, we constructed a phase diagram for the quasi-Keplerian regime for our geometries. There are at least six states in the range $0.5 < q < 2$, $10^2 < Re_S < 10^6$ that can be discerned from the torque measurements. The sub-rotating and sometimes oscillating flow near the outer cylinder for $0 < q \leq 1.258$ at $Re_S = 5.2 \times 10^4$ indicates that there is at least one additional state that was not seen through the torque measurements.

6.2 Ekman Pumping And Accretion Disks

Our velocity profiles and dye visualization provide experimental confirmation of the expectation that the Ekman pumping from the axial boundaries was what destabilized the flow in the Maryland experiment in the Rayleigh-stable regime causing large super-laminar torques on the inner cylinder, instead of Rayleigh-stable Taylor-Couette flow being non-linearly unstable in the absence of Ekman pumping for $Re_S \lesssim 10^6$ (Balbus 2011; Avila 2012; Ji and Balbus 2013; Edlund and Ji 2014). This work, combined with the work of Avila (2012), Schartman et al. (2012), and Edlund and Ji (2014), resolves the apparent discrepancy between the approximately laminar Taylor-Couette angular momentum transport in the wide-gap, low aspect-ratio experiments with axial boundaries split into rings rotating at speeds intermediate that of the cylinders such as the Princeton MRI and HTX experiments (Ji et al. 2006; Schartman et al. 2012; Edlund and Ji 2014) and large super-laminar angular momentum transport in the medium-gap higher aspect-ratio Maryland experiment with axial boundaries attached to the outer cylinder such as our torque measurements in this thesis and those of Paoletti and Lathrop (2011). Moreover, we found that the Ekman pumping from the axial boundaries does more than just destabilize the flow in the Rayleigh-stable regime when the axial boundaries are attached to the outer cylinder. In the quasi-Keplerian regime, it causes the flow to be split radially into three regions and nearly all of the angular momentum to be transported to the axial boundaries instead of the outer cylinder when an outer region is present. The Ekman pumping essentially causes the axial boundaries to

become the primary sink of angular momentum. The super-rotating flow in the quasi-Keplerian regime and the super-rotating flow in the sub-rotating regime are likely due to the Ekman pumping.

Astrophysical accretion disks have open axial boundaries, which do not cause Ekman pumping, and are thought or assumed to have primarily radial transport of angular momentum (Zeldovich 1981; Richard and Zahn 1999; Richard 2001; Dubrulle et al. 2005a; Ji and Balbus 2013; Ostilla-Mónico et al. 2014c). Due to the strong Ekman pumping effects, including the primarily axial transport of angular momentum, Taylor-Couette flow with an aspect ratio up to $\Gamma \sim 10$ with no-slip axial boundaries attached to the outer cylinder is an imperfect model of accretion disks, especially with regard to stability. Ideally, one would like to have axial boundaries that are free-slip or rotate at different rates along their radius such that they match the mean rotation rate of what the flow would be in the absence of axial boundaries, which may not be the laminar Taylor-Couette profile.

There are practical options available to experimental Taylor-Couette flow to mitigate the Ekman pumping and make a better model of accretion disks.

1. An experiment could be made where the aspect ratio is great enough that the axial transport mechanism of the angular momentum saturates and Ekman pumping can no longer directly affect the flow near midheight. However, tall experiments are difficult to handle and expensive to make, and research would be needed to ascertain whether indirect effects would still be a problem.

2. Another way, which has been followed by the Princeton group (Ji et al. 2006;

Schartman et al. 2012; Edlund and Ji 2014) for over a decade, is to split the axial boundaries into rings that are rotated at speeds intermediate to those of the cylinders. This reduces the strength of the Ekman pumping as well as better confining it to the axial boundaries. Implementing the independently rotating rings is difficult and there is still Ekman pumping due to having only a finite number of independently rotating rings. An additional concern is that even with axial boundaries that exactly match the laminar Taylor-Couette profile, the axial boundaries would dampen any flow perturbations by the Ekman pumping they cause in addition to the damping provided by viscosity. This additional dampening could hide a non-linear instability.

3. If the working fluid is a liquid, the top boundary can be made into an open boundary by having gas above it, reducing the Ekman pumping at the top by three orders of magnitude in the case of water and air, though it does introduce the problem of gravity waves on the top surface. For the velocities that are used in the present experiments, air could be entrained by these waves.

4. Similarly, density-mismatched fluids such as mercury and water or stratification (e.g. salt solutions) can be used on the bottom boundary to confine the Ekman circulation near the bottom by reducing axial circulation, although this also introduces the problem of gravity waves and mixing which would destroy the stratification. An additional problem is that stratification can introduce the possibility of baroclinic instabilities, though baroclinic instabilities in Rayleigh-stable flow are of interest in their own right (Dubrulle et al. 2005b;

Le Bars and Le Gal 2007; Le Dizès and Riedinger 2010; Park and Billant 2013; Marcus et al. 2015).

5. The axial boundaries could be constructed of super-hydrophobic materials or be given super-hydrophobic coatings. While free-slip boundaries can never be achieved, boundaries between no-slip and free-slip will have reduced Ekman pumping. A major problem is that the strong shear in the fluid could damage super-hydrophobic surfaces.

In order to accurately represent an accretion disk, one probably has to combine more than one of these methods.

6.3 Open Questions And Future Research

There are a number of open questions and directions for future research. Some of them are listed below.

1. When the axial boundaries rotate with the outer cylinder, the details of the angular momentum transport in the Rayleigh-stable regime are still poorly understood. We only know that most of it goes to the axial boundaries. Measuring the separate torques along the height of the inner cylinder, outer cylinder, and axial boundaries or doing very high resolution Particle Image Velocimetry (PIV) as Huisman et al. (2012a) did for pure inner rotation or Particle Tracking Velocimetry (PTV) would be good ways to determine what fraction of the angular momentum goes to the axial boundaries versus the

outer cylinder and elucidate the axial transport mechanism. PIV and PTV would have the added advantage of possibly being able to discern shear stresses and Reynolds stresses in addition to allowing other analyzes to be done on the flow fields.

2. More work is needed to determine the nature of the flow in the inner, middle, and outer regions of the flow in the quasi-Keplerian regime, such as mixing properties and if the flow is turbulent or not. The dye injection videos provide some information about the outer parts of the gap, but most of the fluid is unsampled such as axial heights other than midheight and near the inner cylinder. In addition, the videos require more analysis to get fluid velocities, oscillation frequencies, and the level of mixing at different radial positions.

3. The remaining gap in Re_S between our torque measurements in the quasi-Keplerian regime and those of Paoletti and Lathrop (2011) needs to be closed. This is mostly a matter of getting the Maryland experiment assembled without even mildly damaging the bearings, which negatively affect torque measurements, that the middle section of the inner cylinder rotate on. In addition, using a more sensitive load cell would give higher precision torque measurements to aid the detection of flow state transitions and to compensate for the low dimensional torques at high Re_S.

4. The phase diagram in Figure 5.13 is far from complete. The phase boundaries need to be better resolved, at least one additional phase boundary found, and the phase diagram extended to lower q and higher Re_S.

5. Even with the measurements presented in this thesis, the Rayleigh-stable regime is still only sparsely investigated. In addition to helping resolve the phase diagram, measurements for a wider range of q and Re_S are needed to better understand the flow states and transport properties of the regime.

6. More investigation is needed to determine the nature of the oscillating flow sometimes seen in the outer parts of the gap in the Rayleigh-stable regime. It could be a known kind of wave, such as Poincaré/inertial waves (Zhang et al. 2001; Liao and Zhang 2009; Zimmerman 2010; Triana 2011).

7. Shifting away from astrophysical accretion disks and towards atmospheric and geophysical flows, beta plane turbulence and transport as well as Rossby waves could be investigated by putting in sloping axial boundaries (beta plane/s). It is already common to use a Taylor-Couette setup with the two cylinders locked together ($\Omega_i = \Omega_o$) with a sloping bottom and maintaining a temperature difference between the two cylinders to drive convection. This would instead be driving flow by shear. Given the analogies between shear in Taylor-Couette flow and temperature difference in Rayleigh-Bénard convection (Eckhardt et al. 2007; Sun and Zhou 2014), this could be an interesting investigation. In addition, many atmospheric flows have both shear and convection taking place in the presence of a local beta plane.

8. More advanced boundary layer modeling can be done for our Taylor-Couette geometries to try to get the flow field than was done by Lathrop et al. (1992a). The work of Beckley (2002) and Edlund and Ji (2014) hold potential. The

latter, based on extensive measurements from the Princeton HTX experiment, is particularly promising.

9. The results in this thesis are for one particular pair of η and Γ. Others should be investigated to see how their phase diagrams, transport, and flow states are different. There is already some research for the wide-gap low-aspect ratio case with axial boundaries attached to the outer cylinder (Kageyama et al. 2004; Ji et al. 2006; Schartman et al. 2012; Edlund and Ji 2014), but most of the geometry parameter space is empty.

6.4 Final Words

Taylor-Couette flow has a long history of investigation dating back to the late 1800's by M. M. Couette and A. Mallock (Donnelly 1991). Despite being one of the simplest enclosed rotating flows (the other two are rotating cylindrical tank and spherical Couette), Taylor-Couette flow still has many unanswered questions. Many of these questions pertain to the rotationally dominated part of its parameter space, the Rayleigh stable regime. The measurements presented in this thesis are an attempt to answer some of those questions, but many more remain.

Chapter 7: GE: Introduction

Adapted from and expanded upon the arXiv preprint

F. Nordsiek and D. P. Lathrop. Collective phenomena in granular and atmospheric electrification. *ArXiv e-prints*, Sept. 2015b.

arXiv: 1509.04214 [cond-mat.soft]

(a)

(b)

Figure 7.1: Images of granular materials in the laboratory. (a) bean-bag chair particles (expanded polystyrene). (b) spill of 750–1000 μm diameter glass spheres on the floor and spread out a bit with a broom before being cleaned up (slipping hazard).

7.1 Granular Materials And Flows

Granular materials are materials composed of large collections of discrete, usually solid, particles (sometimes called grains after the classic example of sand grains) where the particles are large enough that motion due to thermal fluctuations (Brownian motion) is negligible. Examples of granular materials are found across a vast range of scales and applications, such as sand at the beach, snow on the ground, grain in a silo, a pile of dirt, a bin full of tennis balls, powders found in cosmetics, etc. Figure 7.1 shows pictures of two granular materials in our laboratory. These materials can flow, which is referred to as *granular flow*. Examples include avalanches and grain flowing through a hopper and down a chute.

These collections of particles can also be suspended in a fluid such as air or water. When these systems flow, they are sometimes called *granular-fluid flows*, though sometimes the term *granular flows* is used to include both this case and when

the particles are not suspended in a fluid or that fluid can be ignored. Examples include the transport of sediments in rivers, sand blasting, dust storms, snow storms, and volcanic ash plumes. Unlike purely granular flows, granular-fluid flows can have surface tensions effects, exhibit shear-thickening and shear-thinning (effective viscosity of the bulk fluid increases and decreases with shear forces, respectively), etc.

Granular materials and flows exhibit a diverse set of behaviors. They can behave like the three standard states of matter: solids (e.g. sand at the beach), liquids (e.g. avalanches), and gases (e.g. dispersed powder or bearing balls shaken in a large container at high frequency). Images of these states are shown in Figure 7.2. Granular materials can exhibit jamming where the particle force chains extending across the whole system increase resistance to flow in a particular direction and make the particles mechanically stable (Liu and Nagel 1998), separation of two or more types of particles with different sizes and/or densities when mechanically agitated (Knight et al. 1993), and electrification (one of the subjects of this thesis).

General continuum equations of motion and state generally cannot be written down for granular materials, granular flows, and granular-fluid flows unlike fluid flow, plasmas, and the distortion of solids in response to stress, . This is due to the discrete nature of the particles, which require the equations of motion for each one to be treated separately. Naïvely, it might look like granular liquids and gases should be described by continuum equations just as the motion of liquids and gases is described by the Navier-Stokes equations despite both of them being made of discrete atoms and molecules. The key difference between the two is that liquids and gases have an

(a)

(b)

Figure 7.2: Images of a granular solid, liquid, and gas. (a) granular solid inside the bottle. (b) after shaking the bottle and setting it back down, there is a granular liquid in the bottom of it sloshing around and a granular gas in the space above it (opaque).

isotropic structure (Liu et al. 1995; Majmudar and Behringer 2005) and are never far from thermal equilibrium locally, while granular liquids and gases often have complex anisotropic structures and are far from equilibrium since even tiny motion is larger than their Brownian motion ($\frac{1}{2}mv^2 \gg k_BT$). Viscosity is the diffusivity of momentum, a quantity that is intricately tied to equilibrium statistical mechanics and the kinetic theory of matter (existence of atoms and molecules). There are some continuum models of limited applicability that have found some success such as stress transmission in aggregates (Edwards and Oakeshott 1989), shear-thickening fluids (e.g. corn starch in water), shear-thinning fluids, etc. However, there are no continuum equations of motion of general applicability in granular materials, granular flows, and granular-fluid flows.

7.2 Granular Electrification

As mentioned earlier, granular materials (specifically granular flows and granular-fluid flows) may exhibit a phenomenon known as electrification where particles become electrically charged via collisions, which is one focus of this thesis. In the atmosphere, clouds of suspended particles electrify (Latham 1964; Kok and Renno 2008; Saunders 2008; Pähtz et al. 2010; Lacks and Mohan Sankaran 2011; Gu et al. 2013; Cimarelli et al. 2014; Smirnov 2014), leading to the lightning in thunderstorms (Saunders 2008; Pähtz et al. 2010; Smirnov 2014), thunder-snow (Latham 1964), dust storms (Latham 1964; Kok and Renno 2008; Pähtz et al. 2010; Lacks and Mohan Sankaran 2011; Gu et al. 2013), and volcanic ash clouds (Lacks and Mohan

(a) (b)

Figure 7.3: Natural atmospheric electrification and lightning. (a) Lightning in a thunderstorm. Photograph courtesy of John W. Merck, Jr. (b) Volcanic lightning on Sakurajima. Photograph courtesy of Mike Lyvers.

Sankaran 2011; Cimarelli et al. 2014). Figure 7.3 shows images of lightning in a thunderstorm and a volcanic eruption. This granular electrification process is of interest as a natural phenomenon, but it is also an issue in industry where electrical discharges in flammable powders pose explosive hazards (Lacks and Mohan Sankaran 2011). The suspended particles (water droplets, ice, dust, ash, etc.) collide, exchange charge, and transport charge through the system, producing macroscopic electrical potential differences (Latham 1964; Kok and Renno 2008; Saunders 2008; Pähtz et al. 2010; Lacks and Mohan Sankaran 2011; Gu et al. 2013; Cimarelli et al. 2014; Smirnov 2014).

In addition to allowing for lightning to occur, granular electrification can have some major implications for clouds of suspended particles. Electrical charges on the particles effect how they spatially arrange themselves in turbulent flows (Alipchenkov et al. 2004; Lu et al. 2010a,b; Lu and Shaw 2015). In addition, the relative velocities of the particles, especially at the collision scale, are affected (Alipchenkov et al. 2004; Lu and Shaw 2015). For example, in the limit of very large

charges of the same sign on each particle, the particles will arrange themselves into a coulomb crystal in which case they will not collide with each other and will resist motion from the surrounding fluid due to their strong mutual electrostatic repulsion. The spatial distribution of particles has a major impact on the scattering of light by clouds (Shaw et al. 2002). In addition, the electrostatic interactions between the particles affects their collision rate (Lu et al. 2010a,b; Lu and Shaw 2015). In the case of water clouds, the collision rate is very important in understanding the evolution of the distribution of particle sizes, cloud lifetimes, precipitation (the warm rain initiation problem), and their optical properties (Shaw 2003).

Past investigations into granular electrification have mainly focused on two-body collisional charge exchange processes. When imagining two granular particles colliding and considering the charge exchanged, the first ideas that come to mind are the particle surfaces having different electron work functions, conductivities, ion mobilities, etc. In addition, one could imagine that the charge exchanged should be biased by an externally applied electric field due to polarization.

For these reasons, the surface chemistry, electrical properties, material properties, temperature differences, and surface curvature of the colliding particles have been studied extensively (Latham 1964; Lowell and Truscott 1986a,b; Duff and Lacks 2008; Saunders 2008; Forward et al. 2009a,b; Lacks and Mohan Sankaran 2011; Kok and Lacks 2009; Angus et al. 2013; Waitukaitis et al. 2014; Cimarelli et al. 2014; Smirnov 2014). The same goes for investigation into the role of background electric fields (Pähtz et al. 2010; Siu et al. 2014). The presence of other phases of the particle material has had very extensive investigation in the case of H_2O and

thunderstorms and thunder-snow (Saunders 2008; Smirnov 2014). Despite over a century of observations and investigation of granular electrification (Baddeley 1860; Rudge 1914; Lacks and Mohan Sankaran 2011), the actual charging process and the net separation of charges over many kilometers in storms is not well understood in general (Latham 1964; Lowell and Truscott 1986a,b; Duff and Lacks 2008; Kok and Renno 2008; Forward et al. 2009b,a; Kok and Lacks 2009; Pähtz et al. 2010; Lacks and Mohan Sankaran 2011; Gu et al. 2013; Angus et al. 2013; Waitukaitis et al. 2014; Siu et al. 2014; Cimarelli et al. 2014), though there is better understanding in thunder-snow and thunderstorms cold enough to have ice where all three phases of H_2O are present (Saunders 2008; Smirnov 2014).

A particularly difficult case is the electrification of electrically insulating particles (Lowell and Truscott 1986a,b; Duff and Lacks 2008; Forward et al. 2009b,a; Kok and Lacks 2009; Pähtz et al. 2010; Lacks and Mohan Sankaran 2011; Angus et al. 2013; Waitukaitis et al. 2014; Siu et al. 2014), which are found in the industrial setting and in dust storms. This case is made even more difficult if the particles are materially identical, the same size, and aren't fracturing or accreting. This case is particularly difficult because the particles can't support a current due to being insulators, there are no chemical bonds being broken possibly leaving ions behind, and there are no average differences in conductivities, electron work functions, and ion mobilities.

7.3 Collective Phenomena

Since granular flows and granular-fluid flows are composed of a large number of particles where each one can potentially influence the behavior of the others, it is possible for collective phenomena to be occurring. Collective phenomena are behaviors of physical systems at large scales, not easily predicted by the local dynamics. Equilibrium examples include the phases of matter, thermodynamic phase transitions, and critical points. Non-equilibrium examples include fluid turbulence, jamming in granular flows, swarming behavior in animals, and pattern-forming systems. In granular electrification, there are several potential sources for collective phenomena. For example, the macroscopic rearrangement of particles with electrical charge is a prerequisite for electric potential differences to become large enough for a discharge. As well, there should be effects on two-particle contact charging due to the macroscopic electric field of the collection of particles (Pähtz et al. 2010; Siu et al. 2014). In this thesis, we sought to experimentally elucidate and delineate collective effects in particle electrification. We show that they are needed to explain both laboratory and natural phenomena.

7.4 Outline

The granular shaking experiment that we upgraded is described in detail in Chapter 8 along with data analysis. Electrification results from single particle types (material, size range, form) in the experiment are presented in Chapter 9. Chap-

ter 10 presents results from when two particle types are mixed together. Conclusions, open questions, and what needs to be investigated further are detailed in Chapter 11.

Chapter 8: GE: Experiment

Adapted from and expanded upon the arXiv preprint

F. Nordsiek and D. P. Lathrop. Collective phenomena in granular and atmospheric electrification. *ArXiv e-prints*, Sept. 2015b.

arXiv: 1509.04214 [cond-mat.soft]

Characterization data for the powders has been deposited on DRUM at

F. Nordsiek and D. Lathrop. Collective phenomena in granular and atmospheric electrification. Dataset uploaded to Digital Repository at the University of Maryland (DRUM), July 2015a.

DOI: 10.13016/M2ZK87

URL: `http://hdl.handle.net/1903/16867`

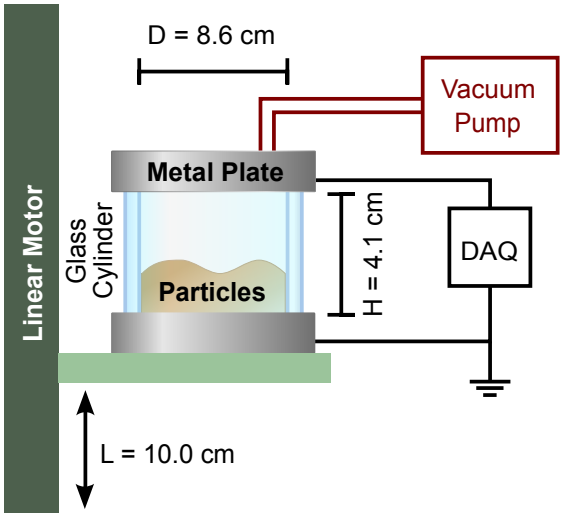

Figure 8.1: Diagram of the experiment. The experiment consists of the cell containing granular particles, the linear servo-motor that shakes the cell vertically, a vacuum pump, and the data acquisition system (DAQ).

8.1 Overview And Basic Results

We investigated granular electrification in a table-top shaking experiment, shown in Figures 8.1 and 8.2. Thousands to millions of particles smaller than 1 mm in diameter are shaken vertically inside a cylindrical cell with conductive aluminum top and bottom plates and a borosilicate glass sidewall. The cell has an inner diameter of $D = 8.6$ cm and a height of $H = 4.12$ cm. The experimental system we present in this thesis is an upgrade from the previous work by Paul Lathrop, Daniel Lathrop, Zack Lasner, Julia Salevan (Salevan 2012), Tyler Holland-Ashford, and Allison Bradford. The upgrades consisted of replacing the vacuum system, redoing the electronics and acquisition, redoing the control and acquisition software, and a few small changes to the cell itself. All three cells over the course of the project are shown in Figure 8.3.

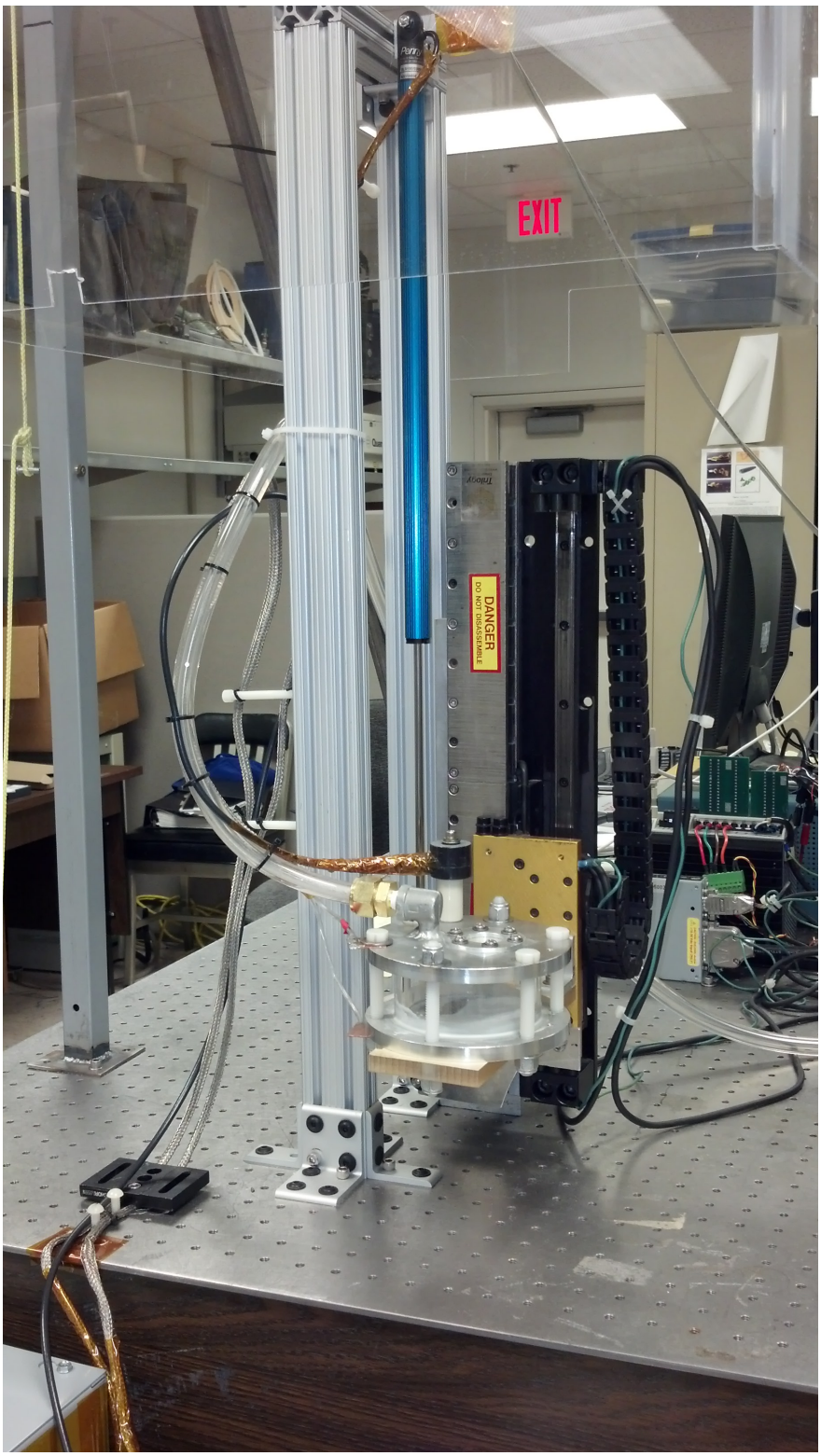

Figure 8.2: Image of the experiment, which includes the cell, linear motor, vacuum system (tubing to the cell can be seen), position encoder (blue), accelerometer, and acrylic shield (raised).

Figure 8.3: The three cells that have been used 2011–2015. The first cell (left), hand-shaken and filled with sand, developed by Paul Lathrop and Daniel Lathrop. The second cell (middle), shaken using the linear motor, was developed and used by Zack Lasner and Julia Salevan (Salevan 2012). The third and current cell (right), able to hold a partial vacuum, was developed and originally used by Tyler Holland-Ashford and Allison Bradford. The yellow ruler in the image is 15 cm long.

We quantified the electrification by measuring the electric potential between the plates (bottom plate is defined as 0 V). Humidity affects electrification, as is seen by the greater ease of generating static electricity in arid climates and the dry of winter. Thus, the cell is held under a partial vacuum to create a consistent low humidity environment. The cell is shaken vertically by a linear motor with a stroke-length of $L = 10.0$ cm using a square-wave acceleration profile with amplitude a, which causes the cell's vertical position to be a sequence of connected parabolas of opposite concavity (dashed line in Figure 8.5a). We measure the vertical position of the cell via an electronic sensor.

While the cell is shaking, the particles form a loose slab that collapses inelastically when it hits either plate and can collisionally exchange charge with each other

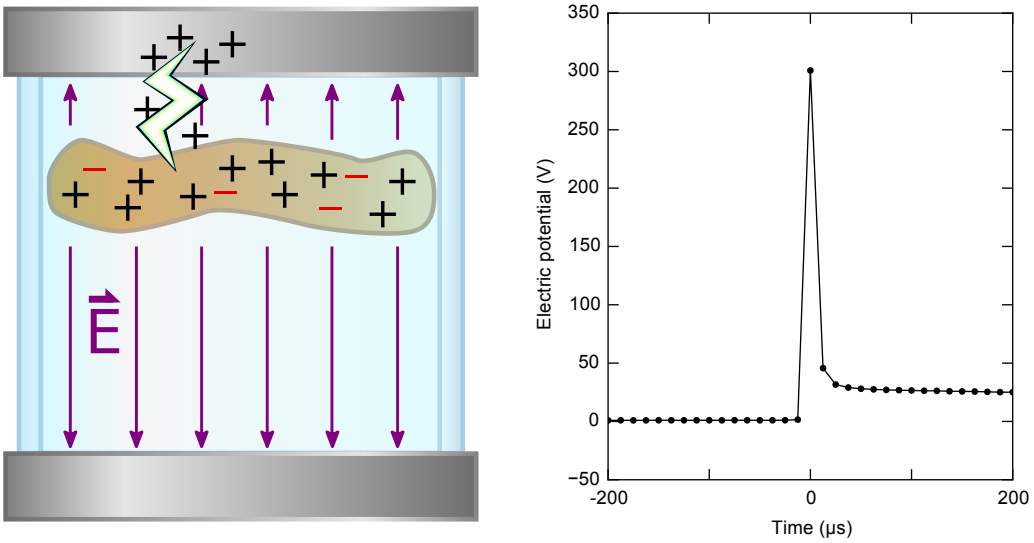

(a) (b)

Figure 8.4: Electrical signals. (a) A schematic of how an electric potential difference between the plates is established. Capacitive coupling from the charges in the slab of particles (light brown) cause electric fields (purple lines) and potential differences between the plates. There is also direct transfer of charge to the plates by electric discharge (drawn as a lightning bolt). (b) Time trace of the electric potential across the cell during an electrical discharge.

and the glass sidewall. They can also exchange charge with the metal plates during the inelastic collapse of the particle slab against the plates. There are two primary mechanisms that can cause an electric potential difference between the plates, which are illustrated in Figure 8.4. First, there can be capacitive coupling between particle charges and the plates while the particles are in flight. Second, the particles can electrically discharge to a plate, depositing charge directly onto it, which may cause much larger potential differences. When the cell is shaken, we observe an oscillating electric potential across the cell (Figures 8.5a and 9.1), typically a few volts peak to peak. There are also occasional multi-hundred volt discharges such as in Figure 8.4b, which can be of either sign. From Figure 8.5a, the electric potential typically has voltage extrema with opposite signs correlated with the extrema in the cell's position (top and bottom of its vertical motion).

While the electric potential is not quite symmetric on both sides of 0 V, we can still describe it as either in-phase with the position (maxima near the top of the cell's motion and a minima near the bottom) or out-of-phase with the position. We call changes between in-phase and out-of-phase *inversions*. After the particles have rested for long periods of time, there is an initial transient of a few tens of cycles when starting to shake. Then, from one cycle to the next, the potential's time dependence changes little (Figure 8.5a). However, over longer time scales the variation is significant (Figure 8.5b), including inversions. For example, in Figure 8.5b, there is an inversion around cycle 800 where the RMS voltage approaches zero.

When the cell is at rest, the particles form a slab on the bottom of the cell. We used various granular particles of different materials, forms (spheres and powders),

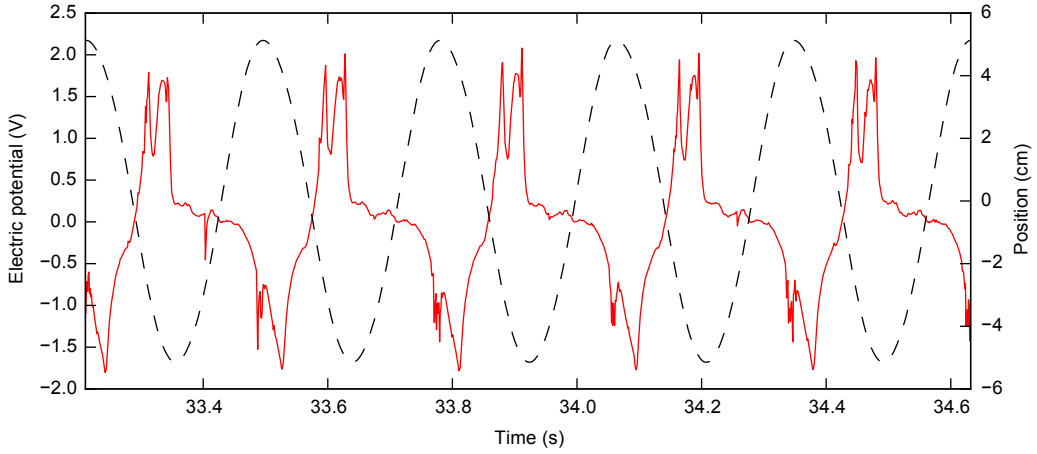

(a)

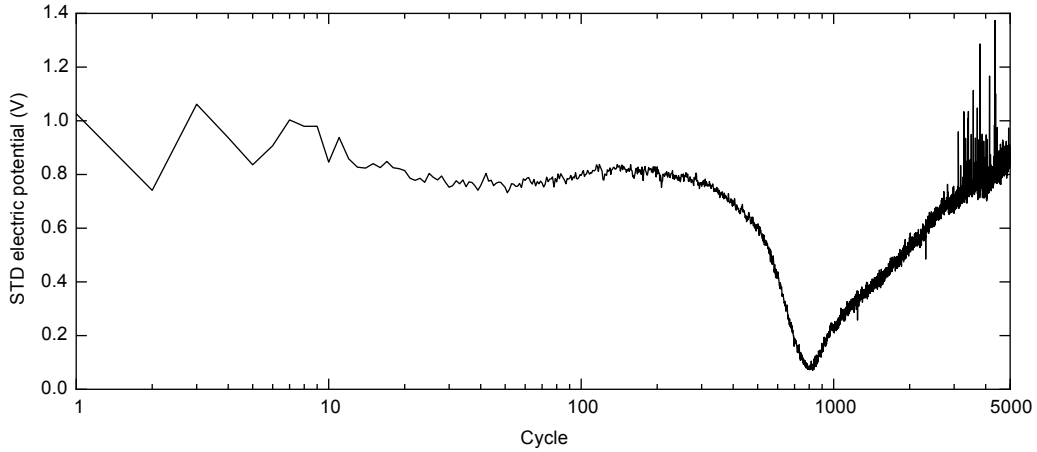

(b)

Figure 8.5: Electric potential difference time dependence for 400–600 μm glass spheres. Time dependence for a quantity $\lambda = 6$ (Eq. 8.2) of 400–600 μm diameter glass spheres shaken at $a = 2.08\,g$ for 5000 cycles. (a) The cell vertical position (black dashed line) and electric potential (red solid line) time series for cycles 100–105 (b) Standard deviation of the electric potential for each cycle. There is an inversion around cycle 800.

and diameter ranges with the largest diameter being under 1 mm. Materials included plastics (polystyrene and polytetrafluoroethylene, which is known as PTFE), glass (lead free soda-lime glass), ceramic (69%:31% ZrO_2:SiO_2), and conductive metal (aluminum and copper).

There are several different ways to quantify the amount of granular material in the cell. We decided to use the thickness of the slab of particles formed when the cell is at rest and make it dimensionless. Ignoring the voids between the particles, the thickness of the slab at rest, h, is the total particle volume $\frac{1}{6}\pi N_p d^3$ divided by the cross-sectional area of the cell $\frac{1}{4}\pi D^2$, which is

$$h = \frac{2N_p d^3}{3D^2} \quad , \tag{8.1}$$

where N_p is the number of particles, d is the particle diameter, and D is the diameter of the cell. We then define the dimentionless thickness of the slab to be

$$\lambda = \frac{h}{d} = \frac{2N_p d^2}{3D^2} \quad . \tag{8.2}$$

This is proportional to the total surface area of the particles, which is $4\pi N_p d^2$. Considering that electrification is a process that happens on the particle surfaces, this is a useful property to have. In addition, λ is approximately how many mono-layers of particles can be put in the cell since it is the height of the slab in units of d.

8.2 Hardware

8.2.1 Cell

The cell (images in Figure 8.6) is cylindrical with a diameter of $D = 8.6$ cm and a height of $H = 4.12$ cm. The cylindrical sidewall is a borosilicate glass (pyrex) cylinder (G. Finkenbeiner) with a 10.0 cm outer diameter, $D = 8.6$ cm inner diameter, and 5.0 cm height. The end caps are two 13.67 cm diameter and 1.0 cm thick circular aluminum plates (top and bottom) with annular slots to accommodate the glass sidewall and seal the cell (epoxy for bottom plate and o-ring for top plate). Six insulating nylon bolts hold the plates tightly together with the glass sidewall between them. The cell is held under a partial vacuum of 30–60 mTorr (4×10^{-5} to 8×10^{-5} atm). For comparison, the saturated vapor pressure of water at the approximate lab temperature of 23 C is 21.08 Torr (Lide 2003). The cell is continuously pumped through a tube fitting and hole in the top plate (vacuum system in Figure 8.7a). The hole is covered in a metal mesh to keep particles out of the vacuum system. The pressure was measured behind the last filter by a convection vacuum gauge (Duniway CVT-275-101 with a Granville-Phillips 275 Analog Convectron Gauge Controller). The inside of the top plate is not flat due to the mesh, a sheet of aluminum covering a previously cut window, and seven small round-head bolts holding the former two items in place.

The cell was attached with an electrically insulating plate of acrylic to a linear servo-motor (Trilogy T2SA19-3NCTS) mounted so that motion is vertical (Fig-

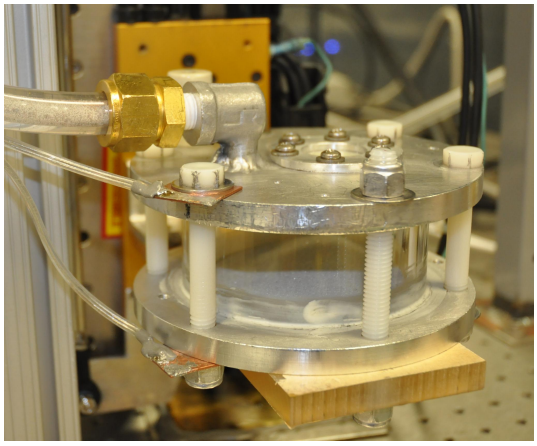

(a)

(b)

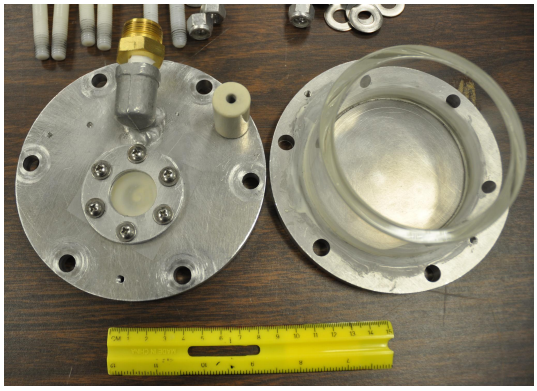

(c)

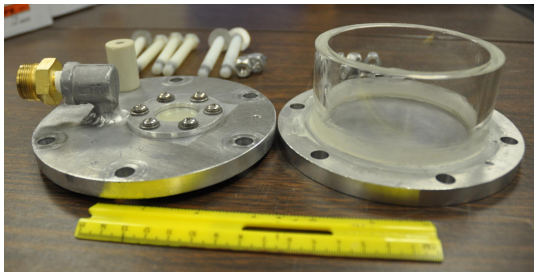

(d)

Figure 8.6: Images of the cell. (a) The cell (filled with glass particles) is mounted to the linear motor, wired, and connected to the vacuum system. (b) The open cell filled with glass particles with the inside face of each plate visible (top plate on the left). (c) The open cell with no particles and the outside face of the top plate visible (on the left). (d) Side view of the open cell with the outside face of the top plate visible (on the left). The yellow ruler in three of the images is 15 cm long.

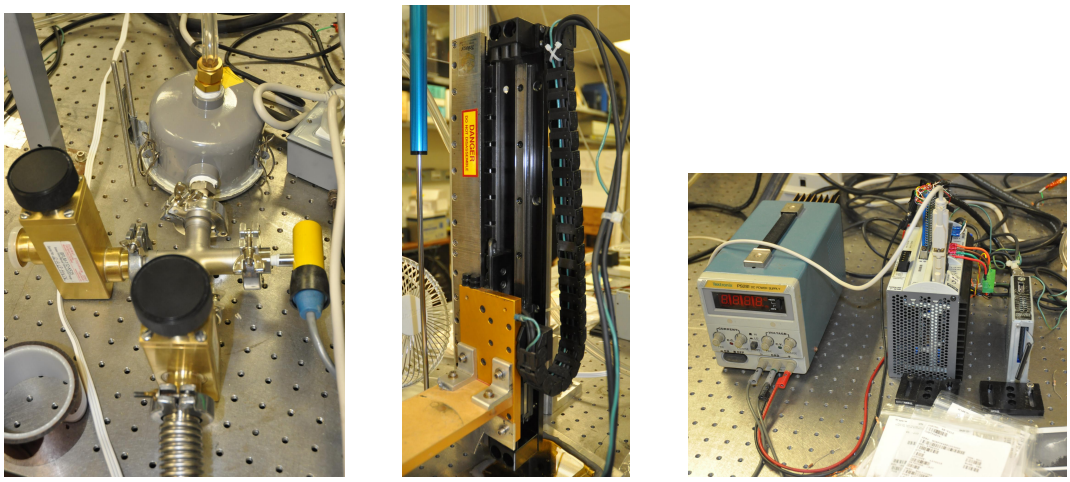

(a) (b) (c)

Figure 8.7: (a) Image of the vacuum system comprising a filter to the tube to the cell (top), the pressure sensor (right), the valve to the hose to the pump (bottom), and the valve to let in lab air when done (left). (b) Image of the linear motor with the acrylic plate attached and part of the desk fan used to cool it visible. (c) Image of the servo-motor drive (middle), the decoder for the motor's internal sensors (right), and its power supply (left).

ure 8.7b, with a maximum stroke-length of 24.13 cm. The motor was controlled by a Parker Hannifin Gemini GV6-U3E-DN servo-motor drive (Figure 8.7c). The vertical position of the cell was measured by a continuous linear potentiometer (Penny+Giles SLS190/0300/L/66/01/N) with a 30 cm stroke. As the cell could implode due to the partial vacuum it contains, the experiment is enclosed in an acrylic shield. A small desk fan is placed inside the shield to keep the motor cool when it is run for long periods of time.

8.2.2 Particles

The particle types were aluminum powder, copper powder, lead-free soda-lime glass spheres, polystyrene powder and spheres, PTFE (polytetrafluoroethylene)

Table 8.1: Detailed information on the particles. Composition, manufacturer, and size information for all particle types used. The spheres come with a manufacturer nominal diameter range. The powders were characterized and the statistics of their effective diameters shown here. n stands for minimum, x stands for maximum, M stands for mean, R stands for Root Mean Squared, and T stands for standard deviation. We show the excess kurtosis. GM and GF stand for GlenMills and GoodFellow respectively. PS and ZrO stand for polystyrene and ZrO_2:SiO_2 respectively.

				Nominal dia. and effective dia. statistics (μm)							
Mat.	Form	Mfg	Product #	Nom.	n	x	M	R	T	Skew	Kurt
Al	P	GF	AL006010	< 400	58	376	231	242	74	-0.308	-0.408
Cu	P	GF	CU006045	< 200	5	166	43	49	24	1.09	1.84
Glass	S	GM	7200-000200	200-300	-	-	-	-	-	-	-
Glass	S	GM	7200-000400	400-600	-	-	-	-	-	-	-
Glass	S	GM	7200-000750	750-1000	-	-	-	-	-	-	-
PS	P	GF	ST316051	< 250	12	324*	111	131	70	1.2	1.75
PS	S	GM	7192-PB-2	360-610	-	-	-	-	-	-	-
PS	S	GM	7192-PB-1	610-990	-	-	-	-	-	-	-
PTFE	P	GF	FP306068	< 675	35	636†	212	303	218	1.88	3.84
ZrO	S	GM	7305-000002	200-300	-	-	-	-	-	-	-
ZrO	S	GM	7305-000004	400-600	-	-	-	-	-	-	-
ZrO	S	GM	7305-000010	800-1000	-	-	-	-	-	-	-

* There was one outlier, which was excluded, whose effective diameter was 438 μm.
† There was one outlier, which was excluded, whose effective diameter was 1037 μm.

powder, and 69%:31% ZrO_2:SiO_2 spheres. The manufacturer and size information for all particle types is shown in Table 8.1.

Each powder was characterized by taking three images under a microscope (Leitz Ergolux) while backlit. The cross-sectional areas of the particles were obtained by outlining each particle by hand with interpolation for overlapping particles in an image editor and counting the number of pixels. The diameter of a circle with the same cross-sectional area was defined to be the effective diameter of the particle. One image of each powder and histograms of their effective diameters are shown in Figures 8.8 and 8.9. The particles, whether spheres or powders, were poly-disperse. For the spheres, the range of particle diameters was 20-50% of the maximum diameter. For the powders, the effective diameters of the largest particles

are an order of magnitude larger than for the smallest particles.

For the calculation of λ, we use the manufacturer-provided particle densities. For d, we use the mean of the manufacturer-provided diameter bounds for spherical particles and the RMS (Root Mean Squared) effective diameter for powders. The mass of particles is measured on a scale and λ is calculated, or the target mass is calculated for a desired λ and then that quantity is measured out.

8.2.3 Electronics and data acquisition

The vertical position sensor (linear potentiometer) was operated as a voltage divider with a fixed regulated 5 V across it and the potential from the center tap measured by the acquisition system through an instrumentation amplifier. The top and bottom plates are connected by separate high voltage wires (insulation rated to 12 kV) to the acquisition system and ground respectively. Since potentials up to 1 kV had been previously measured across the cell before the work presented in this paper, the electric potential of the top plate was stepped down by a factor of 11.0 (or 101.0 for the discharge measurement in Figure 8.4b) using two high impedance resistors of 10.0 MΩ and 1.00 MΩ (100.0 kΩ for the discharge measurement in Figure 8.4b) before passing through an instrumentation amplifier (Analog Devices AD624). With regulated DC rails of ±9 V, measurements are clipped to ±70 V (±600 V for the discharge measurement in Figure 8.4b). The instrumentation amplifier provides a 20 pF capacitance between the input for the top plate and ground. An additional 10 pF capacitor is connected across the 10.0 MΩ resistor. With a plate capacitance

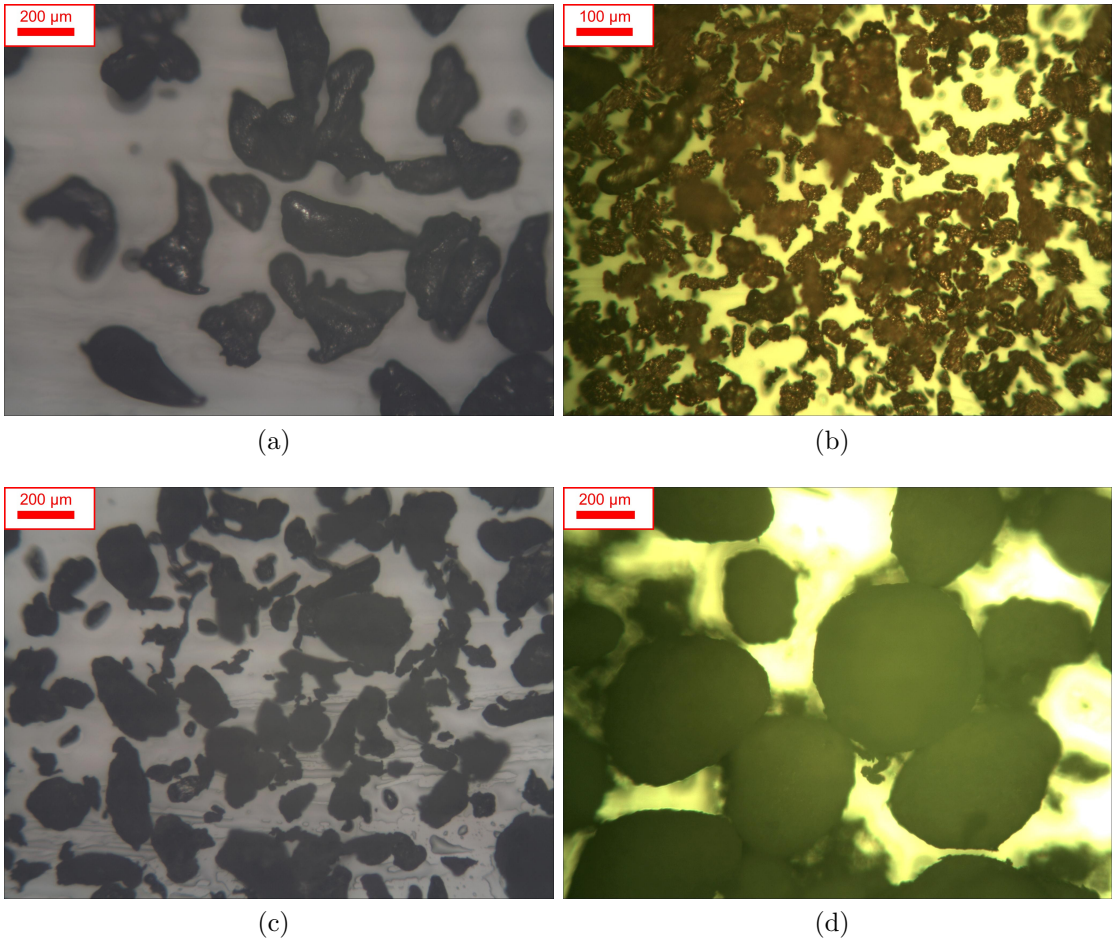

(a) (b)

(c) (d)

Figure 8.8: One microscope (Leitz Ergolux) image (courtesy of John Abrahams III) of each of the powders used in this paper. (a) 60–375 μm aluminum, which had 49 particles characterized. (b) 5–165 μm copper, which had 457 particles characterized. (c) 10–325 μm polystyrene (PS), which had 224 particles characterized. (d) 35–635 μm PTFE, which had 42 particles characterized. Distributions of their effective diameters are in Figure 8.9.

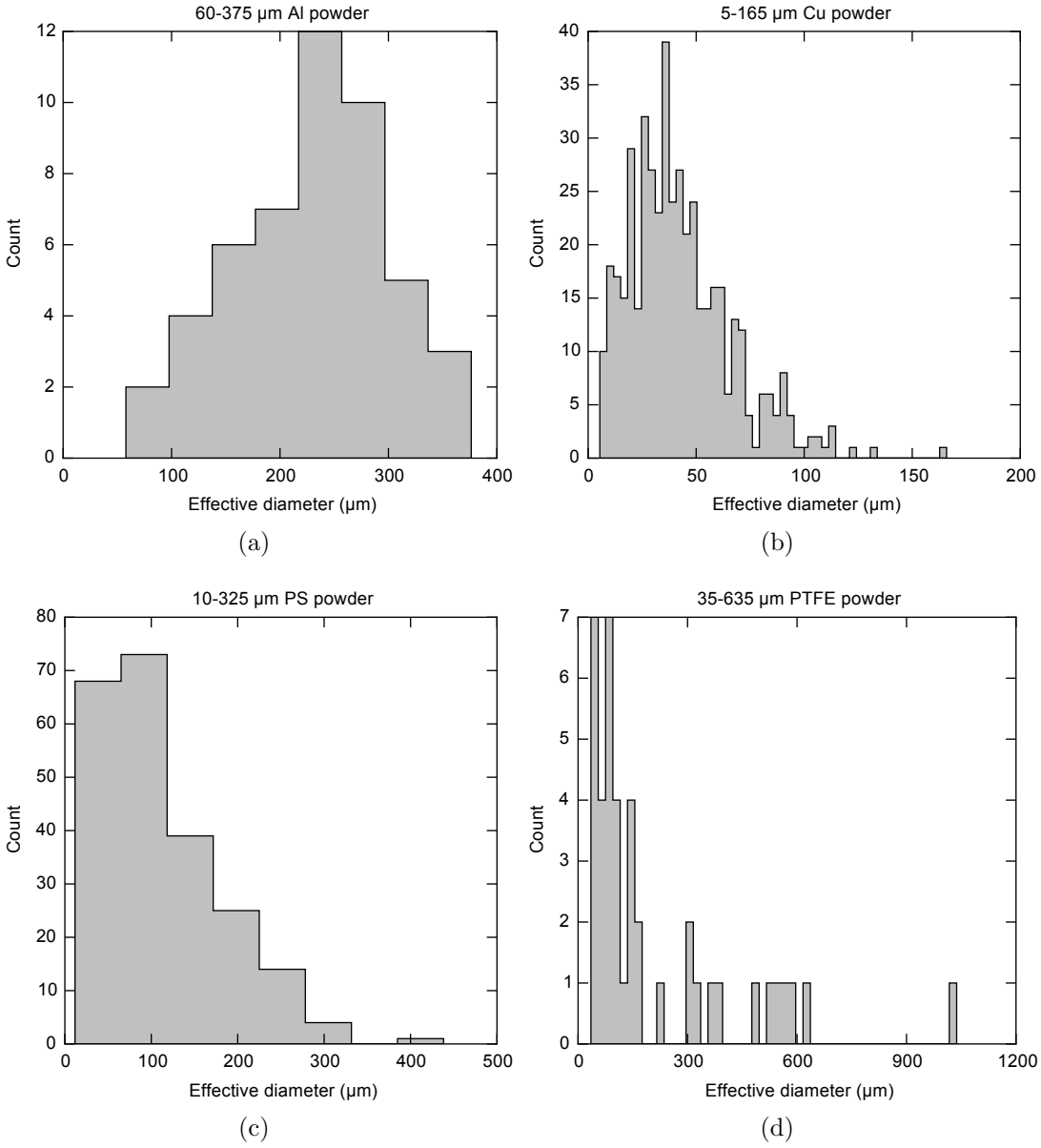

Figure 8.9: Powder effective diameter distributions produced from their microscopy images (Figure 8.8) as described in Methods.(a) 60–375 μm aluminum, which had 49 particles characterized. (b) 5–165 μm copper, which had 457 particles characterized. (c) 10–325 μm polystyrene (PS), which had 224 particles characterized. (d) 35–635 μm PTFE, which had 42 particles characterized.

of 3.15 pF, the total capacitance between the top plate and ground is 13 pF if we approximate the connection to the instrumentation amplifier as ground since the drain resistor between it and ground is 11.0 or 101 times smaller. The RC time constant for the potential difference is then ≈ 130 μs. The outputs of the two instrumentation amplifiers are read by a high speed DAQ (Data AcQuisition system) at 80 kHz each (National Instruments USB-6211). To reduce interference and noise, standard practices were used such as twisted shielded wire, an electrically conductive enclosure for the electronics, no ground loops in the acquisition electronics, regulated AC-DC power, and isolation between the acquisition computer and motor drive from the acquisition electronics.

8.2.4 Calibration of the vertical position

To calibrate the vertical position measurement with the linear potentiometer, the cell was set to 21 vertical positions over the full range and the potentials across the whole linear potentiometer and at the center tap acquired at each step. The linear servo-motor itself has a precise position encoder which allows the cell's position to be set precisely programmatically, though it cannot be read in real time while the motor is in motion. A linear fit is done between the measured potentials at the center tap and the positions of each step. The potential from the regulated power supply across the whole potentiometer is approximately constant.

8.3 Data Processing and Models

8.3.1 Data processing

When we break our time series into the individual shaking cycles, the tops of the oscillation cycles are used as the cycle boundaries and then all the acquired data points between successive tops are averaged into 1 ms bins. Since the cell starts and ends at the bottom of the shaking cycle, half a cycle is discarded from the beginning and end. For shaking with a square-wave acceleration profile of magnitude $a = 2.08\,g$ (shaking frequency of 3.522 Hz) and stroke-length 10.0 cm, this corresponds to 284 bins in each cycle (about 80 samples per bin at the 80 kHz acquisition rate). The tops and bottoms of the oscillation cycles (extrema in the vertical position signal) were found by taking the full vertical position time series before it is put into 1 ms long bins, subtracting the mean, finding all intervals in the time series where the position is more than 1 cm away from the mean position continuously for at least 10 ms, and the extremum taken to be the location of the maximum/minimum position value in the interval.

The measured vertical cell position profile gives an acceleration profile that is approximately a square-wave. We get the acceleration amplitude, a, from $aT^2 = 4L$ using the measured peak-peak vertical position L and oscillation period T.

8.3.2 Kinematic model

It is helpful to consider the particles in their flight between the plates using a simple kinematic model. Using the motion and geometry of the cell, we simulate the ballistic motion of a hypothetical point particle within the cell that is inelastic, which means it does not bounce from the plates nor does it have any adhesive forces between it and the plates. Let z_c and z_p be the vertical positions of the cell bottom and the particle respectively. We define $z_c(t)$ for the profile over a cycle of the measured vertical position. We simulate the hypothetical particle's motion using its equations of motion. Its equations of motion when against the top and bottom plates are, respectively,

$$\begin{aligned} z_p &= z_c + H \qquad \text{when } z_p = z_c + H \text{ and } \ddot{z}_c \leq -g \\ z_p &= z_c \qquad\quad\;\; \text{when } z_p = z_c \text{ and } \ddot{z}_c \geq -g \end{aligned} \tag{8.3}$$

Otherwise, the particle is in free fall between the plates moving as

$$\ddot{z}_p = -g \quad . \tag{8.4}$$

From the simulated trajectories, we find when the particle hits and leaves the two plates, which are the beginnings and ends of periods of time when $z_p = z_c,\, z_c + H$.

Chapter 9: GE: Single Particle Type

Adapted from and expanded upon the arXiv preprint

F. Nordsiek and D. P. Lathrop. Collective phenomena in granular and atmospheric electrification. *ArXiv e-prints*, Sept. 2015b.

arXiv: 1509.04214 [cond-mat.soft]

Data has been deposited on DRUM at

F. Nordsiek and D. Lathrop. Collective phenomena in granular and atmospheric electrification. Dataset uploaded to Digital Repository at the University of Maryland (DRUM), July 2015a.

DOI: 10.13016/M2ZK87

URL: `http://hdl.handle.net/1903/16867`

9.1 Shape of The Electric Potential Profile over A Cycle

For each particle type, Figure 9.1 shows cycle profiles of the potential across the cell for cycles 10, 100, 1000, and 3000 shaken at $a = 2.08\,g$ (shaking frequency of 3.522 Hz). The cell's vertical position is also shown. The profile shapes for all particle types are qualitatively similar as detailed in the next paragraph. As well, the amplitudes of the oscillating potential are within an order of magnitude of each other for all particle types.

It is helpful to consider the particles in their flight between the plates using a simple kinematic model (Section 8.3.2). We mark where this hypothetical inelastic particle hits and leaves each plate using dashed vertical lines in Figure 9.1. Some patterns are:

1. The electric potential trends towards zero while the particles are in contact with either plate (grey shaded regions).

2. The profiles show an extremum in the potential right before hitting the top plate.

3. The profiles show another extremum of the opposite sign before particles hit the bottom plate, with a decay towards zero potential afterwards that is usually quicker.

4. There is often an extremum when the particles are in mid-flight after leaving the top plate before they hit the bottom plate.

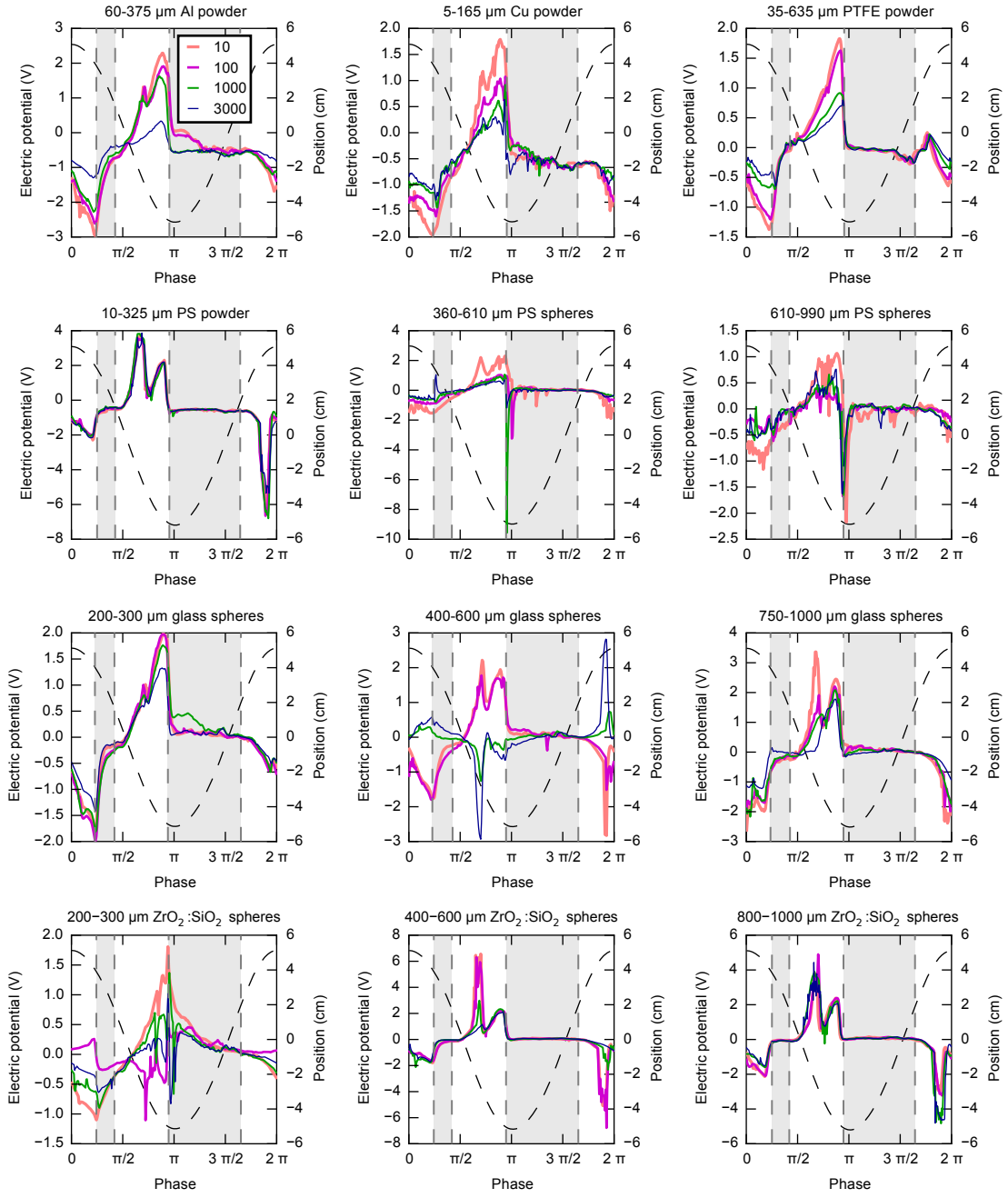

Figure 9.1: Signal profiles during the shaking cycle by particle type. The cell vertical position (black dashed line) and electric potential for cycles 10, 100, 1000, and 3000 are shown by phase (legend in top-left figure) are shown by phase in the shaking cycle for $\lambda = 6$ of each particle type (figure titles) shaken 5000 cycles with $a = 2.08\,g$. A particle in the kinematic model is on either plate in the grey regions, and the dashed vertical lines, from left to right, are when it hits the top plate, leaves the top plate, hits the bottom plate, and leaves the bottom plate respectively. Polystyrene is abbreviated as PS.

5. Less often, there is an extremum when the particles are in mid-flight before they reach the top plate after leaving the bottom plate.

9.2 Particle Quantity Dependence

We find a strong dependence on the observed electrification due to particle quantity. We shook polystyrene powder samples with different λ at different accelerations for 1000 or 500 cycles. To improve consistency and reduce the effects of initial transients when investigating the λ dependence of electrification, each particle sample was shaken first for $10,000$ cycles at $a = 2.08\,g$. Then, the particles were shaken at the desired a for 1000 or 500 cycles, which was taken to be our results. If the λ dependence was measured for a particle sample at more than one a, the particles were shaken for at least 100 cycles at $a = 2.08\,g$ between each measurement.

The standard deviations of the electric potentials between the plates (skipping the first 10 cycles) are shown in Figures 9.2a and 9.2b. The number of particle-particle collisions increases with increasing λ and a/g (forcing strength), and they become more energetic for increasing a/g. The measured potential increases with increasing a/g, though it is approximately zero for $a < g$ as expected since the acceleration is not strong enough for the particles to lift off the bottom plate. We note that the particles can reach the top plate by $a/g = 1.2$. The strength of the measured potentials has a non-monotonic and highly non-linear dependence on λ. There is a threshold at $\lambda \sim 1$ with the plate potential being less than 20 mV for smaller λ. The dependence on λ also shows threshold behavior for the two

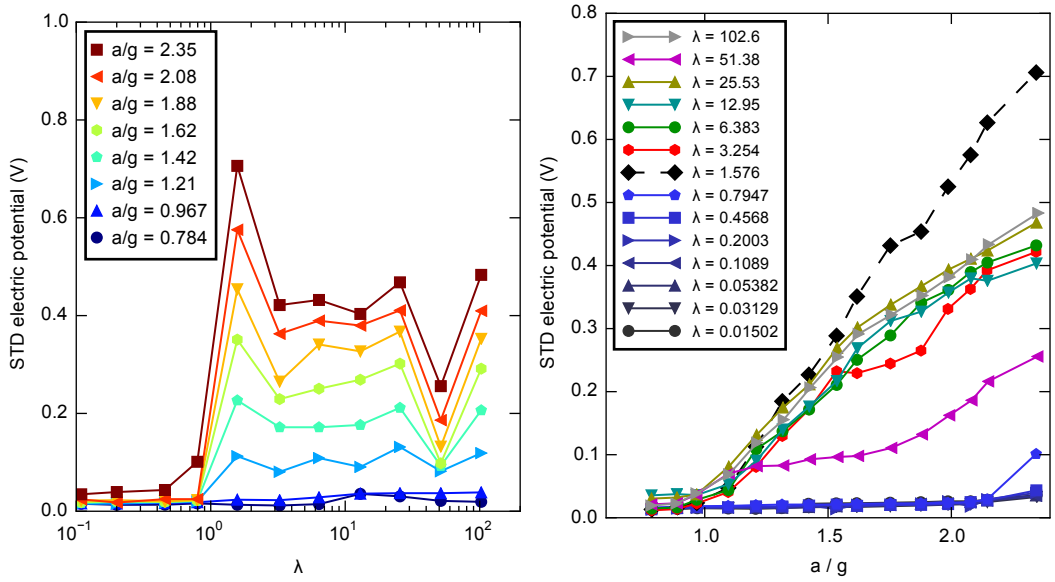

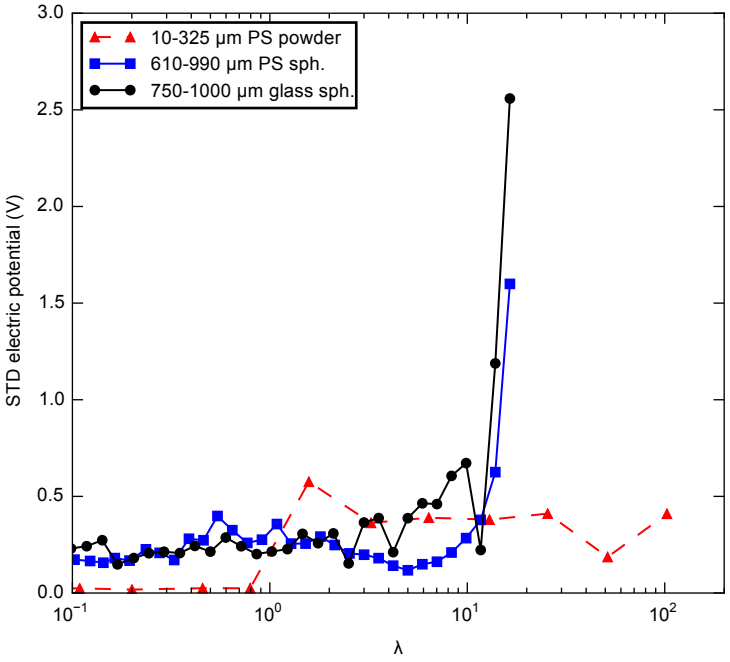

Figure 9.2: Strength of electric potential by particle quantity and acceleration strength for different particle types. We show standard deviation of the measured potential between the plates for different quantities, λ and a/g, shaken for 1000 or 500 cycles (the first 10 cycles were skipped to remove the initial transient). (a) Different acceleration strengths for 10–325 μm polystyrene powder. (b) The same as (a) but plotted for different λ as a function of a/g. (c) Three different particle types (polystyrene abbreviated as PS) shaken at $a = 2.08\,g$ (shaking frequency of 3.522 Hz.

other particles tested (polystyrene and glass spheres) in Figure 9.2c. However, the dependence for these particles has a threshold of $\lambda \sim 10$ and the potential difference is ≈ 0.2 V for λ below the threshold. As the threshold value of λ is approximately the same for 610–990 μm polystyrene spheres and 750–1000 μm glass spheres, we expect that the threshold will be the same for the other types of particles that are spheres. The 60–375 μm aluminum powder, 5–165 μm copper powder, and 35–635 μm PTFE powder might have λ dependences more similar to the 10–325 μm polystyrene powder.

The time evolution of the electrification for the initial $10,000$ cycles of shaking at $a = 2.08\,g$ run for each λ of 10–325 μm polystyrene powder is shown in Figure 9.3, split into the λ less than and greater than the value resulting in the strongest electrification ($\lambda = 1.58$) in Figure 9.2a. For $\lambda < 1.58$, the electrification shows an initial transient in the form of a bump before the potential goes to zero. The bumps start to from low electrification (< 0.1 V) at around cycle 10. The bumps then grow logarithmically with approximately the same slope before reaching a peak value and then decaying towards zero. The length of time that the bump grows, and therefore the height of the peak of the bump, increases with increasing λ. The pattern continues till $\lambda = 1.58$, where the electric potential starts to stay approximately constant or decay much more slowly after the peak (around cycle 2500). For $\lambda > 1.58$, the electric potentials start to grow earlier and usually faster than for $\lambda < 1.58$, either reaching a peak around cycle 100 or growing in two stages with another increase after that peak to a higher value by cycle 1000. As with $\lambda = 1.58$, the electric potential is either staying approximately constant or decaying slowly after reaching

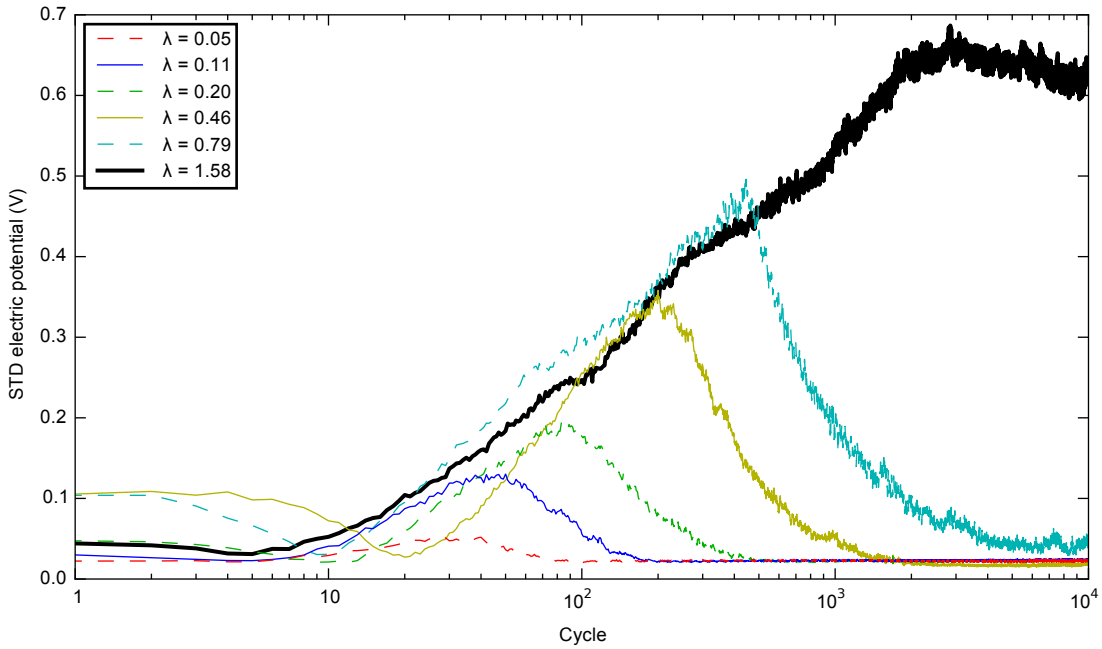

(a)

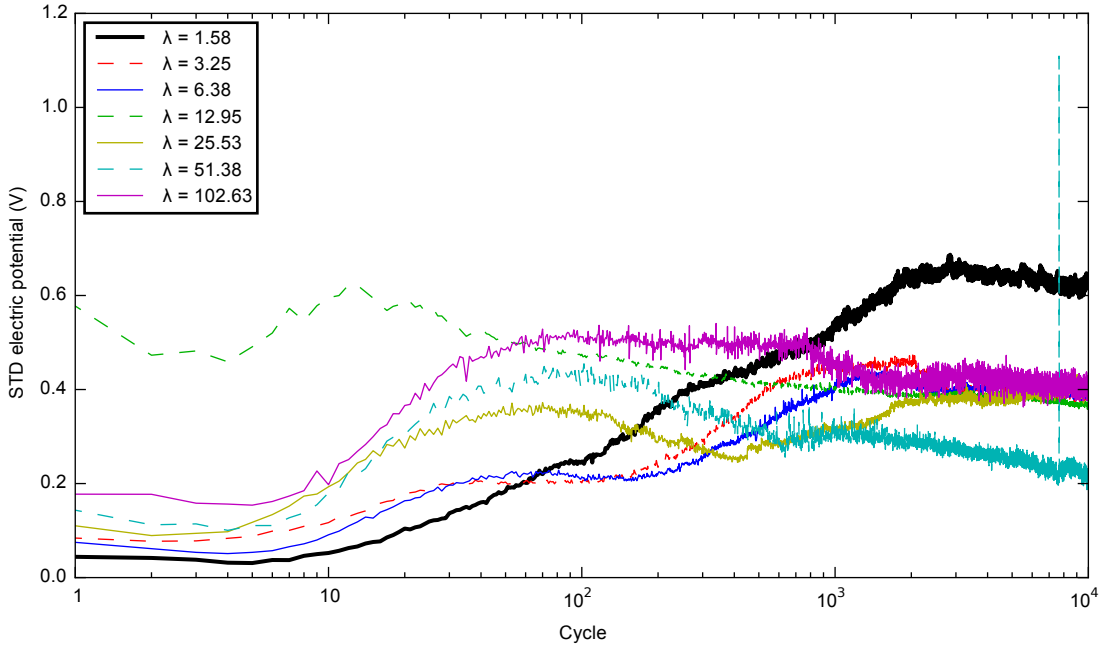

(b)

Figure 9.3: Standard deviation of the electric potential for each cycle for different λ of 10–325 μm polystyrene powder shaken 10,000 cycles at $a = 2.08\,g$. The different values of λ are separated into two plots for clarity about the λ closes to the threshold which is $\lambda = 1.58$. (a) The values below the threshold ($\lambda \leq 1.58$) with the threshold value drawn as a thick black line. (b) The values above the threshold ($\lambda \geq 1.58$) with the threshold value drawn as a thick black line

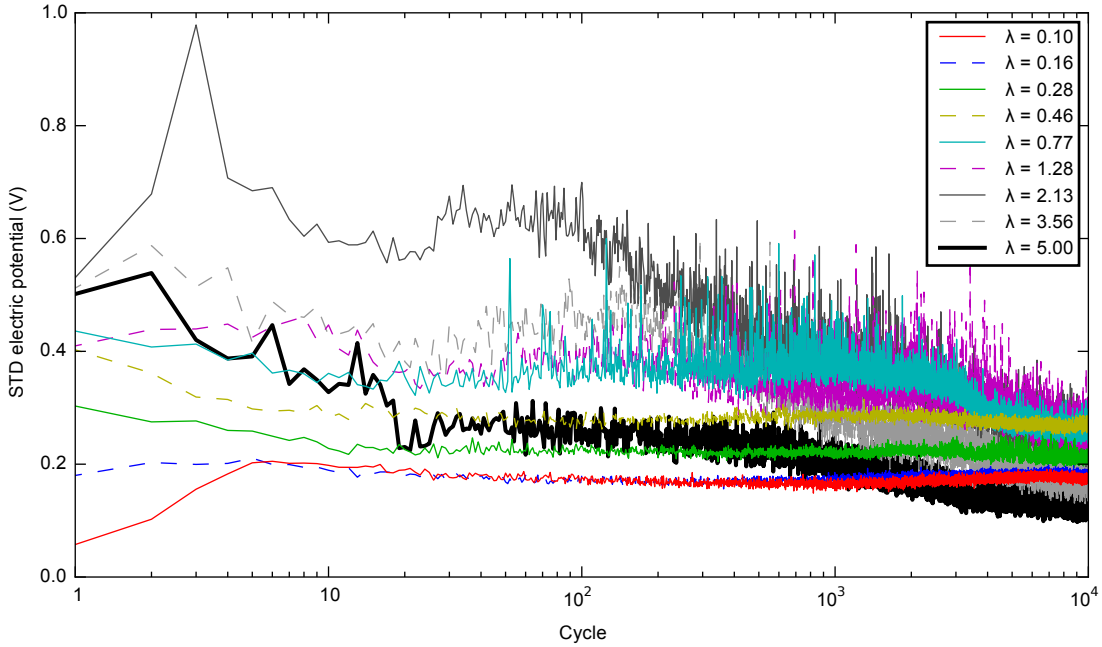

(a)

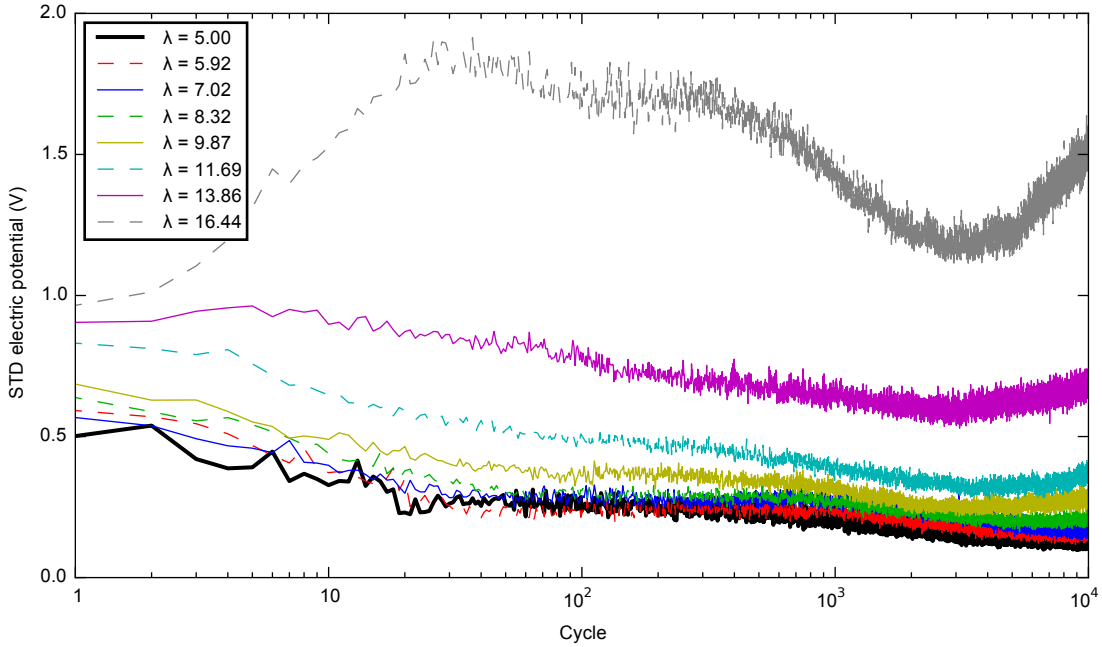

(b)

Figure 9.4: Standard deviation of the electric potential for each cycle for different λ of 610–990 μm polystyrene spheres shaken 10,000 cycles at $a = 2.08\,g$. The different values of λ are separated into two plots for clarity about the $\lambda = 5.00$, which is where the electrification begins to increase with increasing λ. (a) The values below the threshold ($\lambda \leq 5.00$) with $\lambda = 5.00$ drawn as a thick black line. (b) The values above the threshold ($\lambda \geq 5.00$) with $\lambda = 5.00$ drawn as a thick black line

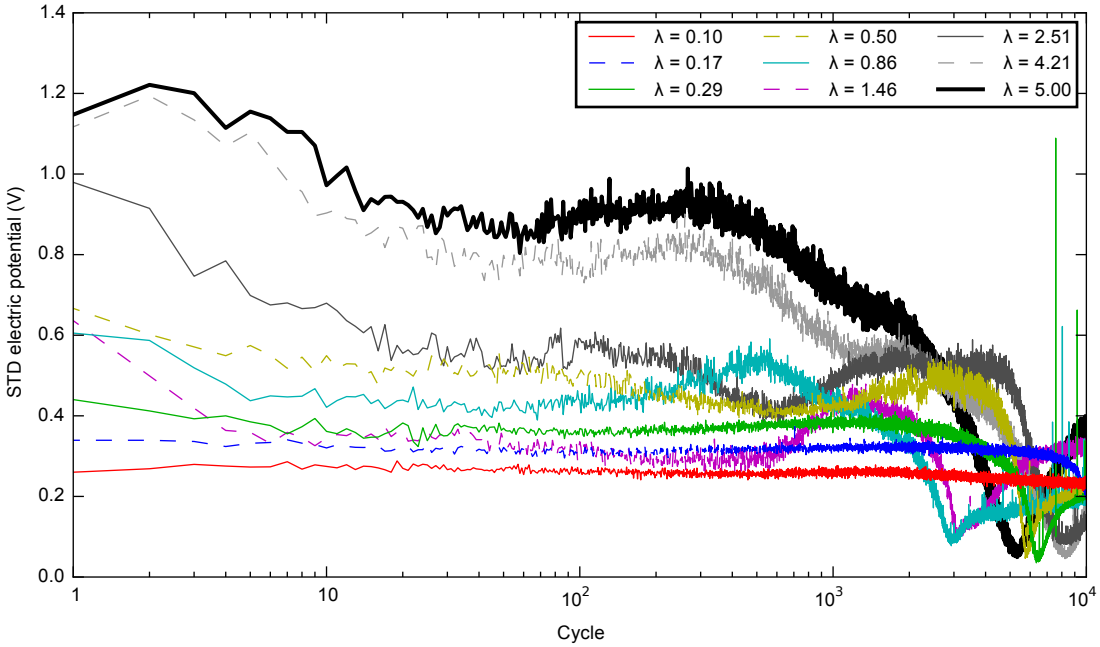

(a)

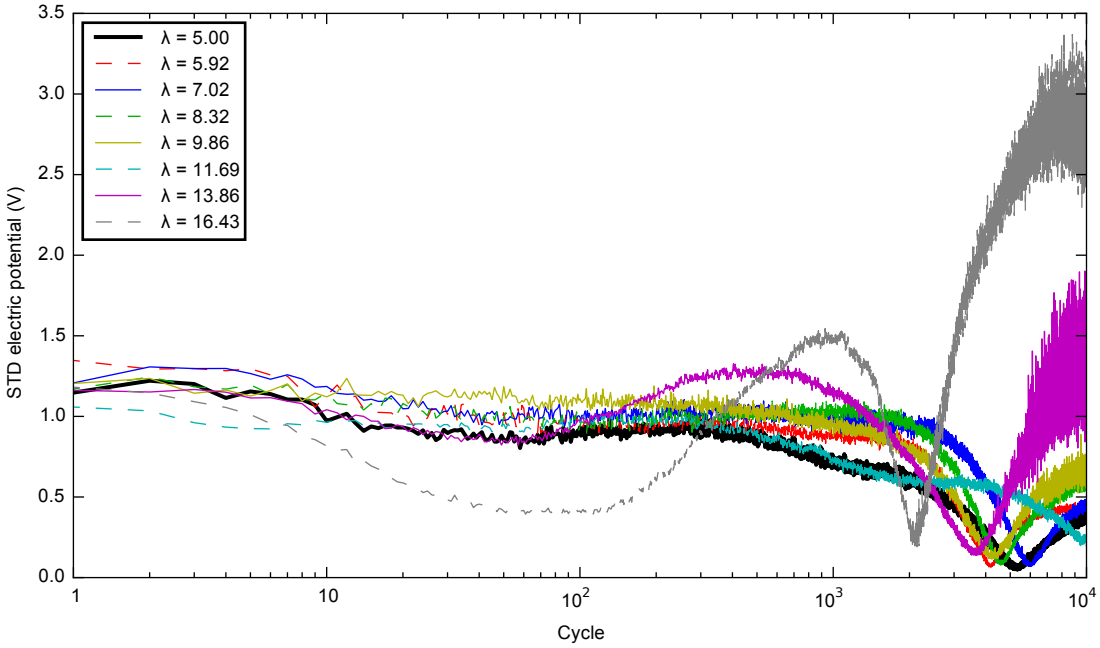

(b)

Figure 9.5: Standard deviation of the electric potential for each cycle for different λ of 750–1000 μm glass spheres shaken 10,000 cycles at $a = 2.08\,g$. The different values of λ are separated into two plots for clarity about the $\lambda = 5.00$ to match Figure 9.4. (a) The values below the threshold ($\lambda \leq 5.00$) with $\lambda = 5.00$ drawn as a thick black line. (b) The values above the threshold ($\lambda \geq 5.00$) with $\lambda = 5.00$ drawn as a thick black line

their highest value for $\lambda > 1.58$.

The dynamics in the electric potential are a bit different for the 610–990 μm polystyrene spheres shown in Figure 9.4, split into the λ less than and greater than the value at the local minimum ($\lambda = 5.00$) right before increasing rapidly at $\lambda \approx 10$. The electric potential by cycle is only shown for a subset of those with $\lambda < 5.00$ for visual clarity. Unlike the 10–325 μm polystyrene powder, there is less variability over time for λ below the threshold, and the electric potential stays approximately constant at a higher value (≈ 0.2 V compared to < 20 mV) from cycle to cycle or decays slowly. For all $\lambda > 5.00$, in addition to the magnitude of the electric potential increasing with increasing λ, there is a slow decay in the potential after possibly an initial increase until around cycle 3000 where, with increasing λ, it starts to become more constant and then increase for $\lambda \geq 9.87$.

The dynamics of the electric potential by cycle for 750–1000 μm glass spheres are shown in Figure 9.5, split into λ less than and greater than the same value as used for the 610–990 μm polystyrene spheres ($\lambda = 5.00$) for consistency, though that does appear to be where the rate of increase in the magnitude of the electrification with respect to λ begins to increase leading up to the threshold in Figure 9.2c. For all λ, the magnitude of the electric potential is initially decaying. Then, the magnitude dips towards zero as part of an inversion for most of them in the 1000–$10,000$ cycle range, some with a bump in the magnitude right before the inversion, before growing in magnitude after the inversion.

For these three particle types, there is significant time dependence even in the magnitude of the electrification over the duration of shaking ($10,000$ cycles).

This is the case even for λ smaller than the threshold, though for the 10–325 μm polystyrene powder, the whole time dependence seems to be a short lived transient bump. Given the time dependence seen in Figure 9.1, this suggests that the other particle types have significant time dependences for both $\lambda < 6$ and $\lambda > 6$ as well.

Chapter 10: GE: Two Particle Types Mixed Together

Partially adapted from and expanded upon the arXiv preprint

F. Nordsiek and D. P. Lathrop. Collective phenomena in granular and atmospheric electrification. *ArXiv e-prints*, Sept. 2015b.

arXiv: 1509.04214 [cond-mat.soft]

Some data has been deposited on DRUM at

F. Nordsiek and D. Lathrop. Collective phenomena in granular and atmospheric electrification. Dataset uploaded to Digital Repository at the University of Maryland (DRUM), July 2015a.

DOI: 10.13016/M2ZK87

URL: `http://hdl.handle.net/1903/16867`

10.1 Shape of The Electric Potential Profile over A Cycle

Extending the results of Chapter 9, we put two different particle types together. We restrict our investigations to all three sizes of only three materials (glass, ZrO_2:SiO_2, and polystyrene) making for a total of nine particle types. We used $\lambda = 3.0$ for each particle type except for 10–325 μm RMS effective diameter polystyrene powder, for which we used $\lambda = 5.7$ (we originally thought the powder had larger diameters). The shaking strength was fixed at $a = 2.08\,g$ (shaking frequency of 3.522 Hz). Every combination of two different particle types was done. In addition, single particle type runs were done with double the quantity ($\lambda = 10.4$ for 10–325 μm RMS effective diameter polystyrene powder, and $\lambda = 6.0$ for the others). This makes for a total of 45 combinations. The eight combinations with $\lambda = 6.0$ of a single particle type (excludes 10–325 μm diameter polystyrene powder) were taken from Chapter 9 (Nordsiek and Lathrop 2015a).

As was done for with the cell filled with only a single type of particle in Section 9.1, we show the cycle profiles of the potential across the cell for cycles 10, 100, 1000, and 3000 along with the cell's vertical position and where a particle from the simple kinematic model (Section 8.3.2) would hit and leave each plate. They are shown for each particle type, one by one, combined with more of itself and each other particle type in Figures 10.1, 10.2, 10.3, 10.4, 10.5, 10.6, 10.7, 10.8, and 10.9.

The shapes for the profiles are qualitatively similar, whether the cell was filled with one particle type, two particle types of the same material, two particle types having a similar size, or two particle types having different materials and dissimilar

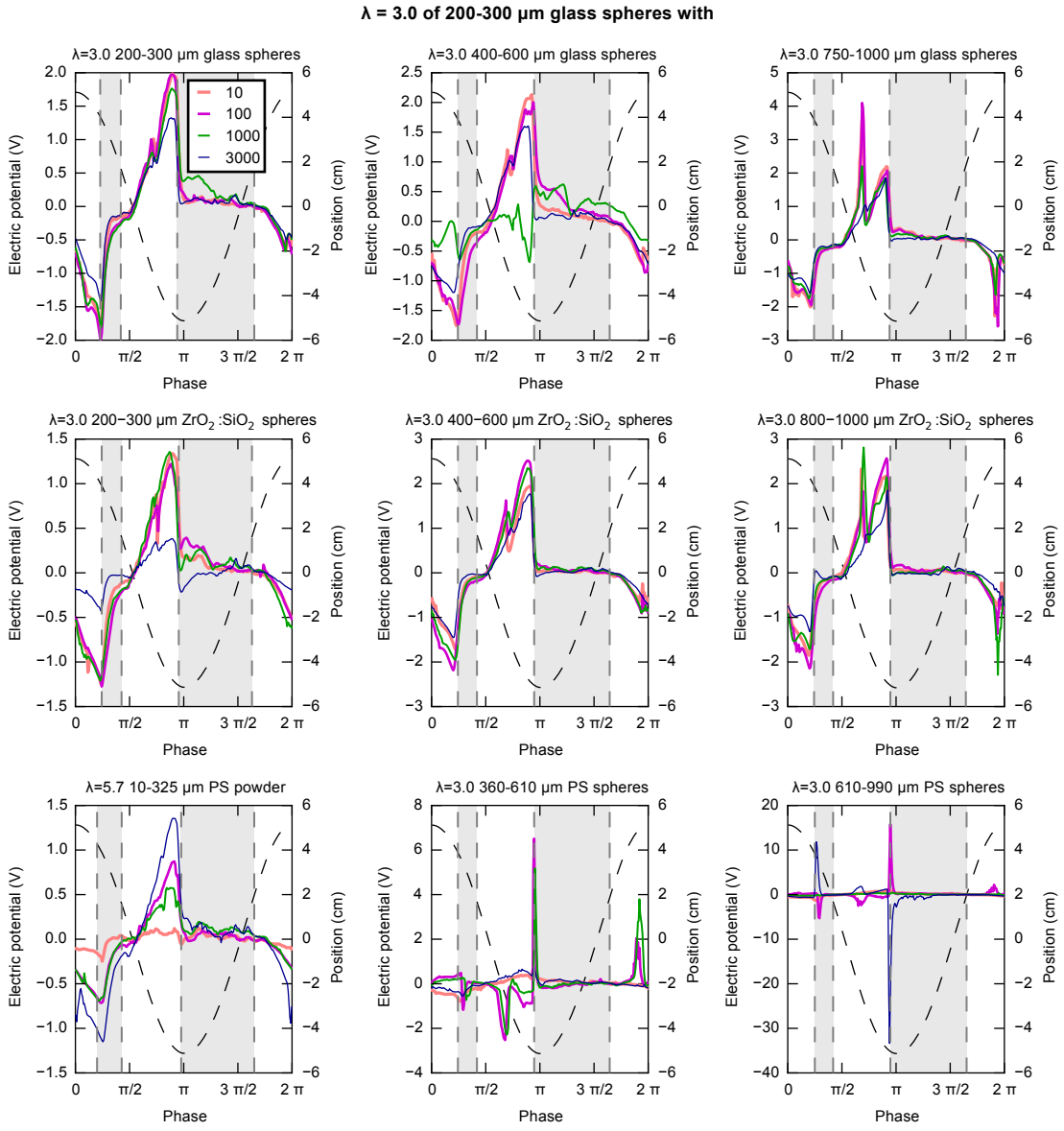

Figure 10.1: Signal profiles during the shaking cycle for $\lambda = 3.0$ of 200–300 μm glass spheres mixed with $\lambda = 3.0$, 5.7 of each particle type (figure titles). The cell vertical position (black dashed line) and electric potential for cycles 10, 100, 1000, and 3000 are shown by phase (legend in top-left figure) are shown by phase in the shaking cycle for particles shaken 5000 cycles with $a = 2.08\,g$. A particle in the kinematic model is on either plate in the grey regions, and the dashed vertical lines, from left to right, are when it hits the top plate, leaves the top plate, hits the bottom plate, and leaves the bottom plate respectively. Polystyrene is abbreviated as PS.

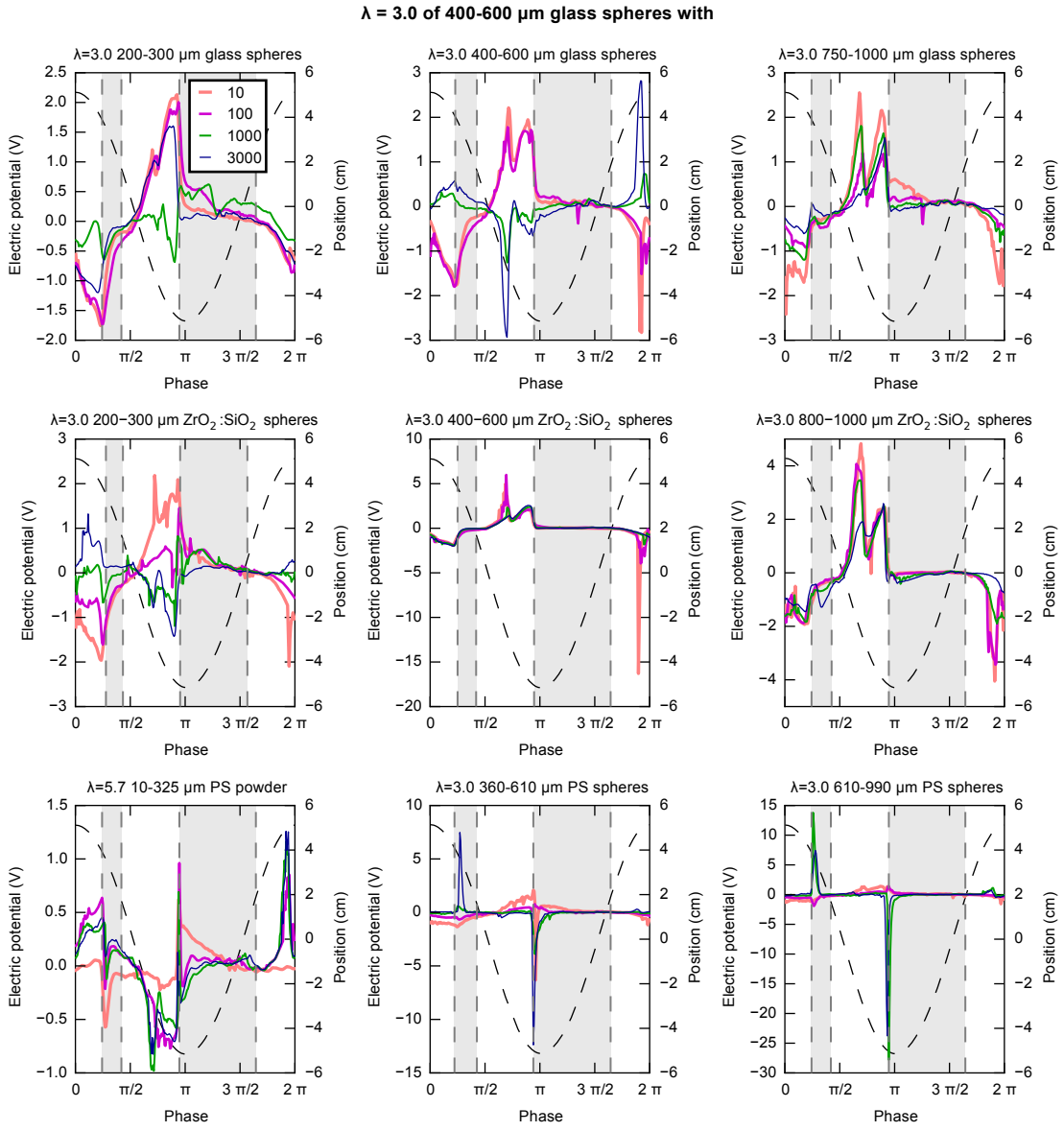

Figure 10.2: Signal profiles during the shaking cycle for $\lambda = 3.0$ of 400–600 μm glass spheres mixed with $\lambda = 3.0$, 5.7 of each particle type (figure titles). The cell vertical position (black dashed line) and electric potential for cycles 10, 100, 1000, and 3000 are shown by phase (legend in top-left figure) are shown by phase in the shaking cycle for particles shaken 5000 cycles with $a = 2.08\,g$. A particle in the kinematic model is on either plate in the grey regions, and the dashed vertical lines, from left to right, are when it hits the top plate, leaves the top plate, hits the bottom plate, and leaves the bottom plate respectively. Polystyrene is abbreviated as PS.

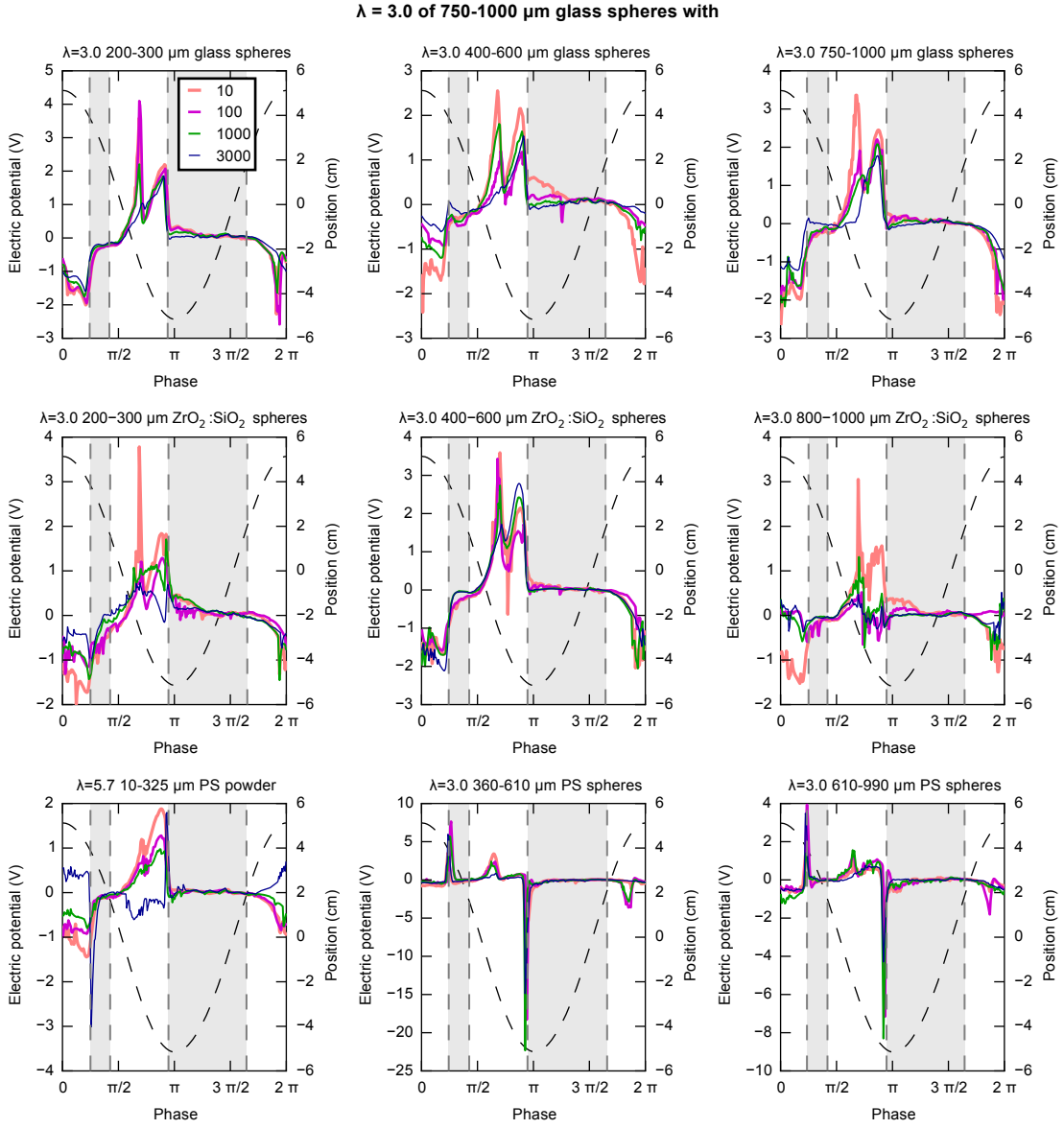

Figure 10.3: Signal profiles during the shaking cycle for $\lambda = 3.0$ of 750–1000 μm glass spheres mixed with $\lambda = 3.0$, 5.7 of each particle type (figure titles). The cell vertical position (black dashed line) and electric potential for cycles 10, 100, 1000, and 3000 are shown by phase (legend in top-left figure) are shown by phase in the shaking cycle for particles shaken 5000 cycles with $a = 2.08\,g$. A particle in the kinematic model is on either plate in the grey regions, and the dashed vertical lines, from left to right, are when it hits the top plate, leaves the top plate, hits the bottom plate, and leaves the bottom plate respectively. Polystyrene is abbreviated as PS.

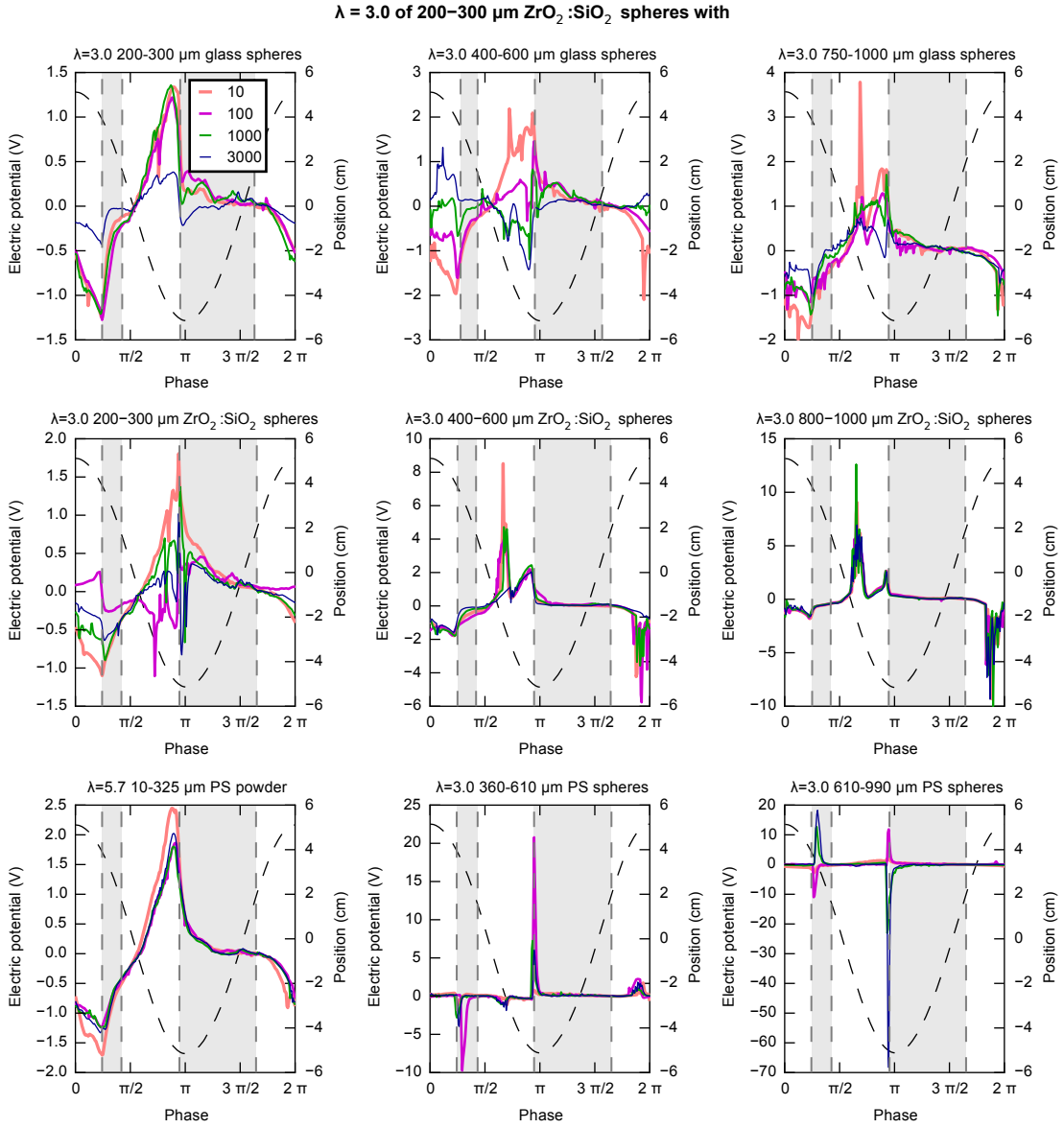

Figure 10.4: Signal profiles during the shaking cycle for $\lambda = 3.0$ of 200–300 μm ZrO_2:SiO_2 spheres mixed with $\lambda = 3.0$, 5.7 of each particle type (figure titles). The cell vertical position (black dashed line) and electric potential for cycles 10, 100, 1000, and 3000 are shown by phase (legend in top-left figure) are shown by phase in the shaking cycle for particles shaken 5000 cycles with $a = 2.08\,g$. A particle in the kinematic model is on either plate in the grey regions, and the dashed vertical lines, from left to right, are when it hits the top plate, leaves the top plate, hits the bottom plate, and leaves the bottom plate respectively. Polystyrene is abbreviated as PS.

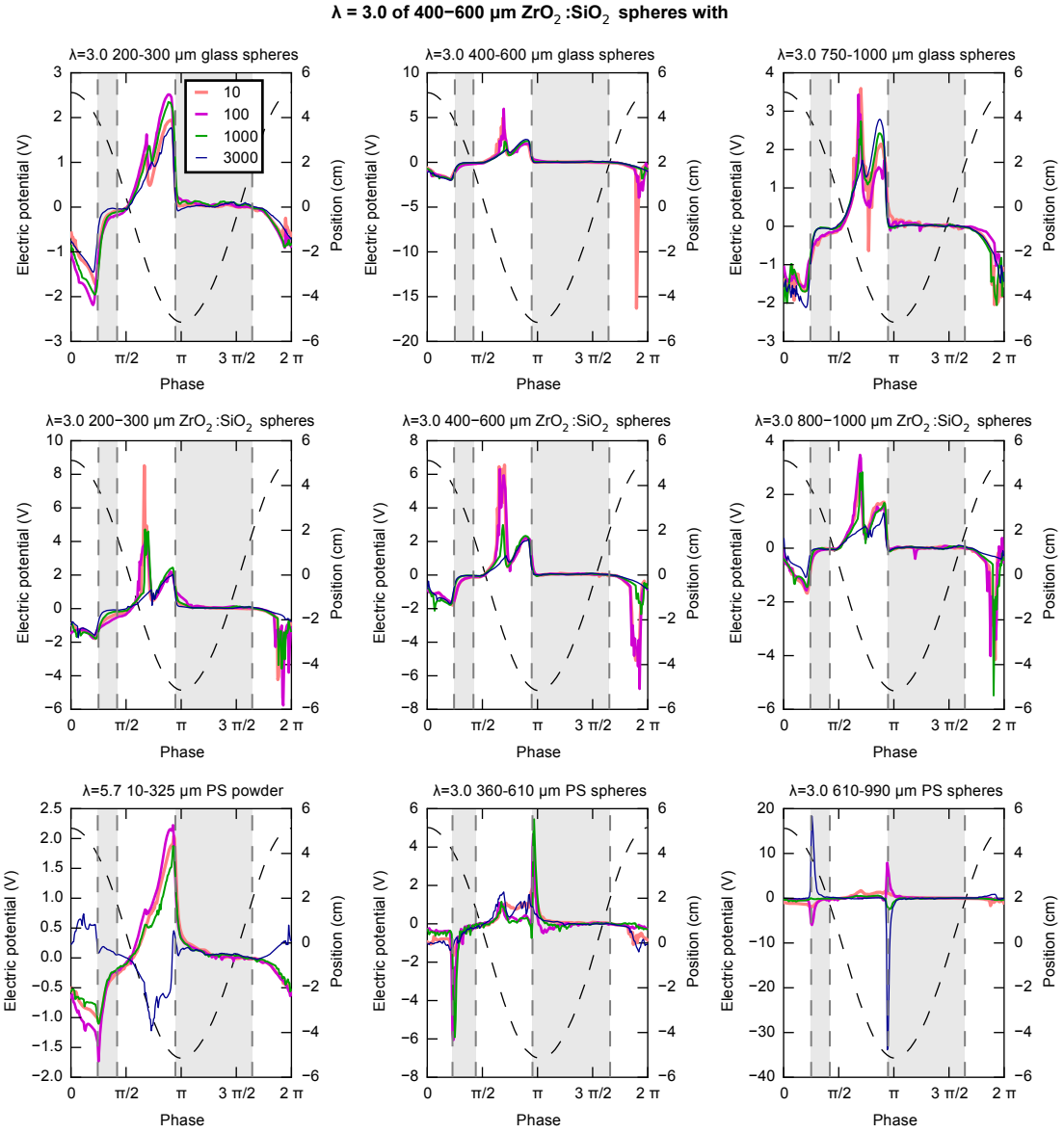

Figure 10.5: Signal profiles during the shaking cycle for $\lambda = 3.0$ of 400–600 μm ZrO_2:SiO_2 spheres mixed with $\lambda = 3.0$, 5.7 of each particle type (figure titles). The cell vertical position (black dashed line) and electric potential for cycles 10, 100, 1000, and 3000 are shown by phase (legend in top-left figure) are shown by phase in the shaking cycle for particles shaken 5000 cycles with $a = 2.08\,g$. A particle in the kinematic model is on either plate in the grey regions, and the dashed vertical lines, from left to right, are when it hits the top plate, leaves the top plate, hits the bottom plate, and leaves the bottom plate respectively. Polystyrene is abbreviated as PS.

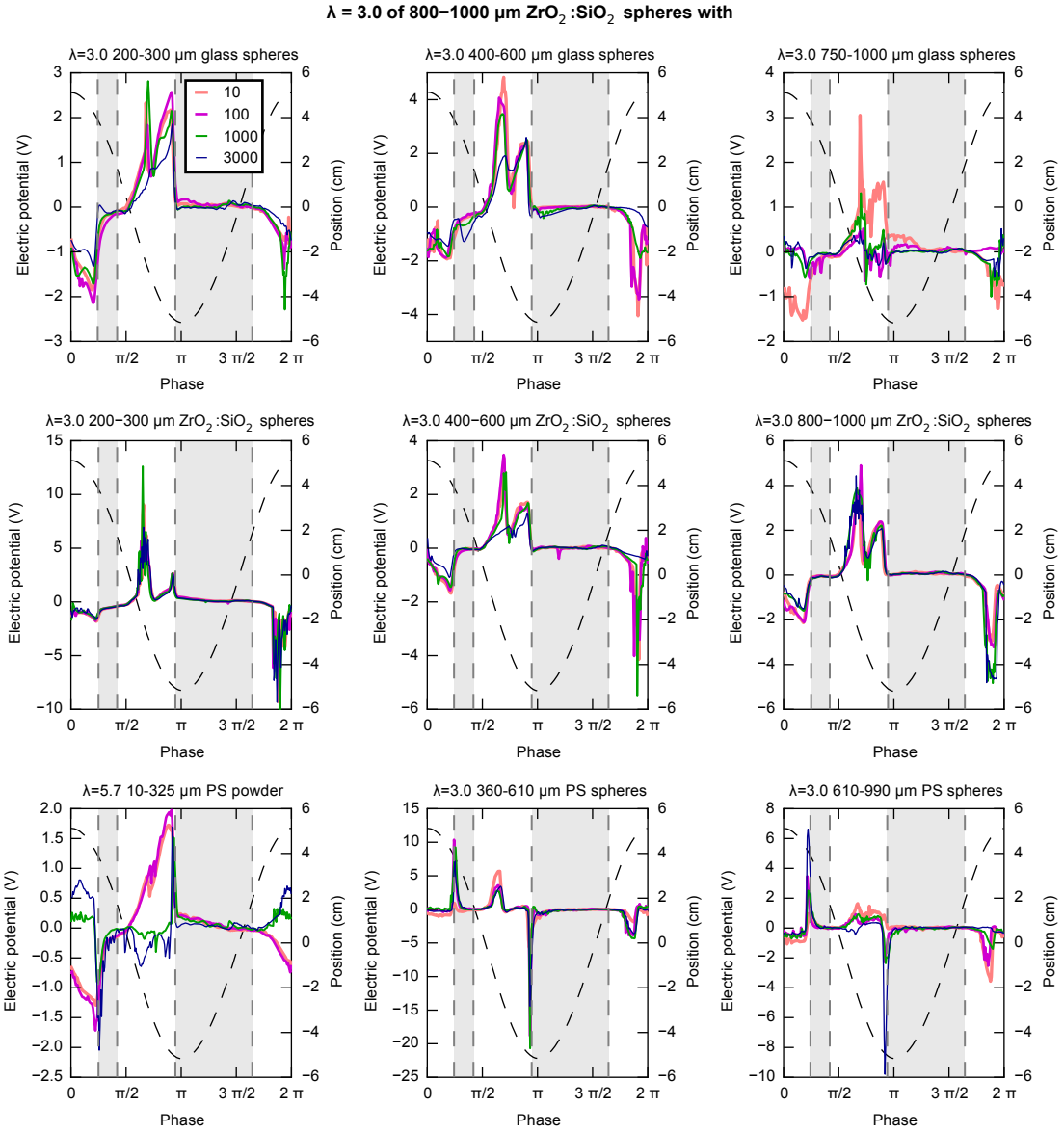

Figure 10.6: Signal profiles during the shaking cycle for $\lambda = 3.0$ of 800–1000 μm ZrO_2:SiO_2 spheres mixed with $\lambda = 3.0$, 5.7 of each particle type (figure titles). The cell vertical position (black dashed line) and electric potential for cycles 10, 100, 1000, and 3000 are shown by phase (legend in top-left figure) are shown by phase in the shaking cycle for particles shaken 5000 cycles with $a = 2.08\,g$. A particle in the kinematic model is on either plate in the grey regions, and the dashed vertical lines, from left to right, are when it hits the top plate, leaves the top plate, hits the bottom plate, and leaves the bottom plate respectively. Polystyrene is abbreviated as PS.

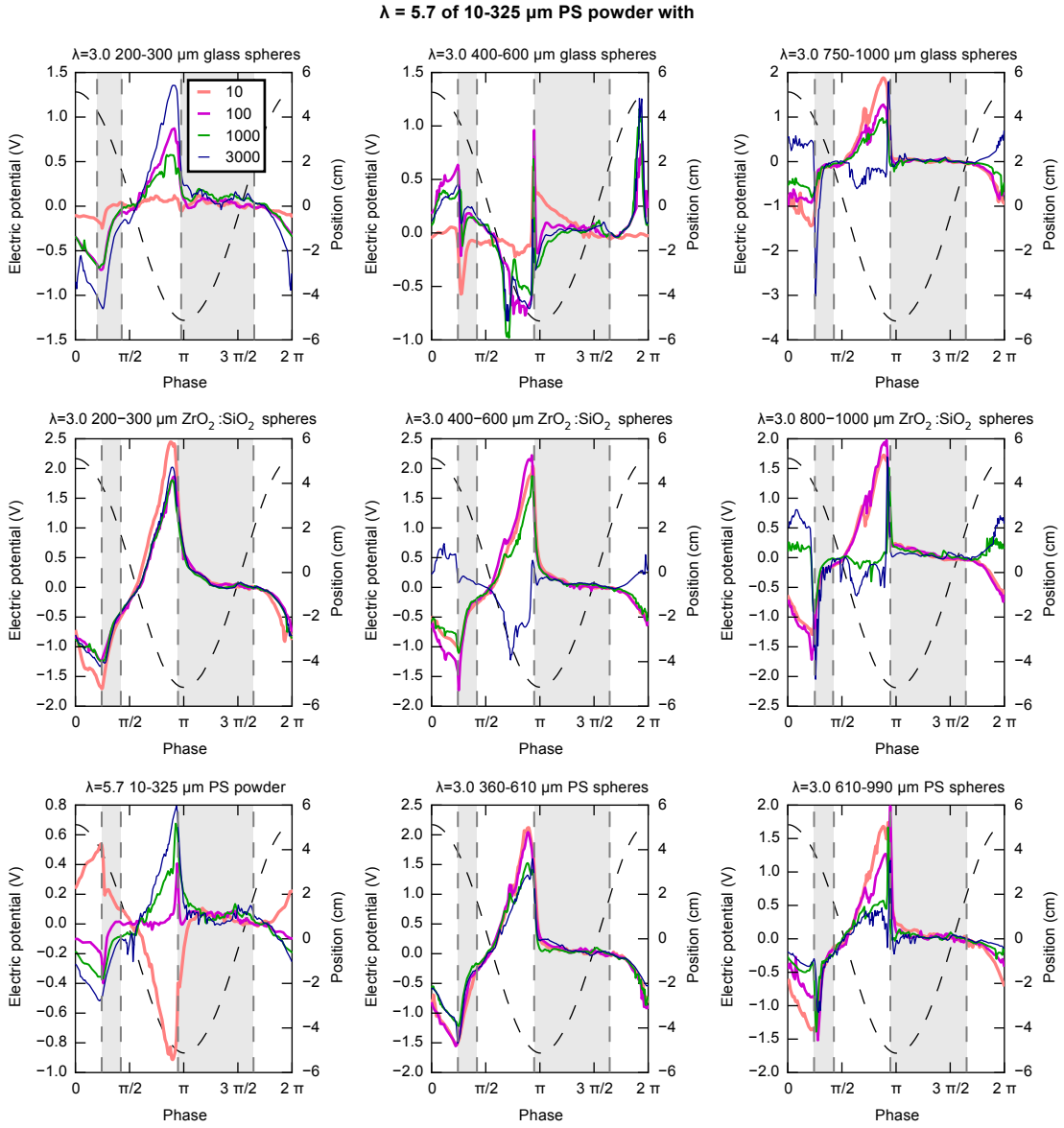

Figure 10.7: Signal profiles during the shaking cycle for $\lambda = 5.7$ of 10–325 μm polystyrene (PS) powder mixed with $\lambda = 3.0$, 5.7 of each particle type (figure titles). The cell vertical position (black dashed line) and electric potential for cycles 10, 100, 1000, and 3000 are shown by phase (legend in top-left figure) are shown by phase in the shaking cycle for particles shaken 5000 cycles with $a = 2.08\,g$. A particle in the kinematic model is on either plate in the grey regions, and the dashed vertical lines, from left to right, are when it hits the top plate, leaves the top plate, hits the bottom plate, and leaves the bottom plate respectively. Polystyrene is abbreviated as PS.

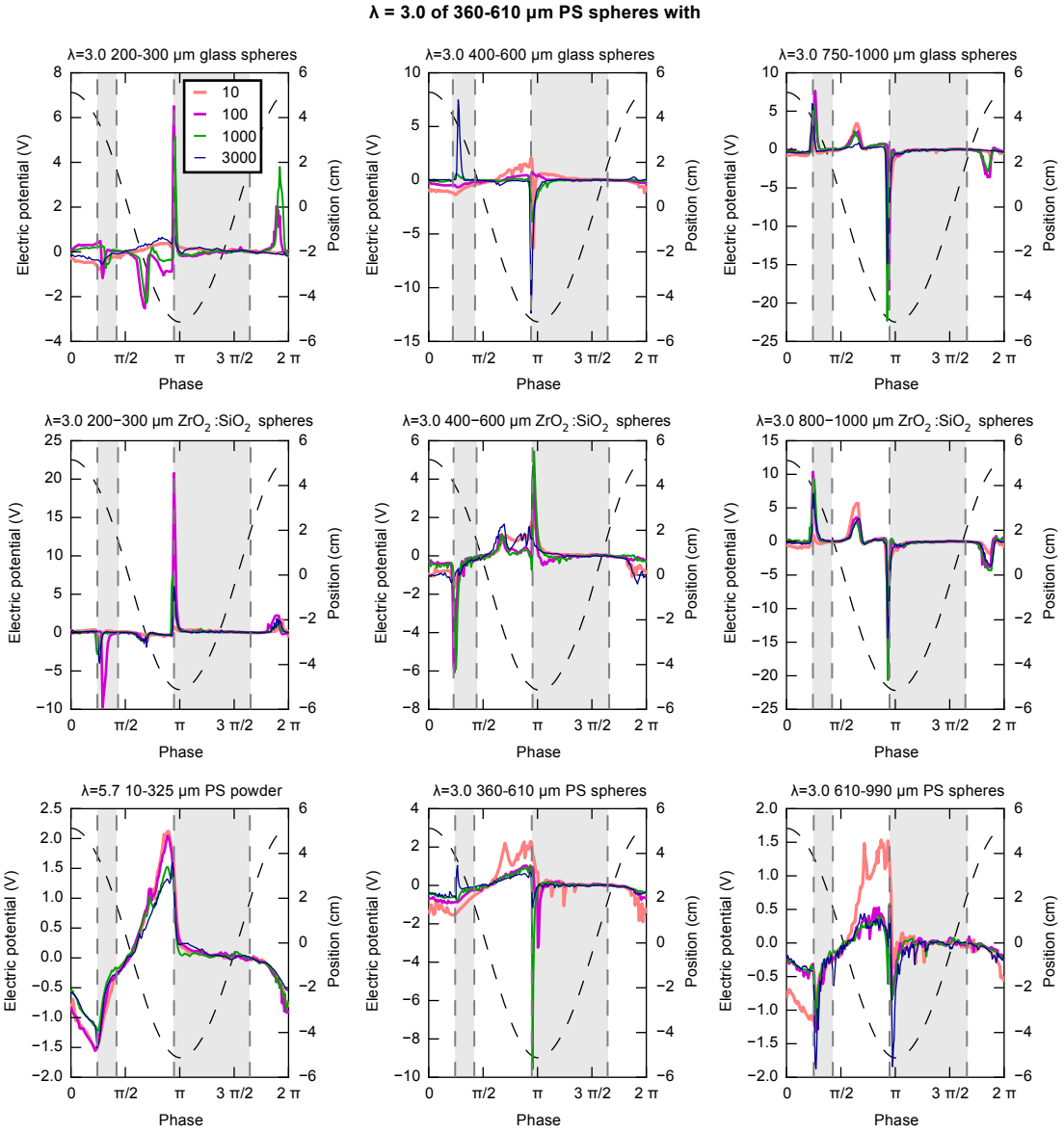

Figure 10.8: Signal profiles during the shaking cycle for $\lambda = 3.0$ of 360–610 μm polystyrene (PS) spheres mixed with $\lambda = 3.0$, 5.7 of each particle type (figure titles). The cell vertical position (black dashed line) and electric potential for cycles 10, 100, 1000, and 3000 are shown by phase (legend in top-left figure) are shown by phase in the shaking cycle for particles shaken 5000 cycles with $a = 2.08\,g$. A particle in the kinematic model is on either plate in the grey regions, and the dashed vertical lines, from left to right, are when it hits the top plate, leaves the top plate, hits the bottom plate, and leaves the bottom plate respectively. Polystyrene is abbreviated as PS.

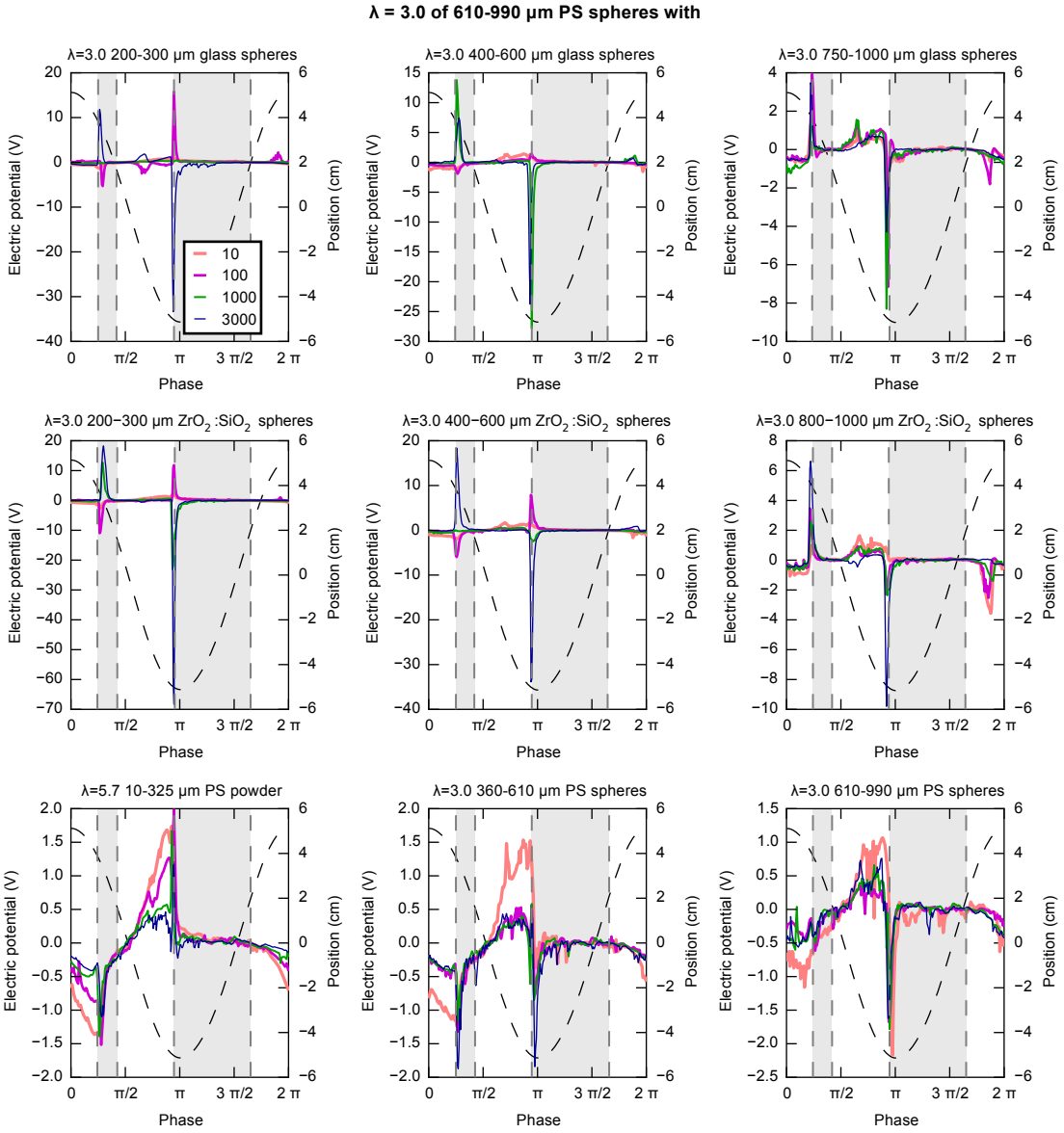

Figure 10.9: Signal profiles during the shaking cycle for $\lambda = 3.0$ of 610–990 μm polystyrene (PS) spheres mixed with $\lambda = 3.0$, 5.7 of each particle type (figure titles). The cell vertical position (black dashed line) and electric potential for cycles 10, 100, 1000, and 3000 are shown by phase (legend in top-left figure) are shown by phase in the shaking cycle for particles shaken 5000 cycles with $a = 2.08\,g$. A particle in the kinematic model is on either plate in the grey regions, and the dashed vertical lines, from left to right, are when it hits the top plate, leaves the top plate, hits the bottom plate, and leaves the bottom plate respectively. Polystyrene is abbreviated as PS.

sizes. The qualitative patterns for the shaking of a single type of particle (Figure 9.1) in Section 9.1 apply, and are reproduced below.

1. The electric potential trends towards zero while the particles are in contact with either plate (grey shaded regions).

2. The profiles show an extremum in the potential right before hitting the top plate.

3. The profiles show another extremum of the opposite sign before particles hit the bottom plate, with a decay towards zero potential afterwards that is usually quicker.

4. There is often an extremum when the particles are in mid-flight after leaving the top plate before they hit the bottom plate.

5. Less often, there is an extremum when the particles are in mid-flight before they reach the top plate after leaving the bottom plate.

However, the qualitative similarity between the profiles is lower than between the profiles for single particle type only. Namely, there is one group of particle type combinations which has noticeably different profiles. They are the combinations of 360–610 μm or 610–990 μm polystyrene (PS) spheres with non-polystyrene particles, which is seen in the differences from Figures 10.8 and 10.9 to Figures 10.1, 10.2, 10.3, 10.4, 10.5, 10.6, and 10.7. The measured potentials are often much larger, with the scale (left vertical) exceeding $\pm$10 V for many combinations. With the extrema in the potential right before the particles hit the plate, the potential changes sign

very quickly when very close to the plate producing a much stronger extremum of the opposite sign before the potential decays towards zero. While these short opposite extrema are found for some of the other particle type combinations, almost all combinations with 360–610 μm and 610–990 μm polystyrene spheres have them and they are much larger in magnitude. Some of these opposite extrema are large enough to be clipped by the acquisition system, such as the combination of $\lambda = 3.0$ of 610–990 μm polystyrene spheres with $\lambda = 3.0$ of 200–300 μm ZrO_2:SiO_2 spheres (center-left plot in Figure 10.9).

10.2 Clumping of Polystyrene Spheres with Glass and ZrO_2:SiO_2

The differences in the profiles for combinations of 360–610 μm or 610–990 μm polystyrene spheres with non-polystyrene particles suggests that there must be some difference in the granular flow and/or electrical dynamics between the particle types. Compared to the other types of particles in the form of spheres, the 360–610 μm or 610–990 μm polystyrene spheres tend to stick to other particles and the cell plates. When shaken with the glass and ZrO_2:SiO_2 spheres, the particles stick together in clumps. Figure 10.10 shows pictures of the clumping for one such combination after being shaken $30,000$ cycles, specifically the one that produced the largest magnitudes of the electric potential (610–990 μm polystyrene spheres and 200–300 μm ZrO_2:SiO_2 spheres). The larger particles in a combination with a number of small particles stuck to them superficially look like a molecule between a big non-metal atom and several small non-metals. This clumping is likely related to the experimen-

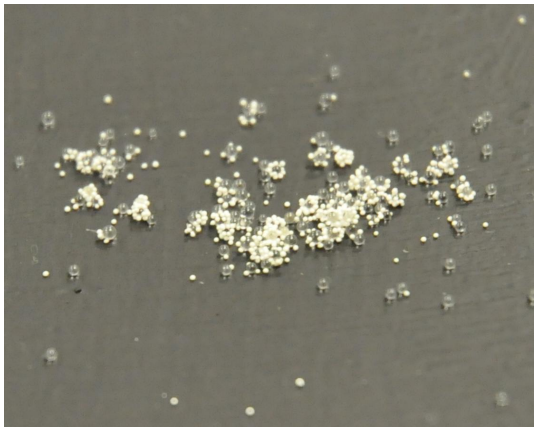

(a)

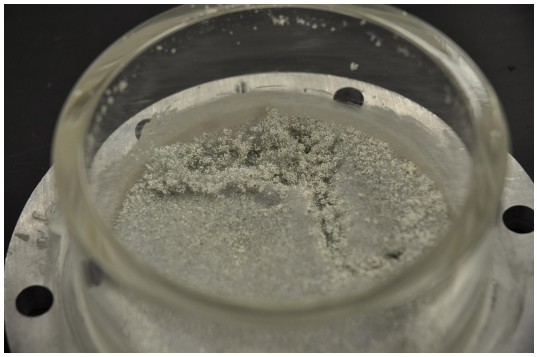

(b)

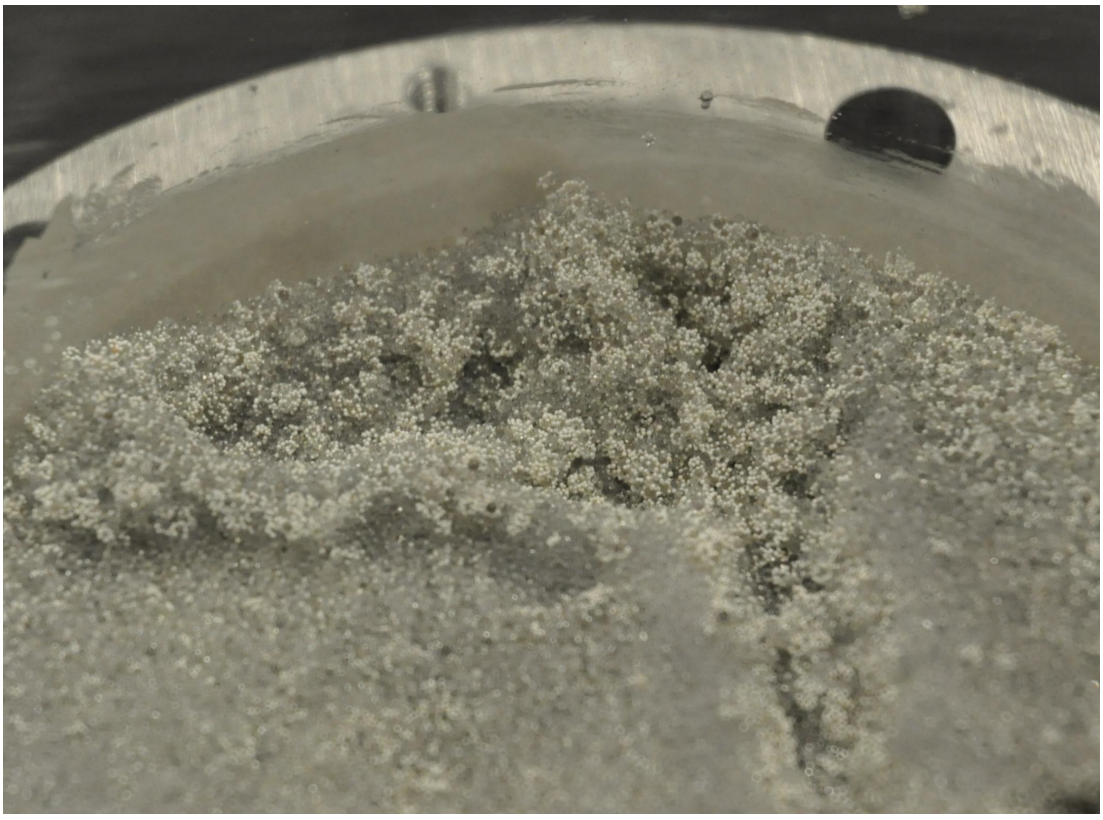

(c)

Figure 10.10: Pictures of 610–990 μm polystyrene spheres and 200–300 μm ZrO_2:SiO_2 spheres (both $\lambda = 3.0$) sticking together after being shaken together for 30,000 cycles at $a = 2.08\,g$. The polystyrene spheres are transparent while the ZrO_2:SiO_2 spheres are opaque and yellow-white in color. (a) small sample of particles scooped out of the cell and set on a surface. (b) particle slab resting in the bottom of the cell after part of the slab was dug up and overturned with a scoop. (c) expansion of (b) about the dug up and overturned region.

tal clustering of ZrO_2:SiO_2 particles (from the same manufacturer, GlenMills) into molecule shaped structures found by Lee et al. (2015). These polystyrene with glass or ZrO_2:SiO_2 particle clumps stayed together to some degree even when scooped out. From the videos, the clusters found by Lee et al. (2015) were comparatively fragile to our clumps. This suggests that the forces holding our clumps together are considerably stronger than those holding ZrO_2:SiO_2 particles together. This explains why we didn't see noticeable clumping when the cell was filled only with ZrO_2:SiO_2 particles.

It is reasonable to expect that the motion of clumps of particles and individual non-clumped particles would be different, rather than the clumps merely acting as larger non-spherical particles since there can be motion within the clump and clumps can form and break. Due to this different motion, it makes sense that the combinations that form clumps would have different dynamics in the electrification, and therefore different dynamics in the measured electric potential like we see.

10.3 Time Evolution of The Electric Potential

It is useful to consider both the magnitude of the electric potential from cycle to cycle and its polarity (whether it is in-phase or out-of-phase with the position oscillation). The magnitude is defined as the standard deviation of the electric potential over the cycle as was done in Figures 9.3, 9.4, and 9.5. As for getting the polarity, a straightforward way is to take the electric potential over a cycle and and integrate its sign at each phase ($+1$ if positive, -1 if negative, 0 if zero) with a

kernel chosen to make the integral give the polarity. If we let $U_n(\phi_i)$ be the electric potential for the n'th cycle as a function of the phases of the bins ϕ_i, then we define our measure of the polarity value of the n'th cycle as

$$P_n = \sum_i K_i \text{ sign}\left[U_n(\phi_i)\right] \tag{10.1}$$

where K_i is the polarity kernel.

A useful feature of oscillation is that the period where the kinematic model particle (Section 8.3.2) is in flight between the two plates after leaving the bottom plate before hitting the top plate corresponds to positive position and the part where it is in flight after leaving the top plate before hitting the bottom plate corresponds to negative position. At the same time, the electric potential tends towards zero when the particles are against the plate. A simple kernel would then be

$$K_i = \begin{cases} (N_{b\to t})^{-1} & \text{in flight from bottom plate to top plate} \\ 0 & \text{on either plate} \\ -(N_{t\to b})^{-1} & \text{in flight from top plate to bottom plate} \end{cases} \tag{10.2}$$

where $N_{b\to t}$ and $N_{t\to b}$ are the total number of phases (ϕ_i) for that value of K_i — the number of phases in flight from bottom to top plate and from top to bottom plate respectively. These two constants serve to make the positive and negative parts of K_i have equal weight, normalizing it so that $\sum_i K_i = 0$. The polarity kernel for a typical $a = 2.08\,g$ run is shown in Figure 10.11.

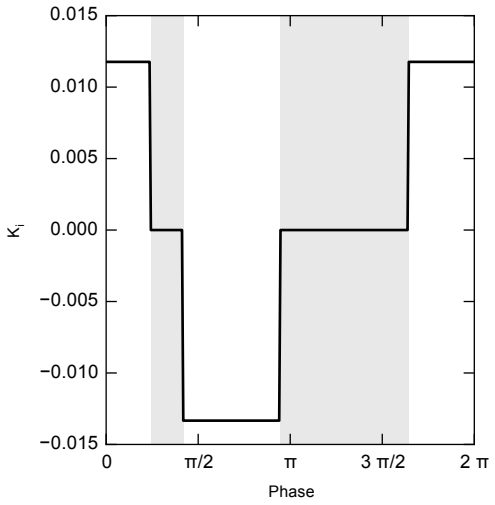

Figure 10.11: The polarity kernel K_i (Equation 10.11) as a function of phase. The shaded regions are where the kinematic model particle (Section 8.3.2) is touching one of the plates. The discontinuities in K_i from left to right are where the model particle hits the top plate, leaves the top plate, hits the bottom plate, and leaves the bottom plate.

With this definition of K_i, $P_n > 0$ indicates that the electric potential across the plates is in-phase with the position oscillation, and $P_n < 0$ indicates that it is out-of-phase. Inversions then are where P_n crosses zero.

Timeseries of the electrification magnitude and polarity value (P) for each cycle are shown for each particle type, one by one, by itself and combined with each other particle type in Figures 10.19 and 10.20 to Figures 10.12, 10.13, 10.14, 10.15, 10.16, 10.17, and 10.18. The magnitudes and polarity values are shown together (top and bottom panels respectively) for clarity.

As was the case with the electric potential magnitudes for different single particle type runs with different λ in Figures 9.3 and 9.5 (and to a lesser degree, Figure 9.4), most particle type combinations do not have constant electric potential magnitudes with time, and instead vary over large time scales of 100's and 1000's

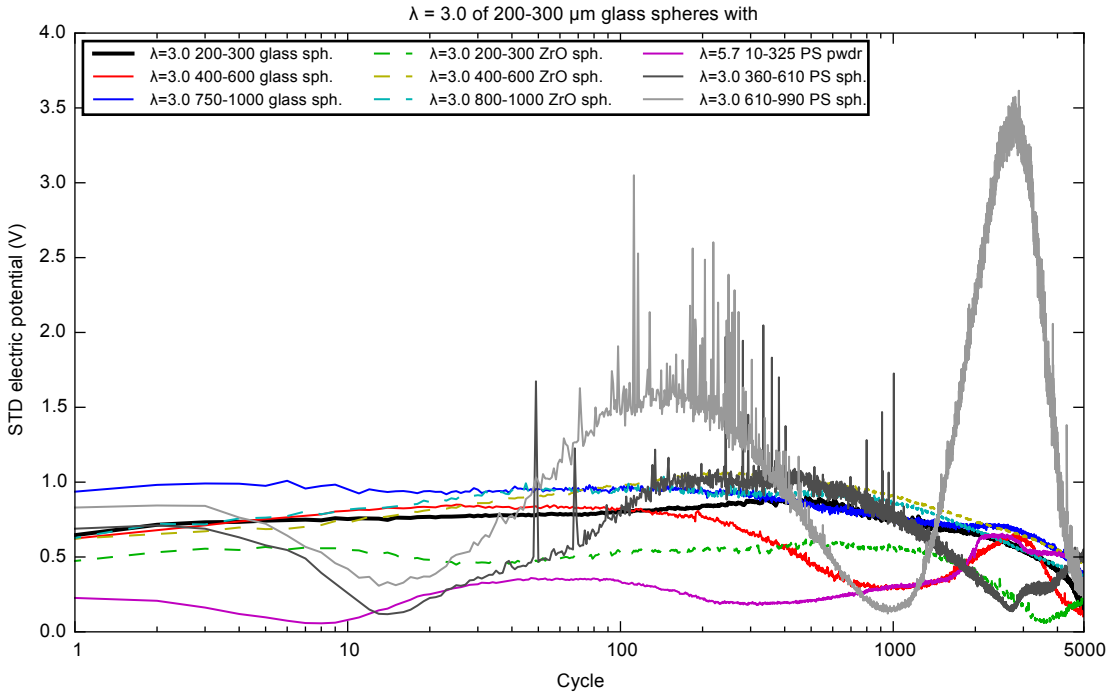

(a)

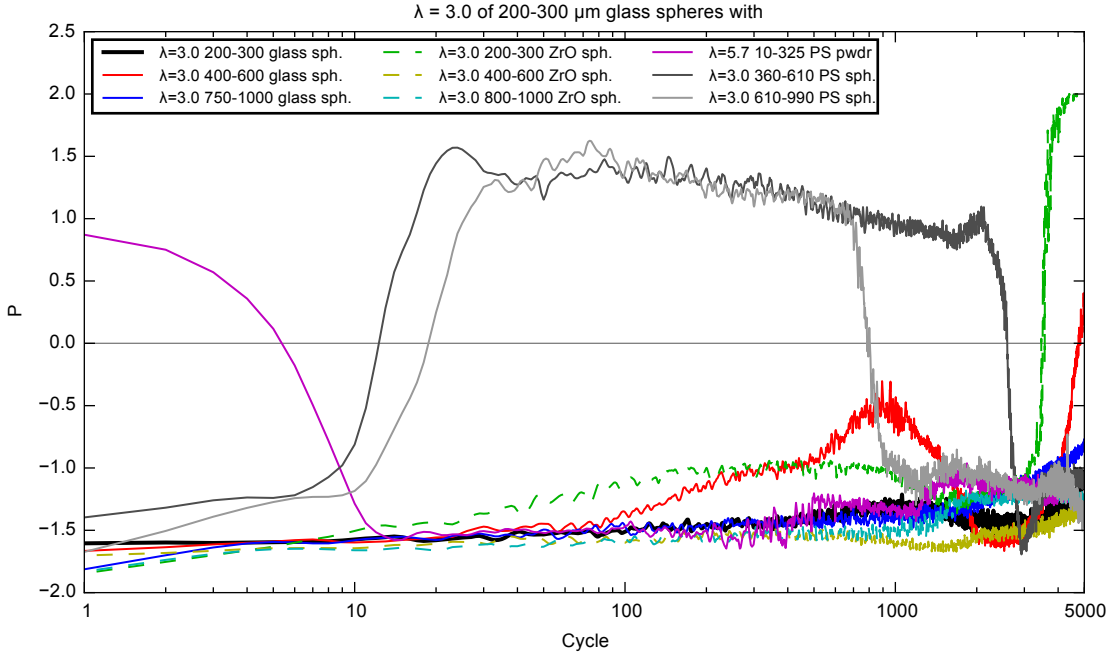

(b)

Figure 10.12: The magnitude and polarity value of the electric potential for each cycle for $\lambda = 3.0$ of 200–300 μm glass spheres mixed with $\lambda = 3.0$, 5.7 of each particle type (legend). The particles were shaken 5000 cycles at $a = 2.08\,g$. Polystyrene and ZrO_2:SiO_2 were abbreviated as PS and ZrO respectively. (a) The magnitude of each cycle, which is quantified by the standard deviation of the electric potential over the cycle. (b) The polarity value of each cycle P (Equation 10.1).

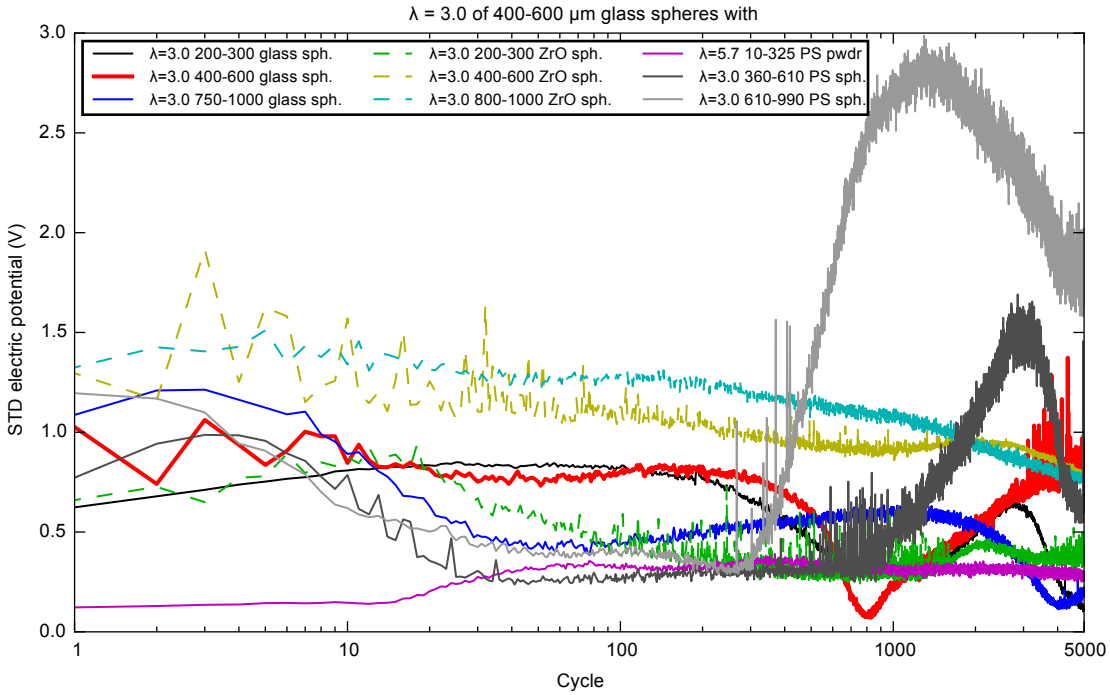

(a)

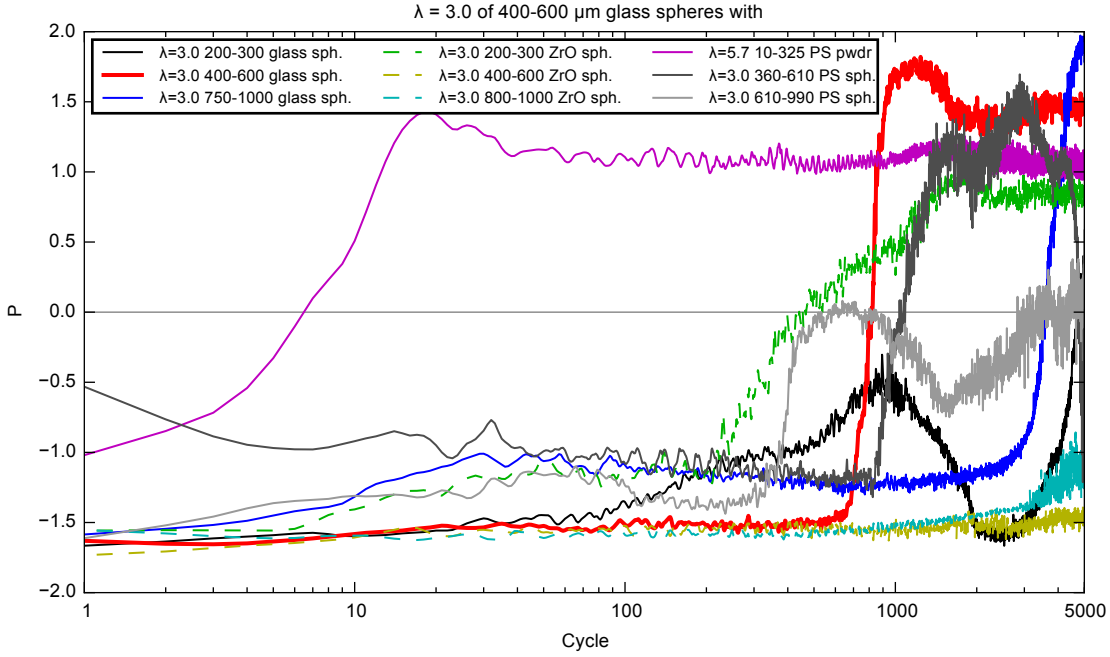

(b)

Figure 10.13: The magnitude and polarity value of the electric potential for each cycle for $\lambda = 3.0$ of 400–600 μm glass spheres mixed with $\lambda = 3.0$, 5.7 of each particle type (legend). The particles were shaken 5000 cycles at $a = 2.08\,g$. Polystyrene and ZrO_2:SiO_2 were abbreviated as PS and ZrO respectively. (a) The magnitude of each cycle, which is quantified by the standard deviation of the electric potential over the cycle. (b) The polarity value of each cycle P (Equation 10.1).

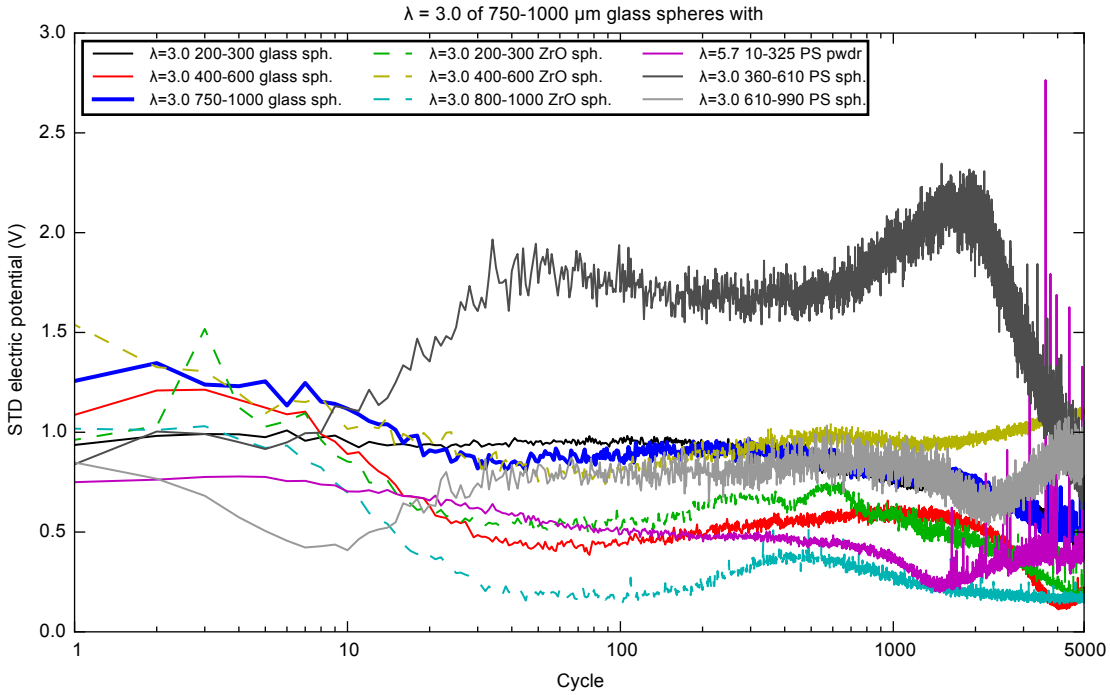

(a)

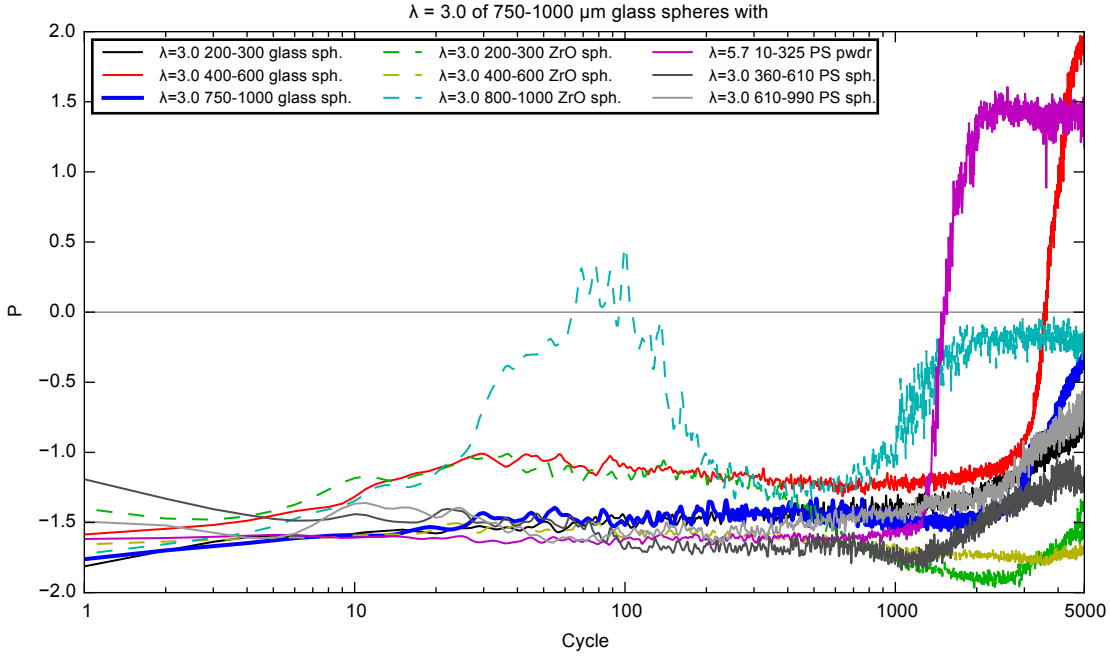

(b)

Figure 10.14: The magnitude and polarity value of the electric potential for each cycle for $\lambda = 3.0$ of 750–1000 μm glass spheres mixed with $\lambda = 3.0$, 5.7 of each particle type (legend). The particles were shaken 5000 cycles at $a = 2.08\,g$. Polystyrene and ZrO_2:SiO_2 were abbreviated as PS and ZrO respectively. (a) The magnitude of each cycle, which is quantified by the standard deviation of the electric potential over the cycle. (b) The polarity value of each cycle P (Equation 10.1).

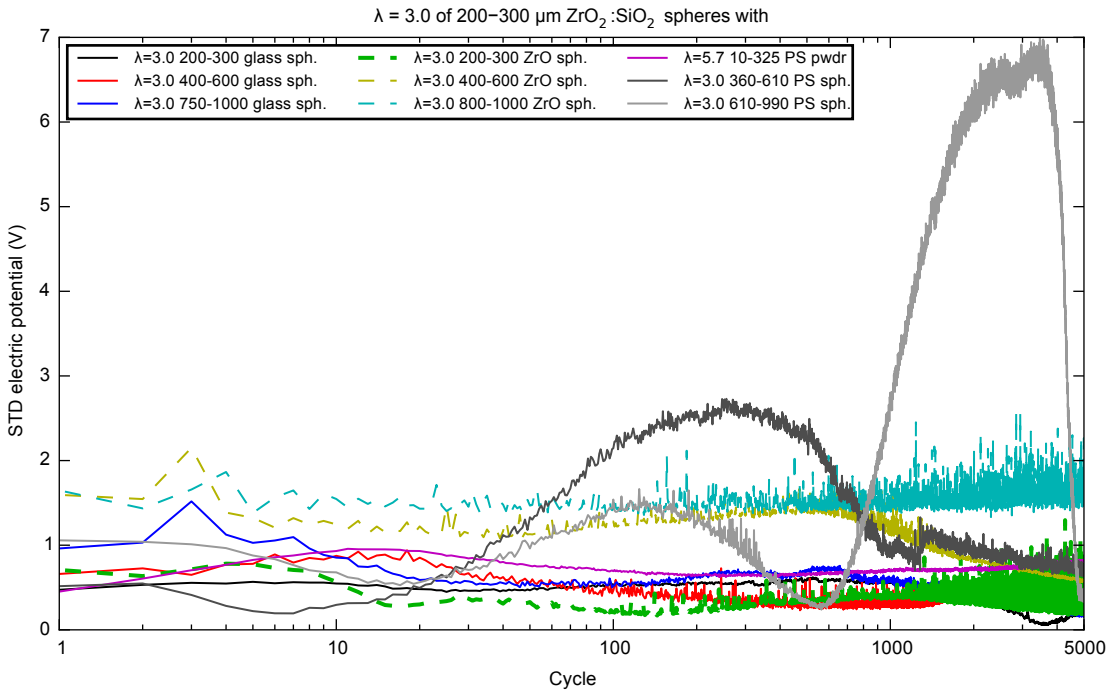

(a)

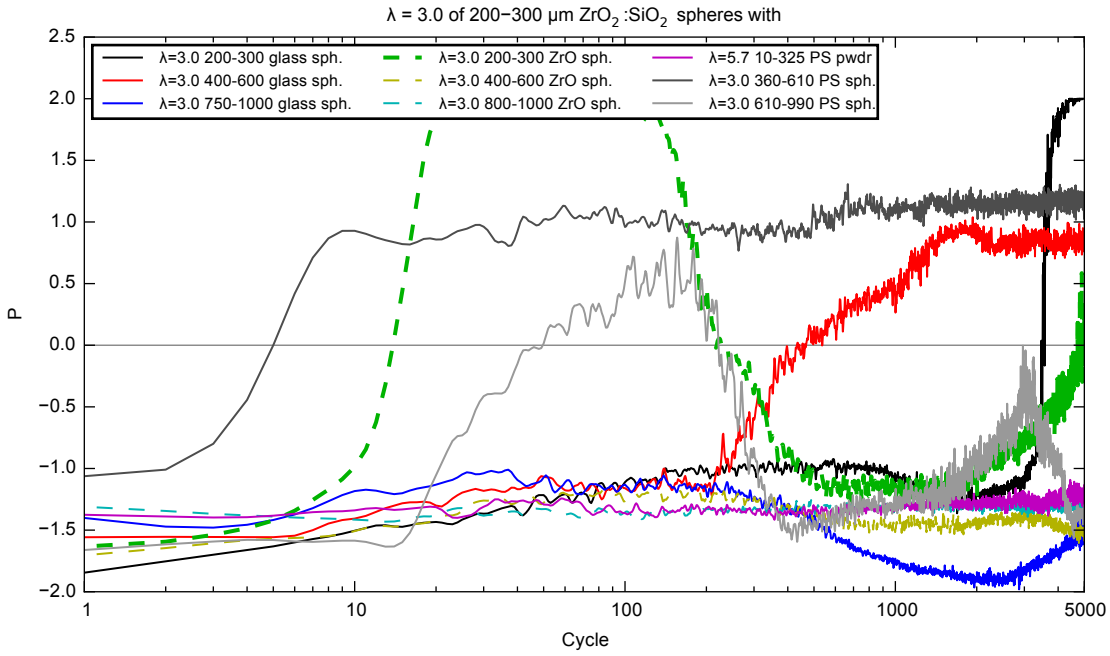

(b)

Figure 10.15: The magnitude and polarity value of the electric potential for each cycle for $\lambda = 3.0$ of 200–300 μm ZrO_2:SiO_2 spheres mixed with $\lambda = 3.0, 5.7$ of each particle type (legend). The particles were shaken 5000 cycles at $a = 2.08\,g$. Polystyrene and ZrO_2:SiO_2 were abbreviated as PS and ZrO respectively. (a) The magnitude of each cycle, which is quantified by the standard deviation of the electric potential over the cycle. (b) The polarity value of each cycle P (Equation 10.1).

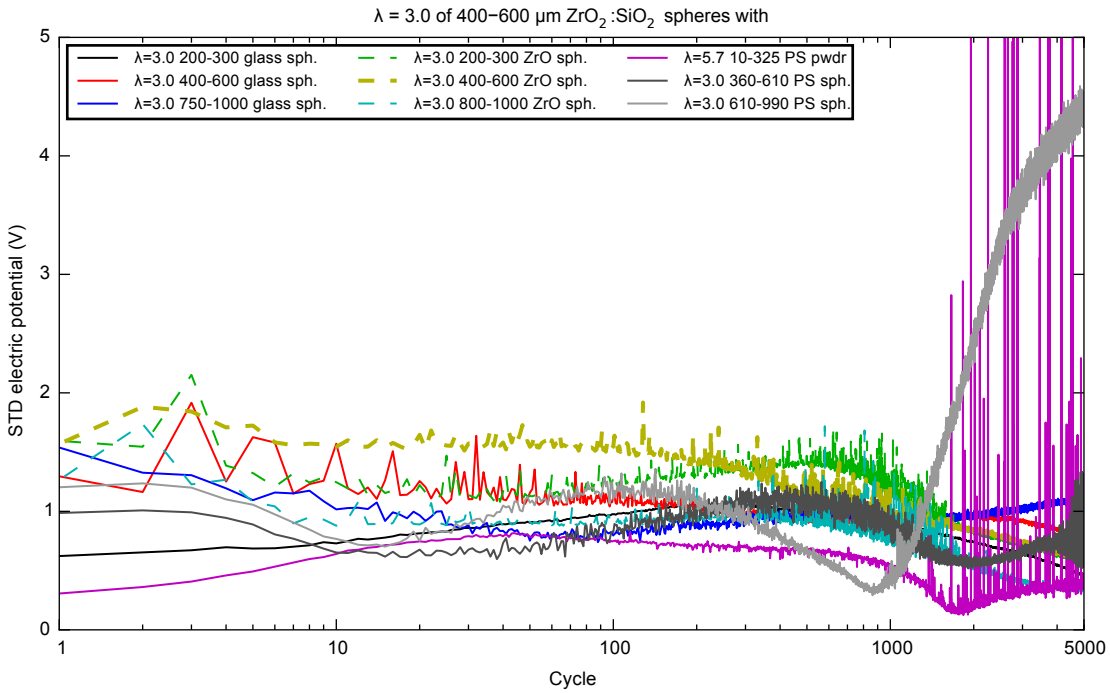

(a)

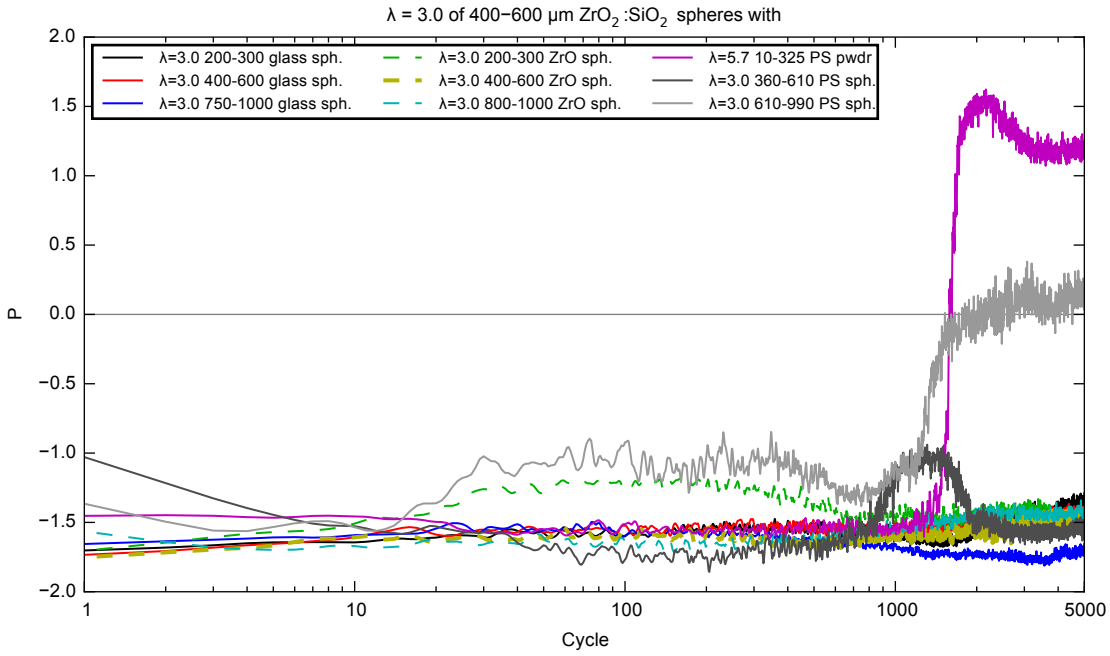

(b)

Figure 10.16: The magnitude and polarity value of the electric potential for each cycle for $\lambda = 3.0$ of 400–600 μm ZrO_2:SiO_2 spheres mixed with $\lambda = 3.0, 5.7$ of each particle type (legend). The particles were shaken 5000 cycles at $a = 2.08\,g$. Polystyrene and ZrO_2:SiO_2 were abbreviated as PS and ZrO respectively. (a) The magnitude of each cycle, which is quantified by the standard deviation of the electric potential over the cycle. (b) The polarity value of each cycle P (Equation 10.1).

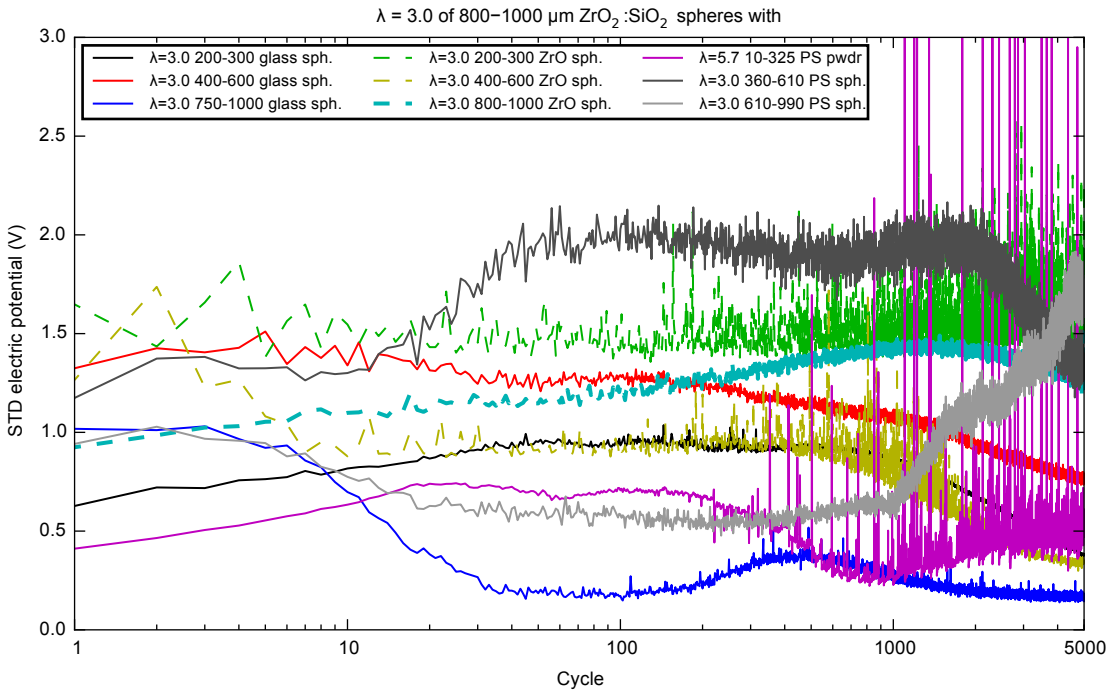

(a)

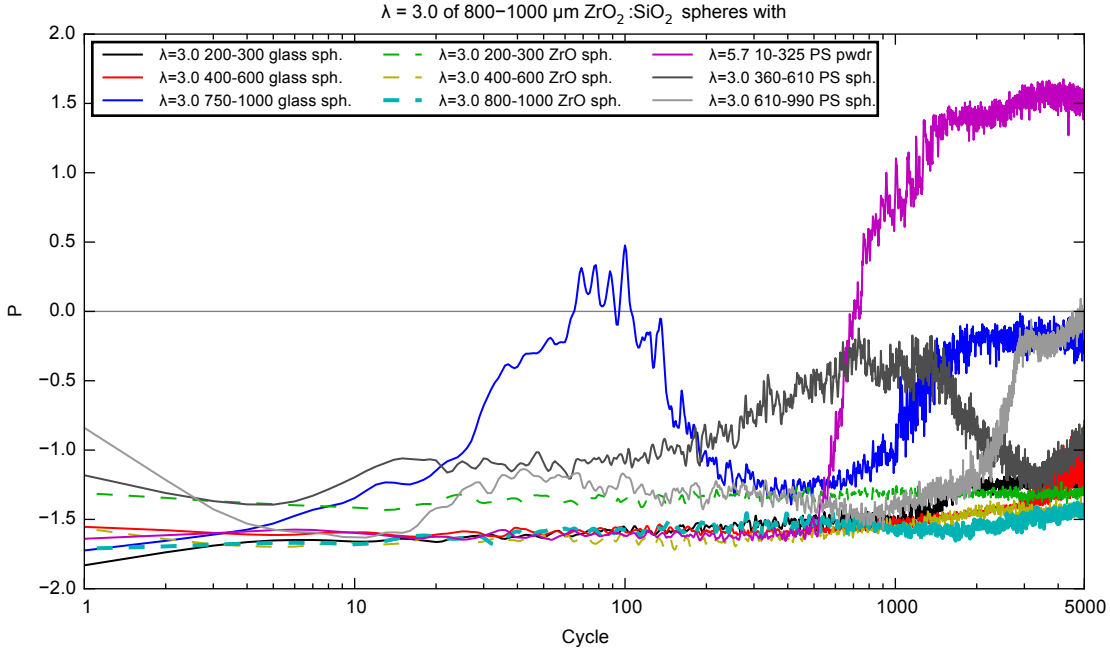

(b)

Figure 10.17: The magnitude and polarity value of the electric potential for each cycle for $\lambda = 3.0$ of 800–1000 μm ZrO_2:SiO_2 spheres mixed with $\lambda = 3.0, 5.7$ of each particle type (legend). The particles were shaken 5000 cycles at $a = 2.08\,g$. Polystyrene and ZrO_2:SiO_2 were abbreviated as PS and ZrO respectively. (a) The magnitude of each cycle, which is quantified by the standard deviation of the electric potential over the cycle. (b) The polarity value of each cycle P (Equation 10.1).

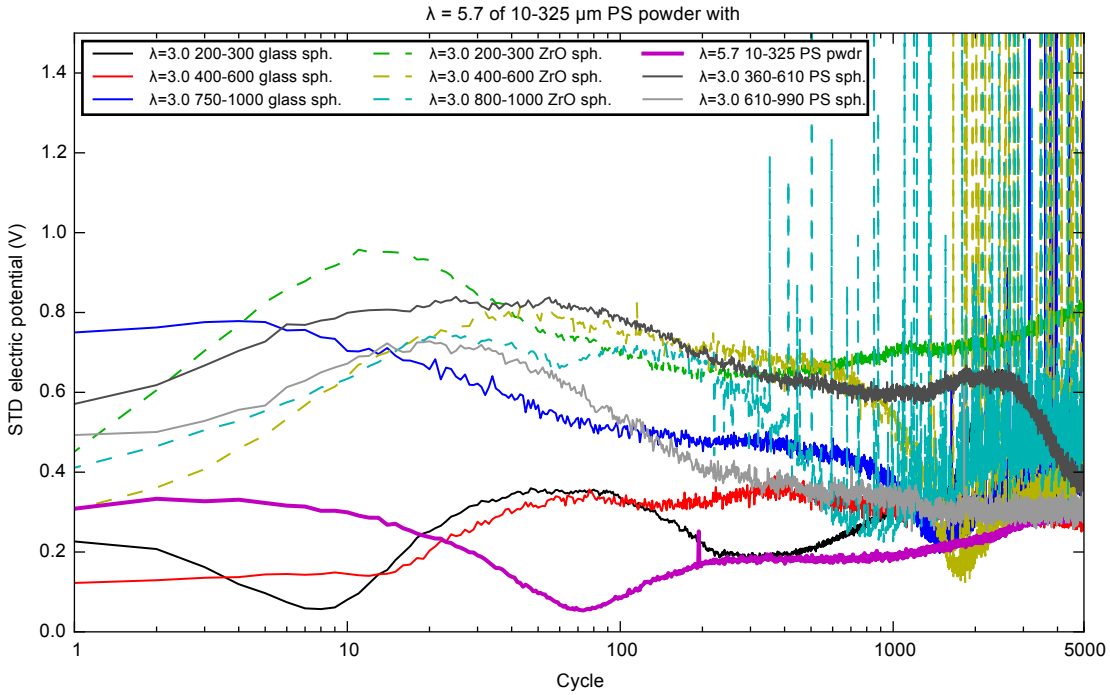

(a)

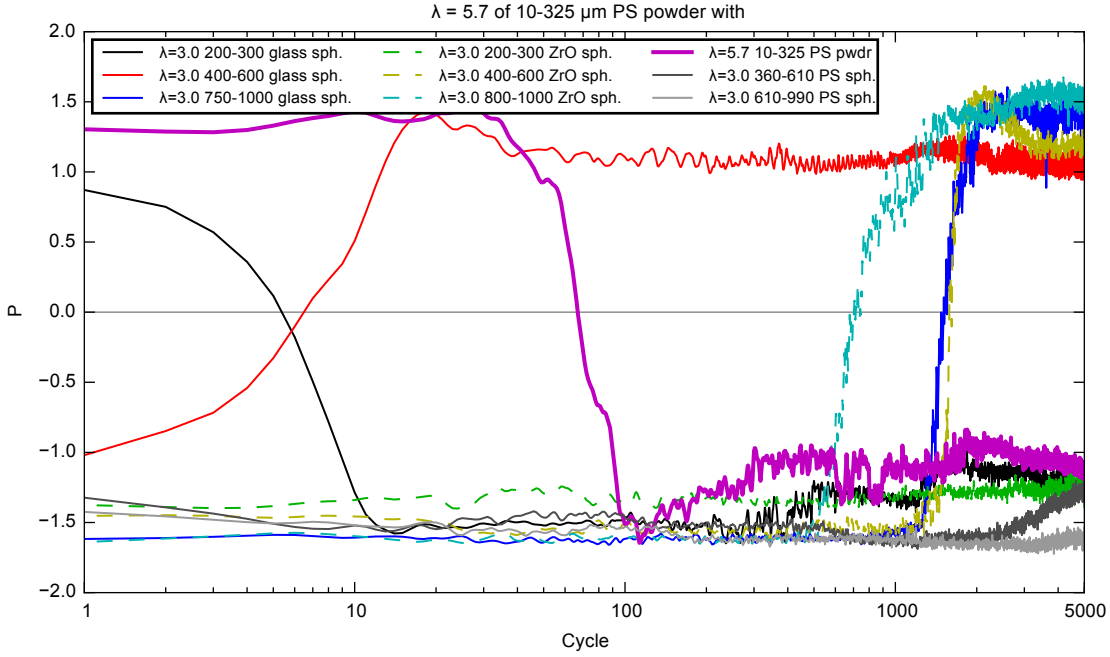

(b)

Figure 10.18: The magnitude and polarity value of the electric potential for each cycle for $\lambda = 5.7$ of 10–325 μm polystyrene (PS) powder mixed with $\lambda = 3.0$, 5.7 of each particle type (legend). The particles were shaken 5000 cycles at $a = 2.08\,g$. Polystyrene and ZrO_2:SiO_2 were abbreviated as PS and ZrO respectively. (a) The magnitude of each cycle, which is quantified by the standard deviation of the electric potential over the cycle. (b) The polarity value of each cycle P (Equation 10.1).

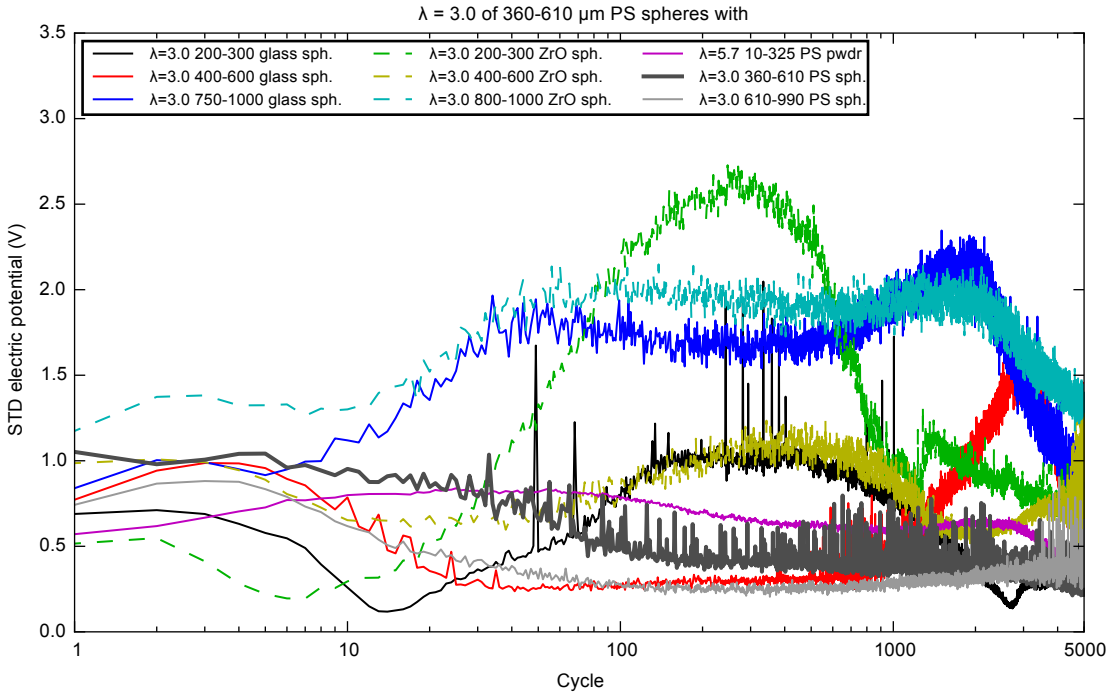

(a)

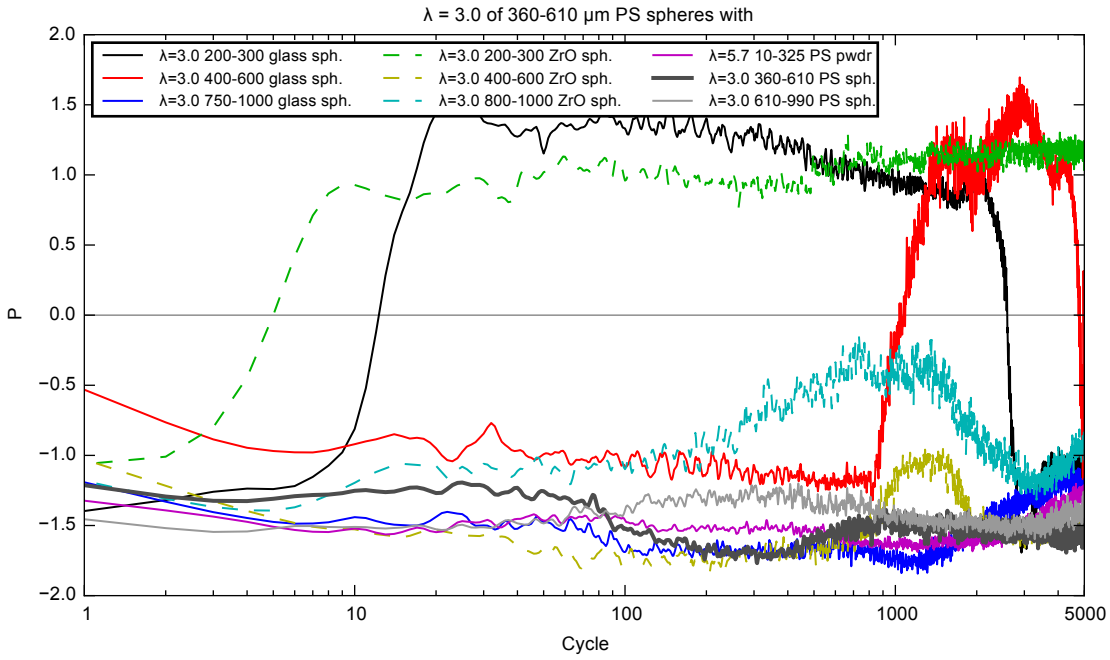

(b)

Figure 10.19: The magnitude and polarity value of the electric potential for each cycle for $\lambda = 3.0$ of 360–610 μm polystyrene (PS) spheres mixed with $\lambda = 3.0$, 5.7 of each particle type (legend). The particles were shaken 5000 cycles at $a = 2.08\,g$. Polystyrene and ZrO_2:SiO_2 were abbreviated as PS and ZrO respectively. (a) The magnitude of each cycle, which is quantified by the standard deviation of the electric potential over the cycle. (b) The polarity value of each cycle P (Equation 10.1).

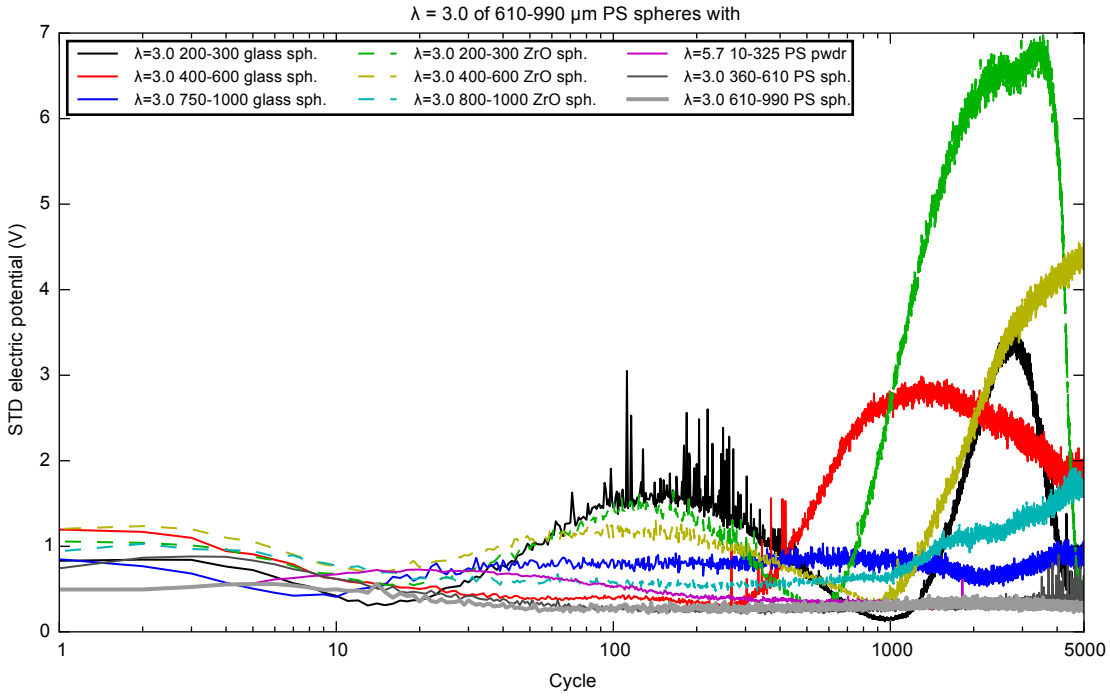

(a)

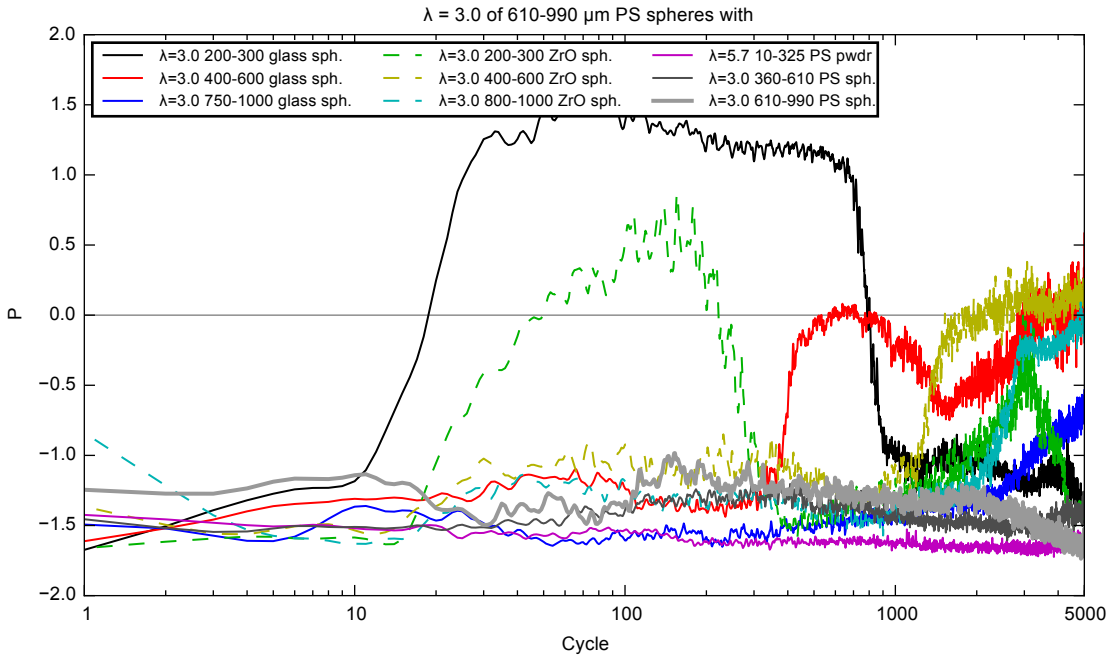

(b)

Figure 10.20: The magnitude and polarity value of the electric potential for each cycle for $\lambda = 3.0$ of 610–990 μm polystyrene (PS) spheres mixed with $\lambda = 3.0$, 5.7 of each particle type (legend). The particles were shaken 5000 cycles at $a = 2.08\,g$. Polystyrene and ZrO_2:SiO_2 were abbreviated as PS and ZrO respectively. (a) The magnitude of each cycle, which is quantified by the standard deviation of the electric potential over the cycle. (b) The polarity value of each cycle P (Equation 10.1).

of cycles. Again, we see that combinations between 360–610 μm and 610–990 μm polystyrene spheres with non-polystyrene particles have larger magnitudes.

The magnitudes for many particle type combinations dip towards zero for a bit. Looking at the polarity values, some of these dips correspond to inversions, with P crossing zero. Some particle type combinations have no inversions, some have one, and some have two or possibly more (some are easier to see with a linear horizontal axis, which are not shown).

But for some of the dips in magnitude, P goes towards zero but instead of crossing, it returns towards its previous value. This is a bit like the geomagnetic field which can reverse, or can have a decreasing dipole moment like the lead up to a reversal but then the dipole wanders a bit before returning to close its original orientation and then regaining strength, which are called excursions. Borrowing the terminology, we will call the periods where the electric potential magnitude decreases and P goes towards zero but then reverses and the electric potential magnitude grows again *polarity excursions*.

All combinations start out-of-phase ($P < 0$) except for two. Those two exceptions are 10–325 μm polystyrene powder by itself and with 360–610 μm polystyrene spheres (Figure 10.18). The majority of combinations are still out-of-phase at the end of the runs (cycle 5000), though the fraction that are in-phase has increased by that time.

10.4 Electrification Rankings

In order to elucidate the relative importances of collective phenomena, material differences, and size differences, we compare the electrification magnitudes between combinations where the materials and/or/nor sizes were different. This is most easily done by ranking the electrification magnitudes in order for the different groups combinations in isolation and together; and seeing how their rankings compare.

There are four different situations regarding particle types.

single

One particle type by itself.

same material

Both particle types are of the same material but in different size ranges.

similar size

Both particles types are in a similar and overlapping size range (but possibly not identical) but are different materials.

different

Both particle types are of different materials and in different size ranges.

The standard deviation of the electric potential over all the cycles put together is taken as the electric potential magnitude of the whole run. For each run, the number of inversions were counted by hand from the plots of P for each run individually (not shown), making note of places where it is difficult to count the exact num-

Table 10.1: The strength of the electrification for each particle type by itself, shaken for 5000 cycles at $a = 2.08\,g$. The particle quantity is $\lambda = 6.0$ except for the 10–325 μm polystyrene (PS) powder which has $\lambda = 11.5$. Polystyrene and ZrO_2:SiO_2 were abbreviated as PS and ZrO respectively. The particle types are ranked in decreasing order of electrification, which is quantified by the standard deviation (STD) of the electric potential over the run.

Material	Form	d (μm)	STD (V)	Inversions
ZrO	spheres	800-1000	1.3574	0
ZrO	spheres	400-600	0.8692	0
glass	spheres	750-1000	0.6827	0
glass	spheres	400-600	0.6532	1
glass	spheres	200-300	0.6099	0
ZrO	spheres	200-300	0.3827	2–3
PS	spheres	360-610	0.3651	0
PS	spheres	610-990	0.3117	0
PS	powder	10-325	0.2432	1

ber of inversions or where the presence of an inversion is ambiguous (e.g. as when $P \approx 0$ for a long period). The combinations for each situation are put into tables sorted in descending order of the magnitude of the electric potential. **single** is in Table 10.1, **same material** is in Table 10.2, **similar size** is in Table 10.3, and **different** is in Table 10.4. The particle type combinations from all four tables/situations are shown together in Table 10.5. The particle combinations that clump, which are 360–610 μm and 610–990 μm polystyrene spheres with non-polystyrene particles, are highlighted in the tables by their rows being bold and red.

All four situations have at least one particle type combination having an inversion, which indicates that each situation does support inversions. For combinations with the same material (Tables 10.1 and 10.2), the ordering of electric potential magnitudes from greatest to least is typically ZrO_2:SiO_2 (ZrO), glass, polystyrene (PS).

The minimum and maximum electric potential magnitudes as well as the ranges and the fraction of combinations with inversion are shown for each situa-

Table 10.2: The strength of the electrification for each combination of two particle types (1 and 2) with the same material, shaken for 5000 cycles at $a = 2.08\,g$. The particle quantity is $\lambda = 3.0$ for each particle type except for the 10–325 μm polystyrene (PS) powder which has $\lambda = 5.7$. Polystyrene and ZrO_2:SiO_2 were abbreviated as PS and ZrO respectively. A dash (-) is put under a characteristic for particle type 2 if it is the same as for type 1. The particle types are ranked in decreasing order of electrification, which is quantified by the standard deviation (STD) of the electric potential over the run.

	Form		d (μm)			
Material	1	2	1	2	STD (V)	Inversions
ZrO	spheres	-	200-300	800-1000	1.5742	0
ZrO	spheres	-	200-300	400-600	0.9092	0
glass	spheres	-	200-300	750-1000	0.6814	0
ZrO	spheres	-	400-600	800-1000	0.5955	0
PS	powder	spheres	10-325	360-610	0.5706	0
glass	spheres	-	200-300	400-600	0.4571	1
glass	spheres	-	400-600	750-1000	0.4272	1
PS	spheres	-	360-610	610-990	0.3315	0
PS	powder	spheres	10-325	610-990	0.3277	0

Table 10.3: The strength of the electrification for each combination of two particle types (1 and 2) with a similar size range, shaken for 5000 cycles at $a = 2.08\,g$. The particle quantity is $\lambda = 3.0$ for each particle type except for the 10–325 μm polystyrene (PS) powder which has $\lambda = 5.7$. Polystyrene and ZrO_2:SiO_2 were abbreviated as PS and ZrO respectively. A dash (-) is put under a characteristic for particle type 2 if it is the same as for type 1. The particle types are ranked in decreasing order of electrification, which is quantified by the standard deviation (STD) of the electric potential over the run. Rows for particle combinations that clump (Section 10.2) are in a bold red font.

Material		Form		d (μm)			
1	2	1	2	1	2	STD (V)	Inversions
PS	**ZrO**	**spheres**	**-**	**610-990**	**800-1000**	**1.2239**	**0**
PS	**glass**	**spheres**	**-**	**360-610**	**400-600**	**0.9891**	**2–3**
glass	ZrO	spheres	-	400-600	-	0.9107	0
PS	**glass**	**spheres**	**-**	**610-990**	**750-1000**	**0.7991**	**0**
PS	**ZrO**	**spheres**	**-**	**360-610**	**400-600**	**0.7454**	**0**
PS	ZrO	powder	spheres	10-325	200-300	0.7371	0
PS	glass	powder	spheres	10-325	200-300	0.4719	1
glass	ZrO	spheres	-	200-300	-	0.3680	1
glass	ZrO	spheres	-	750-1000	800-1000	0.2209	0 or 2

Table 10.4: The strength of the electrification for each combination of two particle types (1 and 2) with different materials and non-similar sizes, shaken for 5000 cycles at $a = 2.08\,g$. The particle quantity is $\lambda = 3.0$ for each particle type except for the 10–325 μm polystyrene (PS) powder which has $\lambda = 5.7$. Polystyrene and ZrO_2:SiO_2 were abbreviated as PS and ZrO respectively. A dash (-) is put under a characteristic for particle type 2 if it is the same as for type 1. The particle types are ranked in decreasing order of electrification, which is quantified by the standard deviation (STD) of the electric potential over the run. Rows for particle combinations that clump (Section 10.2) are in a bold red font.

Material		Form		d (μm)			
1	2	1	2	1	2	STD (V)	Inversions
PS	**ZrO**	**spheres**	**-**	**610-990**	**200-300**	**4.9097**	**2**
PS	**ZrO**	**spheres**	**-**	**610-990**	**400-600**	**3.0661**	**> 1 (P≈0)**
PS	**glass**	**spheres**	**-**	**610-990**	**400-600**	**2.1949**	**> 1 (P≈0)**
PS	**glass**	**spheres**	**-**	**610-990**	**200-300**	**1.8729**	**2**
PS	**ZrO**	**spheres**	**-**	**360-610**	**800-1000**	**1.7269**	**0**
PS	**glass**	**spheres**	**-**	**360-610**	**750-1000**	**1.6062**	**0**
PS	**ZrO**	**spheres**	**-**	**360-610**	**200-300**	**1.1628**	**1**
glass	ZrO	spheres	-	750-1000	400-600	1.0050	0
glass	ZrO	spheres	-	400-600	800-1000	0.9425	0
glass	ZrO	spheres	-	200-300	400-600	0.7343	0
glass	ZrO	spheres	-	200-300	800-1000	0.6629	0
PS	ZrO	powder	spheres	10-325	800-1000	0.6180	1
PS	**glass**	**spheres**	**-**	**360-610**	**200-300**	**0.5555**	**2**
PS	ZrO	powder	spheres	10-325	400-600	0.5494	1
glass	ZrO	spheres	-	750-1000	200-300	0.4320	0
PS	glass	powder	spheres	10-325	750-1000	0.3831	1
glass	ZrO	spheres	-	400-600	200-300	0.3782	1
PS	glass	powder	spheres	10-325	400-600	0.3083	1

Table 10.5: The strength of the electrification for each combination of two particle types (1 and 2), shaken for 5000 cycles at $a = 2.08\,g$. The particle quantity is $\lambda = 3.0$ for each particle type except for the 10–325 μm polystyrene (PS) powder which has $\lambda = 5.7$. Polystyrene and ZrO_2:SiO_2 were abbreviated as PS and ZrO respectively. A dash (-) is put under a characteristic for particle type 2 if it is the same as for type 1. The particle types are ranked in decreasing order of electrification, which is quantified by the standard deviation (STD) of the electric potential over the run. The first column label's the situation as being a single particle type (single), both particle types being the same material (same material), both particle types having a similar size (similar size), and both particles having different materials and non-similar sizes (different). Rows for particle combinations that clump (Section 10.2) are in a bold red font.

	Material		Form		d (μm)			
Situation	1	2	1	2	1	2	STD (V)	Inversions
different	**PS**	**ZrO**	**spheres**	**-**	**610-990**	**200-300**	**4.9097**	**2**
different	**PS**	**ZrO**	**spheres**	**-**	**610-990**	**400-600**	**3.0661**	**>1 ($P\approx0$)**
different	**PS**	**glass**	**spheres**	**-**	**610-990**	**400-600**	**2.1949**	**>1 ($P\approx0$)**
different	**PS**	**glass**	**spheres**	**-**	**610-990**	**200-300**	**1.8729**	**2**
different	**PS**	**ZrO**	**spheres**	**-**	**360-610**	**800-1000**	**1.7269**	**0**
different	**PS**	**glass**	**spheres**	**-**	**360-610**	**750-1000**	**1.6062**	**0**
same material	ZrO	-	spheres	-	200-300	800-1000	1.5742	0
single	ZrO	-	spheres	-	800-1000	-	1.3574	0
similar size	**PS**	**ZrO**	**spheres**	**-**	**610-990**	**800-1000**	**1.2239**	**0**
different	**PS**	**ZrO**	**spheres**	**-**	**360-610**	**200-300**	**1.1628**	**1**
different	glass	ZrO	spheres	-	750-1000	400-600	1.0050	0
similar size	**PS**	**glass**	**spheres**	**-**	**360-610**	**400-600**	**0.9891**	**2–3**
different	glass	ZrO	spheres	-	400-600	800-1000	0.9425	0
similar size	glass	ZrO	spheres	-	400-600	-	0.9107	0
same material	ZrO	-	spheres	-	200-300	400-600	0.9092	0
single	ZrO	-	spheres	-	400-600	-	0.8692	0
similar size	**PS**	**glass**	**spheres**	**-**	**610-990**	**750-1000**	**0.7991**	**0**
similar size	**PS**	**ZrO**	**spheres**	**-**	**360-610**	**400-600**	**0.7454**	**0**
similar size	PS	ZrO	powder	spheres	10-325	200-300	0.7371	0
different	glass	ZrO	spheres	-	200-300	400-600	0.7343	0
single	glass	-	spheres	-	750-1000	-	0.6827	0
same material	glass	-	spheres	-	200-300	750-1000	0.6814	0
different	glass	ZrO	spheres	-	200-300	800-1000	0.6629	0
single	glass	-	spheres	-	400-600	-	0.6532	1
different	PS	ZrO	powder	spheres	10-325	800-1000	0.6180	1
single	glass	-	spheres	-	200-300	-	0.6099	0
same material	ZrO	-	spheres	-	400-600	800-1000	0.5955	0
same material	PS	-	powder	spheres	10-325	360-610	0.5706	0
different	**PS**	**glass**	**spheres**	**-**	**360-610**	**200-300**	**0.5555**	**2**
different	PS	ZrO	powder	spheres	10-325	400-600	0.5494	1
similar size	PS	glass	powder	spheres	10-325	200-300	0.4719	1
same material	glass	-	spheres	-	200-300	400-600	0.4571	1
different	glass	ZrO	spheres	-	750-1000	200-300	0.4320	0
same material	glass	-	spheres	-	400-600	750-1000	0.4272	1
different	PS	glass	powder	spheres	10-325	750-1000	0.3831	1
single	ZrO	-	spheres	-	200-300	-	0.3827	2–3
different	glass	ZrO	spheres	-	400-600	200-300	0.3782	1
similar size	glass	ZrO	spheres	-	200-300	-	0.3680	1
single	PS	-	spheres	-	360-610	-	0.3651	0
same material	PS	-	spheres	-	360-610	610-990	0.3315	0
same material	PS	-	powder	spheres	10-325	610-990	0.3277	0
single	PS	-	spheres	-	610-990	-	0.3117	0
different	PS	glass	powder	spheres	10-325	400-600	0.3083	1
single	PS	-	powder	-	10-325	-	0.2432	1
similar size	glass	ZrO	spheres	-	750-1000	800-1000	0.2209	0 or 2

Table 10.6: The minimum and maximum electric potential amplitudes for each situation as well as their ranges and the percentage of particle type combinations for that situation that have an inversion. The number of particle type combinations (#) in each situation is also given. For the maximum and the range, it is given both with the particle combinations that clump (Section 10.2) included (Total) and excluded (w/o Clump.).

			Total		w/o Clump.		
Situation	#	Min. (V)	Max. (V)	Range (V)	Max. (V)	Range (V)	Have Inv. (%)
single	9	0.2432	1.3574	1.1142	1.3574	1.1142	33
same material	9	0.3277	1.5742	1.2465	1.5742	1.2465	22
similar size	9	0.2209	1.2239	1.003	0.9107	0.6898	33 or 44
different	18	0.3083	4.9097	4.6014	1.0050	0.6967	61

tion in Table 10.6. If the clumping combinations are excluded, the electric potential magnitudes for each situation are over similar intervals and have ranges $\sim$ 1 V, which is about 5 times the smallest magnitude in each situation. This suggests that mixing different materials and/or sizes together does not significantly increase or decrease the electric potential magnitudes measured, ignoring the particle type combinations that clump. Due to the low number of combinations in each situation (9, 9, 9, and 18) and the limited set of materials tested (three), it is hard to conclude much about whether combinations for each situation are more or less likely to have inversions within 5000 cycles of shaking. It appears that mixing particle types with both a different material and different size range results in a higher likelihood of inversions, but further investigation is needed to see if this difference is due to the small number of combinations and materials involved.

10.5 Particle Size Segregation

Collisional charge exchange effects due to dissimilar sized particles have already been documented. Small particles tend to become negatively charged, while larger

ones become positively charged (Lacks and Mohan Sankaran 2011; Duff and Lacks 2008; Forward et al. 2009b,a; Kok and Lacks 2009; Angus et al. 2013; Waitukaitis et al. 2014). That phenomenon, taken together with the well documented ability of granular flows to segregate by size when convecting, could lead to macroscopic charging (Lacks and Mohan Sankaran 2011; Duff and Lacks 2008; Forward et al. 2009b,a; Kok and Lacks 2009; Angus et al. 2013; Waitukaitis et al. 2014).

Due to this feature of granular flows, we investigated how particles of different sizes spatially segregate in the slab due to shaking. We mixed $\lambda = 3$ of 200–300 μm ZrO_2:SiO_2 and $\lambda = 3$ of 400–600 μm ZrO_2:SiO_2 together and shook the cell for 20,000 cycles at $a = 2.08\,g$. We then carefully took opened the cell carefully so as to not disturb the particle arrangement. The particles were photographed (Figure 10.21a) with a Nikon D90 camera and a Nikkor 110 mm macro lens from above at a resolution of 4288×2848 pixels, such that the full diameter of the cell would be completely visible ($D = 8.6$ cm corresponds to 4110 pixels).

A mapping is needed that will indicate thee regions where each particle size predominated. By eye, regions dominated by larger particles can be distinguished from regions dominated by small particles by the larger and higher contrast gaps between the particles. We used this to produce the map of the spatial pattern of which particle size dominates.

The photographed image was smoothed with a 7 pixel radius disk to smooth over the contrast for regions dominated by small particles but not large particles. Then, a map of the remaining contrast was found by dividing the image into 32×32 pixel squares and taking the standard deviation of the pixel values in

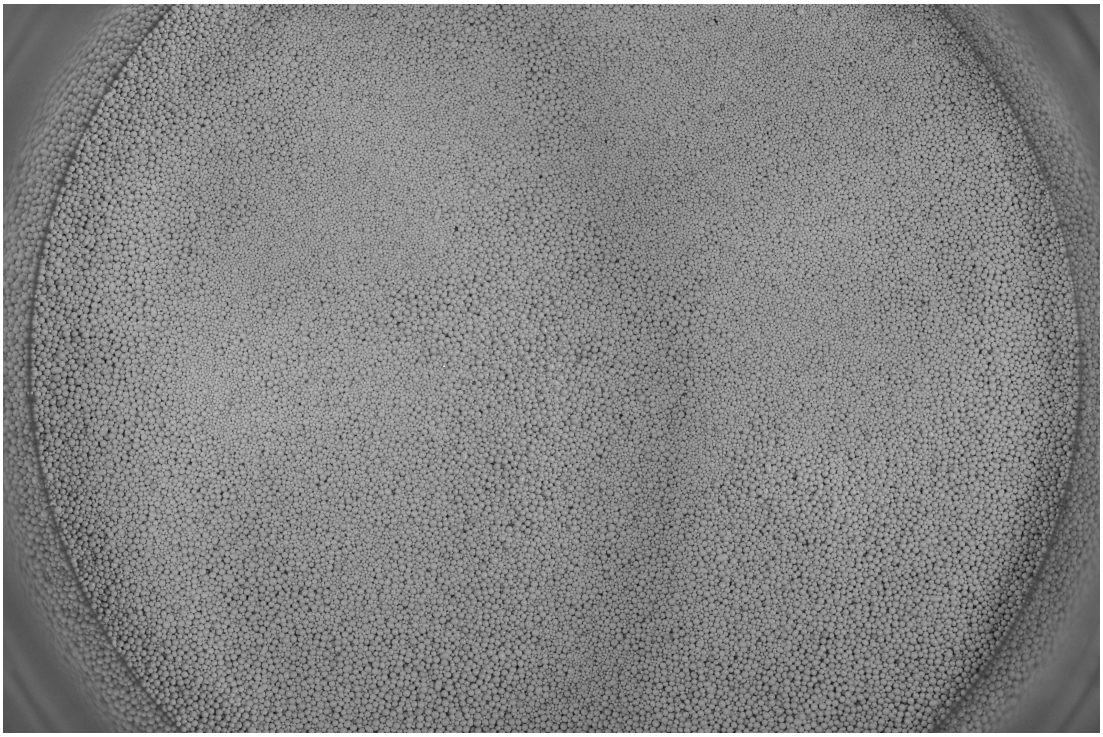

(a)

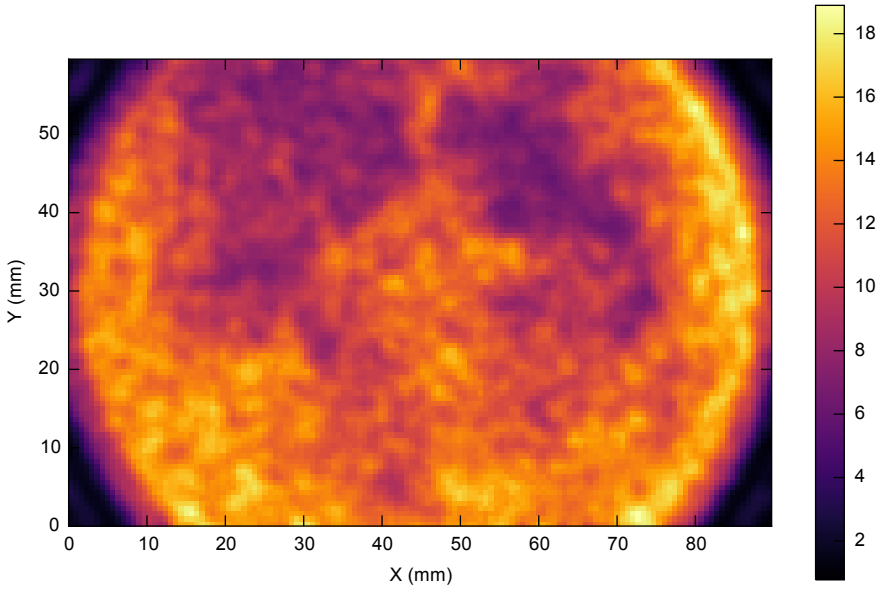

(b)

Figure 10.21: Particle arrangement on the top layer after shaking. Top down view of the particles in the cell after being shaken for 20,000 cycles at $a = 2.08\,g$. We used $\lambda = 3$ of 200–300 μm ZrO_2:SiO_2 and $\lambda = 3$ of 400–600 μm ZrO_2:SiO_2 mixed together. (a) Photograph of the particles. (b) Map of which regions are predominately large particles (large values) vs. small particles (small values). The units for the values are arbitrary.

each square. Increasing the fraction of large particles in a region increases the value of this mapping. The resulting map was then smoothed using a 2 pixel radius disk to make the regions easier to see and not pick out single large particles in the middle of a region of small particles.

The mapping of which particle size dominates each area is shown in Figure 10.21b. Particles of both sizes are visible on the top with patches that are dominated by each size and patches where they are mixed. This means that they did not completely segregate despite the size difference, and that likely, the pattern is evolving over time.

Chapter 11: GE: Conclusions

Partially adapted from and expanded upon the arXiv preprint

F. Nordsiek and D. P. Lathrop. Collective phenomena in granular and atmospheric electrification. *ArXiv e-prints*, Sept. 2015b.

arXiv: 1509.04214 [cond-mat.soft]

Some of the data this chapter is based on has been deposited on DRUM at

F. Nordsiek and D. Lathrop. Collective phenomena in granular and atmospheric electrification. Dataset uploaded to Digital Repository at the University of Maryland (DRUM), July 2015a.

DOI: 10.13016/M2ZK87

URL: `http://hdl.handle.net/1903/16867`

11.1 Collective Phenomena And Particle Properties

Every combination of one or two particle types tested exhibits electrification regardless of forms (spheres or powder), sizes, conductivities, and materials, as seen by the non-zero electric potentials (Figure 9.1 and Section 10.1). This suggests that granular electrification happens for all particles regardless of their form, size, conductivity, and material, whether as a single type or in combination.

That is not to say that those properties do not have an effect on how much electrification occurs and its dynamics. Indeed, some effects can be seen in the differences in electric potential magnitudes in Table 10.5. Conversely, there is a lot in common between the electric potential measured for particles with different properties.

Perhaps the biggest similarity is that the electric potentials for all particle types and their combinations have similar shapes and amplitudes (Sections 9.1 and 10.1). Even materials as different as insulators (glass, polystyrene, PTFE, and ZrO_2:SiO_2) have similar profiles to the conductors (aluminum and copper). Even those with the profiles that are the most different from the others, 360–610 μm or 610–990 μm polystyrene spheres with non-polystyrene particles which clump (Section 10.2), still share many similarities with non-clumping combinations. The amplitudes the electric potential for all combinations including the ones that had clumping are all within a factor of 22 of each other (Table 10.6), and a factor of 7 if the clumping combinations are excluded.

Similarities are also seen in the temporal dynamics of the electric potential

between the plates (Section 10.3). The magnitudes of the electric potentials for the different combinations change over the full range of time scales tested — scales of 10's, 100's, and 1000's of cycles. Looking at both the magnitudes and the polarity values, many combinations have polarity inversions and/or excursions.

These similarities suggest that particle forms, sizes, conductivities, and materials are not the dominant factors controlling the amount of electrification and its dynamics. Instead, we argue that collective phenomena play a key role in the electrification. That is not to say that two-body or multi-body collisions are irrelevant, but instead that the role of the large-scale structure and long-range interactions of large numbers of particles is pivotal. A number of pieces of evidence point to this conclusion.

Ignoring clumping, the ranges of electric potential difference are about the same whether a single particle type is shaken or two are shaken where the size or material are held constant (Section 10.4). If material differences between particles were major contributors, then the **similar size** (but different material) situation combinations (Table 10.3) would have had significantly different electric potential magnitudes. While all of the particle types used were polydisperse (effective diameters varying between 20% and an order of magnitude), if size differences were a major contributor that increases electrification, mixing particle types of the same material but different sizes would most likely increase the electric potential magnitudes. But we observe no noticeable difference (Table 10.2) compared to each particle type by itself (Table 10.1), though it is possible that electrification just requires the presence of polydispersity, even if small, and that the exact level does not matter that much.

There are a number of things that point to collective phenomena being a major contributor. First, collective phenomena being the dominant factor would predict relative independence of the electrification with respect to particle form, size, conductivity, and material for single particle type runs like we observe.

The second is the presence of thresholds in the particle number required for electrification (Section 9.2). This is suggestive of a phase transition, which is a collective phenomenon. Though, the thresholds are different between the one powder (10–325 μm polystyrene) and the types of spheres (610–990 μm polystyrene and 750–1000 μm glass), which does point out that the particle form and/or polydispersity does have some effect.

The long time scale dependence, inversions, and excursions of the electric potential also argue for complex macroscopic dynamics and collective phenomena. If collective phenomena were not important, each particle type combination would tend towards a statistically steady state from whatever their initial state was. This could lead to a single inversion if the starting electric potential profile had the opposite polarity as the steady state one (note that symmetry is broken here by Earth's gravity). Instead, some combinations had more than one inversion just within the first 5000 cycles, there were polarity excursions, and the electric potential varied on a wide range of scales (10's, 100's, and 1000's of cycles).

The particle combinations that clump (360–610 μm and 610–990 μm polystyrene spheres with non-polystyrene particles) show both the collective phenomena operating, but also how the particle properties are not entirely irrelevant in the dynamics. In fact, it is the properties of the polystyrene spheres that effects

the collective dynamics. Rather than the slab of particles being shaken consisting of individual particles moving relatively independently except for collisions, clusters of particles are held together and move as a group and stick to other groups to some degree. This is a very different set of dynamics. The clumping results in larger electric potential magnitudes (Table 10.5) and different electric potential profiles (Section 10.1), but are otherwise similar to the non-clumping combinations.

One of the ways that collective phenomena are manifested is the pattern of segregation of different particle sizes (Section 10.5). When two different size ranges of the same material of particle were mixed together, the particles did not completely segregate with respect to size as they do in many granular systems. Instead, a complex arrangement of patches with different fractions of each particle size were found (Figure 10.21).

All of these patterns point to collective phenomena being the major factor in the granular electrification that we see in our experiment. The particle properties (form, size, conductivity, material) of the one or two particle types in each combination play a more minor role in the electrification, adjusting the electric potential by an order of magnitude, adjusting the threshold in particle quantity, and determining whether the particles clump together or not. Here we make analogy to the observation that gases may exhibit similar thermodynamic behavior independently of their chemical composition (i.e. the ideal gas law is not material-specific).

11.2 Connections to Atmospheric Electrification

Now we consider the implications of collective phenomena on atmospheric electrification (thunderstorms, thunder-snow, volcanic lightning, and lightning in dust storms). Our observations that different materials all exhibit electrification in our experiment parallels natural electrification in ash plumes and dust storms, suggesting that collective phenomena are important in understanding electrification in those systems.

Thunderstorms and thunder-snow do have a few major differences from the experiment presented in this thesis. While the vapor pressures of our materials are low, the same is not true for thunderstorms and thunder-snow where there is a significant amount of water vapor. In addition, all but warm tropical thunderstorms and all but very polar snowstorms have both condensed phases of H_2O present (liquid water and ice). Having all three phases present adds many additional mechanisms for electrification, which are thought to be dominant (Saunders 2008; Smirnov 2014). While the electrification mechanisms at play in our experiment would most likely be present in these storms, they may be minor factors. Warm thunderstorms and cold snowstorms where there is just liquid water and ice, respectively, with water vapor are more similar to our experimental conditions. Like our experiment, they do have something like a particle quantity threshold in that thunderstorms and volcanic ash clouds must be sufficiently tall to exhibit lightning (Saunders 2008; Smirnov 2014). And they do exhibit very rich internal dynamics across all spatial scales like our experiment with the size segregation. This is seen in the measurements of the

electric fields inside thunderstorms, which show a complex spatial dependence over a large range of length scales (Marshall et al. 1995). This suggests the importance of collective phenomena in these types of atmospheric electrification.

Keeping in mind these caveats about thunderstorms and thunder-snow, our experiment suggests that the different atmospheric systems that show granular electrification, despite the different materials involved, have some of the same mechanisms involved. These results suggest that collective phenomena are very important and material properties are less important than thought, with the exception of thunderstorms and snowstorms with all three phases of H_2O.

11.3 Open Questions And Future Research

There are a number of open questions and directions for future research. Some of them are listed below.

1. What is the cause for the difference in the threshold in particle quantity for electrification, between the one powder (10–325 μm polystyrene) and two types of spheres (610–990 μm polystyrene and 750–1000 μm glass) whose λ dependences were found? There is a difference in size, polydispersity, and form (the powder particles are definitely not spherical as seen in Figure 8.8c). Checking the λ dependence for the 200–300 μm glass spheres, the 35–635 μm PTFE powder would give insight into, and a larger diameter polystyrene powder would help elucidate the cause.

2. How does the electric potential between the plates evolve on larger time scales

than tested here (10^4, 10^5, ... cycles)? Do there continue to be changes in the electric potential including polarity inversions and excursions, or is some steady state reached? One difficulty in investigating this is keeping the linear servo-motor sufficiently cool and lubricated.

3. What is the importance, or lack thereof, of polydispersity in the particles? This could be tested by using particles with a very narrow size range.

4. Electrical discharges in the cell should emit light in the visible and/or UV range. Blocking external light from the cell and putting in photodiodes to detect these photon emissions would provide insight into the discharges and allow the detection of discharges that are between the particles rather than to either plate.

5. Mounting a camera to the cell would allow the granular motion to be observed as the cell is shaking, providing insights into the particle rearrangement over the shaking cycle and from one cycle to another.

6. How much electrification is caused by particle collisions with the metal plates? The thresholds with λ suggest that particle-particle collisions are important, but that doesn't necessarily say that particle-plate collisions are irrelevant to the electrification. A way to investigate this is to change the plates in some way, say by covering one or both completely with insulating polyimide film, placing a glass disk over one or both plates, etc. For the case of glass disks, if the disks were borosilicate glass, then the particles in the cell would be

completely enclosed by borosilicate glass and if the particles are borosilicate glass themselves, then all collisions are between objects of the same material.

7. A systematic investigation of the effects of the gas pressure and composition in the cell is needed. All the measurements reported in this thesis were done under a partial vacuum of 30–60 mTorr (4×10^{-5} to 8×10^{-5} atm) with the cell being originally filled with lab air. A few test runs at atmospheric pressure with lab air inside the cell resulted in much larger electric potentials for 10–325 μm polystyrene powder, on the order of $\pm$ 5–20 V depending on the run.

8. While the cell was held under a partial vacuum, there are still molecular layers of H_2O on the particles' surfaces from exposure to the lab air. Adhered water could be affecting the electrification, so it would be useful to use particles that have been backed under a much stronger partial vacuum and then not re-exposed to moist lab air before use.

9. All particle materials tested so far have been insulators or conductors. The experiment should be run with materials that are poor conductors to fill in the gap in conductivities. This is relevant thunderstorms and snowstorms which have ice and liquid water particles which conduct electricity, but poorly.

10. What is the macroscopic pattern of electric charge on the particles and how does it evolve? Are both polarities mixed together heterogeneously like particles of different sizes when two sizes are mixed together like Figure 10.21? Does the charge distribution pattern correspond with the size distribution

pattern for the case of more than one size? A macroscopic evolving charge pattern would be consistent with the long time-scale variations we measure in the electric potential, although it would be very challenging to measure.

11. What are the electric fields inside the cell between the particles? This would be very hard to measure without disturbing the granular flow.

12. The granular flow itself in the cell, which is a loose granular slab surrounded by granular gas that are all periodically compacted, is quite different from the more dilute granular-fluid flows in thunderstorms, thunder-snow, and dust storms. In addition, the cell was operated under a partial vacuum making the fluid effects small compared to atmospheric systems where they are a very large component. These are major differences that limit the applicability of this experiment. Performing a granular electrification experiment with a granular gas in a fluid would be more applicable. One way to do that would be to make a cell having ducts with fans pumping air through them with grids over the ducts to make the flow very turbulent. Particle settling due to gravity could be reduced by performing the experiment under micro-gravity conditions.

13. How does the electric charge on the particles affect their motion and spatial distributions due to their responses to the electric fields they are generating? In the dilute granular-fluid case, there has been some research on their spatial distributions and motion (Alipchenkov et al. 2004; Lu et al. 2010a,b; Lu and Shaw 2015), but more investigation is needed.

11.4 Final Words

There currently is a lack of a detailed theoretical model of granular and atmospheric electrification, though one is surely desirable in the future. The underlying difficulty is that of model complexity: these are far from equilibrium phenomena of two or more phase flows, often embedded in a background turbulent atmospheric flow. This problem is conceptually more difficult than systems with known continuous equations of motion, such as fluid flow without particles. Still, one can speculate on the nature of the theoretical possibilities that occur independently of material properties.

Finally, we hope that our experimental observations may help by conceptually framing atmospheric electrification as a type of macroscopic collective mechanism. This highlights the need for a better theoretical understanding of those processes.

Bibliography

V. Alipchenkov, L. Zaichik, and O. Petrov. Clustering of charged particles in isotropic turbulence. *High Temperature*, 42(6):919–927, nov 2004. ISSN 0018-151X.
DOI: 10.1007/s10740-005-0037-0

C. D. Andereck, S. S. Liu, and H. L. Swinney. Flow regimes in a circular Couette system with independently rotating cylinders. *Journal of Fluid Mechanics*, 164: 155–183, Mar. 1986.
DOI: 10.1017/S0022112086002513
ADS: 1986JFM...164..155A

J. C. Angus, I. Greber, and K. Kash. Size-dependent electron chemical potential: Effect on particle charging. *Journal of Electrostatics*, 71(6):1055–1060, Dec 2013. ISSN 0304-3886.
DOI: 10.1016/j.elstat.2013.10.006

K. Avila, D. Moxey, A. de Lozar, M. Avila, D. Barkley, and B. Hof. The onset of turbulence in pipe flow. *Science*, 333:192–6, July 2011.
DOI: 10.1126/science.1203223
ADS: 2011Sci...333..192A

M. Avila. Stability and angular-momentum transport of fluid flows between corotating cylinders. *Physical Review Letters*, 108(12):124501, Mar. 2012.
DOI: 10.1103/PhysRevLett.108.124501
ADS: 2012PhRvL.108l4501A
arXiv: 1203.4923 [physics.flu-dyn]

P. Baddeley. *Whirlwinds and Dust-storms of India: an investigation into the law of wind and revolving storms at sea*. Bell & Daldy, 1860.
OCLC: 4536022
URL: `http://hdl.handle.net/2027/umn.31951d00015326u`

S. A. Balbus. Fluid dynamics: A turbulent matter. *Nature*, 470:475–476, Feb. 2011.
DOI: 10.1038/470475a
ADS: 2011Natur.470..475B

H. F. Beckley. *Measurements of Annular Couette Flow Stability at the Fluid Reynolds Number Re = 4.4×10^6: The Fluid Dynamic Precursor to a Liquid Sodium $\alpha\omega$ Dynamo*. PhD thesis, New Mexico Institute of Mining and Technology, December 2002.
OCLC: 51915739
URL: `http://physics.nmt.edu/~dynamo/Howard-PhD.pdf`

D. Borrero-Echeverry, M. F. Schatz, and R. Tagg. Transient turbulence in Taylor-Couette flow. *Physical Review E*, 81(2):025301, Feb. 2010.
DOI: 10.1103/PhysRevE.81.025301
ADS: 2010PhRvE..81b5301B
arXiv: 0905.0147 [physics.flu-dyn]

H. J. Brauckmann and B. Eckhardt. Direct numerical simulations of local and global torque in Taylor-Couette flow up to Re = 30 000. *Journal of Fluid Mechanics*, 718:398–427, Mar. 2013.
DOI: 10.1017/jfm.2012.618
ADS: 2013JFM...718..398B
arXiv: 1206.1286 [physics.flu-dyn]

M. J. Burin and C. J. Czarnocki. Subcritical transition and spiral turbulence in circular couette flow. *Journal of Fluid Mechanics*, 709:106–122, Oct. 2012.
DOI: 10.1017/jfm.2012.323
ADS: 2012JFM...709..106B

C. Cimarelli, M. A. Alatorre-Ibargüengoitia, U. Kueppers, B. Scheu, and D. B. Dingwell. Experimental generation of volcanic lightning. *Geology*, 42(1):79–82, Jan 2014. ISSN 1943-2682.
DOI: 10.1130/g34802.1

D. Coles. Transition in circular couette flow. *Journal of Fluid Mechanics*, 21:385–425, 1965.
DOI: 10.1017/S0022112065000241
ADS: 1965JFM....21..385C

R. J. Donnelly. Taylor-Couette flow: The early days. *Physics Today*, 44:32–39, Nov. 1991.
DOI: 10.1063/1.881296
ADS: 1991PhT....44k..32D

B. Dubrulle, O. Dauchot, F. Daviaud, P.-Y. Longaretti, D. Richard, and J.-P. Zahn. Stability and turbulent transport in Taylor-Couette flow from analysis of experimental data. *Physics of Fluids*, 17(9):095103, Sept. 2005a.
DOI: 10.1063/1.2008999
ADS: 2005PhFl...17i5103D
arXiv: 1106.1276 [physics.flu-dyn]

B. Dubrulle, L. Marié, C. Normand, D. Richard, F. Hersant, and J.-P. Zahn. An hydrodynamic shear instability in stratified disks. *Astronomy & Astrophysics*, 429:1–13, Jan. 2005b.
DOI: 10.1051/0004-6361:200400065
ADS: 2005A%26A...429....1D
arXiv: astro-ph/0410224 [astro-ph]

N. Duff and D. J. Lacks. Particle dynamics simulations of triboelectric charging in granular insulator systems. *Journal of Electrostatics*, 66(1-2):51–57, Jan 2008. ISSN 0304-3886.
DOI: 10.1016/j.elstat.2007.08.005

M. Dunst. An experimental and analytical investigation of angular momentum exchange in a rotating fluid. *Journal of Fluid Mechanics*, 55:301–310, 1972.
DOI: 10.1017/S0022112072001879
ADS: 1972JFM....55..301D

B. Eckhardt, S. Grossmann, and D. Lohse. Torque scaling in turbulent taylor couette flow between independently rotating cylinders. *Journal of Fluid Mechanics*, 581: 221–250, May 2007.
DOI: 10.1017/S0022112007005629
ADS: 2007JFM...581..221E

E. M. Edlund and H. Ji. Nonlinear stability of laboratory quasi-Keplerian flows. *Physics Review E*, 89(2):021004, Feb. 2014.
DOI: 10.1103/PhysRevE.89.021004
ADS: 2014PhRvE..89b1004E
arXiv: 1401.6183 [astro-ph.IM]

E. M. Edlund and H. Ji. Reynolds number scaling of influence of boundary layers on the global behavior of laboratory quasi-Keplerian flows. *ArXiv e-prints*, Dec. 2014.
arXiv: 1412.1386 [physics.flu-dyn]

S. F. Edwards and R. B. S. Oakeshott. The transmission of stress in an aggregate. *Physica D Nonlinear Phenomena*, 38:88–92, Sept. 1989.
DOI: 10.1016/0167-2789(89)90176-0
ADS: 1989PhyD...38...88E

K. M. Forward, D. J. Lacks, and R. M. Sankaran. Particle-size dependent bipolar charging of martian regolith simulant. *Geophysical Research Letters*, 36:L13201, July 2009a.
DOI: 10.1029/2009GL038589
ADS: 2009GeoRL..3613201F

K. M. Forward, D. J. Lacks, and R. M. Sankaran. Charge segregation depends on particle size in triboelectrically charged granular materials. *Physical Review Letters*, 102(2):028001, Jan. 2009b.
DOI: 10.1103/PhysRevLett.102.028001
ADS: 2009PhRvL.102b8001F

S. Grossmann. The onset of shear flow turbulence. *Reviews of Modern Physics*, 72: 603–618, Apr. 2000.
DOI: 10.1103/RevModPhys.72.603
ADS: 2000RvMP...72..603G

Z. Gu, W. Wei, J. Su, and C. W. Yu. The role of water content in triboelectric charging of wind-blown sand. *Scientific Reports*, 3(1: 1337):1337, Feb. 2013.
DOI: 10.1038/srep01337
ADS: 2013NatSR...3E1337G

J. R. Holton. *An Introduction to Dynamic Meteorology, Fourth Edition.* International Geophysics. Elsevier Academic Press, 4 edition, 2004.
ISBN: 978-0123540157
OCLC: 54400282
LCCN: 2004044072

S. G. Huisman, D. P. M. van Gils, S. Grossmann, C. Sun, and D. Lohse. Ultimate turbulent taylor-couette flow. *Physical Review Letters*, 108(2):024501, Jan. 2012a.
DOI: 10.1103/PhysRevLett.108.024501
ADS: 2012PhRvL.108b4501H
arXiv: 1111.0063 [physics.flu-dyn]

S. G. Huisman, D. P. M. van Gils, and C. Sun. Applying laser doppler anemometry inside a taylor-couette geometry using a ray-tracer to correct for curvature effects. *European Journal of Mechanics B Fluids*, 36:115–119, Nov. 2012b.
DOI: 10.1016/j.euromechflu.2012.03.013
ADS: 2012EJMF...36..115H
arXiv: 1203.6748 [physics.flu-dyn]

S. G. Huisman, S. Scharnowski, C. Cierpka, C. J. Kähler, D. Lohse, and C. Sun. Logarithmic Boundary Layers in Strong Taylor-Couette Turbulence. *Physical*

Review Letters, 110(26):264501, June 2013.
DOI: 10.1103/PhysRevLett.110.264501
ADS: 2013PhRvL.110z4501H
arXiv: 1302.6081 [physics.flu-dyn]

H. Ji and S. Balbus. Angular momentum transport in astrophysics and in the lab. *Physics Today*, 66(8):27–33, 2013.
DOI: 10.1063/PT.3.2081
ADS: 2013PhT....66h..27J

H. Ji, M. Burin, E. Schartman, and J. Goodman. Hydrodynamic turbulence cannot transport angular momentum effectively in astrophysical disks. *Nature*, 444:343–346, Nov. 2006.
DOI: 10.1038/nature05323
ADS: 2006Natur.444..343J

A. Kageyama, H. Ji, J. Goodman, F. Chen, and E. Shoshan. Numerical and experimental investigation of circulation in short cylinders. *Journal of the Physical Society of Japan*, 73:2424–2437, Sept. 2004.
DOI: 10.1143/JPSJ.73.2424
ADS: 2004JPSJ...73.2424K

J. B. Knight, H. M. Jaeger, and S. R. Nagel. Vibration-induced size separation in granular media: The convection connection. *Physical Review Letters*, 70:3728–3731, June 1993.
DOI: 10.1103/PhysRevLett.70.3728
ADS: 1993PhRvL..70.3728K

J. F. Kok and D. J. Lacks. Electrification of granular systems of identical insulators. *Physical Review E*, 79(5):051304, May 2009.
DOI: 10.1103/PhysRevE.79.051304
ADS: 2009PhRvE..79e1304K
arXiv: 0902.3411 [cond-mat.stat-mech]

J. F. Kok and N. O. Renno. Electrostatics in Wind-Blown Sand. *Physical Review Letters*, 100(1):014501, Jan. 2008.
DOI: 10.1103/PhysRevLett.100.014501
ADS: 2008PhRvL.100a4501K
arXiv: 0711.1341 [cond-mat.other]

D. J. Lacks and R. Mohan Sankaran. Contact electrification of insulating materials. *Journal of Physics D: Applied Physics*, 44:453001, Nov. 2011.
DOI: 10.1088/0022-3727/44/45/453001
ADS: 2011JPhD...44S3001L

L. Landau and E. Lifshitz. *Fluid Mechanics*, volume 6 of *Course of Theoretical Physics*. Pergamon Press, 2 edition, 1987.
ISBN: 0080339336
OCLC: 881165399
LCCN: 86030498

J. Latham. The electrification of snowstorms and sandstorms. *Quarterly Journal of the Royal Meteorological Society*, 90:91–95, Jan. 1964.
DOI: 10.1002/qj.49709038310
ADS: 1964QJRMS..90...91L

D. P. Lathrop. *Turbulent drag and transport in high Reynolds number Couette-Taylor flow*. PhD thesis, University of Texas at Austin, 1992.
OCLC: 28095857

D. P. Lathrop, J. Fineberg, and H. L. Swinney. Transition to shear-driven turbulence in couette-taylor flow. *Physical Review A*, 46:6390–6405, Nov. 1992a.
DOI: 10.1103/PhysRevA.46.6390
ADS: 1992PhRvA..46.6390L

D. P. Lathrop, J. Fineberg, and H. L. Swinney. Turbulent flow between concentric rotating cylinders at large reynolds number. *Physical Review Letters*, 68:1515–1518, Mar. 1992b.
DOI: 10.1103/PhysRevLett.68.1515
ADS: 1992PhRvL..68.1515L

M. Le Bars and P. Le Gal. Experimental Analysis of the Stratorotational Instability in a Cylindrical Couette Flow. *Physical Review Letters*, 99(6):064502, Aug. 2007.
DOI: 10.1103/PhysRevLett.99.064502
ADS: 2007PhRvL..99f4502L
arXiv: 0707.2661

S. Le Dizès and X. Riedinger. The strato-rotational instability of Taylor-Couette and Keplerian flows. *Journal of Fluid Mechanics*, 660:147–161, Aug. 2010.
DOI: 10.1017/S0022112010002624
ADS: 2010JFM...660..147L

V. Lee, S. R. Waitukaitis, M. Z. Miskin, and H. M. Jaeger. Direct observation of particle interactions and clustering in charged granular streams. *Nature Physics*, 11(9):733–737, July 2015. ISSN 1745-2481.
DOI: 10.1038/nphys3396

G. S. Lewis and H. L. Swinney. Velocity structure functions, scaling, and transitions in high-reynolds-number couette-taylor flow. *Physical Review E*, 59:5457–5467,

May 1999.
DOI: 10.1103/PhysRevE.59.5457
ADS: 1999PhRvE..59.5457L

X. Liao and K. Zhang. Inertial oscillation, inertial wave and initial value problem in rotating annular channels. *Geophysical & Astrophysical Fluid Dynamics*, 103 (2-3):199–222, apr 2009. ISSN 1029-0419.
DOI: 10.1080/03091920802326838
ADS: 2009GApFD.103..199L

D. Lide. *CRC handbook of chemistry and physics, 2003-2004*. CRC Press, Boca Raton, 84 edition, 2003.
ISBN: 0849304849
OCLC: 52548731
LCCN: 13011056

A. J. Liu and S. R. Nagel. Nonlinear dynamics: Jamming is not just cool any more. *Nature*, 396:21–22, Nov. 1998.
DOI: 10.1038/23819
ADS: 1998Natur.396...21L

C.-H. Liu, S. R. Nagel, D. A. Schecter, S. N. Coppersmith, S. Majumdar, O. Narayan, and T. A. Witten. Force Fluctuations in Bead Packs. *Science*, 269:513–515, July 1995.
DOI: 10.1126/science.269.5223.513
ADS: 1995Sci...269..513L

J. M. Lopez, F. Marques, and M. Avila. The Boussinesq approximation in rapidly rotating flows. *Journal of Fluid Mechanics*, 737:56–77, Dec. 2013.
DOI: 10.1017/jfm.2013.558
ADS: 2013JFM...737...56L
arXiv: 1304.5941 [physics.flu-dyn]

J. Lowell and W. S. Truscott. Triboelectrification of identical insulators. I. An experimental investigation. *Journal of Physics D: Applied Physics*, 19:1273–1280, July 1986a.
DOI: 10.1088/0022-3727/19/7/017
ADS: 1986JPhD...19.1273L

J. Lowell and W. S. Truscott. Triboelectrification of identical insulators. II. Theory and further experiments. *Journal of Physics D: Applied Physics*, 19:1281–1298, July 1986b.
DOI: 10.1088/0022-3727/19/7/018
ADS: 1986JPhD...19.1281L

J. Lu and R. A. Shaw. Charged particle dynamics in turbulence: Theory and direct numerical simulations. *Physics of Fluids*, 27(6):065111, June 2015.
DOI: 10.1063/1.4922645
ADS: 2015PhFl...27f5111L

J. Lu, H. Nordsiek, E. W. Saw, and R. A. Shaw. Clustering of Charged Inertial Particles in Turbulence. *Physical Review Letters*, 104(18):184505, May 2010a.
DOI: 10.1103/PhysRevLett.104.184505
ADS: 2010PhRvL.104r4505L

J. Lu, H. Nordsiek, and R. A. Shaw. Clustering of settling charged particles in turbulence: theory and experiments. *New Journal of Physics*, 12(12):123030, Dec. 2010b.
DOI: 10.1088/1367-2630/12/12/123030
ADS: 2010NJPh...12l3030L

T. S. Majmudar and R. P. Behringer. Contact force measurements and stress-induced anisotropy in granular materials. *Nature*, 435:1079–1082, June 2005.
DOI: 10.1038/nature03805
ADS: 2005Natur.435.1079M

P. S. Marcus, S. Pei, C.-H. Jiang, J. A. Barranco, P. Hassanzadeh, and D. Lecoanet. Zombie Vortex Instability. I. A Purely Hydrodynamic Instability to Resurrect the Dead Zones of Protoplanetary Disks. *The Astrophysical Journal*, 808:87, July 2015.
DOI: 10.1088/0004-637X/808/1/87
ADS: 2015ApJ...808...87M
arXiv: 1410.8143 [astro-ph.SR]

S. Maretzke, B. Hof, and M. Avila. Transient growth in linearly stable Taylor-Couette flows. *Journal of Fluid Mechanics*, 742:254–290, Mar. 2014.
DOI: 10.1017/jfm.2014.12
ADS: 2014JFM...742..254M
arXiv: 1304.7032 [physics.flu-dyn]

T. C. Marshall, M. P. McCarthy, and W. D. Rust. Electric field magnitudes and lightning initiation in thunderstorms. *Journal of Geophysical Research*, 100:7097–7103, Apr. 1995.
DOI: 10.1029/95JD00020
ADS: 1995JGR...100.7097M

S. Merbold, H. J. Brauckmann, and C. Egbers. Torque measurements and numerical determination in differentially rotating wide gap Taylor-Couette flow. *Physical*

Review E, 87(2):023014, Feb. 2013.
DOI: 10.1103/PhysRevE.87.023014
ADS: 2013PhRvE..87b3014M

C. S. Miner and N. N. Dalton. *Glycerol*. Reinhold Publishgin Corporation, New York, 1953.
OCLC: 567532
LCCN: 52014292

F. Nordsiek and D. Lathrop. Collective phenomena in granular and atmospheric electrification. Dataset uploaded to Digital Repository at the University of Maryland (DRUM), July 2015a.
DOI: 10.13016/M2ZK87
URL: `http://hdl.handle.net/1903/16867`

F. Nordsiek and D. P. Lathrop. Collective phenomena in granular and atmospheric electrification. *ArXiv e-prints*, Sept. 2015b.
arXiv: 1509.04214 [cond-mat.soft]

F. Nordsiek, S. G. Huisman, R. C. A. van der Veen, C. Sun, D. Lohse, and D. P. Lathrop. Azimuthal velocity profiles in Rayleigh-stable Taylor-Couette flow and implied axial angular momentum transport. *Journal of Fluid Mechanics*, 774: 342–362, July 2015.
DOI: 10.1017/jfm.2015.275
ADS: 2015JFM...774..342N
arXiv: 1408.1059 [physics.flu-dyn]

R. Ostilla-Mónico, E. P. van der Poel, R. Verzicco, S. Grossmann, and D. Lohse. Exploring the phase diagram of fully turbulent Taylor–Couette flow. *Journal of Fluid Mechanics*, 761:1–26, Dec. 2014a.
DOI: 10.1017/jfm.2014.618
ADS: 2014JFM...761....1O
arXiv: 1405.0124 [physics.flu-dyn]

R. Ostilla-Mónico, E. P. van der Poel, R. Verzicco, S. Grossmann, and D. Lohse. Boundary layer dynamics at the transition between the classical and the ultimate regime of Taylor-Couette flow. *Physics of Fluids*, 26(1):015114, Jan. 2014b.
DOI: 10.1063/1.4863312
ADS: 2014PhFl...26a5114O
arXiv: 1306.2911 [physics.flu-dyn]

R. Ostilla-Mónico, R. Verzicco, S. Grossmann, and D. Lohse. Turbulence decay towards the linearly stable regime of Taylor-Couette flow. *Journal of Fluid Me-*

chanics, 748:R3, June 2014c.
DOI: 10.1017/jfm.2014.242
ADS: 2014JFM...748R...3O
arXiv: 1311.2463 [physics.flu-dyn]

T. Pähtz, H. J. Herrmann, and T. Shinbrot. Why do particle clouds generate electric charges? *Nature Physics*, 6:364–368, May 2010.
DOI: 10.1038/nphys1631
ADS: 2010NatPh...6..364P
arXiv: 1003.5188 [cond-mat.soft]

M. S. Paoletti and D. P. Lathrop. Angular momentum transport in turbulent flow between independently rotating cylinders. *Physical Review Letters*, 106(2):024501, Jan. 2011.
DOI: 10.1103/PhysRevLett.106.024501
ADS: 2011PhRvL.106b4501P
arXiv: 1011.3475 [cond-mat.stat-mech]

M. S. Paoletti, D. P. M. van Gils, B. Dubrulle, C. Sun, D. Lohse, and D. P. Lathrop. Angular momentum transport and turbulence in laboratory models of keplerian flows. *Astronomy & Astrophysics*, 547:A64, Nov. 2012.
DOI: 10.1051/0004-6361/201118511
ADS: 2012A%26A...547A..64P
arXiv: 1111.6915 [physics.flu-dyn]

J. Park and P. Billant. The stably stratified Taylor-couette flow is always unstable except for solid-body rotation. *Journal of Fluid Mechanics*, 725:262–280, Jun 2013.
DOI: 10.1017/jfm.2013.186
ADS: 2013JFM...725..262P

A. Racina and M. Kind. Specific power input and local micromixing times in turbulent Taylor Couette flow. *Experiments in Fluids*, 41:513–522, Sept. 2006.
DOI: 10.1007/s00348-006-0178-x
ADS: 2006ExFl...41..513R

F. Ravelet, R. Delfos, and J. Westerweel. Influence of global rotation and Reynolds number on the large-scale features of a turbulent Taylor-Couette flow. *Physics of Fluids*, 22(5):055103, May 2010.
DOI: 10.1063/1.3392773
ADS: 2010PhFl...22e5103R
arXiv: 0712.2750 [physics.flu-dyn]

L. Rayleigh. On the dynamics of revolving fluids. *Proceedings of the Royal Society of London Series A*, 93(648):148–154, Mar 1917.
DOI: 10.1098/rspa.1917.0010
ADS: 1917RSPSA..93..148R

D. Richard. *Instabilités hydrodynamiques dans les écoulements en rotation différentielle*. Ph.d. thesis, Université Paris-Diderot - Paris VII, Dec 2001.
OCLC: 492387380
ADS: 2001PhDT.....9R
URL: `http://tel.archives-ouvertes.fr/tel-00001393`

D. Richard and J.-P. Zahn. Turbulence in differentially rotating flows. What can be learned from the Couette-Taylor experiment. *Astronomy & Astrophysics*, 347: 734–738, July 1999.
ADS: 1999A%26A...347..734R
URL: `http://aa.springer.de/bibs/9347002/2300734/small.htm`

W. A. D. Rudge. On the electrification produced during the raising of a cloud of dust. *Proceedings of the Royal Society of London Series A*, 90:256–272, May 1914.
DOI: 10.1098/rspa.1914.0050
ADS: 1914RSPSA..90..256R

J. C. Salevan. Granular triboelectric charging in sand and glass. Undergraduate thesis, University of Maryland at College Park, June 2012.
DOI: 10.6084/m9.figshare.1575779

C. Saunders. Charge Separation Mechanisms in Clouds. *Space Science Reviews*, 137:335–353, June 2008.
DOI: 10.1007/s11214-008-9345-0
ADS: 2008SSRv..137..335S

E. Schartman, H. Ji, and M. J. Burin. Development of a Couette-Taylor flow device with active minimization of secondary circulation. *Review of Scientific Instruments*, 80(2):024501, Feb. 2009.
DOI: 10.1063/1.3077942
ADS: 2009RScI...80b4501S

E. Schartman, H. Ji, M. J. Burin, and J. Goodman. Stability of quasi-keplerian shear flow in a laboratory experiment. *Astronomy & Astrophysics*, 543:A94, July 2012.
DOI: 10.1051/0004-6361/201016252
ADS: 2012A%26A...543A..94S
arXiv: 1102.3725 [astro-ph.IM]

H. T. Schlichting. *Boundary Layer Theory.* McGraw-Hill Science/Engineering/Math, 1979.
ISBN: 0070553343
OCLC: 3965880
LCCN: 78017794

R. A. Shaw. Particle-Turbulence Interactions in Atmospheric Clouds. *Annual Review of Fluid Mechanics*, 35:183–227, 2003.
DOI: 10.1146/annurev.fluid.35.101101.161125
ADS: 2003AnRFM..35..183S

R. A. Shaw, A. B. Kostinski, and D. D. Lanterman. Super-exponential extinction of radiation in a negatively correlated random medium. *Journal of Quantitative Spectroscopy and Radiative Transfer*, 75:13–20, Aug. 2002.
DOI: 10.1016/S0022-4073(01)00287-4
ADS: 2002JQSRT..75...13S

L. Shi, M. Avila, and B. Hof. Scale invariance at the onset of turbulence in couette flow. *Physical Review Letters*, 110(20):204502, May 2013.
DOI: 10.1103/PhysRevLett.110.204502
ADS: 2013PhRvL.110t4502S
arXiv: 1304.5446 [physics.flu-dyn]

T. Siu, J. Cotton, G. Mattson, and T. Shinbrot. Self-sustaining charging of identical colliding particles. *Physics Review E*, 89(5):052208, May 2014.
DOI: 10.1103/PhysRevE.89.052208
ADS: 2014PhRvE..89e2208S

B. M. Smirnov. Electrical cycle in the Earth's atmosphere. *Physics-Uspekhi*, 57: 1041, Nov. 2014.
DOI: 10.3367/UFNe.0184.201411a.1153
ADS: 2014PhyU...57.1041S

C. Sun and Q. Zhou. Experimental techniques for turbulent Taylor-Couette flow and Rayleigh-Bénard convection. *Nonlinearity*, 27:R89, Sept. 2014.
DOI: 10.1088/0951-7715/27/9/R89
ADS: 2014Nonli..27R..89S

G. I. Taylor. Stability of a Viscous Liquid Contained between Two Rotating Cylinders. *Royal Society of London Philosophical Transactions Series A*, 223:289–343, 1923.
DOI: 10.1098/rsta.1923.0008
ADS: 1923RSPTA.223..289T

G. I. Taylor. Fluid friction between rotating cylinders. i. torque measurements. *Proceedings of the Royal Society of London Series A*, 157(892):546–564, 1936a.
DOI: 10.1098/rspa.1936.0215
ADS: 1936RSPSA.157..546T

G. I. Taylor. Fluid Friction between Rotating Cylinders. II. Distribution of Velocity between Concentric Cylinders when Outer One Is Rotating and Inner One Is at Rest. *Proceedings of the Royal Society of London Series A*, 157:565–578, Dec. 1936b.
DOI: 10.1098/rspa.1936.0216
ADS: 1936RSPSA.157..565T

S. A. Triana. *Inertial waves in a laboratory model of the Earth's core*. PhD thesis, University of Maryland at College Park, 2011.
OCLC: 776907668
URL: `http://hdl.handle.net/1903/11480`

D. P. M. van Gils, G.-W. Bruggert, D. P. Lathrop, C. Sun, and D. Lohse. The Twente turbulent Taylor-Couette (T3C) facility: Strongly turbulent (multiphase) flow between two independently rotating cylinders. *Review of Scientific Instruments*, 82(2):025105, Feb. 2011a.
DOI: 10.1063/1.3548924
ADS: 2011RScI...82b5105V
arXiv: 1011.1572 [physics.flu-dyn]

D. P. M. van Gils, S. G. Huisman, G.-W. Bruggert, C. Sun, and D. Lohse. Torque Scaling in Turbulent Taylor-Couette Flow with Co- and Counterrotating Cylinders. *Physical Review Letters*, 106(2):024502, Jan. 2011b.
DOI: 10.1103/PhysRevLett.106.024502
ADS: 2011PhRvL.106b4502V
arXiv: 1010.0922 [physics.flu-dyn]

D. P. M. van Gils, S. G. Huisman, S. Grossmann, C. Sun, and D. Lohse. Optimal Taylor-Couette turbulence. *Journal of Fluid Mechanics*, 706:118–149, Sept. 2012.
DOI: 10.1017/jfm.2012.236
ADS: 2012JFM...706..118V
arXiv: 1111.6301 [physics.flu-dyn]

S. R. Waitukaitis, V. Lee, J. M. Pierson, S. L. Forman, and H. M. Jaeger. Size-Dependent Same-Material Tribocharging in Insulating Grains. *Physical Review Letters*, 112(21):218001, May 2014.
DOI: 10.1103/PhysRevLett.112.218001
ADS: 2014PhRvL.112u8001W
arXiv: 1309.2578 [cond-mat.soft]

F. Wendt. Turbulente strömungen zwischen zwei rotierenden konaxialen zylindern. *Ingenieurs et architectes suisses*, 4:577–595, 1933. ISSN 0939-1533.
DOI: 10.1007/BF02084936

Y. B. Zeldovich. On the Friction of Fluids Between Rotating Cylinders. *Proceedings of the Royal Society of London Series A*, 374:299–312, Feb. 1981.
DOI: 10.1098/rspa.1981.0024
ADS: 1981RSPSA.374..299Z

K. Zhang, P. Earnshaw, X. Liao, and F. H. Busse. On inertial waves in a rotating fluid sphere. *Journal of Fluid Mechanics*, 437:103–119, jun 2001. ISSN 1469-7645.
DOI: 10.1017/s0022112001004049
ADS: 2001JFM...437..103Z

D. S. Zimmerman. *Turbulent Shear Flow in a Rapidly Rotating Spherical Annulus*. PhD thesis, University of Maryland at College Park, 2010.
OCLC: 746851357
URL: `http://hdl.handle.net/1903/11184`